

Efficient and Reliable Mathematical Modeling Techniques for Multi-Phase Environmental Flows

By

KAVEH ZAMANI

B.S. (Iran University of Science and Technology) 2004

M.S. (Sharif University of Technology) 2006

DISSERTATION

Submitted in partial fulfilment of the requirements for the degree of

Doctor of Philosophy

in

Civil and Environmental Engineering

in the

Office of Graduate Studies

of the

University of California, Davis

Approved:

Fabián A. Bombardelli (Chair)

Timothy R. Ginn

Carlos E. Puente

Committee in Charge

2015

Efficient and Reliable Mathematical Modeling Techniques for Multi-Phase Environmental Flows

Abstract

This research is on using recent techniques of Software Quality Assurance (SQA) and developing Verification and Validation and Uncertainty Quantification (VVUQ) tools to improve mathematical models of contaminant, sediment, and air-bubble transport in natural aquatic bodies. A comprehensive toolkit for VVUQ is developed for: a) code and calculation verification with Methods of Exact Solutions (MES), Method of Manufactured Solutions (MMS), and cross-code verification; b) Richardson extrapolation for code and calculation verification; c) model validation via common statistical methods and model skill assessment metrics; d) quantification of uncertainty in numerical discretization of PDEs. In the next section of this dissertation, seven new closed-form analytical solutions of scalar transport equation devised for code verification with MES. The set of developed analytical solutions was complete in the sense that it is able to check nonlinearity as well as spatial and temporal non-homogeneity in all terms of scalar ADR equation. In addition, a 2D analytical description of air-bubbles distribution in hydraulic jumps was derived. The new analytical model was validated versus various empirical datasets via common model skill assessment metrics. The experimental dataset was also used to design an analytical-empirical model for air entrainment/detrainment in the two-phase flows of hydraulic jumps. In the rest of this dissertation the emphasis was changed from two-phase flows of air and water into two-phase flows of sediment particles and water. First, a comprehensive assessment of former methods of computing total sediment discharge with Einstein's method was conducted. Sequential and parallel subroutines of computing the Einstein's integrals with existing methods

developed. Then local and global accuracy, convergence behavior, singularities, CPU time and parallelization efficiency were studied via common metrics of model skill assessment. Second, four new methods of computing Einstein's integrals for calculation of total sediment discharge were devised: a) a numerical technique which exploits the similarity of integrand functions to devise a numerical recycling of values for reduction of computational time; b) nested adaptive Gauss-Kronrod quadrature; c) perturbation techniques to find a fast asymptotic series representation to approximate the Einstein integrals; d) semi-analytical solutions based on Gauss hypergeometric function. All of the developed methods were benchmarked against machine-precision-accurate results. Efficiency of those new methods in parallel computing was evaluated.

Acknowledgments

I would like to thank my advisor, Fabián Bombardelli, for his patient support, humble mentoring, and endless help throughout my uneven PhD studies. I truly appreciate Timothy Ginn for his scholarly support, wise advice and intellectual integrity. I would also like to thank Carlos Puente for his valuable inputs on my papers and compassionate helps in my PhD qualification exam. During my PhD, I asked many questions from David Schoellhamer and Peter Smith about sediment transport and computational hydraulics, they either answered me or referred me to the most appropriate literature. Robert Guy, Lynn Bennethum, Roland Freund, Greg Miller, and Joongcheol Paik patiently answered my naive (even funny!) mathematical/numerical questions. Mohamed Hafez, Bahram Ravani, Farshid Mojaver, Abbas Afshar and Wolfgang Kollmann helped me with academic and scientific challenging problems. Learning through collaboration with William Fleenor, and Kirk Nelson is thoroughly acknowledged. Masoud Kayhanian kindly aided me with revision of manuscripts and proposals writing. Collaboration with Eli Ateljevich, Parviz Nader, and Jamie Anderson from Department of Water Resources was a unique experience. Sashi Kunnath, Gerry Puckett, Ali Daddel, and Shrini Upadhyaya provided me with opportunities of not only improving my teaching skills but also put food on the table. I sincerely appreciate scholarly conversations and nice classes by Zia Hosseinipour, Levent Kavvas, Wesley Wallander, Jay Lund and Yannis Dafalias. Last but not least, one of the key factors which vividly smoothed the burden of PhD - in diaspora - for me, and helped me barely climbing up the never-ending wall of PhD was the accompany of my colleagues in 1011 Lab. Tim, Mohamed, Ahmed, Sevinc, Shima, Mehrdad, Devi, Andrew, Amin, Mehdi, Arash, Babak, Alex, Titus, Juan Pablo, Kervi, Dane, Patricio, Kristin, Arti, Linsey, James, Davinder, Laura, and Arturo, I will never forget the unique and friendly work environment, discussions and mutual learning we had.

Dedication

To all my teachers, peers and students

Not only for the things I learned from them, for things they showed me I still have to learn

تقدیم بہ معلمان صدیق، یاران دلسوز، راہنمایان سلیم النفس و خردمندم

خانم پری قاسمیان و آقایان صفر زمانی و ایرج آجودانی

Table of Contents

List of Tables	xi
List of Figures	xiii
Chapter 1: Introduction	
1.1. Purpose	1
1.2. Organization	2
Chapter One References	3
Chapter 2: Review of Contamination and Sediment Transport Modeling in Vadose Zone, Wetlands and Marshes	
2.1. Pollutant Transport in Vadose Zone	4
2.1.1. Water potential in the unsaturated zone	5
2.1.2. Governing equation of flow in vadose zone	5
2.1.3. Preferential flow	11
2.1.4. Deterministic approach to model solute transport in the vadose zone	13
2.1.5. Codes for numerical solution of vadose zone flow and transport	22
2.2. Review of Wetland Sediment Transport Modeling	27
2.2.1 Wetland sediment process	27
2.2.2. Mathematical representation of sediment transport in wetlands	29
2.2.3. Sediment transport models – hierarchy in complexity	32
2.2.4. Final remarks on sediment transport modeling in wetlands	35
Chapter Two References	37
Chapter 3: Analytical Solutions of Nonlinear and Variable-Parameter Transport Equations for Verification of Numerical Solvers	
3.1. Introduction	50
3.2. Background Methodologies	54
3.2.1. Reduction of ADR equation to heat equation	54
3.2.2. Transformation to simplify time dependent ADR	55

3.2.3. Fundamental solution of the inhomogeneous heat equation	55
3.3. Analytical Solutions to Test Nonlinearity	56
3.3.1. Diffusion with nonlinear dispersion coefficient and source term	56
3.3.2. Uniform advection dispersion with nonlinear source term	58
3.3.3. Burgers' equation for verification of transport solver	59
3.4. Analytical Solutions for Mass Conservative, Variable-Parameter Transport Equations	60
3.4.1. ADR equation with spatially varying coefficients	61
3.4.2. ADR equation with time-dependent transport variables	62
3.4.3. Spatiotemporal varying flow field	63
3.5. Application of the Derived Solutions in Code Verification	65
3.5.1. Verification with the constant ADR solution	66
3.5.2. Verification with the nonlinear diffusion-reaction solution	67
3.5.3. Verification with advection dispersion with nonlinear source term	67
3.5.4. Verification with nonlinear burgers' equation	68
3.5.5. Verification with spatially-varying coefficient ADR solution	68
3.5.6. Verification with temporally-varying coefficient ADR solution	69
3.5.7. Verification with analytical solution of tidal flow	69
3.6. Metrics for Code Verification and Accuracy Validation	70
3.7. Alternative Code Verification Approaches	71
3.8. Conclusions and Final Remarks	72
Appendices of Chapter 3	
3-A. Derivation of time dependent transport equation	74
3-B. Numerical discretization of the ADR equation	75
Chapter Three References	77
Chapter 4: Assessment of Sequential and Parallel Implementation of Current Methods for The Evaluation of Einstein's Integrals	
4.1. Introduction	102
4.2. Methods for the Calculation of Einstein's Integrals	104
4.3. Assessment of the Efficiency and Accuracy of Existing Methods	107

4.4. Parallelization Efficiency of Algorithms	110
4.5. Summary and Conclusions	111
Appendices of Chapter 4	
4-A. Existing methods of approximation of Einstein's integrals	113
4-B. Composite Simpson's rule	116
4-C. Statistics of model skill assessment	117
Chapter Four References	119
Chapter 5: Novel methods to Calculate Sediment Volumetric Flow Rate with Einstein's Integrals: Semi-Analytical and Numerical Approaches	
5.1. Introduction	128
5.2. New Numerical Schemes for Integration of J1 and J2	132
5.2.1 Gauss-Kronrod quadrature	132
5.2.2. Expedite calculation via recycling the evaluated integrand	134
5.3. Approximation via Asymptotic Expansion	136
5.4. Semi-analytical Solution by Hypergeometric Functions	138
5.4.1. Manipulation of the hypergeometric function solution	139
5.4.2. Approximation based on hypergeometric function	141
5.5. Efficiency of Parallelization of New Algorithms	142
5.6. Discussion of New Methods	143
5.7. Summary and Conclusions	146
Appendices of Chapter 5	
5-A. Analytical solutions of Einstein's integrals in integer Rouse numbers	148
5-B. Quantitative measures of method adequacy	148
5-C. Coefficients of Gauss-Kronrod method	150
5-D. Expansion of Einstein's integrals using Maclaurin series	151
5-E. Numerical solvers for Gauss hypergeometric function	152
Chapter Five References	154
Chapter 6: Air Distribution in Hydraulic Jumps via Two-Phase Flow Theory	
6.1. Introduction	170

6.2. Formulation of Interpretative Model	173
6.3. Analytical Solutions for Lower and Upper Regions	177
6.3.1. Approximation for the lower and shear region	177
6.3.2. Analytical solution procedure	178
6.3.3. Boundary conditions	180
6.3.4. Analytical solution for air bubbles distribution in the upper region	180
6.4. Experimental Validation of the Analytical Solution	181
6.5. Air Entrainment and Detrainment	183
6.5.1. Distribution and location of maximum air concentration	183
6.5.2. Distribution of mass of air in hydraulic jump	184
6.6. Summary and Conclusions	185
Appendix of Chapter 6	
6-A. Bubbles rise velocity under hydrostatic conditions	187
Chapter Six References	189
Chapter 7: Numerical Model Verification	
7.1. Introduction	212
7.2. Verification Criteria for Numerical Solvers	213
7.2.1. Mesh-convergence study as a verification method	214
7.2.2. Ambiguity in the mesh convergence test	216
7.2.3. Error measures and their qualification	219
7.2.4. Observed order of accuracy	220
7.3. VAVUQ: Toolkit for Verification and Validation, and Uncertainty Quantification in Environmental-Fluid-Mechanics Simulations	222
7.3.1. Example one: Richardson Extrapolation	223
7.3.2. Example two: mesh convergence test with known benchmark (MES)	224
7.3.3. Example three: quantitative model skill assessment (validation)	226
7.3.4. Example four: visualization of the results' difference in various meshes	227
7.3.5. Example five: numerical uncertainty quantification	228
Appendix of Chapter 7	
7-A. Snapshots from VAVUQ GUI	231

Chapter Seven References	233
Chapter 8: Conclusions and Future Path of Research	
8.1. Final words	235
Chapter Eight References	242
Appendix A: Using Software Quality and Algorithm Testing to Verify a One-dimensional Transport Model	
A.1. Introduction	244
A.2. Testing Requirements	246
A.3. Testing Principles	247
A.4. Algorithm Test Suite Description	253
A.5. Challenges and Issues with Tests	256
A.6. Conclusions	257
Appendix A References	259
Appendix B: Hydrogeologic Characterization	
B.1. Introduction	261
B.2. Borehole Samples and Groundwater Monitoring Wells	262
B.2.1. Investigation borehole drilling	262
B.2.2. Cone penetrometry, permeametry, and electrical conductivity logging	264
B.2.3. Electrical resistivity survey	266
B.3. Hydraulic Methods for In-situ Conductivity Measurement	268
B.3.1. Characterization of the hydraulic gradient and flow rates	269
B.3.2. Recharge estimation	271
B.4. Summary	272
Appendix B References	274

List of Tables

Table 2-1. Average values of soil water characteristic curve parameter obtained by experimental means.	9
Table 2-2. Summary of the vadose zone models by USGS, EPA and USDA.	26
Table 3-1. Summary of analytical solutions of primarily single-species transport equations. The described literature possesses particular emphasis on the purpose of code verification.	97
Table 3-2. Accuracy metrics for assessment of numerical model results versus benchmark values.	100
Table 3-3. Summary of the seven analytical solutions for numerical verification of transport solvers discussed in this paper.	101
Table 4-A1. Regression coefficients for Equations (4-11) and (4-12).	115
Table 4-1. Global accuracy of existing methods of calculation or approximation of Einstein's integrals (tested over a data set of 960 bedload-layer thicknesses and Rouse numbers).	126
Table 4-2. Accuracy of the partial sum in the J2 convergent series approximations with various number of terms (in %).	127
Table 5-A1. Analytical solutions of Einstein's integrals in integer Rouse numbers.	148
Table 5-A2. Weights of Gauss-Kronrod (7-15) abscissae.	150
Table 5-1. Relative speed up of J1/J2 integration methods via retrieving the integrand functional values from the J2/J1 numerical integration. Values averaged based on a dataset of 960 values of bedload-layer thickness and Rouse number.	167
Table 5-2. Global accuracy of new methods of calculation or approximation of Einstein integrals (tested over a dataset of 960 bedload-layer thicknesses and Rouse numbers).	168
Table 5-3. Speedup factor for parallel computing of new methods with various parameters, run on a dataset of 10000 pairs of (E, z) values.	169
Table 6-1. Summary of experimental investigations of hydraulic jump with particular emphasis on air entrainment.	207
Table 6-2. Flow and measurement condition of experimental data which is used for validation of equations (6-18) and (6-22).	209

Table 6-3. Validation statistics of new analytical solution (6-18) for lower region compared to observation and numerical simulation.	210
Table 6-4. Validation statistics of upper part analytical solution (6-22) compared to observation and numerical simulation.	211
Table 7-1. Convergence rates of two dimensional lid driven cavity flow on the grid resolutions of $h_4=92\times 92$; $h_3=128\times 128$; $h_2=182\times 182$ and $h_1=256\times 256$ and $r_{12}=h_1/h_2$; $r_{23}=h_2/h_3$; $r_{34}=h_3/h_4$.	224
Table 7-2. Metrics of models skill validation for three different simulation of free surface profile of air-water mixture in hydraulic jump.	227

List of Figures

- Figure 2-1.** Schematic of Soil-water characteristic curve, shown for generic cases of sandy or clayey soils. Both curves reach water contents equal to porosity when suction is zero (at the water table). Matric suction is defined as the negative of the pressure head, and h_b is the air entry suction at which air will enter the porous media. Insert: the SWC curve measured in the drying of a given soil differs from that determined by wetting of the same soil, as a result of residual entrapment during drying and residual air entrapment during wetting. The resulting hysteresis is not an artifact but is a real behavior of soil hydraulics in situ. 7
- Figure 3-1.** Schematic of the tidal forcing domain in a dead-end harbor basin. (top) Basin cross section with the initial position of the free surface. (bottom) Position of the pollution mass subjected to the tidal forcing. Tidal compression happens in mid tidal period [adopted from Wang et al., 2008]. 87
- Figure 3-2.** Comparison of analytical (exact) and numerical solutions of the advection-diffusion-reaction equation with uniform flow, linear decay and constant dispersivity, $\Delta t=100$ s and $\Delta x=100$ m. 88
- Figure 3-3.** Evolution in time of the numerical and exact solutions to the nonlinear diffusion-reaction equation, $\Delta t=0.001$ s and $\Delta x=0.312$ m. 89
- Figure 3-4.** Analytical and numerical solutions for the advection-diffusion-reaction equation with uniform flow and constant dispersivity, subjected to nonlinear decay, $\Delta t=0.01$ s and $\Delta x=0.12$ m. 90
- Figure 3-5.** Comparison of numerical and analytical solutions of the Burgers' equation for verification purpose of an ADR equation, $\Delta t=0.05$ s and $\Delta x=1.0$ m. Numerical solution evolves in time and shows over-shooting near the front. 91
- Figure 3-6.** Evolution in time of a pollution front subjected to non-uniform advection and spatially-varying dispersion coefficient. Comparison of numerical and analytical solutions, $\Delta t=7.81$ s and $\Delta x=39.06$ m. 92
- Figure 3-7.** Evolution in time of a pollution front subjected to non-uniform advection and temporally-varying dispersion coefficient. Comparison of numerical and analytical solutions, $\Delta t=0.06$ s and $\Delta x=0.28$ m. 93

Figure 3-8. Evolution in time of a pollutant mass subjected to a tidal flow field. Concentration distribution subjected to one cycle of tidal advection is compared with its initial distribution as benchmark. Tidal compression of plume in half of the tidal period is noticeable, $\Delta t=174.5$ s and $\Delta x=400$ m.	94
Figure 3-9. Evolution in time of a pollutant mass subjected to tidal flow field and linear decay, $\Delta t=174.5$ s and $\Delta x=400$ m.	95
Figure 3-10. Observed versus formal order of accuracy. Mesh convergence study for the tidal advection-reaction test. Norm L_∞ measures the worst error in the domain; L2 is the energy norm of the errors; and norm L1 denotes the average of absolute errors in the	96
Figure 4-1. Local relative error of five methods for the calculation of the J_1 Einstein integral for different values of bedload-layer thickness, over various Rouse numbers (Guo and Julien’s method with 10 terms in the partial sum of Eq. (4-7)).	122
Figure 4-2. Local relative error of five methods for the calculation of the J_2 Einstein integral for different values of bedload-layer thickness, over various Rouse numbers (Guo-Julien’s method with Eq. (4-10) closure for the first infinite sum and 50 terms in the second partial sum).	123
Figure 4-3. CPU time of various methods for computing Einstein’s integrals for a set of 960 pair values of Rouse number and bedload-layer thickness. The number after “Guo Julien” refers to the number of terms in the partial sum of the infinite series (left term in Equation (4-8)). Composite Simpson method results were obtained with 500 points.	124
Figure 4-4. Speedup for the parallelization of existing methods for the calculation of Einstein’s integrals (left: J_1 and right: J_2 integral). In this case, Guo and Julien’s method was executed with Eq. (4-10) closure and the first 100 terms in the partial sum of Eq. (4-8) for computing the J_2 integral. It is worth mentioning that the above curves are computed for a dataset of 9000 Rouse numbers and bedload-layer thicknesses.	125
Figure 5-2. Schematic of sediment particles and velocity distribution in free surface flow.	158
Figure 5-2. Schematics of adaptive integration mesh size based on rate of change of integrand function with various Rouse numbers for the first and second Einstein’s integrals.	159
Figure 5-3. Plot of the Einstein integrals computed by Gauss-Kronrod 7-15 quadrature.	160

Figure 5-4. Error of Maclaurin expansion of the J1 integral with different number of terms.	161
Figure 5-5. Error of Maclaurin expansion of the J2 integral with different number of terms.	162
Figure 5-6. Plot of the Einstein integrals J_1 and J_2 computed by two term Maclaurin series expansion of Einstein integrals.	163
Figure 5-7. Plot of the Einstein integrals J_1 and J_2 computed by Gauss hypergeometric function via method of Eq. (5-A6).	164
Figure 5-8. Plot of the Einstein integrals J_1 and J_2 computed by Gauss hypergeometric function via numerical library by Jin (2015).	165
Figure 5-9. CPU time of new developed methods for computing a set of 960 Rouse numbers for various bed layer thicknesses (same platform and same dataset as Figure 5-5).	166
Figure 6-1. Schematic of air concentrations in hydraulic jumps.	195
Figure 6-2. Approximation $\sqrt{(1-c)}$ with the first two terms of Taylor series expansion, exact value (solid blue) versus approximated (maroon color dashed line), normalized truncation error versus concentration (right axes).	196
Figure 6-3. Comparison of air distribution in depth at location $x-x_{toe}=0.2$ m from the jump toe, analytical solution (solid line) versus measurements (dots), and former formula by Chanson (1995), (cross). Run T8-5 by Chanson and Brattberg (2000); $Fr=8.48$.	197
Figure 6-4. Comparison of air distribution in depth at location $x-x_{toe}=0.4$ m from the jump toe, analytical solution (solid line) versus measurements (dots) and former formula by Chanson (1995), (cross). Run T8-5 by Chanson and Brattberg (2000), $Fr=8.48$.	198
Figure 6-5. Comparison of air distribution in depth at location $x-x_{toe}=0.07$ m from the jump toe, analytical solution (solid line) versus measurements (dots) and former formula by Chanson (1995), (cross). Run P10-C5, $Fr=6.05$, (Chanson 1995).	199
Figure 6-6. Comparison of air distribution in depth at location $x-x_{toe}=0.1$ m from the jump toe, analytical solution (solid line) versus measurements (dots), and former formula by Chanson (1995), (cross). Run P10-C6, $Fr=6.05$, Chanson (1995).	200

Figure 6-7. Comparison of air distribution in depth at location $x-x_{\text{toe}}=0.2$ m from the jump toe, analytical solution (solid line) versus, run P10-C7 Chanson 1995 (dots), and former formula by Chanson (1995), (cross), $Fr=5.66$.	201
Figure 6-8. Comparison of normalized depth versus air concentration data with and analytical solution given by equation (6-22) (solid line). Froude numbers vary from 2 to 14, statistics of the comparison in the recirculation and shear layer regions are provided in Table 6-3. Datasets of $Fr=1.98, 2.43, 3.65$ and 4.82 are tests a, b, c, and d of Murzyn et al. (2005), respectively. All data of $Fr=6.05$ were measured by Chanson (1995). $Fr=8.47$ measured by Chanson and Brattberg (2000) and $Fr=10.76$ and $Fr=14.27$ are reported by Gualtieri and Chanson (2007).	202
Figure 6-9. Location of maximum air concentration, experiment versus empirical formulae by Rajaratnam (1962).	203
Figure 6-10. Air concentration distribution along the hydraulic jump.	204
Figure 6-11. Schematic of interfacial air mass exchange calculation methodology based on mass balance.	205
Figure 6-12. Entrapped air mass distribution along the hydraulic jump.	206
Figure 7-1. Suggested procedural flow of code verification actions in different situations.	215
Figure 7-2. Schematic of asymptotic zone of convergence (after Graziani, 2008). In the zone one, round off error and iteration error take over; zone two is appropriate zone for numerical modeling and mesh convergence test; and zone three is mesh sizes where the problem is under resolved.	218
Figure 7-3. Schematic of lid-driven cavity flow (after Ghia et al., 1982).	223
Figure 7-4. Numerical and analytical solution of concentration plume in a dead-end harbor subjected to tidal forcing (Zamani and Bombardelli, 2014).	225
Figure 7-5. Mesh convergence study for four mesh sizes, tidal advection reaction of a pollution in dead-end harbor basin.	225
Figure 7-6. Numerical model of hydraulic jump: Modeled free surface profile versus laboratory measurements by Murzyn et al. (2007).	227

Figure 7-7. Difference in pressure numerical calculation between two different meshes sizes, for a lid-driven cavity flow. Most of the difference happens in the top right and top left corners next to the moving lid.	228
Figure 7-8. Pressure numerical solution difference between the finest mesh and the second finest mesh.	229
Figure 7-9. Upper and lower range of numerical calculation difference based of GCI for confidence interval of 99% and four mesh refinements (structured mesh).	230
Figure 7-10. Choose between Verification and Validation subroutines.	231
Figure 7-11. Verification with and without known benchmark solution.	231
Figure 7-12. Interpolation method for conversion of results to same grid points	231
Figure 7-13. Selection of output level of details.	232
Figure 7-14. Confidence level for uncertainty quantification.	232
Figure A-1. Relationship between software testing components and algorithmic testing.	247
Figure A-2. Transport algorithm testing with incremental complexity.	254

Chapter 1: Introduction

1.1. Purpose

River, estuarine, wetlands and vadose-zone transport phenomena have tremendous implications on environmental processes, and therefore on ecosystem health. As a consequence, they have notable implications on local economies, agriculture, and on management and planning of coastal civil works. Numerical models are often used to increase our understanding of contaminant transport, water quality and sediment transport processes, and to solve practical, crucial problems associated with tidal marshes environments. Numerical models are relatively inexpensive and they are employed as an essential tool by operators, decision makers and regulators in different estuaries of the world. In particular, diverse numerical simulations of flow and water quality have been developed to date, many directly or indirectly addressing transport phenomena in environmental aquatic body.

In the last decades of the 20th century, computational power increased dramatically and numerical “modeling” to some extent substituted experimentally driven knowledge acquisition. Comparison of the design process of e.g. the Boeing 727 in the 1950s and the Boeing 787 in the 2000s reveals the severe changes that have occurred in the design and analysis tools over five decades. The former was completely designed based on analytical methods and wind tunnel testing, whereas 85% of the latter was designed and tested with computational soil/fluid mechanic codes (Hale, 2006; Oberkampf and Roy, 2010). As computational methods continue to play a larger role in the world of science and engineering, crucial questions arise: How far we can trust a model? And if there is an error is it does it originate in computational flaws? or in the models inherent structure? or uncertainty in parameters and initial/boundary conditions. The

methods to assess reliability of numerical models are basically developed for Nuclear Engineering Safety and Aeronautical Science in 1990s (Roache, 2009; Oberkampf and Roy, 2010). The main stream of this research is about putting light on the questions of reliability of numerical codes for environmental fluid mechanics. In particular, I study models of sediment transport and air-bubble water mixture in surface water and passive scalar transport in tidal river networks.

This research has two major parts; in one I developed tool/methods for verification and validation, uncertainty quantification (VVUQ) of transport numerical models and in the other I used toward designing more efficient models for two-phase flows of sediment and water and oxygen and water mixtures. A brief overview of this dissertation is given in the next section.

1.2. Organization

This dissertation is divided into eight chapters. A short overview of motivation and organization of the study is presented in this chapter. The second chapter is literature review and has two parts: first, review of pollutant transport modeling in unsaturated zone, and second review of sediment transport modeling in shallow-water vegetated tidal marshes and wetlands. The former is published in “Chow’s Handbook of Applied hydrology, 2nd Edition” by Vijay Singh as a book chapter. The latter is accepted for publication in special issue on wetland modeling in ASCE-Journal of Hydrologic Engineering.

Chapter three devised methods for verification of one dimensional scalar transport equation. Methods in that chapter are comprehensive and can be employed to check any nonlinearity or non-homogeneity in the solver. This chapter is published as a research article in Journal of Environmental Fluid Mechanics in 2014.

Chapter four is on comprehensive validation of methods of computing total sediment discharge with Einstein's integrals, which has been done in parallel and sequential computing. Chapter five is the following of the work of chapter four, which is designing new methods for the same purpose and again validation of them via common model skill assessment metrics. Chapter four is under review in ASCE Journal of Hydraulic Engineering as a technical note and chapter five is submitted to the same journal for possible publication as technical paper.

Chapter six is on analytical and empirical models for description of air distribution in hydraulic jumps. In this chapter I validate my developments versus experimental data from various sources. This chapter will be submitted to the special issue of two-phase flow in the Journal of Environmental Engineering.

Chapter seven is on a novel toolkit for general purpose verification, validation and uncertainty quantification (VVUQ). I discussed the basic equations and provide five examples to introduce the new open source software. The material presented in this chapter will be submitted to the Journal of Computers and Geoscience. The final chapter (chapter eight) summarizes key findings and presents conclusions and suggestions for future path of research. This dissertation has two appendixes: A) on the application SQA techniques in development of a transport code test suite. B) on the hydrogeological characterization, both has been published.

Chapter One References

1. Oberkampf, WL, Roy, CJ (2010) Verification and validation in scientific computing. Cambridge University Press, Cambridge
2. Roache, PJ (2009) Fundamentals of verification and validation. Hermosa Publishers
3. Hale, J (2006). Accessed online on 12/01/2015, http://www.boeing.com/commercial/aeromagazine/articles/qtr_4_06/AERO_Q406_article4.pdf

Chapter 2: Review of Contamination and Sediment Transport

Modeling in Vadose Zone, Wetlands and Marshes

2.1. Pollutant Transport in Vadose Zone¹

The vadose zone extends downward from the terrestrial land surface to the groundwater table. In this zone soil pores are filled with both air and water, and depths can range from zero as in wetlands and marshes, to hundreds of meters in arid areas. Movement of water, vapor, chemicals and microbes through the vadose zone controls groundwater recharge rates and quality, surface runoff and flooding, surface and subsurface ecosystem community dynamics, and agrichemical impacts to groundwater. The vadose zone often serves as a buffer because through the processes of infiltration, evapotranspiration, and redistribution, infiltrating aqueous solutions are exposed to air, mineral, and biotic phases that can attenuate groundwater pollution impacts from surface activities. Therefore, understanding of transport in the vadose zone is essential in water quality management, soil and irrigation management, and preventing groundwater contamination. In this chapter firstly we briefly review the basic processes that govern flow and transport of solutes and suspensions in the unsaturated zone, and secondly we consider analytical and numerical techniques of quantifying transport in unsaturated zone. The scope of this brief review is restricted to continuum-mechanical representations of aqueous flow and transport processes, and does not cover phase change, soil-matrix deformations, pore-scale representations or transport via vapor or other (multiple) phases. As most problems associated with pollution of infiltration water focus on vertical flow, we restrict our consideration to vertical infiltration processes.

¹ Section 2.1 of Chapter 2 was accepted for publication as a book chapter: Zamani, K, and Ginn, T.R. (2016) "Pollutant Transport in Vadose Zone" Chapter 68 in "Chow's Handbook of Applied Hydrology, Second Edition" Ed. Vijay Singh, McGraw-Hill.

2.1.1. Water potential in the unsaturated zone

Soil water potential (in energy per self-weight, units of length) is a convenient collection of causes for water to move to another location in a soil matrix into a single quantity h :

$$h = \psi_s + \psi_e + \psi_z + \psi_p \quad (2-1)$$

where ψ_s is the solute (or osmotic) potential, ψ_e the electrochemical potential, ψ_z is gravimetric potential equal to elevation z , and ψ_p is matric potential. The matric potential (or tensiometer pressure potential) describes the effects of all the forces on the soil water other than gravity and solutes (Jury and Horton, 2004, p. 54-55), In sandy media, the matric potential is primarily due to presence of the air-water interfaces in the porous matrix, that leads to a jump discontinuity between pressures in the air and water phases called the capillary pressure, so that $p_c = p_a - p_w$. With air pressure assumed constant and set to zero ('gage' pressure), the water phase pressure is negative and the matric potential is commonly defined as $\psi_p = p_w/(\rho g)$ where ρ is the water density and g the acceleration due to gravity. For practical concerns solute and electrochemical potentials are usually considered spatially and temporally invariant (Hillel, 1998), so that the total potential of water in the vadose zone is commonly written as $h = -\psi_p + \psi_z = -\frac{p_w}{\rho g} + z$. "Matric suction" ψ_p is defined as the negative of the pressure head, $-p_w/(\rho g)$. Note that as we approach the water table from above the (negative) p_w increases to zero (gage pressure) so that at the water table $h = z$.

2.1.2. Governing equation of flow in vadose zone

Vertical flow of water in unsaturated soil satisfies mass (here volume) conservation

$$\frac{\partial \theta}{\partial t} = -\frac{\partial q}{\partial z} - S \quad (2-2)$$

In which, θ is the volumetric water content [$\frac{L^3}{L^3}$], t is time [T], z is vertical coordinate [L], q refers to flow per unit area [$\frac{L}{T}$], and S accounts for all forms of sink and source [$\frac{1}{T}$], for example root uptake. Combining Eq. (2-2) with the Darcy law in z direction $q = -K \frac{\partial h}{\partial z}$ gives:

$$\frac{\partial \theta}{\partial t} = \frac{\partial}{\partial z} \left[K \frac{\partial h}{\partial z} \right] - S \quad (2-3)$$

where K is unsaturated hydraulic conductivity of the soil [$\frac{L}{T}$] and h is total soil-moisture potential [L]. Expanding the total potential in Equation (2-3) yields:

$$\frac{\partial \theta}{\partial t} = \frac{\partial}{\partial z} \left[K(\theta) \left(-\frac{\partial \psi_p}{\partial z} + \frac{\partial \psi_z}{\partial z} \right) \right] - S = -\frac{\partial}{\partial z} \left(K(\theta) \frac{\partial \psi_p}{\partial z} \right) + \frac{\partial}{\partial z} K(\theta) - S \quad (2-4)$$

where we have used the fact that $\psi_z = z$. Equation 4, known as Richards' equation, is the partial differential equation (PDE) governing the vertical flow of water in variably saturated soil. On the right hand side, the first term reflects flow of water by matric forces, that can dominate e.g. during infiltration into a dry soil, where the force draws water from wet locations toward drier locations. The second term reflects the flow due to gravity. In cases where the first term dominates the resulting equation is one of nonlinear diffusion; in cases where the second term dominates the matric term may be ignored and the resulting equation is a kinematic wave equation (Charbeneau, 2006). In the derivation of eq. (2-4) we assumed constant temperature, constant air pressure and no resistance to water flow due to the air phase, non-deformable soil structure, incompressible water, and dilute solute (constant water density).

2.1.2.1 Soil-water characteristic curves

Equation (2-4) requires closure by specifications of functions linking θ to ψ_p and K to θ .

The former is defined through the soil-water characteristic curve (SWC), $\theta(\psi_p)$ (or $\psi_p(\theta)$), that defines the amount of water retained in a particular soil at a given matric potential. The SWC curve shape is related to the distribution of size and connectivity of pores in soil structure. Figure 2-1 shows generic SWC curves for soils of different textures, particle size and pore size

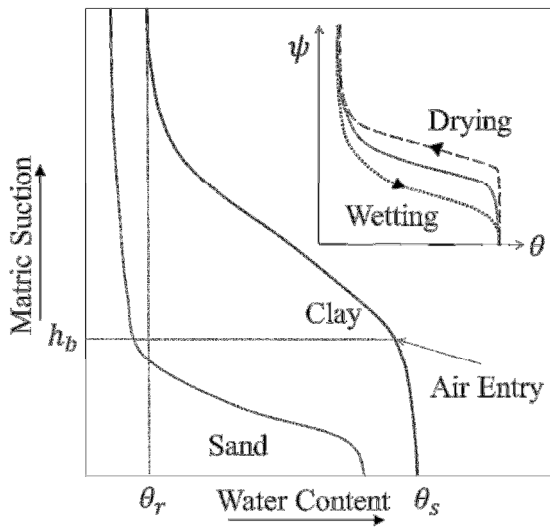


Figure 2-1. Schematic of Soil-water characteristic curve, shown for generic cases of sandy or clayey soils. Both curves reach water contents equal to porosity when suction is zero (at the water table). Matric suction is defined as the negative of the pressure head, and h_b is the air entry suction at which air will enter the porous media. Insert: the SWC curve measured in the drying of a given soil differs from that determined by wetting of the same soil, as a result of residual entrapment during drying and residual air entrapment during wetting. The resulting hysteresis is not an artifact but is a real behavior of soil hydraulics in situ.

distributions. Soil-water characteristic curves are nonlinear and not easy to measure.

The SWC curve typically exhibits hysteresis behavior as noted in the insert in Figure 2-1, due to water entrapment during drying and air entrapment during wetting (Charbeneau, 2006). The main cause of hysteresis is known as the "ink bottle" effect. In the drying phase water is drained from pores, however, narrow necks tend to keep large pores filled at suctions above that which would drain them. Analogous mechanism occurs during wetting. A second phenomenon is the "rain drop" effect, the contact angle of water and soil particles is greater when the water front is

advancing (wetting cycle) as opposed to the time it is retreating (drying cycle). This phenomenon

tends to cause higher water contents during the drying cycle compared to the wetting cycle. Similar hysteresis effects as $\theta(\mathbf{h})$ come about in $\mathbf{K}(\mathbf{h})$ as well. This effect is less noticeable for $\mathbf{K}(\theta)$, however it is not negligible for all soil textures (Nielson et al., 1986; Hillel, 1998).

Brooks and Corey (1966) proposed a relation between soil water content and matric potential:

$$\theta = \theta_r + \Delta\theta \left(\frac{\psi_p}{h_b}\right)^{-\lambda} \quad (2-5)$$

where θ is volumetric water content, $\Delta\theta = \theta_s - \theta_r$ is soil moisture capacity, θ_s is volumetric water content at saturation (maximum moisture), θ_r is residual volumetric water content (irreducible moisture), ψ_p is matric potential, h_b is bubbling pressure of the soil (height of capillary fingering), and λ is empirically derived parameter of Brooks-Corey method known as the “pore size index”. A smoothed version of the Brooks and Corey SWC model is proposed by van Genuchten (1980):

$$\theta = \theta_r + \frac{\Delta\theta}{\left[1 + (\alpha|\psi_p|)^n\right]^m} \quad (2-6)$$

where n and m are dimensionless parameters and α has the dimensions of reciprocal head and given m and h_b , n and α may be calculated as follows.

$$n = \frac{1}{1-m} \quad (2-7)$$

$$\alpha = \frac{1}{h_b} \left(2^{\frac{1}{m}} - 1\right)^{1-m} \quad (2-8)$$

Details of deriving the m parameter are given in Fetter (1999). For large capillary pressures van Genuchten and Brooks-Corey formula become identical (Charbeneau, 2006). In this case we can relate the parameters of two models through $\lambda = n - 1$.

Table 2-1 shows the average empirical values for the van Genuchten parameters and the residual and saturated water content for various soil textural classes.

Table 2-1. Average values of soil water characteristic curve parameter obtained by experimental means (Leij et al., 1996).

Soil Texture	Porosity: $\theta_s \left[\frac{L^3}{L^3} \right]$	Residual Water Content: $\theta_r \left[\frac{L^3}{L^3} \right]$	α $\left[\frac{1}{cm} \right]$	n (dimensionless)
Sand	0.37	0.058	0.035	3.19
Loamy Sand	0.39	0.074	0.035	2.39
Sandy Loam	0.37	0.067	0.021	1.61
loam	0.46	0.083	0.025	1.31
Silt	0.48	0.123	0.006	1.53
Silt Loam	0.43	0.061	0.012	1.39
Sandy Clay Loam	0.40	0.086	0.033	1.49
Clay Loam	0.47	0.129	0.030	1.37
Silty Clay Loam	0.55	0.098	0.027	1.41
Silty Clay	0.47	0.163	0.023	1.39
Clay	0.51	0.102	0.021	1.20

2.1.2.2. Hydraulic conductivity curve models

Equation (2-4) also requires the $K(\theta)$ dependence to be defined from data relating hydraulic conductivity to water content θ . Here we briefly outline measurement of $K(\theta)$; further studies can be reviewed in Dane and Topp (2002), and the standard method is described in ASTM D7664-01 (2010). Unsaturated hydraulic conductivity can be measured e.g., in situ via *Guelph Permeameter* or GPM (Reynolds and Elrick, 1987) or in laboratory via *Temp Cell* or *Volumetric Pressure Plate Extractor* (Fredlund et al., 2012). It is often convenient to estimate unsaturated hydraulic conductivity from soil SWC parameters (Charbeneau, 2006). Hydraulic conductivity in unsaturated soils $K(\theta)$ is a nonlinear function of hydraulic conductivity of the

soil at saturation K_s and degree of saturation $S_e \equiv (\theta - \theta_r)/(\theta_s - \theta_r)$. Brooks and Corey (1966) proposed a power-law model for unsaturated hydraulic conductivity as:

$$K(\theta) = K_s S_e^{3+2/\lambda} \quad (2-9)$$

where λ the pore size index of the soil. Another popular model for unsaturated soil hydraulic conductivity was derived by van Genuchten (1980) based on the work of Mualem (1976):

$$K(\theta) = K_s S_e^L \left[1 - \left(1 - S_e^{\frac{1}{m}} \right)^m \right]^2 \quad (2-10)$$

where m is the van Genuchten soil parameter as in equation (2-6), S_e is defined above, and L , the pore-connectivity coefficient, is originally $\frac{1}{2}$, Schaap and Leij (2000) suggested variable values of L in a study of different soil types.

2.1.2.3. Temperature and salinity effects on hydraulic properties of vadose zone

Compared to hysteresis, effects of temperature and salinity on hydraulic properties of soils are secondary (Hillel, 1998). At a given pressure head, in particular in fine-texture soils, more water will be retained as temperature decreases. Hydraulic properties of unsaturated fine-texture soil can be altered by salinity; however, studies on this are few (Hillel, 1998, page 278; Mitchell and Soga, 2005, page 276). The size of the electrostatic double layer grows with decreasing ionic strength of the soil-water solution and can cause swelling in clay particles and

reduce hydraulic conductivity (Fetter, 1999). Shainberg et al. (1981) showed that as the sodium absorption ratio (SAR)² increases the relative hydraulic conductivity decreases.

2.1.3. Preferential flow

Richards' equation (2-4) pertains to flow in porous media that behaves as a continuum; however, in the presence of fractures, macropores, or sloping layers of different soil textures, water may move preferentially in horizontal or vertical directions. This “*preferential flow*” allows much faster transport of pollutants through the vadose zone to potentially impact groundwater quality. (Charbeneau, 2006; Šimůnek and van Genuchten, 2007). There are three causes of preferential flow: firstly, decayed root channels, wormholes, burrows, soil surface shrinkage cracks serve as macropores that form preferential paths for water and solute transport (Germann and Beven, 1985). Secondly, flow instability caused by pore-scale permeability variation in the wetting front can lead water in coarse soils to form a number of pathways called *fingers* (e.g., Šimůnek et al., 2003). Thirdly, preferential flow occurs when a sloping layer of coarse grain soil or sediment causes pore water to flow laterally towards a lower region in the vadose zone, this phenomenon is known as *funneling* (e.g., Walter et al., 2000).

In addition to these factors affection flow directly, solute and/or colloid suspensions may reflect transport through unsaturated and saturated porous media that appears faster than that accorded to the mean porewater velocity. This may occur for instance with anionic and generally non-reactive solutes such as chloride or bromide in porous media characterized by a predominately negative surface charge (quartzitic sands). The like charges result in repulsion of the solutes from the pore walls and consequently greater residence times in the middle of pore

² The sodium adsorption ratio is a measure of the ratio of the concentration of monovalent sodium to divalent calcium and magnesium

space flow channels, so that the resulting average velocity of the charged solutes is greater than the average velocity of the water itself. This phenomenon is termed “ion-exclusion” (e.g. Gvirtzman and Gorelick, 1991). In the case of colloidal suspensions, even when characterized by neutral surface charges, the colloid by virtue of its size is prevented also from residence near pore walls where the velocities are relatively slow, and the same result is attained (e.g., Ginn, 2002).

2.1.3.1. Closed-form solutions of the Richards’ equation without and with preferential flow

Since eq. (2-4) is a nonlinear PDE only limited closed-form analytical solutions exist. As noted above when matric forces dominate eq. (2-4) may be written without the gravity term, yielding a nonlinear diffusion equation (absent of source term):

$$\frac{\partial \theta}{\partial t} = - \frac{\partial}{\partial z} \left(K(\theta) \frac{\partial \psi_p}{\partial z} \right) \quad (2-11)$$

This model is solvable for particular idealized cases that specify a mathematically manageable function for $K(\theta)$ and are worked out for some evaporation processes (Charbeneau, 2006). When the pressure gradient is small (such as high water contents in coarse grain media) the matric term may be ignored and Richards’ equation reduces to (again without source term for simplicity):

$$\frac{\partial \theta}{\partial t} = \frac{\partial}{\partial z} K(\theta) \quad (2-12)$$

that is a kinematic wave equation. Note that in this case the Darcy flow (flow per unit area) is vertically downward at rate $K(\theta)$. This form is solvable by the method of characteristics for a number of mathematical forms for $K(\theta)$ as detailed in e.g. Singh (1997).

The full Richards' equation including both matrix and gravity terms can be converted to a Burger's equation when $K(\theta) \frac{\partial \psi_p}{\partial \theta}$ is assumed to be a constant and $K(\theta)$ is treated as a quadratic function of S_e and can be solved using a Hopf-Cole transformation. Details and example cases for this approach are given in Warrick and Parkin (1995), Basha (2002) and Rumynin (2011).

Several conceptual models have been suggested to quantify the complex behavior of vadose zone flow with preferential flow. In particular, Germann and Beven (1985) propose a "two-domain" approach that applies the capillary flux component of Richards' equation (2-4) to flow in the soil matrix, and the gravity flux component of equation (2-4) to flow in macropores; the two fluxes are linked by a mass balance relation. This and other approaches are reviewed in Singh (1997), Šimůnek et al. (2003).

For general cases of unsaturated flow in natural porous media numerical solution is the primary option for quantification of flow by the deterministic Richards' equation (e.g., Nielson et al., 1986), and we present a brief summary of such computer codes below, as they generally pertain to modeling both flow and transport processes. First however we turn to the discussion of transport processes in the vadose zone.

2.1.4. Deterministic approach to model solute transport in the vadose zone

Once the flow process is represented to the extent that water infiltration and redistribution flow rates are quantified in terms of the Darcy flux q , the transport in the vadose zone can be characterized using the mean porewater velocity of water, $v = q/\theta$, as parameter that in general is a function of space and time both (and θ is the water content). Transport of solute or suspensions in the vadose zone is governed by the Advection-Dispersion-Reaction equation (ADR, also

called ADE). This expression combines the statement of continuity (mass balance) that the change in local mass of a given chemical species, or number density of a colloid suspension, c , per bulk volume is proportional to the divergence of the transport of that quantity by diffusion, dispersion, or advection through that volume. The result in one-dimension is

$$\frac{\partial(\theta c)}{\partial t} + \frac{\partial(qc)}{\partial z} - \frac{\partial}{\partial z} \left(\theta D \frac{\partial c}{\partial z} \right) = R \quad (2-13)$$

where the first term is the change in bulk-volumetric mass density, the second is divergence of advective flow in the z direction, the third is divergence of the combined diffusive/dispersive flow, and the last term is source or sink due to reactions. In the commonly-encountered case where water flow is governed by equation 2 without sources S , then eq. (2-13) reduces by the chain rule to:

$$\frac{\partial c}{\partial t} + v \frac{\partial c}{\partial z} - \frac{1}{\theta} \frac{\partial}{\partial z} \left(\theta D \frac{\partial c}{\partial z} \right) = \frac{R}{\theta} \quad (2-14)$$

where D is the effective hydrodynamic dispersion coefficient that is the coefficient of molecular diffusion, scaled by tortuosity τ so that it represents diffusion in the porous medium, plus the coefficient of kinematic dispersion, that is typically assumed to be linear in velocity (Biggar and Nielsen, 1967):

$$D = D_o \tau + \alpha v \quad (2-15)$$

where α is the dispersivity coefficient [L]. The tortuosity factor accounts for the decrease in diffusion domain associated with the presence of phase interfaces and is commonly quantified using the model of Millington and Quirk (1961) as $\tau = \theta^{7/3} / \theta_s^2$.

The final term in eq. (2-14) represents reactions that serve as a source or sink of aqueous volumetric mass density, and potentially include the complete suite of biogeochemical reactions affecting solutes or colloids in natural porous media. The complexity inherent in quantifying such reactions, in addition to the fact that the velocity appearing in both equations (2-14) and (2-15) is generally a function of both space and time determined only by numerical solution of Richards' eq. (2-4), render eq. (2-14) generally unsolvable except by numerical methods. Fortunately a number of such tools exist, but before turning to these we briefly review the closed-form solutions that are available, and the cases to which they pertain.

2.1.4.1. Closed form solutions for transport in the vadose zone: non-reactive species

Analytical solutions for simple cases are tabulated in Zamani and Bombardelli (2014) including solutions for cases of nonhomogeneous media (Zoppou and Knight, 1997), multidimensional flow (Logan, 2001), multi-domain (Lassey, 1988; 1989), and multicomponent transport (Cho, 1971). These solutions are useful both for verification of numerical solutions, and as characteristic solutions for simple boundary/initial conditions that can be used to construct solutions to more complicated boundary/initial value problems. In particular, the solutions to cases involving idealized (constant or instantaneous pulse) boundary/initial conditions serve as “Green’s functions” that can be used with the principle of superposition to determine transport solutions when boundary concentrations vary with time (e.g., Toride et al., 1993; Logan, 2001; Cannon, 2008). Because the integrations that result must be solved numerically, these solutions are called “semi-analytical solutions”.

Most of the analytical solutions of ADR are derived based on a change of variable which removes the advective term of ADR equation and then the remaining diffusion equation is solved via common methods of solving diffusion equation including Kirchoff or Boltzmann transformations (Cannon, 2008; Zamani and Bombardelli, 2014). An outline of the basic solution method is given as follows, for the cases of initial value problems where the initial concentration is given as $c(z, 0)$, and then in the case of boundary-value problems where the boundary concentration in the influent solution is given as $c(0, t)$. Consider an advection-dispersion equation of the form of (2-14) in which the dispersivity, water content, and velocity are varying with time but constant in space, and where there are no reactions or source/sink terms:

$$\frac{\partial c}{\partial t} + v(t) \frac{\partial c}{\partial z} - D(t) \frac{\partial}{\partial z} \left(\frac{\partial c}{\partial z} \right) = 0 \quad (2-16)$$

Let $\xi = \int_0^t v(\tau) d\tau$, $x = z - \xi$, and $c(z, t) = c(x + \xi, t) = C(x, t)$; under these transformations, eq. (16) becomes:

$$\frac{\partial C(x, t)}{\partial t} = D(t) \frac{\partial^2 C(x, t)}{\partial x^2}; \quad -\infty < x < \infty, \quad 0 < t \quad (2-17)$$

Now, by introducing the Kirchoff transformation $T = \int_0^t D(\tau) d\tau$ the above equation reduces to the dimensionless form of the heat equation (e.g., Cannon, 2008):

$$\frac{\partial C(x, T)}{\partial T} = \frac{\partial^2 C(x, T)}{\partial x^2} \quad (2-18)$$

It can be shown that the analytical solution of equation (2-18) is of the form (Cannon, 2008):

$$C(x, T) = \int_{-\infty}^{\infty} G(x - \xi, T) f(\xi) d\xi \quad (2-19)$$

where $f(x)$ is the initial concentration and $G(x, t)$ is the Green's function associated with the heat operator on the infinite domain, given by the classical Gaussian distribution (Logan, 2001):

$$G(x, t) = \frac{1}{\sqrt{4\pi D_0 t}} e^{-\frac{x^2}{4D_0 t}} \quad (2-20)$$

In the boundary value case, we consider the conservative form of the ADR equation in 1D as in equation (2-14) but now with constant dispersion coefficient and constant velocity, without the sink term, in the domain $0 < x < \infty, 0 < t$, subjected to the following boundary conditions: constant concentration upstream, $c(0, t) = c_0$; concentration value asymptotic to zero downstream, $c(x \rightarrow \infty, t) = 0$; and initial condition, $c(x, 0) = 0$. Applying the Laplace transformation to equation (2-16) and its boundary conditions in the time domain, it is possible to obtain the following results in the Laplace domain (\tilde{C}, x, s):

$$s\tilde{C} - c(z, 0) = D\tilde{C}_{zz} - v\tilde{C}_z \quad (2-21a)$$

$$\tilde{C}(0, s) = \frac{c_0}{s} \quad (2-21b)$$

$$\tilde{C}(z \rightarrow \infty, s) = 0 \quad (2-21c)$$

The solution to the ordinary differential equation set (2-21) is:

$$\tilde{C}(z, s) = \frac{c_0}{s} \exp\left(-\frac{z}{2D}(\sqrt{v^2 + 4sD} - v)\right) \quad (2-22)$$

Taking the inverse Laplace of \tilde{C} , Ogata and Banks (1961) obtained

$$c(z, t) = \frac{c_0}{2} \left\{ \operatorname{erfc}\left(\frac{z-vt}{2\sqrt{Dt}}\right) + \exp\left(\frac{vz}{D}\right) \operatorname{erfc}\left(\frac{z+vt}{2\sqrt{Dt}}\right) \right\} \quad (2-23)$$

where *erfc* refers to the complementary error function.

2.1.4.2. Closed Form Solutions for Transport in the Vadose Zone: Reactive Species or Two-Domain Transport

Extensions of the above for the case of irreversible decay reactions where R is given algebraically are found in Cannon (2008) and in Zamani and Bombardelli (2014). Here we focus on reversible reactions that are more challenging. There are only few reactions models for which eq. (2-14) with nonzero R representing reversible reactions remains tractable for closed-form

solutions, two of which are noted here. In the case of equilibrium linear sorption of the quantity represented by c , so that $s = K_d c$, with s in units of massic mass (and $\rho_b s / \theta$ is the aqueous-volumetric mass) and K_d is the equilibrium coefficient [Volume aqueous per mass solid] then the reaction term may be written exclusively for this transfer as $\frac{R}{\theta} = -\frac{\rho_b}{\theta} \frac{\partial s}{\partial t} \Big|_{sorption} = -\frac{\rho_b K_d}{\theta} \frac{\partial c}{\partial t}$

and then eq. (2-14) becomes

$$\frac{\partial c}{\partial t} + v \frac{\partial c}{\partial z} - \frac{1}{\theta} \frac{\partial}{\partial z} \left(\theta D \frac{\partial c}{\partial z} \right) = -\frac{\rho_b K_d}{\theta} \frac{\partial c}{\partial t} \quad (2-24)$$

or, with $R_d \equiv 1 + \frac{\rho_b K_d}{\theta}$, termed the “retardation coefficient,”

$$R_d \frac{\partial c}{\partial t} + v \frac{\partial c}{\partial z} - \frac{1}{\theta} \frac{\partial}{\partial z} \left(\theta D \frac{\partial c}{\partial z} \right) = 0 \quad (2-25)$$

It should be noted from eq. (2-25) that such a single sorption reaction that is both linear and equilibrium makes the transport of the solute mimic that of a passive tracer (because there are no reactions term on the right-hand side of eq. (2-25)), but one with time rescaled by the retardation coefficient. In other words, if one divides through eq. (2-25) by the retardation coefficient, one regains eq. (2-14) with zero reactions and with both velocity and dispersion coefficient reduced by R_d . Therefore the solutions eq. (2-19) or (2-23) may be utilized (for initial or boundary value problems, respectively) given properly retarded velocity and dispersion coefficients. It must also be emphasized that this result pertains to only the simplest representation of interfacial reactions between solute and sorbate and is not realistic for many cases, such as surface complexation or ion exchange reactions that require multicomponent chemistry accounting, discussed below.

In the case that the surface reaction includes not only equilibrium linear sorption but also another surface reaction that remains linear but is not at equilibrium in general, eq. (2-25) is partnered with another equation balancing the mass of the non-equilibrium sorbate, so that the new system is

$$R_d \frac{\partial c}{\partial t} + v \frac{\partial c}{\partial z} - \frac{1}{\theta} \frac{\partial}{\partial z} \left(\theta D \frac{\partial c}{\partial z} \right) = - \frac{\rho_b}{\theta} \frac{\partial s}{\partial t} \quad (2-26a)$$

$$\frac{\partial s}{\partial t} = k_1 c - k_2 s \quad (2-26b)$$

where k_1 and k_2 are the rate coefficients of the linear sorption reaction [$1/T$] and the right-hand side of eq. (2-26b) represents kinetically-controlled first-order mass transfer between solute and sorbed mass. Equations (2-26) are solved in Lassey (1988, 1989), with the result for the boundary value problem where initial concentration is zero and the concentration at the surface is $c_o(t)$:

$$c(z, t) = d(\xi(x), \tau(t)) \equiv \int_0^{\tau(t)} \{c_o(\tau(t) - \tau') \int_0^{\tau'} \Omega(\xi(x), y) \psi(\tau' - y, y) dy\} d\tau' \quad (2-27a)$$

where the dimensionless variables used are $\xi(x) = xv/D$ and $\tau(t) = tv^2/(R_d D)$, and

$$\Omega(\xi, y) = \frac{\xi}{\sqrt{4\pi y^3}} \exp\left(-\frac{(\xi-y)^2}{4y}\right) \quad (2-27b)$$

$$\psi(\tau' - y, y) = \exp(-\kappa_1 y - \kappa_2(\tau' - y)) [\delta(\tau' - y) + \kappa_1 \kappa_2 y I(\kappa_1 \kappa_2 y(\tau' - y))] \quad (2-27c)$$

and where $I(a) \equiv a^{-\frac{1}{2}} I_1(2a^{1/2})$ where I_1 is the modified 1st order Bessel function of the 1st kind, and finally κ_1 is $k_1 D/v^2$, and κ_2 is $k_2 R_d D/v^2$. Despite the fact that the foregoing analysis requires constant velocity and dispersion coefficient, this remarkable solution is among the most useful and general available. It not only pertains to the conditions stated above, but it also is the

solution to the problem where the non-equilibrium mass transfer between the c and s phases is due to two-domain mass transfer (Coats and Smith, 1964; Nkedi-Kizza et al., 1984) where the surface reaction is replaced by an approximate (1st order) diffusive mass transfer into and out of the immobile aqueous domain associated with the microscopic pores of the solid phase of a soil matrix.

The Lassey (1988) solution set also covers the case of colloid filtration in saturated soils, and by approximate extension, bacterial transport (Ginn et al., 2006). In these cases the forward rate coefficient k_f is classically approximated by

$$k_1 = \frac{3(1-\theta)}{2d_c} \alpha \eta \quad (2-28)$$

where d_c is the characteristic diameter of the granular porous media grains, α is the frequency with which the colloids that contact the surface actually stay there, and η is the frequency with which the colloids in the suspension contact the surface. It must be recognized that in the presence of unsaturated conditions however, there is also the process of colloid immobilization by attachment to the soilwater-air interface, and this is not covered by the foregoing models. Further readings on this as well as the more complex topic of colloid-facilitated transport can be found in Bekhit and Hassan (2005) and in Massoudieh and Ginn (2007).

The analytical solutions presented above are all in fact “semi-analytical” as numerical integrations must be performed to obtain the solution to particular boundary or initial conditions. During the past decades, many software packages have been developed based on analytical solutions of vadose zone transport for analyzing in situ and laboratory experiments. Most of these codes are based on simplifying assumptions including: constant water content, constant flux, steady state flow field, and/or homogeneous porous media (Šimůnek and van Genuchten,

2007). One of the most commonly used among the 1D packages of analytical solution of flow and transport in the vadose zone are CXTFIT and CXTFIT2 (Toride et al., 1995) that includes degradation and sorption process models. In addition, this code is able to solve both direct and inverse problems; the latter is the problem of using observed data on effluent or in-situ solute concentrations in order to estimate parameters v , D , and R_d . It should be mentioned that parameter estimation using CXTFIT and other tools should be constrained by the mathematical physics of the problem at hand. For instance, it is possible to obtain values of R_d less than unity in inverse parameter fitting; this represents transport of the solute or suspension (colloids) at rates that are actually faster than the mean porewater velocity as reflected in v . Of course R_d must be greater than unity by definition. Observation of such “early breakthrough” is indicative of either preferential flow, ion exclusion (e.g., Gvirtzman and Gorelick, 1991), or in the case of colloids, size exclusion (e.g., Ginn, 2002).

ICE-1 is a code for 1D transport of heat and solute in heaving frozen soils (El-Kadi and Cary, 1989). Another popular 1D analytical model is PESTAN by U.S. EPA. PESTRAN is for evaluating the one-dimensional vertical transport of organic pollutants through homogeneous soil to ground-water. It calculates organic movement based on a linear isotherm, first-order degradation, and longitudinal dispersion (Enfield et al., 1982).

Several 2D and 3D codes based on analytical solutions have been developed, including: 3DADE by Leij and Bradford (1994), N3DADE by Leij and Toride, (1997), and MYGRT by Unger et al. (1998). Šimůnek et al. (1999) integrated seven separate codes of analytical solutions of solute transport in unsaturated/saturated porous media in a public domain Windows-based package STANMOD.

2.1.5. Codes for numerical solution of vadose zone flow and transport

The general problem of solute transport in the vadose zone requires treatment of arbitrary boundary conditions on infiltration and solute concentrations, transient and heterogeneous water contents and velocities, multidimensional flow and transport, and multicomponent biogeochemical reactions. The only avenue currently available for treating these cases involves large codes that treat these processes simultaneously. The governing equations of flow and solute transport in vadose zone are solved numerically for almost all practical cases mainly through the Finite Element Method (FEM) and Finite Volume/Difference Methods (FVM/FDM). Historically, FEM was the more popular numerical solution approach in porous media as shocks are slighter and capturing complex geometries is more natural with FEM. However in the 1990's, with advancement of mesh generation methods, FVM/FDM are used more widely since those method are mass conservative and more advanced in handling sharp gradients. Many codes have been developed for simulation of flow and transport in unsaturated zone. U.S. Geological Survey developed a 2D/3D hybrid FEM and FDM freeware SUTRA for saturated/unsaturated zones with the ability to simulate density dependent flow (Voss and Provost, 2002). VS2DT is a USGS program based on the FDM for flow and solute transport in variably-saturated, single-phase flow in porous media. Simulated regions include one-dimensional columns, two-dimensional vertical cross sections, and axially-symmetric, three-dimensional cylinders (Healy, 1990). VS2DT has a Windows-based graphical user interface (GUI). There are several codes originating from U.S. Salinity Laboratory, including HYDRUS (Šimůnek et al. 2006) for flow, and UNSATCHEM/UNSATCHEM2D (Šimůnek and Suarez, 1993) for reactive transport. More recently, HP1 and HP2 (Jacques and Šimůnek, 2010) which are based on the coupling of

HYDRUS-1D and PHREEQC (Parkhurst and Appelo, 1999) have become available for combined flow and reactive transport.

HYDRUS is a FEM model for 1D, 2D and 3D solute and heat transport simulations in variably saturated media. The flow equation incorporates a sink term to account for water uptake by plant roots. The boundary conditions for flow, and heat and solute transport can vary with time. A finite source also can be modeled. Soil parameters are described by the van Genuchten parameters (van Genuchten, 1980). The model also considers hysteresis in the SWC (Figure 2-1). Solute transport and transformation incorporates molecular diffusion, hydrodynamic dispersion, linear equilibrium reactions between the liquid and gaseous phases, nonlinear nonequilibrium partitioning (sorption) between the solid and liquid phases, zero-order production, and first-order decay/degradation reaction. UNSATCHEM-2D is two-dimensional FEM software for modeling ion equilibrium and kinetic non-equilibrium chemistry in the vadose zone. The model is designed for prediction of major ion chemistry and water and solute fluxes for soils under transient conditions. Since the solution chemistry in the vadose zone is influenced by variations in water content, temperature and CO₂ concentrations in the soil gas, all these variables are also simulated by the model. The flow equation incorporates a sink term to account for water uptake by plant roots. The heat transport equation considers the heat transport by conduction and by convection with flowing water (Šimůnek and Suarez, 1993).

The HYDRUS suite of codes provides for a range of combined reactions and transport and are summarized online (http://en.wikipedia.org/wiki/Hydrus_%28software%29, accessed 12 February, 2015). While the HYDRUS 2D and 3D models are combined with the capability of UNSATCHEM, the one-dimensional version HYDRUS 1D includes both UNSATCHEM and the separate code HP1 that is the combination of HYDRUS 1D with the general biogeochemical

program PHREEQCII (Parkhurst and Appelo, 1999). PHREEQC allows treatment of general aqueous speciation, ion exchange, surface complexation, mineral precipitation/dissolution, Henry's law-based buffering with a gaseous phase, and a general Visual Basic-based coding accommodation for kinetics, that allows specification of kinetically-controlled mass transfer into and out of multiple immobile domains, precipitation/dissolution kinetics, and biodegradation and other microbially-mediated processes.

LEACHP (Dust et al., 2000) is a code for transient 1D flow and transport in horizontally-structured soils. The model uses Richards' equation with the soil-water characteristic curve and the $K(\theta)$ model as introduced above with several variations available. Simulated solutes undergo sorption with linear, nonlinear, and two-site models available. RZWQM (Root Zone Water Quality Model) simulates flow and transport of solute nutrients and pesticides associated with 1D flow through an agricultural root zone. The model includes accounting for macropore/lateral flow in addition to Darcy flow per Richards' equation, tile drainage, as well as agricultural management practices including agrichemical applications, plant growth, and irrigation events (DeCoursey, 1992).

TOUGHREACT (Xu et al., 2004) supported by Lawrence Berkeley National Laboratory is capable of simulating flow and transport in three-dimensional porous and fractured media with both physical and chemical heterogeneity. The code can simulate in principle any number of chemical species present in aqueous, gas and solid phases, and provides a variety of equilibrium chemical reactions, including aqueous speciation, gas dissolution/exsolution, ion exchange and mineral dissolution/precipitation. TOUGHREACT also has several models useable for kinetically-controlled precipitation/dissolution, with coupling to changes in porosity and permeability and capillary pressure in unsaturated systems.

The USGS also provides a suite of codes that support generally reactive transport for the vadose zone. The Unsaturated Zone Flow (UZF1) Package (Niswonger et al., 2006) for MODFLOW simulates flow through the unsaturated zone using a kinematic wave approximation for unsaturated flow. UZF1 is coupled to larger number of popular packages such as MODFLOW, MT3DMS, RT3D, and PHT3D and users can more extend existing regional-scale flow and transport models to include the unsaturated zone. STOMP (Subsurface Transport Over Multiple Phases) by Pacific Northwest National Laboratory (White and Oostrom, 2006). Another public domain code is TRACR3D which is a 3D FDM package by Los Alamos National Laboratory, that solves the equations of transient two-phase flow and multicomponent ADR in deformable, heterogeneous reactive unsaturated saturated porous media (Travis, 1984). FEFLOW by DHI (Trefry and Muffels, 2007) is a FEM commercial code for vadose zone and saturated porous media. Table 2-2 shows a summary of capabilities if some vadose zone flow and transport models.

While HP1 and TOUGHREACT are currently among the most general codes for solute transport in the vadose zone, the field of commercial software for environmental applications is growing rapidly, and other initiatives linking general Richards' equations solvers with PHREEQC and other general reactive transport capabilities is growing (e.g., Wissmeier and Barry, 2011; Nardi et al., 2012).

Table 2-2. Summary of the vadose zone models by USGS, EPA and USDA

Process	Model			
	HYDRUS2D	LEACHP	RZWQM	VS2DT
Water Flow				
Mobile/immobile phases	✓			
Macropore flow			✓	
Root water uptake	✓		✓	✓
Surface directed flow	✓	✓	✓	
Heat Transport	✓		✓	
Solute Transport				
Maximum number of parent and degradate compounds simulated	5	5	3	1
Sorption	✓	✓	✓	✓
Volatilization	✓	✓	✓	
Numerical Dispersion	✓			
User-defined dispersion	✓	✓	✓	✓
Degradation	✓	✓	✓	✓
Nitrification-denitrification		✓	✓	
Moist and temperature effect of degradation	✓	✓	✓	
Uptake by Plants	✓	✓	✓	✓

2.2. Review of Wetland Sediment Transport Modeling³

Historically sediment transport science has been developed for riverine morphology, however progressively it has extended to harbors, estuaries, coastal areas, lakes and recently wetlands. Although the crux of sediment transport knowledge was experimental, since the mid-1970s mathematical modeling has opened a new frontier in stream processes and sediment dynamics. Models of sediment transport have gone through a fundamental renaissance in the last decades due to heightened interest in global environmental concerns related to water quality and spread of synthetic chemicals that attach to fine sediments. Instead of studying total load and bed morphology, the objective of sedimentation modeling has been re-directed toward ecohydraulics. In this paper we review the sediment transport models that are applicable to or have been applied to wetlands.

Sedimentation in wetlands⁴ is not only important for morphological landscape concerns but also for pelagic habitats, sediment oxygen demand, turbidity, and biochemical reactions. Contaminations and nutrients are attached to sediment particles therefore the transport of sediment also describes the dynamics of corresponding contamination in wetlands (Luengen and Flegal, 2009). High sediment load may cause extreme biological growth and change in hyporheic flow due to clogs in the bed of wetlands (Kadlec and Wallace, 2009). A major functionality of constructed wetlands is the removal of suspended particles.

2.2.1. Wetland sediment processes

Fundamentals of sediment mechanics in wetlands are very similar to estuaries. Forcing factors of sediment transport are turbulent flows, tidal mixing, wind induced stress, wave action,

³ This subsection was written by Kaveh Zamani solely, and it is part of a review paper by ASCE-EWRI Wetland Hydrology Technical Committee which is accepted for publication in ASCE-Journal of Hydrologic Engineering.

⁴ In this chapter “wetland” refers to free water surface (FWS) wetlands.

animal or boat activities and coastal currents (Malmaeus and Hakanson, 2003; Schoellhamer et al., 2012). However, additional issues are included in wetlands sediment processes: wetlands are strongly influenced by biochemical processes, biological gas may cause uplift and resuspension (Kadlec and Wallace, 2009) biomass and flocculent sediment that exists in some wetlands have low bulk density and their behaviors are not described by classic non-cohesive sediment transport mechanics (Kadlec and Wallace, 2009). Wetland sediment transport characteristics are essentially associated with low water velocities and flora and fauna effects (Kadlec and Wallace, 2009). Low water velocity and plant effects make wetlands a depositional environment rather than erosional which is more common in streams and coastal areas (Mitsch and Gosselink, 2000). Vegetation plays a key role in wetland dynamics in four ways: first, plants in the wetlands affect driving forces induced by flow and turbulence on the sediment particles (Follett and Nepf, 2012), second, root binding hinders bed erosion and resuspension of sediment (Horppila and Nurminen, 2003; Horvath 2004, Follett and Nepf, 2012), third, vegetation of wetlands produce sediment through processes of death, litter fall, seed and litter attrition (Kadlec and Wallace, 2009; Lago et al., 2010), finally, vegetation may even enhance erosion rate in some regions (Follett and Nepf, 2012). In general, as fluid induced forces on the sediment particles exceed the critical threshold inter-particle bonding, there are two common modes of transport: suspended load and bedload. Turbulent flow lifts up fine particles into the water column as suspended load while coarser particles roll, slide or saltate near the bed as bedload. A major distinctive feature of sediment transport mechanics in wetlands is that, bedload transport is negligible in most cases (Schoellhamer et al., 2012).

2.2.2. Mathematical representation of sediment transport in wetlands

There are several continuum and stochastic conceptual models to represent processes in fluid-particle mixture. For sediment transport modeling an Eulerian-Eulerian framework is usually taken rather than an Eulerian-Lagrangian framework for representing fluid and solid particles respectively. Eulerian-Lagrangian sediment transport models are typically used in theoretical research vis-à-vis practical studies (Spasojevic and Holly, 2008; Jha and Bombardelli, 2010). This review does not cover Eulerian-Lagrangian particle transport models, however these models could give a cutting-edge insight into the sediment mechanics of vegetated water-bodies. In Eulerian-Eulerian sediment transport models, there are two general categories that account for sediment transport. One is the tracking of total load movement (Greimann et al., 2008) another is the tracking of the bedload movement and suspended load movement separately after the breakdown of the total load based on the Rouse number (for example: MOBED2 by Spasojevic and Holly, 1990). To the best of our knowledge total load models have not been utilized to simulate sediment transport in wetlands to date. The majority of wetland sediment transport simulations have used suspended load and bedload models (Lee and Shih, 2004; Lago et al., 2010; Chu and Rediske, 2012; Meselhe et al., 2012). Below we discuss the details of bedload and suspended load sediment transport in wetlands.

Bedload transport is mainly related to bed shear stress and less influenced by vegetation induced drag forces (Okabe 1997; Hirano et al, 1999; Wu, 2005; Follett and Nepf, 2012). Vegetation impact on bedload transport was investigated in several studies: Okabe et al. (1997) validated a formula for non-vegetated channels. Wu et al. (2000) derived a formula accounting for the hiding mechanism in bedload transport. Wu et al. (2005) used Wu et al., (2000) formula in a numerical simulation of a vegetated river. Jordanova and James (2003) experimentally

investigated the bedload transport in a flume covered with uniformly distributed vegetation and suggested an empirical formula based on the effective bed shear stress. Kothyari et al. (2009) investigated the effect of rigid stems on the bedload transport. Bedload transport is computed via empirical equations which calculate dimensionless Einstein bedload number “ q^* ” as a function of excess shear stress “ $\tau^* - \tau_c^*$ ” (García, 2008, section 2.6 and the references therein). In general bedload transport is assumed to be negligible in most wetland sediment transport simulations (Lee and Shih, 2004; Lago et al., 2010; Chu and Rediske, 2012). The reasons for it are: blocking effect of plants and low upward shear velocity compared to settling velocity of particles in the wetland environment. This assumption is thoroughly valid in particular for constructed and lacustrine wetlands, and swamps. Ganju et al. (2005) mentioned that bedload contribution in the total sediment load is negligible in coastal wetlands. Several measurements by Dinehart (2002) and Wright and Schoellhamer (2005) showed the daily bedload to be in the range of 0.5 to 2.4% of the total load in an estuary near Sacramento, California. Measurements by Holloway (2010) showed that only less than 5% of the total retained sediment is bedload in a riverine wetland in Elkhorn Slough, California.

The governing equation of suspended sediment transport is based on the conservation of mass for an incompressible dilute mixture (so called ADR). Its most generic form is:

$$\frac{\partial c_k}{\partial t} + u_i \frac{\partial c_k}{\partial x_i} - (K + \epsilon)_{ij} \frac{\partial^2 c_k}{\partial x_i \partial x_j} = E_k - D_k \pm S_k; \quad i, j = 1, 2, 3; k = 1, \dots, N \quad (2-29)$$

where C [L^3/L^3 or M/L^3] is spatially-averaged concentration, t and x are time and space coordinates, k refers to the sediment class for grain sorting, u [L/T] is velocity of flow which is usually assumed to be identical for solid and liquid phases, i and j are the index of coordinates, K [L^2/T] refers to molecular diffusion, ϵ [L^2/T] is hydrodynamic dispersivity (however, the flow regime in wetlands is typically laminar), E and D [$1/T$ or M/T] are entrainment

(resuspension) and deposition respectively, and S accounts for any other sediment sink or source in the water-body. There exist many formulas in literature for entrainment and deposition of particles in suspension (García, 2008; Section 2.9 and references therein). Basically deposition is a function of settling velocity and local concentration and entrainment is a function of explicit particle Reynolds number, kinematic viscosity of water and turbulent shear velocity (García, 2008). Finally other forms of sink or source in wetlands are all categorized under the term S , namely the production of organic sediments or the reduction of suspended sediment load due to submerged vegetation trapping (Schoellhamer et al., 2012).

The ADR equation which governs suspend sediment distribution is mainly discretized with Finite Difference Method (HEC-6, by Thomas and Prashum, 1977), Finite Volume Method (Mike by DHI, 2011), or Finite Element Method (RMA10 by King, 1988). Sediment transport equations are mainly discretized in a Cartesian (Mike by DHI, 2011) or curvilinear coordinate system (MOBBED2 by Spasojevic and Holly, 1990) with either a uniform (HEC-6) or non-uniform mesh (Flow-3D, by Flow Science, 2011), and with either a structured (Mike 21) or unstructured grid (Delft3D by Deltares, 2011). Sediment and hydrodynamic modules are working either decoupled or semi-coupled or coupled (Kassem and Chaudhry, 1998). Choosing the appropriate coupling approach is a crucial issue for wetland sediment transport modeling as the time scales of transport and flow phenomena possess different orders of magnitudes. Sediment transport models are also categorized based on how the flow solver discretizes the shallow water wave equation, for example HEC-6 is steady, SUTRENCH-2D is quasi-steady (van Rijn and Tan, 1985), and Mike 21 is unsteady. Overall, the numerical schemes to solve ADR equation are well-developed and reliable after almost five decades (Zamani and Bombardelli, 2013). The Achilles' heel in sediment transport modeling, in particular for

wetlands, is the quantification of the sink and source terms which are entrainment, deposition and effects of vegetation. These processes are among the most complex phenomena in nature and depend on turbulence, flocculation, irregular geometry, and biochemical activities which are inherently stochastic (van Rijn, 1993). Commonly however, deterministic empirical formulas have been used to define these phenomena. Currently, the mechanistic understanding of entrainment, deposition and cohesive sediment behavior is still immature and heavily relies on physical experimentation. In the next section, four approaches to wetland sediment transport modeling are briefly discussed with increasing complexity from 0D models, which treat flow and sedimentation in wetlands similarly to settling tanks and clarifiers, to sophisticated 3D models, which were developed for morphological studies of stratified estuaries.

2.2.3. Sediment transport models – hierarchy in complexity

The simplest modeling approach for sediment transport in wetlands is one that considers only continuity of mass and uniform steady state inflow and outflow (Kadlec and Wallace, 2009). This approach is similar to sedimentation tank processes in water/wastewater treatment. In the mass balance, re-suspension of particles and vegetation generated sediments are considered as sources while deposition is considered as a sink. These models may have multi-classes of particles unless the inflow sediment is truly of uniform size. In general, the 0D models are only applicable for geometrically regular, spatially uniform wetlands with steady, unidirectional flow. In other words, they can only provide preliminary analysis on the TSS distribution in free surface flow constructed wetlands.

In order, the second simple sediment transport model of wetlands is 1D models. These models are easy to set up and calibrate, and computationally inexpensive (Spasojevic and Holly, 2008). Therefore 1D models are the most cost-efficient choice to simulate morphological

changes occurring over extended time scales in riverine wetlands or large scale policymaking studies (van Rijn, 1993). The main drawback is this: 1D models solve the cross-sectionally averaged shallow water and ADR equations. In this representation, variations in the depth and transverse direction cannot be resolved. However, modelers have developed methods to estimate information on the vertical sediment concentration only based on the 1D sediment transport models (Spasojevic and Holly, 2008). Some 1D sediment transport models are even extended to simulate tidal riverine networks (for example Pereira et al., 2009). Nevertheless, the 2D morphological nature of wetlands is poorly represented with 1D sediment transport models.

As the local details of flow and mobile-bed dynamics are under resolved for 1D wetland sediment transport models, these features are better represented in 2D models. A 2D sediment transport model is the standard choice for analyzing the morphological evolutions in a wetland (Spasojevic and Holly, 2008). 2D wetland models are depth integrated and mostly developed for sediment transport in shallow estuaries. The main assumption in these models is that the water column is well mixed at each computational cell (no stratification) (DHI, 2011). This assumption generally holds for shallow water bodies and wetlands that are less than 4 meters in depth (Chimneya et al., 2006; Chapra, 2008). The 2D sediment transport models solve the nonlinear/linear shallow water and transport equations. Some of those solvers have advanced schemes that incorporate boundary fitted grids (FAST2D by Minh Duc et al., 1998) or wet-dry nodes (Mike 21 by DHI, 2011). Examples of application of 2D sediment transport models in wetland morphological studies are works by Sánchez, 2008; Larsen and Harvey, 2010; and Lago et al., 2010.

3D models provide the most comprehensive quantitative simulation of flow and sediment transport in wetlands. Modelers have to resort to 3D models when density currents are important

in sediment transport or when flow in the vicinity of inlet/outlet structures or obstacles are being investigated (van Rijn, 1993; Spasojevic and Holly, 2008). Even if we choose to resort to 3D modeling it is sufficient to use the vertically hydrostatic pressure in lieu of vertical momentum equation in wetland sediment process (Spasojevic and Holly, 2008). The calibration and computational cost in 3D simulations are resource intensive. One aspect of these models is the choice of turbulent closure due to the fact that turbulence statistics are crucial in the quantification of sediment entrainment and parameters of cohesive sediment in wetlands. However, because wetlands are mainly considered as depositional environment (Mitsch and Gosselink, 2000), thus wetland sediment transport modeling does not highly rely on sophisticated turbulence models unless the effect of local obstacles or strong jet is being studied (Spasojevic and Holly, 2008). Most 3D sediment transport models are unsteady and fully coupled. Therefore, 3D modeling is more commonly used for local scale morphological studies around obstacles/vegetation in wetlands where the boundary conditions are fed by 2D or 1D models (hybrid grid modeling) (Sinha et al., 1998; Lai, 2010). 3D modeling of sediment transport in wetlands is relatively new (Meselhe et al., 2012) and the lengthy and large scale morphological simulations are not currently feasible due to limitations in computational power.

Apart from whether a 1D, 2D or 3D modeling approach is chosen, there are some challenges involved in the modeling of sediment transport in wetlands. If integrated surface water - groundwater exchange is considered then an appropriate time scale must be chosen for each solver to exchange information and sub-stepping option needs to be considered. Given that the behavior of organic and cohesive sediments in wetlands are controlled by factors such as salinity, temperature, seasonal variations, and bio-geochemistry (Kadlec and Wallace, 2009) the associated model has to be capable of simulating water quality constituents (exchange of

chemical fluxes between water column and substrate deposits in parallel to sediment transport). The particles entering or leaving a wetland are not of a single size (Kadlec and Wallace, 2009), therefore a comprehensive wetland sediment transport model should support multiple particle size classes. Wetland sediment transport modeling does not generally require unsteady hydrodynamic modeling due to the scales of the processes. Usually a series of steady-state inflows and water surface elevations are sufficient unless the effects of an extreme flood event are being studied. The process based understanding of the impact of wetland vegetation as sink or source of sediment, root binding, trapping effect, etc. is in its infancy stage and further fundamental knowledge of those mechanisms is the key gap that needs to be filled to provide accurate sedimentation predictions (Papanicolaou et al., 2008; Schoellhamer et al., 2012). The other issue is incorporating the effect of vegetation heterogeneity on flow and sedimentation (Follett and Nept, 2012). Most of the current wetland models consider equivalent homogenous distribution of vegetation (Feng and Molz, 1997; Lago et al., 2012).

2.2.4. Final remarks on sediment transport modeling in wetlands

Sediment transport is one the most difficult processes to simulate in nature (Papanicolaou et al., 2008). To date, many sediment-associated processes are not mechanistically well-understood. Therefore, modelers have resort to empirical/simplifying formula to define them (van Rijn, 1993). This issue manifests itself in wetland sedimentation modeling more than other water-bodies. The reason is most of the suspended solids therein are actively participating in geochemical and biochemical cycle of wetland. The wetland sediment particles are not typically same as other water-bodies. While rivers and costal zones sediment particles are mostly sand and gravel, wetland specified sediments are iron flocs, aluminum flocs, calcium carbonate as well as biomass. Therefore, a crucial key to further advancement in wetland sediment transport models

is improvement of representative models to describe the behavior wetland specified particles. Besides that issue, even with an idealistic conceptual representative model of suspended sediment concentration, bed sediment properties and morphological changes in wetlands, other steps are still required for an “effective” sediment transport modeling in wetlands, specifically, model verification, model calibration and model validation can keep the mismatch between the simulated results and actual values within the reasonable range: First step is verification to check whether the sediment transport model follows the intended design algorithm (Zamani and Bombardelli, 2013), second, calibration to tune the parameters within physically meaningful ranges such that they accurately represent actual phenomena, and finally, validation to quantitatively assess the accuracy of the sediment transport model (Papanicolaou et al., 2008). Model verification is a purely mathematical activity while sufficient field measurements of suspended sediment flux, bed sediment composition and bed elevation are required to conduct model calibration and validation which is crucial for any robust sediment transport modeling (Schoellhamer et al., 2012). Finally, “post-auditing” a former wetland sediment transport model would be beneficial for quantitative model skill assessment after implementing.

In the end, similar to all modeling practices in water resources, in the modeling of wetland sediment transport there is a tradeoff between computational economy and model complexity. Eventually the modeler should realistically adjust the model’s level of complexity based on the project objectives, resources, budget, time constraints and available measured data for model calibration and validation. Vito Vanoni said: “In conclusion, the choice of a model at this time is arbitrary, and the choice of a modeler is probably more important than the choice of a model.” (Dawdy and Vanoni, 1986).

Chapter Two References

1. ASTM D7664-10 (2010). Standard Test Methods for Measurement of Hydraulic Conductivity of Unsaturated Soils, ASTM International, West Conshohocken, PA.
2. Basha, H. A. (2002). Burgers' equation: A general nonlinear solution of infiltration and redistribution. *Water Resources Research*, 38(11), 29-1.
3. Bekhit, H. M., and Hassan, A. E. (2005). Two-dimensional modeling of contaminant transport in porous media in the presence of colloids. *Advances in Water Resources*, 28(12), 1320-1335.
4. Biggar, J. W. and D. R. Nielsen (1967) Miscible displacement and leaching phenomena, *Agronomy* 11:254-274.
5. Brooks, R. H., and A.T. Corey (1966). Hydraulic Properties of Porous Media. Hydrology Paper no. 3, Civil Engineering Dep., Colorado State Univ. Fort Collins.
6. Cannon, J. R. (2008), *The One-Dimensional Heat Equation*. Cambridge University Press
7. Chapra, S. C. (2008). "Surface water-quality modeling." Waveland Press, Illinois.
8. Charbeneau, R. J. (2006). *Groundwater hydraulics and pollutant transport*. Waveland Press.
9. Chimneya, M. J., Wenkertb, L., and Pietroa, K. C. (2006). "Patterns of vertical stratification in a subtropical constructed wetland in south Florida (USA)." *Ecol. Eng.*, 27, 322-330.
10. Cho, C.M. (1971). Convective transport of ammonium with nitrification in soil. *Can J Soil Sci* 51(3):339–350.
11. Chu, X. and Rediske, R. (2012). "Modeling metal and sediment transport in a stream-wetland system." *J. Environ. Eng.*, 138(2), 152–163.
12. Coats, K. H. and B. D. Smith (1964). Dead-end pore volume and dispersion in porous media, *Soc. Pet. Eng.*, 4:73-84.

13. Dane, J.H., and Topp, G.C., eds., (2002). *Methods of Soil Analysis, Part 4, Physical Methods*: Madison, WI, Soil Science Society of America, Soil Science Society of America Book Series Number 5, ISBN 0-89118-810-X, 1692 p.
14. Dawdy, D. R. and Vanoni, V. A. (1986). "Modeling alluvial channels." *Water Resour. Res.*, 22(9), 71-81.
15. DeCoursey, D., L. Ahuja, J. Hanson, M. Shaffer, R. Nash, C. Hebson and K. Rojas (1992). *Root Zone Water Quality Model: version 1.0: technical documentation*. USDA-ARS, GPSR Technical Report No. 2., Great Plains Systems Research Unit, Ft. Collins, Colorado.
16. Deltares (2011). "User Manual Delft3D" version 3.15.
17. DHI (2011). "Mike 21 and Mike 3 flow model FM, hydrodynamic and transport module, scientific documentation", URL: <http://www.dhisoftware.com>
18. Dinehart, R. L. (2002). "Bedform measurement recorded by sequential single-beam surveys in tidal rivers." *J. Hydrol.*, 258:25–39.
19. Dust M., N. Baran, G. Errera, J.L Hutson, C. Mouvet, H. Schäfer, H. Vereecken, and A. Walker, (2000). Simulation of water and solute transport in field soils with the LEACHP model, *Agricultural Water Management* 44(1–3):225-245
20. El-Kadi, A.I. and Cary, J.W. (1989). *Modeling Coupled Heat, Water, and Solute in Freezing Soils, Including Heave*. International Ground Water Modeling Center Colorado School of Mines, Golden, Colorado.
21. Enfield, C.G., Carsel, R.F., Cohen, S.Z., Phan, T. and Walters, D. M. (1982). Approximating pollutant transport to ground water. *Groundwater*, 20: 711–722.
22. Feng, K., and Molz, F. J. (1997). "A 2-D, diffusion-based, wetland flow model." *J. Hydrol.*, 196, 230-250.

23. Fetter, C. W. (1999). *Contaminant Hydrogeology*, 2nd Edn., Prentice Hall.
24. Flow Science (2011). “Flow-3D User Manual” version 9.4.5.
25. Follett, E. M. and Nepf, H. M. (2012). “Sediment patterns near a model patch of reedy emergent vegetation.” *Geomorphology*, 179, 141–151.
26. Fredlund D.G., H. Rahardjo, and M.D. Fredlund (2012). *Unsaturated soil mechanics in engineering practice*. Wiley.
27. Ganju, N. K., Schoellhamer, D. H. and Bergamaschi, B. A. (2005). “Suspended sediment fluxes in tidal wetlands: measurement, controlling factors, and error analysis.” *Estuaries*, 28(6), 812-822.
28. García, M. H. (2008). “Sediment transport and morphodynamics.” in *ASCE Manual of Practice 110 - Sedimentation Engineering: Processes, Measurements, Modeling and Practice*.
29. Germann, P. F. and K. Beven (1985). Kinematic wave approximation to infiltration into soils with sorbing macropores. *Water Resources Research* 21(7):990-996.
30. Ginn T.R., T. Camesano, T.D. Scheibe, K.E. Nelson, T.P. Clement, B.D. Wood (2006). *Microbial Transport in the Subsurface*, *Encyclopedia of Hydrological Sciences*, Edited by D. McKnight, John Wiley & Sons Publishing, New York, NY.
31. Ginn, T. R. (2002). A travel-time approach to effects of size exclusion on colloid transport in porous media, 10.1029/2001WR000865, *Water Resources Research*.
32. Greimann, B., Lai, Y., and Huang, J. (2008). “Two-dimensional total sediment load model equations.” *J. Hydraul. Eng.*, 134(8), 1142–1146.
33. Gvirtzman H. and S. J. Gorelick, (1991). Dispersion and advection in unsaturated porous media enhanced by anion exclusion, *Nature* 352: 793-795.

34. Healy, R.W. (1990). Simulation of solute transport in variably saturated porous media with supplemental information on modifications to the U.S. Geological Survey's Computer Program VS2D, U.S. Geological Survey Water Resour. Investigations Rep. 90-4025, 125 p.
35. Hillel, D. (1998). Environmental Soil Physics: Fundamentals, Applications, and Environmental Considerations, Academic Press.
36. Hirano, M., Hashimoto, H., Tamamatsu, J., Park, K., and Hibako, T. (1999). "Bed-load transport and bed variation in an open channel with multiple rows of cylinders." *Ann. J. Hydr. Engng. JSCE* 43, 1109–1114.
37. Holloway, R. W. (2010). "Annual sediment retention and hydraulic residence time variability in a riverine wetland receiving unregulated inflow from agricultural runoff." MSc thesis, California State University, Monterey Bay.
38. Horppila, J., Nurminen, L. (2003). "Effects of submerged macrophytes on sediment resuspension and internal phosphorus loading in Lake Hiidenvesi (Southern Finland)." *Water Res.* 37(18): 4468–4474.
39. Horvath, T. G. (2004). "Retention of particulate matter by macrophytes in a first-order stream." *Aquatic Botany*, 78: 27–36.
40. Jacques, D., and J. Šimůnek, (2010). Notes on HP1 – a software package for simulating variably-saturated water flow, heat transport, solute transport and biogeochemistry in porous media, HP1 Version 2.2, SCK•CEN-BLG-1068, Waste and Disposal, SCK-CEN, Mol, Belgium, 113 pp.
41. Jha, S. K., and Bombardelli, F. A. (2010). "Toward two-phase flow modelling of non-dilute sediment transport in open channels." *J. Geophys. Res., Earth Surface*, 115, F03015.

42. Jordanova, A. A., and James, C. S. (2003). "Experimental study of bed load transport through emergent vegetation." *J. Hydraul. Eng.* 129(6), 474–478.
43. Jury, W. and R. Horton (2004). *Soil Physics*, 6th Ed. John Wiley and Sons, Inc., Hoboken, New Jersey, 370 Pgs.
44. Kadlec, R. H., and Wallace, D. C. (2009). "Treatment wetlands." 2nd ed., CRC Press,
45. Kassem, A., and Chaudhry, M. (1998). "Comparison of coupled and semicoupled numerical models for alluvial channels." *J. Hydraul. Eng.*, 124(8), 794–802.
46. King, I. P. (1988). "A finite element model for three dimensional hydrodynamic systems." Rep. to Waterways Experiment Station, U.S. Army Corps of Engineers, Vicksburg, Miss.
47. Kothyari, U.C., Hashimoto, H., and Hayashi, K. (2009). "Effect of tall vegetation on sediment transport by channel flows." *Journal of Hydraulic Research*, 47(6), 700-710.
48. Lago, M. E., Miralles-Wilhelm, F., Mahmoudi, M., and Engel, V. (2010). "Numerical modeling of the effects of water flow, sediment transport and vegetation growth on the spatiotemporal patterning of the ridge and slough landscape of the Everglades wetland." *Adv. Water Res.* 33(10), 1268-1278.
49. Lai, Y. (2010). "Two-Dimensional Depth-Averaged Flow Modeling with an Unstructured Hybrid Mesh." *J. Hydraul. Eng.*, 136(1), 12–23.
50. Larsen, L. G., and Harvey, J. W. (2010). "How vegetation and sediment transport feedbacks drive landscape change in the Everglades and wetlands worldwide." *The American Naturalist*, 176, E66–E79.
51. Lassey, K. R. (1988). Unidimensional solute transport incorporating equilibrium and rate-limited isotherm with first-order loss: Model conceptualizations and analytic solutions, *Water Resources Research* 24(3):343-350.

52. Lassey, K. R. (1989). Correction to “Unidimensional Solute Transport Incorporating Equilibrium and Rate-Limited Isotherms with First-Order Loss Model Conceptualizations and Analytic Solutions”. *Water Resources Research* 25(3): 582.
53. Lee, H. Y., and Shih, S. S. (2004). “Impacts of vegetation changes on the hydraulic and sediment transport characteristics in Guandu mangrove wetland.” *Ecol. Eng.*, 23, 85-94.
54. Leij F.J. and Bradford S.A. (1994). 3DADE: A Computer Program for Evaluating Three-Dimensional Equilibrium Solute Transport in Porous Media, Research Report No. 134, U. S. Salinity Laboratory, USDA, ARS, Riverside.
55. Leij F.J. and Toride N. (1997). N3DADE: A Computer Program for Evaluating Nonequilibrium Three-Dimensional Equilibrium Solute Transport in Porous Media, Research Report No. 143, U. S. Salinity Laboratory, USDA, ARS, Riverside.
56. Leij, F.J., W.J. Alves, M.Th. van Genuchten, and J.R. Williams. (1996). The UNSODA unsaturated hydraulic database. EPA/600/R-96/095, U.S. Environmental Protection Agency, Cincinnati, OH.
57. Logan J.D. (2001). *Transport modeling in hydrogeochemical systems, interdisciplinary applied mathematics*, vol 15. Springer, Berlin.
58. Luengen, A.R., and Flegal, A. R. (2009). “Role of phytoplankton in mercury cycling in the San Francisco Bay estuary.” *Limnol. Oceanogr.* 54(1):23–40.
59. Malmaeus, J. M., and Hakanson, L. (2003). “A dynamic model to predict suspended particulate matter in lakes.” *Ecol. Modell.* 167(3): 247–262.
60. Massoudieh, A., and Ginn, T. R. (2007). Modeling colloid-facilitated transport of multi-species contaminants in unsaturated porous media. *Journal of Contaminant Hydrology*, 92(3-4), 162-183.

61. Meselhe, E. A., Georgiou, I., Allison, M. A., and McCorquodale, J. A. (2012). "Numerical modeling of hydrodynamics and sediment transport in lower Mississippi at a proposed delta building diversion." *J. Hydrol.* 472–473, 340–354.
62. Millington, R. J. and J. M. Quirk (1961). Permeability of porous solids, *Transactions of the Faraday Society* 57:1200-1207
63. Minh Duc, B., Wenka, T., and Rodi, W. (1998). "Depth-average numerical modeling of flow and sediment transport in the Elbe River." *Proc., 3rd Int. Conf. on Hydrosience and Eng.*, Berlin.
64. Mitchell, J. K., and K. Soga (2005). *Fundamentals of soil behavior*. 3rd edition, New York: Wiley.
65. Mitsch, W. J., and Gosselink, J. G. (2000). "Wetlands." 3rd ed., John Wiley & Sons.
66. Mualem, Y. (1976). A new model for predicting the hydraulic conductivity of unsaturated porous media. *Water resources research*, 12(3), 513-522.
67. Nardi, A., L. M. de Vries, P. Trinchero, A. Idiart, and J. Molinero (2012). *Coupling Multiphysics with Geochemistry - The COMSOL-PHREEQC Interface: a Powerful Tool for Reactive Transport*, Proceedings of the COMSOL Conference in Milan, Italy.
68. Nielsen, D. R., van Genuchten, M. Th., and Biggar, J. W. (1986). Water flow and solute transport processes in the unsaturated zone. *Water Resources Research*, 22(9S), 89S-108S.
69. Niswonger, R.G., Prudic, D.E., Regan, R.S. (2006). *Documentation of the Unsaturated-Zone Flow (UZFI) Package for modeling unsaturated flow between the land surface and the water table with MODFLOW-2005*, USGS Techniques and Methods 6-A19, 62 pg.
70. Nkedi-Kizza, P., J.W. Biggar, H.M. Selim, M.T. van Genuchten, P.J. Wierenga, J.M. Davidson, and D.R. Nielsen (1984). On the equivalence of two conceptual models for

describing ion exchange during transport through an aggregated oxisol, *Water Resour. Res.*, 20:1123-1130.

71. Ogata A., and Banks R.B. (1961). A solution of differential equation of longitudinal dispersion in porous media. United States Geological Survey, Professional Paper 411-A
72. Okabe, T., Yuuki, T., and Kojima, M. (1997). "Bed-load rate on movable beds covered by vegetation." *Environmental and Coastal Hydraulics: Protecting the Aquatic Habitat*, pp. 1396–1401.
73. Papanicolaou, A., Elhakeem, M., Krallis, G., Prakash, S., and Edinger, J. (2008). "Sediment transport modeling review-current and future developments." *J. Hydraul. Eng.*, 134(1), 1-14.
74. Parkhurst, D.L. and Appelo, C.A.J. (1999) User's guide to PHREEQC (version 2)--A computer program for speciation, batch-reaction, one-dimensional transport, and inverse geochemical calculations: U.S. Geological Survey Water-Resources Investigations Report 99-4259, 312 p.
75. Pereira, J. F., McCorquodale, J. A., Meselhe, E. A., Georgiou, I. Y., and Allison, M. A. (2009). "Numerical simulation of bed material transport in the Lower Mississippi River." *J. Coast. Res.* (56), 1449-1453.
76. Pruess, K. (1987). TOUGH User's Guide, Nuclear Regulatory Commission, Report NUREG/CR-4645 (also Report LBL-20700, Lawrence Berkeley Lab., Berkeley, CA).
77. Radcliffe, D., and J. Šimůnek (2010). *Soil Physics with HYDRUS*, CRC Press.
78. Reynolds, W. D., and Elrick, D. E. (1987). A laboratory and numerical assessment of the Guelph permeameter method. *Soil Science*, 144(4), 282-299.
79. Rumynin, V. G. (2011), *Subsurface Solute Transport Models and Case Histories, Theory and Application of Transport in Porous Media 25*, Springer.

80. Sánchez, A. (2008). "Interactions between wetlands and tidal inlets." Coastal and Hydraulics Engineering Technical Note. ERDC/CHL CHETN-IV-72. Vicksburg, MS: U.S. Army Engineer Research and Development Center.
81. Schaap, M.G., and F.J. Leij (2000) Improved prediction of unsaturated hydraulic conductivity with the Mualem-van Genuchten model. *Soil Sci. Soc. Am. J.* 64:843–851.
82. Schoellhamer, D. H., Wright, S. A., and Drexler, J. Z. (2012). "Conceptual model of sedimentation in the Sacramento - San Joaquin River Delta." *San Francisco Estuary and Watershed Science*, 10(3).
83. Shainberg, I., Rhoades, J. D., and Prather, R. J. (1981). Effect of low electrolyte concentration on clay dispersion and hydraulic conductivity of a sodic soil. *Soil Science Society of America Journal*, 45(2), 273-277.
84. Šimůnek, J. and D. L. Suarez (1993). UNSATCHEM-2D Code for Simulating Two-Dimensional Variably Saturated Water Flow, Heat Transport, Carbon Dioxide Production and Transport, and Multicomponent Solute Transport with Major Ion Equilibrium and Kinetic Chemistry, Version 1.1. Research Report No. 128, USDA-ARS U. S. Salinity Laboratory, Riverside, California.
85. Šimůnek, J., and van Genuchten, M.Th. (2007), Contaminant transport in unsaturated zone theory and modeling. Chapter 22 in "The Handbook of Groundwater Engineering", 2nd ed., Editor Delleur, J.W., CRC Press.
86. Šimůnek, J., Jarvis, N.J., van Genuchten, M.Th. and Gärdenäs, A. (2003), Nonequilibrium and preferential flow and transport in the vadose zone: review and case study. *J. Hydrol.* 272, 14–35.

87. Šimůnek, J., van Genuchten, M.T., & Sejna, M. (2006). The HYDRUS software package for simulating the two-and three-dimensional movement of water, heat, and multiple solutes in variably-saturated media. Technical manual.
88. Šimunek, J., van Genuchten, M.Th., Šejna, M., Toride,N. and Leij, F.J. (1999). The STANMOD computer software for evaluating solute transport in porous media using analytical solutions of convection-dispersion equation. Versions 1.0 and 2.0, IGWMC-TPS-71, International Ground Water Modeling Center, Colorado School of Mines, Golden, Colorado, 32 pp.
89. Singh, V. P., Kinematic Wave Modeling in Water Resources, Environmental Hydrology, (1997) John Wiley & Sons Publishing, 859 pages.
90. Sinha, S.K., Sotiropoulos, F., Odgaard, A.J. (1998). “Three-dimensional numerical model for flow through natural rivers.” J. Hydr. Eng., ASCE 124:13–23.
91. Spasojevic, M. and Holly, F. M. (1990). “2-D bed evolution in natural watercourses - New simulation approach.” J. Waterw. Port Coastal Ocean Eng., 116(4), 425-443.
92. Spasojevic, M. and Holly, F. M. (2008). “Two- and three dimensional numerical simulation of mobile-bed hydrodynamics and sediment.” in ASCE Manual of Practice 110 - Sedimentation Engineering: Processes, Measurements, Modeling and Practice.
93. Suarez, D. L., Rhoades, J. D., Lavado, R., & Grieve, C. M. (1984). Effect of pH on saturated hydraulic conductivity and soil dispersion. Soil Science Society of America, 48(1), 50-55.
94. Thomas, W. A., and Prashum, A. I. (1977). “Mathematical model of scour and deposition.” J. Hydr. Div., 110(11), 1613–1641.

95. Toride, N., F.J. Leij, and M.Th. van Genuchten (1995). The CXTFIT code for estimating transport parameters from laboratory or field tracer experiments. Version 2.0. Res. Rep. 137. U.S. Salinity Lab., Riverside, CA.
96. Toride, N., Leij, F. J., & van Genuchten, M.T. (1993). A comprehensive set of analytical solutions for nonequilibrium solute transport with first-order decay and zero-order production. *Water Resources Research*, 29(7), 2167-2182.
97. Travis, B. J., (1984). "TRACR3D: A Model of Flow and Transport in Porous/Fractured Media", Los Alamos National Laboratory Report LA-9667-MS, 110 pp.
98. Trefry, M.G.; Muffels, C. (2007). "FEFLOW: a finite-element ground water flow and transport modeling tool". *Ground Water* 45 (5): 525–528.
99. Unga, M., Wilkinson, K., and Summers, K. (1998). Users guide for MYGRT, Version 3.0: Software for simulating migration of organic and inorganic chemicals in groundwater, EPRI Report TR-111748, Electric Power Research Institute, Palo Alto, CA.
100. van Genuchten, M. Th. (1980). Closed-form equation for predicting the hydraulic conductivity of unsaturated soils. *Soil Sci. Soc. Amer. Proc.*, Vol. 44, pp. 892-898.
101. van Genuchten, M. Th. (1981). Non-equilibrium transport parameters from miscible displacement experiments, Research Report No. 119 , U. S. Salinity Laboratory, USDA, ARS, Riverside, CA.
102. van Genuchten, M. Th. (1985). Convective-dispersive transport of solutes involved in sequential first-order decay reactions, *Computers & Geosciences*, 11 (2), 129-147.
103. van Rijn, L. C. (1993). "Principles of sediment transport in rivers estuaries and coastal seas." Aqua Publications, Netherlands.

104. van Rijn, L. C., and Tan, G. L. (1985). "SUTRENCH model: Two dimensional vertical mathematical model for sedimentation in dredged channels and trenches by currents and waves." Rijkswaterstaat Communications, 41.
105. Voss, C.I. and Provost, A.M. (2002). SUTRA, a model for saturated-unsaturated variable density ground-water flow with energy or solute transport: US Geological Survey Water-Resources Investigations Report 2002-4231, 291p
106. Walter, M. T., Kim, J. S., Steenhuis, T. S., Parlange, J. Y., Heilig, A., Braddock, R. D., and Boll, J. (2000). Funneled flow mechanisms in a sloping layered soil: Laboratory investigation. *Water Resources Research*, 36(4), 841-849.
107. Warrick, A. W., and Parkin, G.W. (1995). An analytical solution for one-dimensional drainage: Burgers' and simplified forms, *Water Resources Research*, 31, 2891–2894.
108. White, M.D., and M. Oostrom, (2006). STOMP Subsurface Transport Over Multiple Phases, Version 4.0: User's Guide, PNNL-15782, Pacific Northwest National Laboratory, Richland, Washington.
109. Wissmeier, L. and Barry, D.A. (2011). Simulation tool for variably saturated flow with comprehensive geochemical reactions in two-and three-dimensional domains. *Environmental Modelling & Software*, 26:210-218.
110. Wright, S. A., and Schoellhamer, D. H., (2005). "Estimating sediment budgets at the interface between rivers and estuaries with application to the Sacramento– San Joaquin River Delta." *Water Resour. Res.*, 41.
111. Wu, W., Shields, Jr. F. D., Bennett, S. J., and Wang, S. S. Y. (2005). "A depth- averaged two-dimensional model for flow, sediment transport, and bed topography in curved channels with riparian vegetation." *Water Resour. Res.*, 41.

112. Wu, W., Wang S. S. Y., and Jia Y. (2000). "Nonuniform sediment transport in alluvial rivers." *J. Hydraul. Res.* 38 (6), 427–434.
113. Xu, T., E. Sonnenthal, N. Spycher, and K. Pruess (2004). *TOUGHREACT User's Guide: A Simulation Program for Non-isothermal Multiphase Reactive Geochemical Transport in Variably Saturated Geologic Media*, LBNL-55460.
114. Zamani K. and Bombardelli, F.A. (2014). "Analytical solutions of nonlinear and variable-parameter transport equations for verification of numerical solvers." *Environ. Fluid Mech.* 14:711–742.
115. Zoppou, C., Knight, J. H., (1997), "Analytical Solution for Advection and Advection-Diffusion Equation with Spatially Variable Coefficients", *J. Hydraulic Eng.*, Vol. 123(2), pp. 144-148.

Chapter 3: Analytical Solutions of Nonlinear and Variable-Parameter Transport Equations for Verification of Numerical Solvers¹

3.1. Introduction

The transport or Advection-diffusion-reaction (ADR) equation represents a host of natural and man-made phenomena in environmental fluid mechanics, biology, chemistry and applied physics, among other fields. The equation can express the conservation of mass, momentum or energy. The transport of state variable $\phi(\underline{x}, t)$ can be represented by the following generic equation:

$$\frac{\partial \phi}{\partial t} + \nabla \cdot (\underline{u}(\phi, \underline{x}, t)\phi) = \nabla \cdot (\underline{\underline{D}}(\phi, \underline{x}, t) \cdot \nabla \phi) + R(\phi, \underline{x}, t) \quad (3-1)$$

where t and \underline{x} are time and space coordinates, \underline{u} refers to the flow velocity, $\underline{\underline{D}}$ is the diffusivity tensor, and R is the source term which accounts for any form of loss or generation of the property ϕ [Hundsdoerfer and Verwer, 2003]. In most cases of heat and contaminant transport in natural streams and groundwater flow, velocity and diffusivity do not depend upon the state variable ϕ ; therefore, equation (3-1) is a linear partial differential equation (PDE). However, this is not always the case. For example, velocity and dispersivity of density driven flows in lakes and estuaries and saltwater intrusion in coastal aquifers can depend on concentration [Fischer et al., 1979; Fleenor and Bombardelli, 2013]. Diffusivity of hyper-concentrated sediment-laden flows depends on the concentration [Wan and Wang, 1994]. In turn, the entrainment and deposition of

¹ This chapter was published as: Zamani, K., Bombardelli, F. A. (2014). Analytical solutions of nonlinear and variable-parameter transport equations for verification of numerical solvers. *Environmental Fluid Mechanics*, 14(4), 711-742.

sediment can be nonlinear functions of the sediment concentration in the water column [*Jha and Bombardelli*, 2010, 2011]. In addition to nonlinearities, velocity and diffusivity are often functions of space and/or time, reflecting for instance non-uniform and tidal flow, and seasonal or large-scale transients of the porous media.

Numerical models are widely used in quantification of transport phenomena on architectures ranging from PCs to high-performance computing platforms. The growth of numerical simulation generates the need for code verification tools. Analytical solutions (employed in the Method of Exact Solution, MES [*Oberkampf and Roy*, 2010]) constitute the natural tool for verification of numerical codes [*Tracy*, 2006; *Stern et al.*, 2006; *Wang et al.*, 2008; *Roache*, 2009; *Oberkampf and Roy*, 2010] and development of the numerical schemes [*Valocchi and Malmstead*, 1992; *Siegel et al.*, 1997; *Verwer et al.*, 2004; *Oberkampf and Roy*, 2010; *Stockie*, 2011].

There is a considerable body of work on the analytical solution of the ADR equation. In addition to mathematicians [*Crank*, 1979; *Logan*, 1996, 2001, 2008; *Khalifa*, 2003; *Remesikova*, 2004; *Cannon*, 2008; *Stakgold and Holst*, 2011], geo-hydrologists [*Ogata and Banks*, 1961; *Mohsen and Pinder*, 1984; *Barry and Sposito*, 1989; *Yates*, 1990, 1992; *Parlange et al.*, 1998; *Chen et al.*, 2003a, 2003b, 2008a, 2008b, 2011a, 2011b; *Singh et al.*, 2009, 2010], researchers in atmospheric science [*Tirabassi*, 1989; *Costa et al.*, 2006; *Stockie*, 2011], bioengineers [*Khakpour and Vafai*, 2008] and heat-transfer researchers [*Carslaw and Jaeger*, 1959; *Guerrero et al.*, 2009] have all contributed significantly to the analytical solution of the transport equation. To the best of our knowledge, Table 3-1 lists the most relevant analytical solutions of the transport equation for code verification to date. The table primarily shows the solutions of the single-scalar transport equation and a more comprehensive table is outside the scope of this paper. The second

column discusses the dimensionality and the coordinate system in which the solution has been derived; most of the solutions have been derived either in one dimension (1-D), or in simplified/symmetric multi-dimensional space. The next three columns describe the characteristics of advective, diffusive and reactive terms, respectively. They show if those three terms are involved in the equation and, in the case they are, whether they are constant, linear or nonlinear function of the independent/dependent variable(s). The sixth column shows the solution technique, ranging from similarity solutions, to perturbation methods, to eigenfunction expansions.

From inspection of Table 3-1, it becomes apparent that there is no analytical solution for equation (3-1) with all nonlinearities involved. Given that many of the well-developed solution techniques are just viable for linear PDEs, this shortcoming is understandable [Logan, 2001]. Second, in spite of the fact that a number of special cases of nonlinear ADR equations have been solved [see Logan, 2001, 2008; Rajabi et al., 2007; Cannon, 2008; Momani and Yildirim, 2010], some of those solutions have been produced through power series [Chen et al., 2008a; Guerrero et al., 2009] or perturbation theory [Wu and Cheung, 2008; Momani and Yildirim, 2010] which have shortcomings on their own for code verification, since they converge slowly, requiring a relatively large number of terms for adequate accuracy. This is a clear inconvenience if one is interested in testing codes because it is hard to automate the computation of the terms [Roache, 2009, page 86; Oberkampf and Roy, 2010, pages 208, 240]. Third, many existing solutions of the ADR equation with spatially-varying velocity and diffusion/dispersion coefficient are not consistent with the conservation of mass of the carrier fluid (see below). Fourth, to the best of our knowledge, solutions of the ADR equation containing simultaneous spatial and time variability of the velocity and dispersion coefficient do not exist.

The problem motivating this work was the verification of a general code for the simulation of the transport of constituents in tidal networks of channels, i.e., in 1-D [Ateljevich *et al.*, 2011]. In these systems, the velocity and the dispersion coefficients are functions of space and time, and might be functions of the sediment concentration for non-dilute mixtures in very unusual cases. Further, we were interested in the cross-sectionally integrated version of the flow mass and transport equations:

$$\frac{\partial A}{\partial t} + \frac{\partial(UA)}{\partial x} = 0 \quad (3-2)$$

$$\frac{\partial(AC)}{\partial t} = \frac{\partial}{\partial x} \left(AD \frac{\partial C}{\partial x} \right) - \frac{\partial(UAC)}{\partial x} + R \quad (3-3)$$

where A denotes the cross-sectional area [L^2], C is the cross-sectional average concentration [$mass/L^3$ or L^3/L^3], U denotes the velocity averaged over the wetted area [L/T], and D refers to the effective dispersion in the x direction [L^2/T]. We were interested in the *coupled* solution of the above system. Regarding this particular important issue, Neelz [2006] discussed the deficiencies of a given spatially-variable analytical solution of the ADR equation which did not satisfy equation (3-2), leading to inconsistencies in the results from the physical standpoint.

In this paper, we present “clean” analytical solutions for the verification of 1-D transport solvers considering many possible combinations in equation (3-1). The word “clean” refers to a solution given in explicit form and expressed in terms of elementary functions. Series-based solution or solutions in terms of hypergeometric functions or integral forms are not included in our definition of the word “clean.” In the next section (Section 3.2), a brief review of the methods of solving the transport equation is given. Then we provide analytical solutions to the ADR equation for verification of the following variants: a) nonlinear velocity, dispersivity and sink/source (Section 3.3); b) spatiotemporal changes in flow field and dispersivity; these

analytical solutions hold mass continuity for the ambient flow field (Section 3.4). In particular, the derived analytical solutions are provided in the general form. Therefore, they are applicable for any required form of boundary conditions (Dirichlet, Neumann and Robin) and arbitrary Péclet and Damköhler numbers. In Section 3.5, we give hypothetical examples that utilize the derived solutions. Section 3.6 discusses quantitative metrics of error for model skill assessment and code verification. We also proceed with a critical discussion on the alternative methods of code verification in the Section 3.7, followed by conclusions.

3.2. Background Methodologies

In this section, concise reviews of the techniques we use to derive the analytical solutions of the transport equation are provided.

3.2.1. Reduction of ADR equation to heat equation

Consider the following ADR equation where u_0 and D_0 indicate constant velocity and dispersivity respectively:

$$\frac{\partial \hat{C}}{\partial t} = \frac{\partial}{\partial \hat{x}} \left(D_0 \frac{\partial \hat{C}}{\partial \hat{x}} \right) - \frac{\partial (u_0 \hat{C})}{\partial \hat{x}} - \beta \hat{C}; \quad -\infty < \hat{x} < \infty, \quad 0 < t \quad (3-4)$$

Since there is comprehensive literature on the analytical solution of the heat equation, oftentimes we recast a given ADR equation in the classical form of the former to find an analytical solution [Logan, 2001]. To that end, we follow a transformation discussed in *Singh et al. (2009)* and *Yadav et al. (2010)*:

$$\hat{C}(x, t) = C(x, t) e^{\left(\frac{u_0 x}{2D_0} - \frac{u_0^2 t}{4D_0} - \beta t \right)} \quad (3-5)$$

Under this transformation, the advective and source terms are eliminated from (3-4). Cases of variable velocity will be considered in the next subsection.

3.2.2. Transformation to simplify time dependent ADR

Take an advection-diffusion equation in which the dispersivity and velocity are varying with time:

$$\frac{\partial \hat{C}(X,t)}{\partial t} = \frac{\partial}{\partial X} \left(D(t) \frac{\partial \hat{C}(X,t)}{\partial X} \right) - \frac{\partial (u(t)\hat{C}(X,t))}{\partial X}, \quad -\infty < X < \infty, 0 < t \quad (3-6)$$

Let $\xi = \int_0^t u(\tau) d\tau$, $x = X - \xi$, and $\hat{C}(X,t) = \hat{C}(x + \xi, t) = C(x, t)$; under these transformations, equation (3-6) becomes:

$$\frac{\partial C(x,t)}{\partial t} = D(t) \frac{\partial^2 C(x,t)}{\partial x^2}, \quad -\infty < x < \infty, 0 < t \quad (3-7)$$

Now, by introducing $T = \int_0^t D(\tau) d\tau$ the above equation reduces to the dimensionless form of the heat equation [*Kirchhoff*, 1894]:

$$\frac{\partial C(x,T)}{\partial T} = \frac{\partial^2 C(x,T)}{\partial x^2} \quad (3-8)$$

These transformations were utilized by various researchers [*Crank*, 1979; *Barry and Sposito*, 1989; *Basha and El-Habel*, 1993; *Kumar et al.*, 2009; *Singh et al.*, 2009].

3.2.3. Fundamental solution of the inhomogeneous heat equation

The following is an initial value problem on an infinite domain, where $F(C, x, t)$ is a linear/nonlinear function of dependent and independent variables (forcing function):

$$\frac{\partial C}{\partial t} = D_0 \frac{\partial^2 C}{\partial x^2} + F(C, x, t); \quad -\infty < x < \infty, 0 < t \leq T$$

$$C(x, 0) = f(x) \quad (3-9)$$

where $f(x)$ and its first derivative are smooth bounded functions. It can be shown that the analytical solution of equation (3-9) is given by an integral, convoluting the Green's function of heat equation and the bounded function and the non-homogenous forcing [*Cannon*, 2008]:

$$C(x, t) = \int_{-\infty}^{\infty} G(x - \xi, t) f(\xi) d\xi - \int_0^t \int_{-\infty}^{\infty} G(x - \xi, t - \tau) F(C(\xi, \tau), \xi, \tau) d\xi d\tau \quad (3-10)$$

where $G(x, t)$ is the fundamental solution (Green's function) associated with the heat operator on the infinite domain, given by [Logan, 2001]:

$$G(x, t) = \frac{1}{\sqrt{4\pi D_0 t}} e^{-\frac{x^2}{4D_0 t}} \quad (3-11)$$

In the next section, we will use the above mentioned techniques to degenerate various forms of the ADR equation to simpler cases which can be approached by conventional PDE solving methods (direct integration, separation of variables, and travelling wave solution). Those transformations will be used to either eliminate the advective term, or linearize variable diffusivities, or solve the nonhomogeneous heat equation.

3.3. Analytical Solutions to Test Nonlinearity

Common cases where nonlinearities manifest themselves in the numerical solution of ADR equations are those with stiff source terms, where adaptive time steps are needed to address the different time scales [Radhakrishnan, 1983; Massoudieh et al., 2010]; also, nonlinear dispersivity may generate instability of the numerical solution [Hundsdorfer and Verwer, 2003]. In turn, a nonlinear advective term can develop jump discontinuities at finite times (shock formation) [LeVeque, 2002]. Considering those challenges, analytical solutions serving as verification benchmarks for nonlinear cases are needed.

3.3.1. Diffusion with nonlinear dispersion coefficient and source term

Take the following nonlinear diffusion equation where both the dispersivity and decay terms are exponential functions of concentration:

$$\frac{\partial C(x,t)}{\partial t} = \frac{\partial}{\partial x} \left(D_0 e^{C(x,t)} \frac{\partial C(x,t)}{\partial x} \right) - \beta e^{C(x,t)}; \quad -\infty < x < \infty, \quad 0 < t, \quad 0 < D_0, \quad 0 < \beta \quad (3-12)$$

This situation can occur close to streambeds in the cases of very dense sediment concentration [Wan and Wang, 1994]. In addition to that, for the sake of rigor, we consider exponential decay as an extreme form of nonlinear source.

In what follows, we present a solution to equation (3-12). Substitution of $c(x, t) = e^{C(x,t)}$ leads to the equation with the form of:

$$\frac{\partial c}{\partial t} = c \frac{\partial}{\partial x} \left(D_0 \frac{\partial c}{\partial x} \right) - \beta c^2 \quad (3-13)$$

With multiplicative separation of variables ($c(x, t) = X(x)T(t)$) we would reduce the above PDE to two autonomous ODEs for $X(x)$ and $T(t)$, the final solution is:

$$c(x, t) = \frac{e^{x\sqrt{\frac{\beta}{D_0+K_1}} e^{-x\sqrt{\frac{\beta}{D_0+\frac{\lambda}{\beta}}}}}{K_2 - \lambda t} \quad (3-14)$$

where λ is a positive separation constant [Stakgold and Holst, 2011] and the K_i s are constants to be determined based on the boundary conditions and code verification needs. Hence, the final analytical solution of the equation (3-12) would be in the form of:

$$C(x, t) = \ln \left(\frac{e^{x\sqrt{\frac{\beta}{D_0+K_1}} e^{-x\sqrt{\frac{\beta}{D_0+\frac{\lambda}{\beta}}}}}{K_2 - \lambda t} \right) \quad (3-15)$$

Equation (3-15) provides the most generic form of the solution up to arbitrary constants; the selection of spatial domain and boundary conditions can be established based on the needs of the code verification. It is worth noting that the conservation of mass of the carrier fluid was not imposed herein since there is no advection in equation (3-12). This analytical solution cannot capture any arbitrary form of initial condition. However this solution is useful for the purpose of this study, as shown below. We acknowledge that a similar solution can be obtained with

Wolfram Mathematica, but this is the first time this solution has been proposed as part of a framework for code verification.

3.3.2. Uniform advection dispersion with nonlinear source term

Consider a plume of contaminant which moves with constant flow and diffusivity, while subjected to a nonlinear decay. Among the various possible forms for the nonlinear decay, the cubic one is chosen herein to assure exercising a severe case of stiff source term. The ADR equation is, therefore, in the following form:

$$\frac{\partial c}{\partial t} = \frac{\partial(u_0 c)}{\partial x} + \frac{\partial}{\partial x} \left(D_0 \frac{\partial c}{\partial x} \right) - \beta c^3; \quad -\infty < X < \infty, 0 < t, 0 < D_0, 0 < \beta \quad (3-16)$$

where β is a parameter that represents the decay of constituent C . The solution strategy is to recast (3-16) into the corresponding heat equation and solve it. Consider therefore a moving frame of reference and moving boundary conditions as in subsection 3.2.2: $x = X + u_0 t$ and $C(X, t) = C(x - u_0 t, t) = c(x, t)$; under those transformations, equation (3-16) becomes:

$$\frac{\partial c}{\partial t} = D_0 \frac{\partial^2 c}{\partial x^2} - \beta c^3 \quad (3-17)$$

Taking into account the scales in diffusion process, we build a similarity solution to reduce the above PDE to an ODE as: $c(x, t) = \frac{v(\xi)}{\sqrt{t}}$; where $\xi = \frac{x}{\sqrt{t}}$ (called Boltzmann transform [*Boltzmann*, 1894]). Substitution of these transformations reduces equation (3-17) to the following ODE:

$$D_0 v_{\xi\xi} + \frac{1}{2} \xi v_{\xi} + \frac{1}{2} v - \beta v^3 = 0 \quad (3-18)$$

The above ODE is a form of *Abel* ODE, and it is solved based on the tables given in the literature [*Polyanin and Zaitsev*, 2003]:

$$c(x, t) = t^{-\frac{1}{2}} v(\xi) = \sqrt{\frac{2D_0}{\beta}} \frac{2x}{x^2 + 6D_0 t} \quad (3-19)$$

The exact solution defined in the variables of equation (3-16) is:

$$C(X, t) = \sqrt{\frac{2D_0}{\beta}} \frac{z(X+u_0t)}{(X+u_0t)^2+6D_0t} \quad (3-20)$$

where any type of boundary condition for numerical verification can be reconstructed from the general solution (3-20). Note that this analytical solution can be derived employing the fundamental solution mentioned in the subsection 3.2.3 as well. This solution is not a “fundamental solution” in terms of Green’s function and is not able to capture any arbitrary initial condition. However, it is useful for the purpose of code verification. Finally, equation (3-13) holds conservation of mass for the ambient flow field.

3.3.3. Burgers’ equation for verification of transport solver

The Burgers’ equation is a second order nonlinear PDE that has become a prototype for phenomena which involve effects of nonlinearity in concomitance with dissipation. It is worth mentioning that the state variable of Burgers’ equation is usually denoted by “ u ” while we named it “ C ” here [Logan, 2008]:

$$\frac{\partial C}{\partial t} = D_0 \frac{\partial^2 C}{\partial x^2} - C \frac{\partial C}{\partial x}; \quad -\infty < x < \infty, \quad 0 < t, \quad 0 < D_0 \quad (3-21)$$

Since Burgers’ and ADR equations have similar structures, here we take advantage of the Burgers’ equation analytical solutions for verification of ADR solvers. To the best of our knowledge, papers employing this technique are relatively rare and recent. *Hills and Warrick* [1993] employed an analytical solution of Burgers’ equation to verify numerical solutions of Richards’ equation. Later on, a similar trick was employed by *Verwer et al.* [2004] to test an ADR solver. Several closed-form traveling wave and asymptotic solutions have been derived for the Burgers’ equation [Logan, 2008]. After the works by *Hopf* [1950] and *Cole* [1951], it is well

known that Burgers' equation and its boundary conditions can be converted to the linear heat equation by the Hopf-Cole transformation (3-22) and solved via the fundamental solution given in subsection 3.2.3

$$C(x, t) = -D \frac{2}{c(x, t)} \frac{\partial c(x, t)}{\partial x} \quad (3-22)$$

Consider equation (3-21) with its boundary/initial conditions: $C(x \rightarrow -\infty, t) = c_1$ upstream; $C(x \rightarrow \infty, t) = c_2$ downstream; and $C(x, 0) = c_2$ as initial condition. Applying the Hopf-Cole transformation to equation (3-21) and its boundary conditions, the analytical solution of the Burgers' equation is:

$$C(x, t) = c_1 + \frac{c_2 - c_1}{1 + e^{(c_2 - c_1)\left(x - \frac{(c_2 + c_1)t}{2}\right)/2D_0}} \quad (3-23)$$

In the following section, three analytical solutions to test spatial and temporal changes in velocity and diffusivity of transport solvers are given.

3.4. Analytical Solutions for Mass Conservative, Variable-Parameter Transport Equations

In this section, we first recast a former spatially varying coefficients ADR equation such that it also satisfies the equation of continuity for ambient flow (3-2). Then, we solve it based on the solution given by *Ogata and Banks* [1961]. Next, we derive the time-dependent ADR equation for groundwater and estuarine pollution transport and solve it via transformation to the solution by *Ogata and Banks* [1961]. Finally, we employ a well-known exact solution for tidal forcing in a rectangular basin [*Wang et al.*, 2008] for the purpose of exercising the ADR solver with spatiotemporal varying flow field.

3.4.1. ADR equation with spatially varying coefficients

Consider the following equation:

$$\frac{\partial c}{\partial t} = D_0 \xi^2 \frac{\partial^2 c}{\partial \xi^2} - u_0 \xi \frac{\partial c}{\partial \xi}, \quad \xi_0 < \xi < \infty, 0 < t \quad (3-24)$$

where initial and boundary conditions are $c(\xi, 0) = 0$, where $\xi_0 < \xi$, $c(\xi_0, t) = c_0$ where $\xi_0 \geq \xi$, and $c(\xi \rightarrow \infty, t) = 0$. *Zoppou and Knight* [1997] employed a change of variable ($\xi = \ln x$) to homogenize the above spatially varying coefficient ADR equation in the space domain. Subsequently, they derived an exact solution based on the *Ogata and Banks* [1961] solution:

$$c(\xi, t) = \frac{c_0}{2} \left\{ \operatorname{erfc} \left(\frac{\ln\left(\frac{\xi}{\xi_0}\right) - u_0 t}{2\sqrt{D_0 t}} \right) + \exp \left(\frac{u_0 \ln\left(\frac{\xi}{\xi_0}\right)}{D_0} \right) \operatorname{erfc} \left(\frac{\ln\left(\frac{\xi}{\xi_0}\right) + u_0 t}{2\sqrt{D_0 t}} \right) \right\} \quad (3-25)$$

As we discussed before, we are interested in the conservative form of the transport equation which also holds continuity for ambient flow. The latter is crucial in verification of two-way coupled hydrodynamic-transport solvers and so we employ the method of undetermined coefficients. We assume $A = K_3 x^\alpha$, $U = K_4 x^\beta$ and $D = K_5 x^\gamma$, insert A , U and D in equations (3-2 and 3-3), and match the coefficients for a non-trivial solution:

$$\begin{aligned} \frac{\partial(K_3 x^\alpha)}{\partial t} + \frac{\partial(K_3 x^\alpha K_4 x^\beta)}{\partial x} &= 0 \Rightarrow \alpha + \beta = 0 \\ \frac{\partial(K_3 x^\alpha C)}{\partial t} &= \frac{\partial}{\partial x} \left(K_3 K_5 x^{\alpha+\gamma} \frac{\partial C}{\partial x} \right) - \frac{\partial(K_3 K_4 C x^{\alpha+\beta})}{\partial x} \\ \frac{\partial C}{\partial t} &= K_5 x^\gamma \frac{\partial^2 C}{\partial x^2} - (K_4 x^{-\alpha} - K_5(\alpha + \lambda) x^{\gamma-1}) \end{aligned} \quad (3-26)$$

Considering the structure of equation (3-2), it is possible to set $A = K_3 x^{-1}$, $U = K_4 x$, and $D = K_5 x^2$. Therefore, the solution for the mass conservative ADR equation with spatially-variable coefficients can be rebuilt analogous to equation (3-25) as shown below, where C is the cross-sectionally averaged concentration:

$$C(x, t) = \frac{C_0}{2} \left\{ \operatorname{erfc} \left(\frac{\ln\left(\frac{x}{x_0}\right) - (K_4 - K_5)t}{2\sqrt{K_5 t}} \right) + \exp \left(\frac{(K_4 - K_5) \ln\left(\frac{x}{x_0}\right)}{K_5} \right) \operatorname{erfc} \left(\frac{\ln\left(\frac{x}{x_0}\right) + (K_4 - K_5)t}{2\sqrt{K_5 t}} \right) \right\} \quad (3-27)$$

It is worth mentioning that this solution initially has a singularity at $x = x_0$ which needs to be considered in the numerical implementation.

3.4.2. ADR equation with time-dependent transport variables

For many cases of groundwater and estuarine flows, it can be shown that the transport equation has the following form (see Appendix 3-A for derivation of the equation):

$$\frac{\partial(A_0 C)}{\partial t} = \frac{\partial}{\partial x} \left(A_0 D_0 (K_6 + \cos \omega_t t) \frac{\partial C}{\partial x} \right) - \frac{\partial(A_0 u_0 (K_6 + \cos \omega_t t) C)}{\partial x} \quad (3-28)$$

where the value of $K_6 > 1$ needs to be assumed herein. This formula demonstrates the conservative form of the pollutant transport equation subjected to a flow composed of periodic components, in which ω_t refers to the tidal frequency [$1/T$] (seasonal fluctuation frequency for groundwater); all of the other notations are the same as before. Equation (3-28) is cross-sectionally averaged and it satisfies the conservation of mass for water. Initial and boundary conditions are sharp front of mass with constant concentration at the upstream boundary and zero concentration at the downstream boundary, i.e.: $C(x, 0) = 0$, at $0 < x$; $C(x = 0, 0) = C_0$, and $C(x \rightarrow \infty, t) = 0$. The technique to solve this equation was mentioned in subsection 3.2.2; we employ the following nonlinear time mapping:

$$\tau = \int_0^t (K_6 + \cos(\omega_t \tau)) d\tau = K_6 t + \frac{\sin(\omega_t t)}{\omega_t} \quad (3-29)$$

Dividing equation (3-28) by $A_0 u_0 (K_6 + \cos \omega_t t)$ we can rework this equation in the familiar form below, for which the analytical solution is known from *Ogata and Banks* [1961]:

$$\frac{\partial C}{\partial \tau} = \frac{\partial}{\partial x} \left(D_0 \frac{\partial C}{\partial x} \right) - u_0 \frac{\partial C}{\partial x}$$

$$\begin{aligned}
C(x, 0) &= 0, \quad 0 < x \\
C(x, \tau) &= C_0, \quad x = 0 \\
C(x, \tau) &= 0, \quad x \rightarrow \infty
\end{aligned} \tag{3-30}$$

The final analytical solution of the mass conservative ADR equation in this case is:

$$C(x, t) = \frac{C_0}{2} \left\{ \operatorname{erfc} \left(\frac{x - u_0(K_6 t + \frac{\sin(\omega_t t)}{\omega_t})}{2\sqrt{D_0(K_6 t + \frac{\sin(\omega_t t)}{\omega_t})}} \right) + \exp\left(\frac{u_0 x}{D_0}\right) \operatorname{erfc} \left(\frac{x + u_0(K_6 t + \frac{\sin(\omega_t t)}{\omega_t})}{2\sqrt{D_0(K_6 t + \frac{\sin(\omega_t t)}{\omega_t})}} \right) \right\} \tag{3-31}$$

3.4.3. Spatiotemporal varying flow field

In this section, we present a combined method to verify an advection-reaction numerical solver. The analytical solution we utilize for the hydrodynamic portion of the problem is not new, and was derived by *Defant* [1925] for tidal forcing in a dead-end harbor basin [*Wang et al.*, 2008]. The issue here is not the verification of the hydrodynamic solution, but the way we set up a transport problem to verify an advection-reaction process benefiting from this hydrodynamic analytical solution.

The derivation of the analytical solution of flow field involves several assumptions: a) interfacial and bottom friction are negligible; b) no stratification is present; c) the frame of reference is non-rotating; d) the second order channel-wise advection terms are neglected; e) horizontal velocity is not a function of depth; and f) tidal water surface fluctuations (a) are much smaller than channel depth (d). The domain of the problem is shown in Figure 3-1.

The analytical solution of the transport equation subjected to this flow field is unknown, but it is still advantageous to use this solution as follows. Due to the periodic nature of the tidal flow field, we expect any distribution of mass to be located in its initial position after an integer number of tidal cycles, i.e., $C_0(x, 0)$ is equal to the mass distribution subjected to advection

$\hat{C}(x, t + kT)$ where T is the tidal period and k is a positive integer. The only remaining problem is the definition of the boundary condition. To practically overcome this problem, remote boundary conditions are considered. (By the word “remote” we mean the extension of the domain length such that the concentration of pollutant at the boundary is kept below the computer precision, or practically zero.) The velocity and water surface elevation of the tidally induced mass-conservative flow field are:

$$u(x, t) = m \sin(n(l - x)) \sin(\omega_t t)$$

$$\zeta(x, t) = a \left[\frac{\cos(n(l - x))}{\cos(nl)} \right] \cos(\omega_t t) \quad (3-32)$$

where u is the horizontal velocity [L/T], l is the harbor basin length [L], x and t refer to space and time, ω_t denotes tidal wave frequency [$1/T$], d is the basin depth [L], ζ is the water surface elevation and a is the tidal amplitude [L]. A , the flow wetted area [L^2], can be found based on ζ , d and w (channel width) as $A(x, t) = (d + \zeta(x, t))w$. In turn, m and n are coefficients which are defined based on the basin’s geometry, the celerity of the tidal waves, and tidal amplitude and frequency:

$$n = \frac{\omega_t}{\sqrt{gd}}; \quad m = \left[\frac{\left(a \frac{\sqrt{gd}}{d} \right)}{\cos(nl)} \right] \quad (3-33)$$

Here we might assign an arbitrary initial distribution of concentration; the final concentration distribution will be the same as the initial shape after one full tidal cycle. Due to practical issues

we choose a Gaussian profile $C(x, t_0) = K_7 e^{-\frac{(x-K_8)^2}{K_9^2}}$ and set K_i to maintain remote BC in the test.

The other choices might be a square $C(x, t_0) = \{1 \text{ where } |x| \leq \frac{K_7}{2} \text{ and } 0 \text{ otherwise}\}$ or

triangle $C(x, t_0) = \{1 - \frac{|x|}{K_7} \text{ where } |x| \leq K_7 \text{ and } 0 \text{ otherwise}\}$. A Gaussian profile provides a better performance due to its light tailed frequency spectrum (A detailed discussion of its adequacy can be found in *McRae et al.* (1982)).

3.5. Application of the Derived Solutions in Code Verification

In this section, several hypothetical test-cases are constructed to illustrate the use of the analytical solutions. This work is part of a comprehensive transport solver test suite, where the solver is tested against various probable estuarine transport scenarios exhaustively [*Ateljevich et al.*, 2011; *Zamani and Bombardelli*, 2011]. There is a hierarchical increase in the tests' complexity for complete verification of the transport code. We start with a classical test case of advection-diffusion-decay with uniform flow and constant diffusivity (Section 3.5.1). Later on, three nonlinear cases (Sections 3.5.2 to 3.5.4), and finally test cases of spatial and temporal varying parameters (Sections 3.5.5 to 3.5.7), are examined.

Two practical issues need to be considered before implementation of the derived solutions in code verification. First, rigorous numerical verification of a code has to be carried out in the special ranges of dimensionless numbers regardless of the physical scales of phenomena the solver is intended to simulate [*Knupp and Salari*, 2003]. To be more precise, the Péclet and Damköhler numbers must be close to one to avoid misinterpretation of results in convergence study [*Knupp and Oberkampf*, personal communication, 2012]. The second practical issue prior to mesh convergence study is that, cell-averaged results obtained from the FVM (Finite Volume Method) cannot be compared to the analytical values, because they have different bases; FVM values are volume-averaged quantities whereas analytical solution are point-wise [*Leveque*, 2002]. Therefore, the analytical solutions are preprocessed before being used as a code

verification benchmark. By preprocess here we mean either analytically integrated or their value computed with a high order numerical integration over the cell. The codes tested in this paper are a suite of codes based on the FVM and the Finite Difference Method (FDM); the schemes are discussed in Appendix 3-B.

3.5.1. Verification with the constant ADR solution

For the sake of completeness of the verification set, we start by simulating a physical process in which a pollution plume is advected by a uniform flow while decaying and being diffused over the spatial domain.

$$\frac{\partial c}{\partial t} = D_0 \frac{\partial^2 c}{\partial x^2} - u_0 \frac{\partial c}{\partial x} - \beta c \quad (3-34)$$

The fundamental solution (Green's function) of the above equation is well-known and widely used in code verification [Bear 1972; Zoppou and Knight, 1997]:

$$c(x, t) = \frac{1}{\sqrt{4\pi D_0 t}} e^{-\beta t - \frac{(x-u_0 t)^2}{4D_0 t}}; 0 < D_0, 0 < t_0 < t \quad (3-35)$$

The setup for the test is as follows: domain length $x \in (0, 25.6) \text{ km}$, $t \in (0, 7.12) \text{ hr}$, dispersivity equal to $16 \text{ m}^2/\text{s}$, velocity = 0.6 m/s , and linear decay coefficient $\beta = 5 \times 10^{-5} \text{ 1/hr}$ (The value of the dispersion coefficient obtained from scaling arguments and values from the literature; see Rutherford [1994] and Deng *et al.* [2001]) Boundary conditions were obtained from the analytical solution. Figure 3-2 shows the numerical solutions pertaining to five different times, together with the analytical solution for the last time. Good agreement is obtained between the predicted solution and the analytical counterpart. Although this is a suitable benchmark to begin with, there are still defects which cannot be uncovered by this test, such as bugs in the

temporal and spatial discretization of velocity, dispersivity or area. Quantitative description of “good” agreement is provided later in Section 6.

3.5.2. Verification with the nonlinear diffusion-reaction solution

Based on equation (3-15), we decided to test the solution for the following case. We picked a domain $x \in (0, 10) \text{ m}$ and $t \in (0, 1) \text{ s}$ with the Dirichlet boundary conditions retrieved based on equation (3-15). The test was conducted with the following selection of parameters: $D_0 = 0.8 \text{ m}^2/\text{s}$, $K_1 = 1$, $K_2 = 7$, $\lambda = 0.4$, and $\beta = 0.02 \text{ 1/s}$. Although this physical setup is probably rare in environmental fluid mechanics, this test is still useful to exercise the solver against nonlinear reaction when the diffusivity is a nonlinear function as well. Figure 3-3 shows the comparison of the numerical and exact solutions, with good agreement.

3.5.3. Verification with advection dispersion with nonlinear source term

The analytical solution given in equation (3-20) provides a valuable benchmark to examine stiff problems, and to assess transport solvers for conservation of mass when they encounter nonlinear sources. Similar to the case in subsection 3.5.2, this analytical solution is given in general parametric form. Figure 3-4 shows the comparison of the numerical and exact solutions which were obtained with the following parameters: $D_0 = 0.3 \text{ m}^2/\text{s}$, $u_0 = 0.4 \text{ m/s}$, and $\beta = 0.05 \text{ 1/s}$ in the space and time domain $x \in (1, 3) \text{ m}$ and $t \in (0, 1) \text{ s}$, with the boundary conditions constructed based on the analytical solution (3-20). Again, good agreement was found.

3.5.4. Verification with nonlinear Burgers' equation

The analytical solution of the Burgers' equation (3-23) provides a valuable benchmark test for assessing shock behavior in numerical solutions. In this case, some practical issues need to be considered in advance. First, a number of numerical solvers will break down if they are given negative concentrations; therefore, a domain of the solution where c is always positive needs to be selected. The second point is that the nonlinear advective term has a shocking-up effect on the initial concentration distribution, where a smooth solution might develop discontinuity as it evolves in time. On the other hand, the dispersive term hinders this effect with smoothing out the solution [LeVeque, 2002]. This shock in the solution can be misleading in code verification studies as follows. In shock-capturing schemes, shock switches on a mechanism to avoid spurious oscillations. For example the action of a flux limiter will reduce the global order of convergence [Saltzman, 1994]. This drop in the order of convergence might be mistaken for a bug in the code. In other words, the low order solution of a flux limiter can be misrepresented as a coding/implementation error. Thus, in general we prefer to use smooth solutions (no shock) in tests for code verification activities.

Figure 3-5 shows a hypothetical test case we set up for verification of an ADR solver with the analytical solution (3-23). Here, the domain extends from $x \in (-30, 30) \text{ m}$, $t \in (0, 10) \text{ s}$, downstream concentration is $c_2 = 1$, the upstream counterpart is $c_1 = 2$, and $D_0 = 0.43 \text{ m}^2/\text{s}$ to assure a severe case on shock to check the code.

3.5.5. Verification with spatially-varying coefficient ADR solution

We setup another test case for uncovering potential spatial coding errors in the transport solver with the spatially varying coefficient analytical solution, equation (3-27). Tests were

performed with $x \in (10, 15) \text{ km}$, $K_3 = 5 \times 10^6 \text{ m}^3$, $K_4 = 10^{-4} \text{ 1/s}$, and $K_5 = 3 \times 10^{-6} \text{ 1/s}$. Accordingly, the area was kept between 500 to 333 m^2 , velocities fell within the range of 1 – 1.5 m/s , and the longitudinal dispersion coefficients were kept between 300 – 675 m^2/s . The test was performed with $t \in (8000, 10000) \text{ s}$ to move away from the initial singularity embedded in equation (3-27), which can cause spurious oscillations in the numerical solution. Figure 3-6 shows the comparison between the analytical and numerical solutions of the space-dependent ADR equation, with satisfactory agreement.

3.5.6. Verification with temporally-varying coefficient ADR solution

The derived time-dependent analytical solution of ADR, equation (3-31), is a powerful tool to detect flaws in the assembly of different operators in fractional-step method. Here, a hypothetical estuarine problem was chosen based on the scaling we conducted for the transport equation in tidal rivers. The following parameters were used in this test: $x \in (1, 9) \text{ km}$, $t \in (0.5, 1.5) \text{ hr}$, $\omega_t = 12.41 \text{ hr}$, $D_0 = 194.4 \text{ m}^2/\text{s}$, $K_6 = 2$, and $u_0 = 0.195 \text{ m/s}$. Values of boundary conditions were retrieved from the analytical solution (3-31) and introduced to the code. Figure 3-7 shows the time evolution of a front of pollution. Agreement of the solutions is satisfactory.

3.5.7. Verification with analytical solution of tidal flow

We set up an advection-reaction test in a dead-end channel (Figure 3-1) with tidal forcing at the mouth. The channel depth was chosen to be $d = 16 \text{ m}$, the tidal amplitude was assumed to be $a = 0.5 \text{ m}$, tidal frequency was $\omega_t = 12.41 \text{ hr}$, and we chose the $l = 52 \text{ km}$; the basin length was set in a way to maintain remote boundaries during the test, and we based the length of

initial distribution of mass on the scales suggested by *Bedford* [1985]. He suggested that the ratio of dissolved constituent intrusion length to estuary depth should range from 10^2 to 10^4 . Hence, we set the test with an initial Gaussian plume with a length of 16 km. Figures 3-8 shows the results in which the plume just advects with tidal currents (no decay) and Figure 3-9 shows time evolution of initial mass distribution, subjected to linear decay, for one tidal cycle over the harbor basin.

3.6. Metrics for Code Verification and Accuracy Validation

The seven analytical solutions we mentioned in Section 3.5 can be utilized for numerical code verification as well as quantitative accuracy assessment. First, major application of the derived solutions is providing a benchmark for *mesh convergence test* for code verification studies. This test compares results' order of accuracy versus formal order of accuracy of the discretization. Mesh convergence study is the most solid criteria for assessing codes [*Roache*, 1997; *Knupp and Salari*, 2003]. The procedure quantifies error norms based on an accurate benchmark solution (here the analytical solutions) and measure the evolution of error as the mesh and time-step size shrink. Detailed discussion of implementation of this test is not within the scope of this study [see *Roache*, 2009]. However, in all cases discussed in this paper, mesh convergence studies were conducted. Figure 3-10 shows an example of such studies for the case of tidal flows. An acceptance criteria was crafted according to principles from both the software and numerical testing fields, measuring the grid convergence index of L_1 , L_2 , and L_∞ (*Roache*, 2009). In this study, we choose the L_∞ since it is the most restrictive norm. The quantities we cared about were: 1) accuracy; 2) mass conservation; 3) quality of the answer (shape preservation). We called exactly 2^{nd} order in L_∞ “perfect” convergence. We called exactly 2^{nd}

order in forgiving norm (L_1 and L_2) “good” convergence. In case we could match one of forgiving norms with low quality of shape preservation (wiggles) we call it “satisfactory” convergence.

The second application of aforementioned analytical solutions is providing a benchmark for models’ accuracy validation. Accuracy validation metrics provides objective quantitative values as opposed to subjective qualitative descriptions as “weak” or “Satisfactory” agreement. Herein, we address the accuracy of the numerical solution based on three commonly used metrics: a) normalized root mean square error (also called *Scatter Index*); a) bias; c) coefficient of determination “ R^2 ”. The first index is a measure of accuracy; the second index indicates model over/under estimation; and the third index is a general measure of goodness of fit [*Montgomery*, 2005]. Comprehensive discussion of various accuracy validation metrics is given in *Roache* (2009), *Oberkampf and Roy* (2010) and *Willmott et al.*, (2012). Table 3-2 provides the values of model accuracy metrics (*SI*, *Bias*, and R^2) for the eight test cases we provided in the Section 3.5.

3.7. Alternative Code Verification Approaches

At this point, it is relevant to address several issues. First, why did not we use alternative code verification techniques (other than MES)? Three alternatives to MES are the Method of Manufactured Solution (MMS), Richardson Extrapolation, and cross-solver verification [*Roache*, 2009; *Oberkampf and Roy*, 2010]. Although we attempted to apply those methods, they could not carry out our comprehensive verification needs. MMS was not able to provide an appropriate benchmark for stiff source terms, given the fact that MMS applies to linear operators. Even if the above mentioned obstacle is overcome, still practical difficulties of utilizing the MMS exist,

because linking a complex solution structure to the source code of any solver is an error prone and resource-intensive task. After MMS, we tried Richardson Extrapolation [Roache, 2009] where the convergence behavior of the code can be observed although it would not provide information on the level of accuracy. Therefore, we strongly believe we cannot rely on Richardson Extrapolation solely as a perfect error probing tool. On top of that, Richardson extrapolation needs several steps of numerical post-process. There are several cases of using of cross-solver verification as the last resort [Oberkampf and Roy, 2010]. However, even if the benchmark code already shows extensive empirical evidence, it is still thoroughly impossible to believe it is error-free without conducting formal verification tests. Furthermore, there would be tedious practical difficulties in verifying a code based on another code's results [Roache, 2009].

3.8. Conclusions and Final Remarks

This work was oriented towards devising useful tools for the verification of a scalar transport solver, via the MES. For the sake of completeness, we started the code verification with a well-known analytical solution of the ADR equation with uniform flow, constant dispersivity, and decay. Then, four new closed-form analytical solutions were presented and used for verification of one dimensional ADR solver. In general, the conservative form of the transport equation is of interest for researchers; thus, this study delivered results in the conservative form. Analytical solutions of ADR equation covered the cases of: 1) stagnant flow, nonlinear dispersivity and nonlinear source; 2) uniform conservative flow, constant dispersivity and nonlinear source; 3) spatially varying flow and dispersivity, conservative flow and no source; 4) time-dependent flow and dispersivity, conservative flow, no source. In addition, we employed two analytical solutions of the tidal-flow and Burgers' equations with simple tricks to make appropriate benchmarks for verification of specific aspects of the transport code. The former has spatially- and temporally-

varying conservative flow, no diffusivity and linear reaction, and the latter evaluates the nonlinearity in the advective term. Altogether, the suite of seven exact solutions we provided in this study is complete in the sense that it would be enough to uncover any probable scheme limitation or coding error in the one-dimensional form of the scalar transport equation (3-1). This set of solutions is able to test all terms in the complex, nonlinear structure of the transport equation, in the most generic form.

The analytical solutions presented in this paper were employed to verify a sediment transport code. Several temporal and spatial mis-indexing and coding errors were detected which could not be detected with previous analytical solutions. These solutions perform better than alternative exact solutions from the literature because they were able to discover defect in spatiotemporal discretization of velocity, area and dispersion coefficient. Furthermore, the new solutions satisfy continuity of water, while the former analytical solutions did not. Therefore, they would be employed for evaluating solvers wherein the hydrodynamic module and transport module are working coupled. The six analytical solutions we derived are in the most general form, they are carefully checked for common mistakes in the solution procedure. Finally, although the new analytical solutions are one-dimensional, they could be employed for preliminary verification of multi-dimensional transport codes as well.

Appendices of Chapter 3

3-A. Derivation of time dependent transport equation

In riverine mixing, *Deng et al.* [2001] characterized the longitudinal dispersion coefficient as follows:

$$D = \frac{0.15}{8\varepsilon_{t0}} \left(\frac{w}{d}\right)^{5/3} \left(\frac{U}{u_*}\right)^2 d u_* \quad (3-A1)$$

where w [L] indicates the river width, d [L] refers to the average water depth, ε_{t0} is a dimensionless coefficient, U [L/T] is the cross-sectionally averaged velocity, and u_* [L/T] is the shear velocity. Thus, if we assume the geometry of flow is not changing with time, it can be shown that the longitudinal dispersion coefficient in rivers only varies due to the average velocity (given that shear velocity is proportional to the average velocity).

On the other hand, values of dispersion in porous media change with the absolute value of the Darcy velocity [*Bear*, 1972]. D can be considered as:

$$D = \omega D_m + \alpha_L |U| \quad (3-A2)$$

where D_m [L²/T] is the constituent's molecular diffusion in porous media, ω [L³/L³] is the porosity, α_L [L] refers to the intrinsic dispersivity, and U refers to the Darcy velocity. In most of the groundwater flow regimes, the longitudinal dispersion coefficient only depends on flow condition and the molecular diffusion contribution is negligible [*Bear*, 1972; *Logan*, 2001].

The velocity in the river can be considered as the superposition of tidal flow (bidirectional) and river base flow (unidirectional). In the subsurface flow, for an aquifer located in tropical regions, groundwater velocity could exhibit a similar flow pattern: a sinusoidal component which induces fluctuation over a base flow [*Kumar and Kumar*, 1998; *Kumar et al.*, 2009]. Considering

the abovementioned scenarios, we can build up a hypothetical velocity field and hydrodynamic dispersivity as:

$$u = u_{base} + u_{periodic} = u_0(K_6 + \cos \omega_t t) \quad (3-A3)$$

$$D(t) = D_0 u(t) = D_0(K_6 + \cos \omega_t t) \quad (3-A4)$$

where K_6 is a constant. Given that the dispersion coefficient has to be positive, we have to assume $K_6 > 1$ for stability reasons; thus equation (3-3) without sink/source term becomes:

$$\frac{\partial(A_0 C)}{\partial t} = \frac{\partial}{\partial x} \left(A_0 D_0 (K_6 + \cos \omega_t t) \frac{\partial C}{\partial x} \right) - \frac{\partial(A_0 u_0 (K_6 + \cos \omega_t t) C)}{\partial x} \quad (3-A5)$$

3-B. Numerical discretization of the ADR equation

Three schemes were applied to solve these problems numerically. First, in cases 5.1, 5.5, 5.6 and 5.7, we discretized the hyperbolic (advective) term of the ADR equation with the modified two-step version of Lax-Wendroff method in the FVM framework. This method is second order accurate, whereas it has third order phase error of $(CFL^2 - 1) \frac{(2\pi k \Delta x)^3}{6D^3} + O(\Delta x^5)$. As the scheme's local truncation error equals to $-\frac{1}{6} u \Delta x^2 (1 - CFL^2) \frac{\partial^3 c}{\partial x^3} + O(\Delta t^3)$, it has a low numerical diffusion [Hundsdoerfer and Verwer, 2003]. The diffusive term was discretized with a weighted time scheme. The reactive term was treated with the Heun ODE solver which is incorporated in the advection solver [Radhakrishnan, 1984]. Finally, the above three operators were assembled by employing the fractional-step method to obtain second order accuracy in both time and space discretization [LeVeque, 2002; Zamani and Bombardelli, 2011]. Second, in case 5.2, we employed a weighted time scheme for the diffusion operator, coupled with a Heun ODE solver, in a FDM. Third, in cases 5.3 and 5.4, we employed a Lax-Wendroff method in the FDM

framework for the advective term, and Crank-Nicolson for the diffusive term, coupled with the Heun ODE solver [*LeVeque*, 2002].

Chapter Three References

1. Ateljevich E, Zamani K, Bombardelli FA, Anderson J (2011) Using software quality and algorithm testing to verify a one-dimensional transport model. ASCE/EWRI World Environmental and Water Resources Congress, Palm Springs, CA
2. Barry DA, Sposito G (1989) Analytical solution of a convection-dispersion model with time-dependent transport coefficients. *Water Resour Res* 25:2407-2416. doi:10.1029/WR025i012p02407
3. Basha HA, El-Habel FS (1993) Analytical solution of the one-dimensional time-dependent transport equation. *Water Resour Res* 29:3209-3214. doi:10.1029/93WR01038
4. Bear J (1972) *Dynamics of flow in porous media*. Elsevier, New York
5. Bedford KW (1985) Selection of turbulence and mixing parameterization for estuary water quality models. US Army Corps of Engineers, Environmental Impact Research Program, Paper EL-85-2, Vicksburg, MS, p-153
6. Boltzmann L (1894) Zur integration der diffusionsgleichung bei variablen diffusionkoeffizienten. *Annalen der Physik und Chemie* 53:959-964
7. Cannon JR (2008) The one-dimensional heat equation, encyclopedia of mathematics and its applications. Cambridge University Press, Cambridge
8. Carslaw HS, Jaeger JC (1959) *Conduction of heat in solids*. 2nd ed. Clarendon Press, Oxford
9. Chen JS, Chen JT, Liu CW, Liang CP, Lin CW (2011) Analytical solutions to two-dimensional advection-dispersion equation in cylindrical coordinates in finite domain subject to first- and third-type inlet boundary conditions. *J Hydrol* 405(3-4):522-531. doi:10.1016/j.jhydrol..06.002

10. Chen JS, Liu CW, Hsu HT, Liao CM (2003) A Laplace transform power series solution for solute transport in a convergent flow field with scale-dependent dispersion. *Water Resour Res* 39(8). doi:10.1029/2003WR002299
11. Chen JS, Liu CW, Liao CM (2003) Two-dimensional Laplace-transformed power series solution for solute transport in a radially convergent flow field. *Adv Water Resour* 26(10):1113-1124. doi:10.1016/S0309-1708(03)00090-3
12. Chen JS, Liu YH, Liang CP, Liu CW, Lin CW (2011) Exact analytical solutions for two-dimensional advection-dispersion equation in cylindrical coordinates subject to third-type inlet boundary condition. *Adv Water Resour* 34(3):365-374. doi:10.1016/j.advwatres.2010.12.008
13. Chen JS, Ni CF, Liang CP (2008) Analytical power series solutions to the two-dimensional advection-dispersion equation with distance-dependent dispersivities. *Hydrol Processes* 22(24):4670-4678. doi:10.1002/hyp.7067
14. Chen JS, Ni CF, Liang CP, Chiang CC (2008) Analytical power series solution for contaminant transport with hyperbolic asymptotic distance-dependent dispersivity. *J Hydrol* 362(1-2):142-149. doi:10.1016/j.jhydrol.2008.08.020
15. Cho CM (1971) Convective transport of ammonium with nitrification in soil. *Can J Soil Sci* 51(3):339-350. doi:10.4141/cjss71-047
16. Cole JD (1951) On a quasilinear parabolic equation occurring in aerodynamics. *Quart Appl Math* 9:225-236
17. Costa CP, Vilhena MT, Moreira DM, Tirabassi T (2006) Semi-analytical solution of the steady three-dimensional advection-diffusion equation in the planetary boundary layer. *Atmos Environ* 40(29):5659-5669. doi:10.1016/j.atmosenv.2006.04.054
18. Crank J (1979) *The mathematics of diffusion*. 2nd ed. Oxford

19. Defant A (1925) Gezeiten probleme des meers in landnahe [Problems of ocean tides near the land]. Probleme der Kosmischen Physik 6, Hamburg: H. Grand
20. Demetriou E, Christou MA, Sophocleous C (2007) On the classification of similarity solutions of a two-dimensional diffusion-advection equation. Appl Math Comput 187(2):1333-1350. doi:10.1016/j.amc.2006.09.043
21. Deng ZQ, Singh VP, Bengtsson L (2001) Longitudinal dispersion coefficient in straight rivers. J Hydraul Eng 127(11):919-927. doi:10.1061/(ASCE)0733-9429(2001)127:11 (919)
22. Ellsworth TR, Butters GL (1993) 3-dimensional analytical solutions to the advection-dispersion equation in arbitrary Cartesian coordinates. Water Resour Res 29(9):3215-3225. doi:10.1029/93WR01293
23. Fischer BH, List JE, Koh RC, Imberger J, Brooks NH (1979) Mixing in inland and coastal waters. Academic Press, New York
24. Fleenor WE, Bombardelli FA (2013) Simplified 1-D hydrodynamics modeling of the Sacramento- San Joaquin Delta - sea level rise and water diversion effects. In review, San Francisco Estuary and Watershed Science
25. Fourier J (1822) The analytical theory of heat. [translated with notes by Freeman A 1955] Dover, New York
26. Guerrero JS, Pimentel LCG, Skaggs TH, van Genuchten MT (2009) Analytical solution of the advection-diffusion transport equation using a change-of-variable and integral transform technique. Int J Heat Mass Transfer 52(13-14):3297-3304. doi:10.1016/j.ijheatmass transfer .2009.02.002

27. Guerrero JS, Skaggs TH (2010) Analytical solution for one-dimensional advection-dispersion transport equation with distance-dependent coefficients. *J Hydrol* 390(1-2):57-65. doi:10.1016/j.jhydrol.2010.06.030
28. Hills RG, Warrick AW (1993) Burgers' equation: A solution for soil water flow in a finite length. *Water Resour Res* 29(4):1179-1184
29. Hopf E (1950) The partial differential equation $u_t + uu_x = \mu u_{xx}$. *Commun Pure Appl Math* 3:201–230
30. Hundsdorfer W, Verwer JG (2003) Numerical solution of time-dependent advection-diffusion-reaction equation. *Springer Series in Computational Mathematics* 33, Springer
31. Jaiswal DK, Kumar A, Kumar N, Singh MK (2011) Solute transport along temporally and spatially dependent flows through horizontal semi-infinite media: dispersion proportional to square of velocity. *J Hydrol Eng* 16(3):228-238. doi:10.1061/(ASCE)HE.1943-5584.0000312
32. Jaiswal DK, Kumar A, Kumar N, Yadav RR (2009) Analytical solutions for temporally and spatially dependent solute dispersion of pulse type input concentration in one-dimensional semi-infinite media. *J Hydro-environ Res* 2(4):254-263. doi:10.1016/j.jher.2009.01.003
33. Jha SK, Bombardelli FA (2010) Toward two-phase flow modeling of nondilute sediment transport in open channels. *J Geophys Res* 115, F03015. doi:10.1029/2009JF001347
34. Jha SK, Bombardelli FA (2011) Theoretical/numerical model for the transport of non-uniform suspended sediment in open channels. *Adv Water Resour* 34(5):577-591. doi:10.1016/j.advwatres.2011.02.00
35. Khakpour M, Vafai K (2008) A comprehensive analytical solution of macromolecular transport within an artery. *Int J Heat Mass Transfer* 51(11-12):2905-2913. doi:10.1016/j.ijheatmasstransfer.2007.09.019

36. Khalifa ME (2003) Some analytical solutions for the advection–dispersion equation. *Appl Math Comput* 139:299–310. doi:10.1016/S0096-3003(02)00181-9
37. Kirchhoff GR (1894) *Vorlesungen über die Theorie der Wärme*
38. Knupp PM, Salari K (2003) *Verification of computer codes in computational science and engineering*. Chapman and Hall/CRC
39. Kumar A, Jaiswal DK, Kumar N (2009) Analytical solutions of one-dimensional advection-diffusion equation with variable coefficients in a finite domain. *J Earth Syst Sci* 118(5):539-549
40. Kumar A, Jaiswal DK, Kumar N (2010) Analytical solutions to one-dimensional advection-diffusion equation with variable coefficients in semi-infinite media. *J Hydrol* 380(3-4):330-337. doi:10.1016/j.jhydrol.2009.11.008
41. Kumar N, Kumar M (1998) Solute dispersion along unsteady groundwater flow in a semi-infinite aquifer. *Hydrol and Earth Syst Sci* 2(1):93–100
42. Lassey KR (1988) Unidimensional solute transport incorporating equilibrium and rate-limited isotherms with first-order loss: 1. Model conceptualization and analytical solutions. *Water Resour Res* 24(3):343-350. doi:10.1029/WR024i003p00343
43. Leij FJ, Priesack E, Schaap MG (2000) Solute transport modeled with Green's functions with application to persistent solute sources. *J Contam Hydrol* 41(1):155-173. doi:10.1016 /S0169-7722(99)00062-5
44. Leij FJ, van Genuchten MT (2000) Analytical modeling of nonaqueous phase liquid dissolution with Green's functions. *Transp Porous Media* 38:141-166. doi:10.1023/A:10066112 00487

45. LeVeque JR (2002) Finite Volume Methods for hyperbolic problems. Cambridge University Press, Cambridge
46. Logan JD (1996) Solute transport in porous media with scale-dependent dispersion and periodic boundary. *J Hydrol* 184(3-4):261-276
47. Logan JD (2001) Transport modeling in hydrogeochemical systems. *Interdisciplinary Applied Mathematics*. Volume 15, Springer
48. Logan JD (2008) An introduction to nonlinear partial differential equations. *Pure and Applied Mathematics*, 2nd ed. John Wiley & Sons, New York
49. Massoudieh A, Bombardelli FA, Ginn TR (2010) A biogeochemical model of contaminant fate and transport in river waters and sediments. *J Contam Hydrol* 112(1-4):103-117. doi:10.1016/j.jconhyd.2009.11.001
50. McRae, GJ, Goodin, WR, Seinfeld JH (1982) Numerical solution of the atmospheric diffusion equation for chemically reacting flow. *J Comput Phys* 45:1-42.
51. Mohsen MFN, Pinder GF (1984) Analytical solution of the transport equation using a polynomial initial condition for verification of numerical simulators. *Int J Numer Meth Fluids* 4:701-707
52. Momani S, Yildirim A (2010) Analytical approximate solutions of the fractional convection-diffusion equation with nonlinear source term by He's homotopy perturbation method. *Inte J Computer Math* 87(5):1057-1065. doi:10.1080/0020716090302 3581
53. Montgomery DC (2005) Design and analysis of experiments. 6th ed. John Wiley and Sons
54. Neelz S (2006) Limitations of an analytical solution for advection–diffusion with spatially variable coefficients. *Commun Numer Methods Eng* 22:387–396. doi:10.1002/cnm.820

55. Oberkampf WL, Roy CJ (2010) Verification and validation in scientific computing. Cambridge University Press, Cambridge
56. Ogata A, Banks RB (1961) A solution of differential equation of longitudinal dispersion in porous media. United States Geological Survey, Professional Paper 411-A
57. Parlange JY, Hogarth WL, Parlange MB, Haverkamp R, Barry DA, Ross PJ, Steenhuis TS (1998) Approximate analytical solution of the nonlinear diffusion equation for arbitrary boundary conditions. *Water Resour Res* 25(8):1923-1924. doi:10.1023/A:1006508721609
58. Philip JR (1994) Some exact-solutions of convection-diffusion and diffusion-equations. *Water Resour Res* 30(12):3545-3551. doi:10.1029/94WR01329
59. Polyanin AD, Zaitsev VF (2003) Handbook of exact solutions for ordinary differential equations. Chapman & Hall/CRC
60. Radhakrishnan K (1984) Comparison of numerical techniques for integration of stiff ordinary differential equations arising in combustion chemistry. NASA Technical Paper 2372
61. Rajabi A, Ganji DD, Taherian H (2007) Application of homotopy perturbation method in nonlinear heat conduction and convection equations. *Phys Lett A* 360(4-5):570-573. doi:10.1016/j.physleta.2006.08.079
62. Remesikova M (2004) Solution of convection–diffusion problems with nonequilibrium adsorption. *J Comput Appl Math* 169:101-116. doi:10.1016/j.cam.2003.11.005
63. Roache PJ (1997) Quantification of uncertainty in computational fluid dynamics. *Annu Rev Fluid Mech* 29:123–60
64. Roache PJ (2009) Fundamentals of verification and validation. Hermosa Publishers
65. Rutherford JC (1994) River mixing. John Wiley & Sons, New York

66. Saltzman J (1994) An Unsplit 3D Upwind Method for Hyperbolic Conservation Laws. *J Comput Phys* 115:153-168.
67. Savovic S, Djordjevic A (2012) Finite difference solution of the one-dimensional advection-diffusion equation with variable coefficients in semi-infinite media. *Int J Heat Mass Transfer* 55(15-16):4291-4294
68. Siegel P, Mose R, Ackerer PH, Jaffre J (1997) Solution of the advection–diffusion equation using a combination of discontinuous and mixed finite elements. *Int J Numer Meth Fluids* 24: 595-613
69. Singh MK, Singh P, Singh VP (2010) Analytical solution for two-dimensional solute transport in finite aquifer with time-dependent source concentration. *J Eng Mech* 136(10): 1309-1315. doi:10.1061/(ASCE)EM.1943-7889.0000177
70. Singh MK, Singh VP, Singh P, Shukla D (2009) Analytical solution for conservative solute transport in one-dimension homogeneous porous formations with time-dependent velocity. *J Eng Mech* 135:1015-1021. doi:10.1061/(ASCE)EM.1943-7889.0000018
71. Stakgold I, Holst M (2011) Green’s functions and boundary value problems. 3rd ed. John Wiley & Sons, New York
72. Stern F, Wilson R, Shao J (2006) Quantitative V&V of CFD simulations and certification of CFD codes. *Int J Numer Meth Fluids* 50:1335–1355
73. Stockie JM (2011) The mathematics of atmospheric dispersion modeling. *SIAM Review* 53(2):349–372. doi:10.1137/10080991X
74. Sun Y, Petersen NJ, Clement TP (1999) Analytical solutions for multiple species reactive transport in multiple dimensions. *J Contam Hydrol* 35:429–440. doi:10.1016/S01697722(98)00105-3

75. Tirabassi T (1989) Analytical air-pollution advection and diffusion-models. *Water Air Soil Pollut* 47(1-2):19-24. doi:10.1007/BF00468993
76. Tracy FT (2006) Clean two -and three- dimensional analytical solutions of Richards' equation for testing numerical solvers. *Water Resour Res* 4. doi:10.1029/2005WR 004638
77. Valocchi AJ, Malmstead M (1992) Accuracy of operator splitting for advection-dispersion-reaction problems. *Water Resour Res* 28(5):1471-1476. doi:10.1029/92WR00 423
78. van Genuchten MT, Alves WJ (1982) Analytical solutions of the one-dimensional convective-dispersive solute transport equation. U.S. Department of Agriculture, Technical Bulletin No. 1661, p-151
79. Verwer JG, Sommeijer BP, Hundsdorfer W (2004) RKC time-stepping for advection–diffusion–reaction problems. *J Comput Phys* 201(1):61-79. doi:10.1016/j.jcp.2004 .05. 002
80. Wan ZZ, Wang ZZ (1994) Hyperconcentrated flow. IAHR Monographs, Taylor & Francis
81. Wang SY, Roache PJ, Schmalz RA, Jia Y, Smith PE (2008) Verification and validation of 3D free-surface flow models. ASCE, EWRI
82. Willmott CJ, Robeson SM, Matsuura K (2012) A refined index of model performance. *Int J Climatol* 32: 2088 – 2094
83. Wu Y, Cheung KF (2008) Explicit solution to the exact Riemann problem and application in nonlinear shallow-water equations. *Int J Numer Meth Fluids* 57:1649–1668. doi:10.1002/fluid.1696
84. Yadav RR, Jaiswal DK, Yadav HK, Rana G (2010) One-dimensional temporally dependent advection-dispersion equation in porous media: analytical solution. *Nat Resour Model* 23(4):521-539. doi:10.1111/j.1939-7445.2010.00072.x

85. Yates SR (1990) An analytical solution for one-dimensional transport in heterogeneous porous-media. *Water Resour Res* 26(10):2331-2338. doi:10.1029/90WR00993
86. Yates SR (1992) An analytical solution for one-dimensional transport in porous-media with an exponential dispersion function. *Water Resour Res* 28(8):2149-2154. doi:10.1029/92WR01006
87. Zamani K, Bombardelli FA (2011) Development of a general transport module for DSM2, including sediment transport. Final Report, California Department of Water Resources
88. Zoppou C, Knight JH (1997) Analytical solution for advection and advection-diffusion equation with spatially variable coefficients. *J Hydraul Eng* 123(2):144-148. doi:10.1061/(ASCE)0733-9429(1997)123:2(144)
89. Zoppou C, Knight JH (1999) Analytical solution of a spatially variable coefficient advection-diffusion equation in up to three dimensions. *Appl Math Modell* 23(9):667-685. doi:10.1016/S0307-904X(99)00005-0

Figures

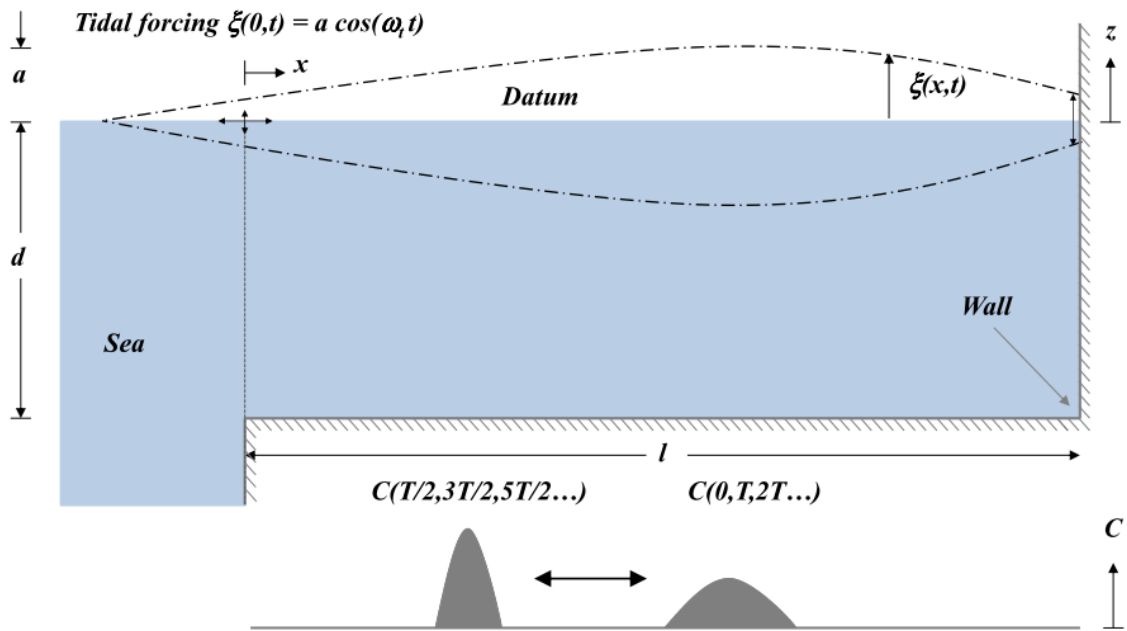


Figure 3-1. Schematic of the tidal forcing domain in a dead-end harbor basin. (top) Basin cross section with the initial position of the free surface. (bottom) Position of the pollution mass subjected to the tidal forcing. Tidal compression happens in mid tidal period [adopted from Wang *et al.*, 2008].

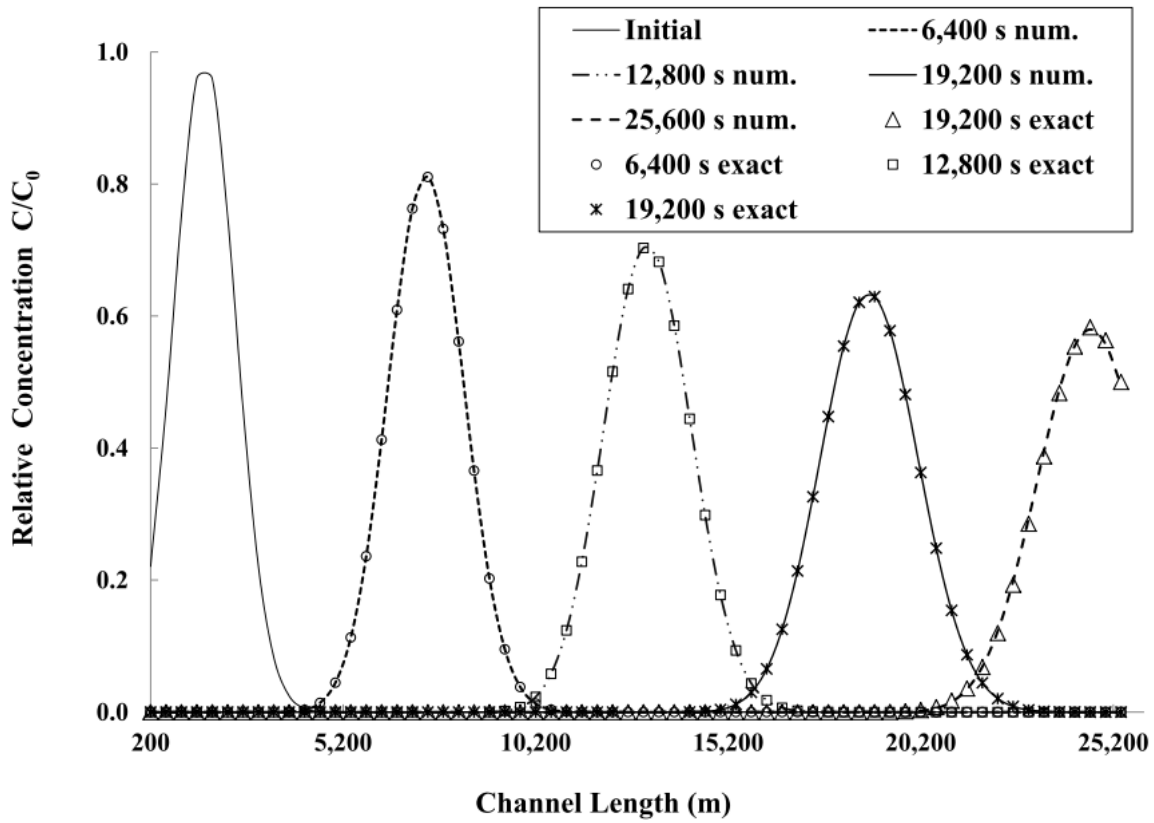


Figure 3-2. Comparison of analytical (exact) and numerical solutions of the advection-diffusion-reaction equation with uniform flow, linear decay and constant dispersivity, $\Delta t = 100$ s and $\Delta x = 100$ m.

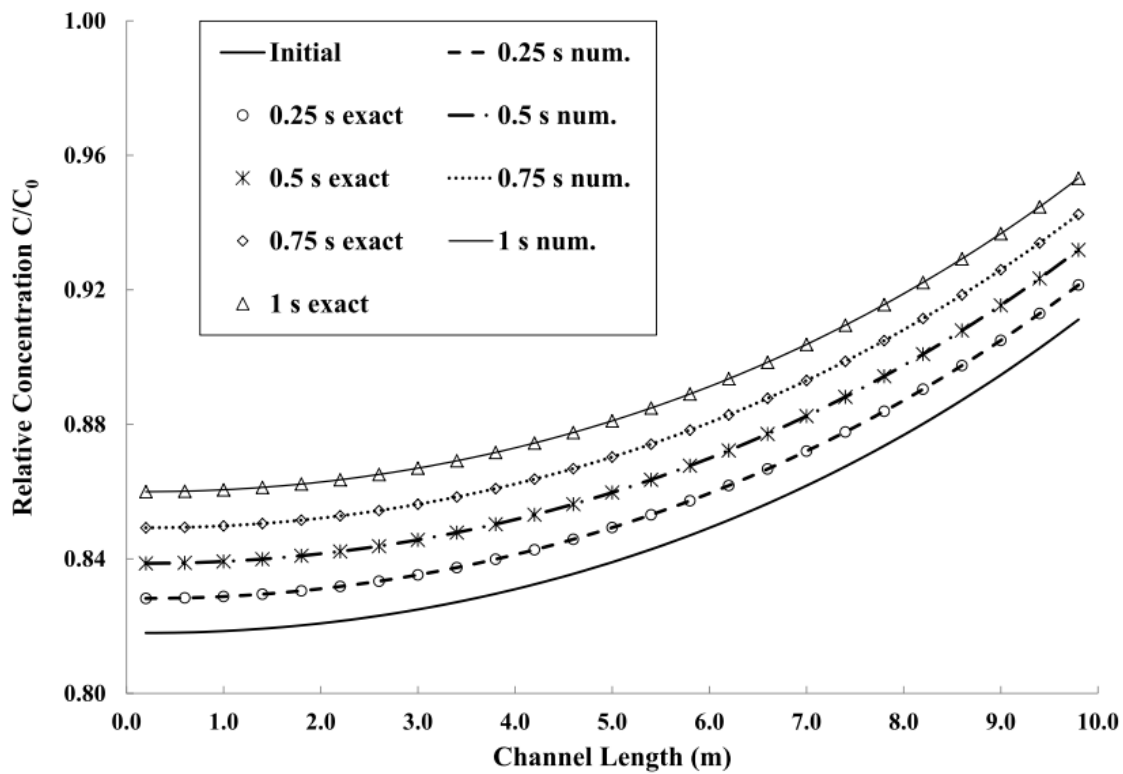


Figure 3-3. Evolution in time of the numerical and exact solutions to the nonlinear diffusion-reaction equation, $\Delta t = 0.001$ s and $\Delta x = 0.312$ m.

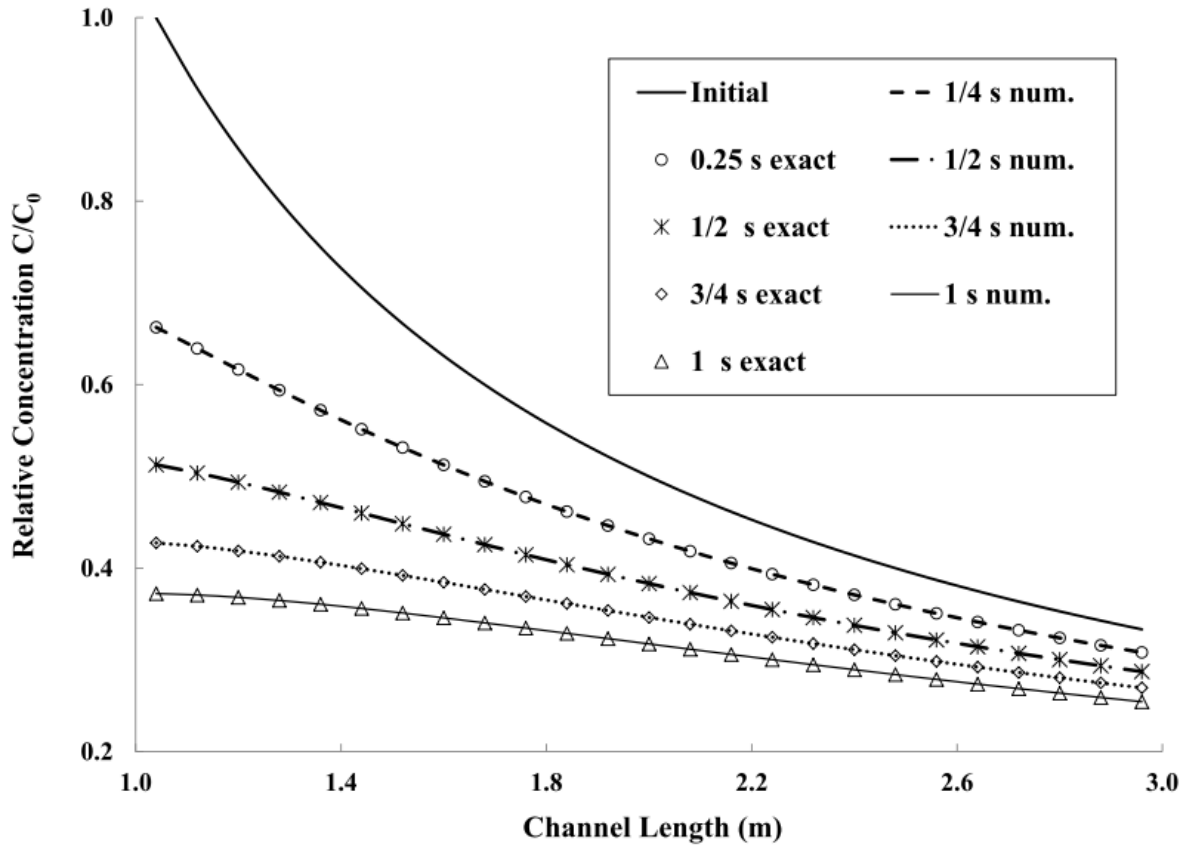


Figure 3-4. Analytical and numerical solutions for the advection-diffusion-reaction equation with uniform flow and constant dispersivity, subjected to nonlinear decay, $\Delta t = 0.01 \text{ s}$ and $\Delta x = 0.12 \text{ m}$.

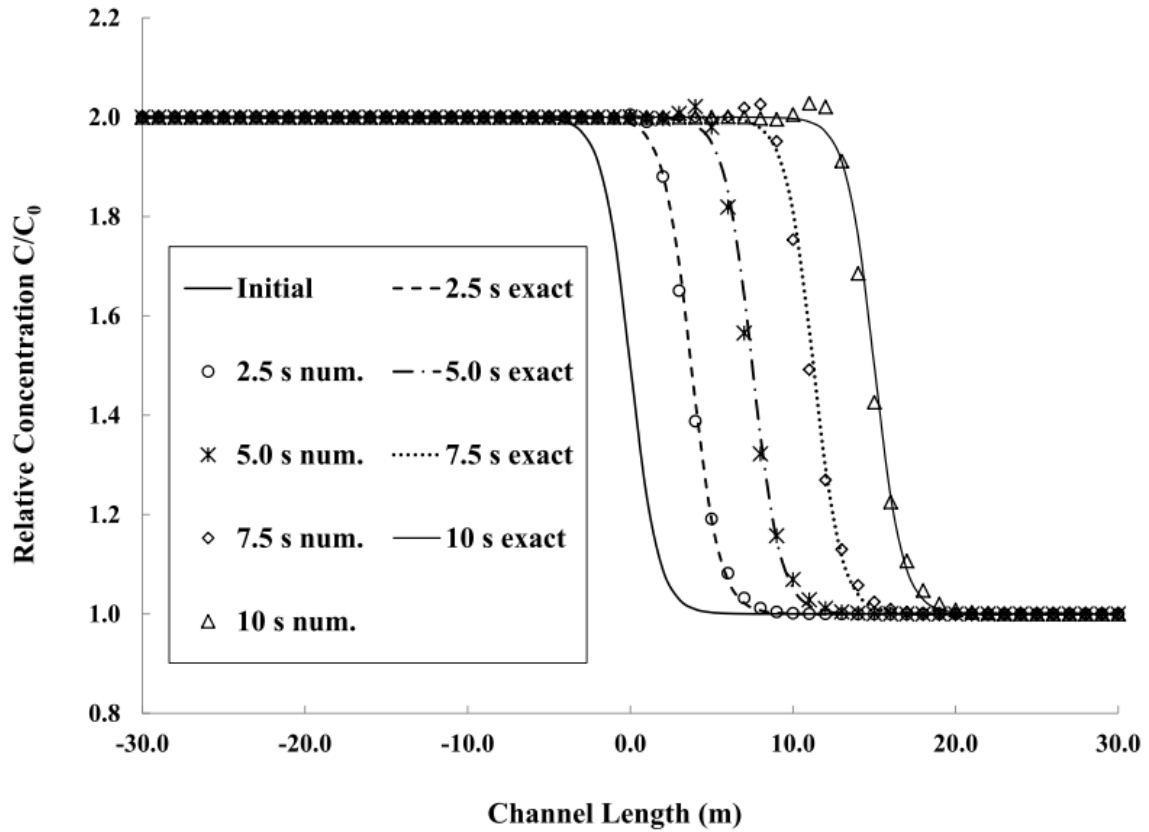


Figure 3-5. Comparison of numerical and analytical solutions of the Burgers' equation for verification purpose of an ADR equation, $\Delta t = 0.05$ s and $\Delta x = 1.0$ m. Numerical solution evolves in time and shows over-shooting near the front.

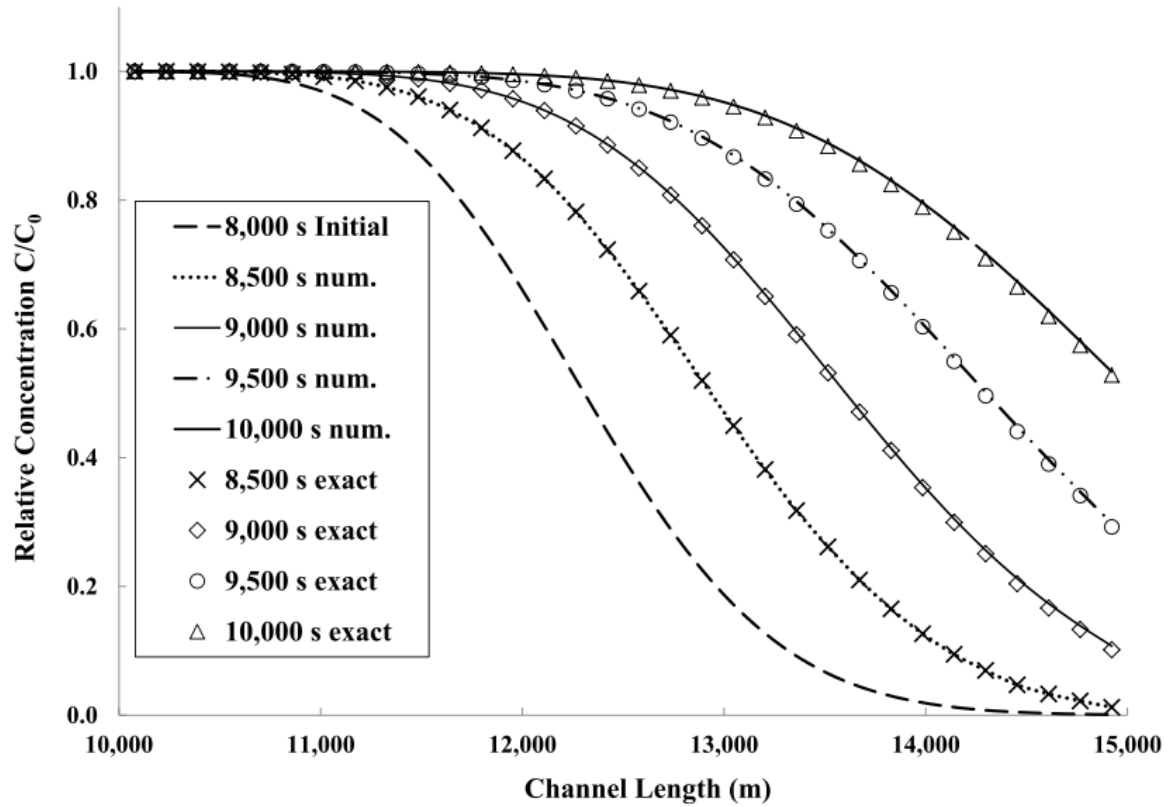


Figure 3-6. Evolution in time of a pollution front subjected to non-uniform advection and spatially-varying dispersion coefficient. Comparison of numerical and analytical solutions,

$$\Delta t = 7.81 \text{ s and } \Delta x = 39.06 \text{ m.}$$

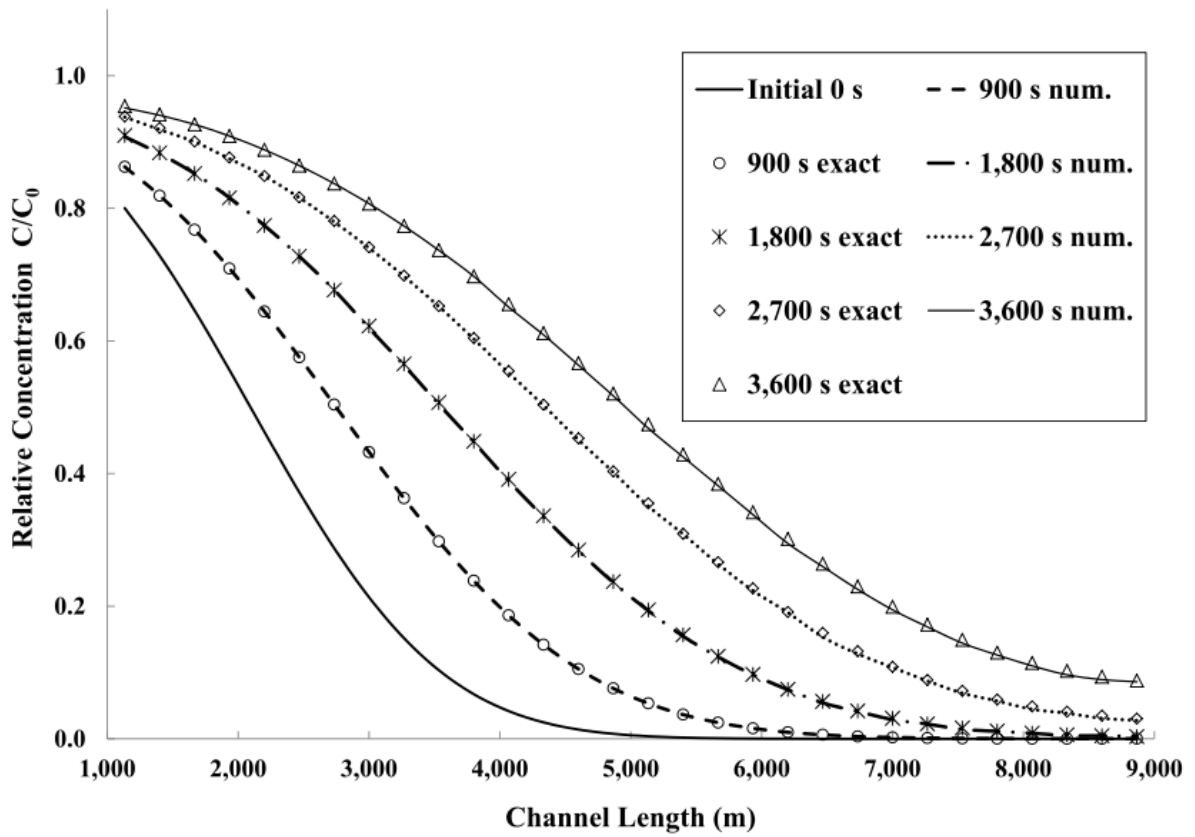


Figure 3-7. Evolution in time of a pollution front subjected to non-uniform advection and temporally-varying dispersion coefficient. Comparison of numerical and analytical solutions,

$$\Delta t = 0.06 \text{ s and } \Delta x = 0.28 \text{ m.}$$

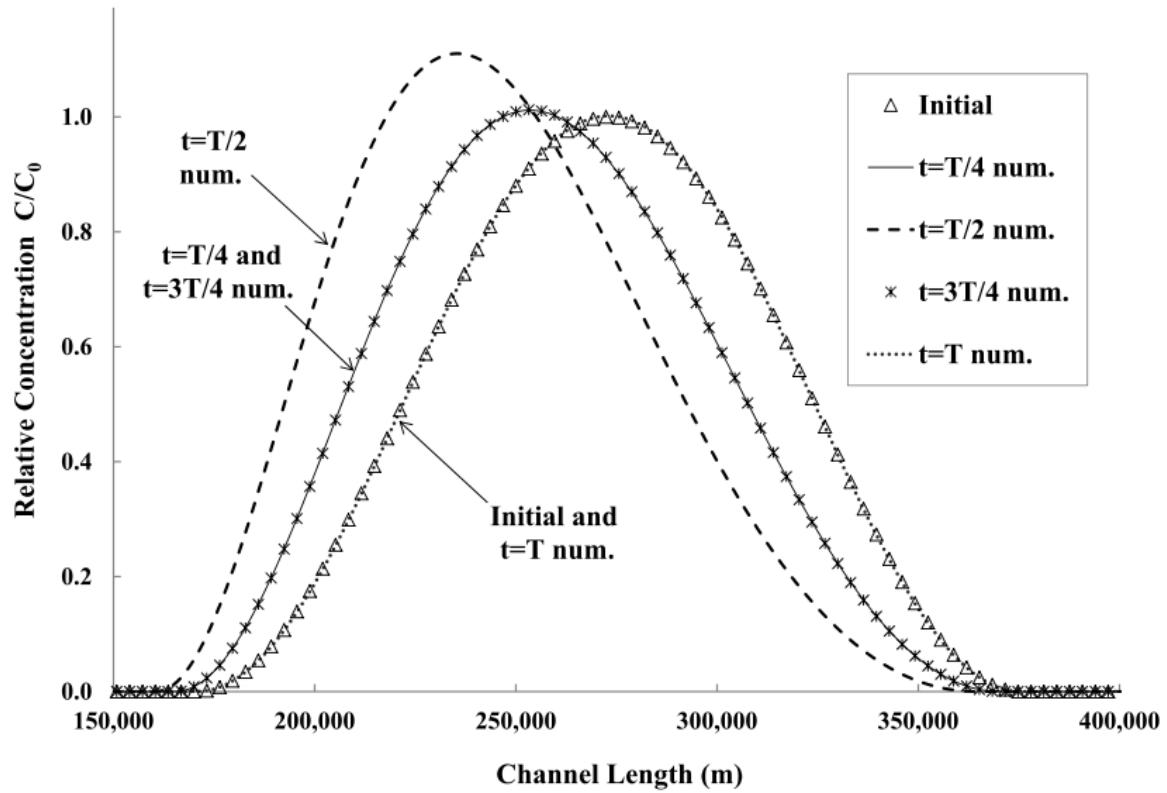


Figure 3-8. Evolution in time of a pollutant mass subjected to a tidal flow field. Concentration distribution subjected to one cycle of tidal advection is compared with its initial distribution as benchmark. Tidal compression of plume in half of the tidal period is noticeable, $\Delta t =$

174.5 s and $\Delta x = 400$ m.

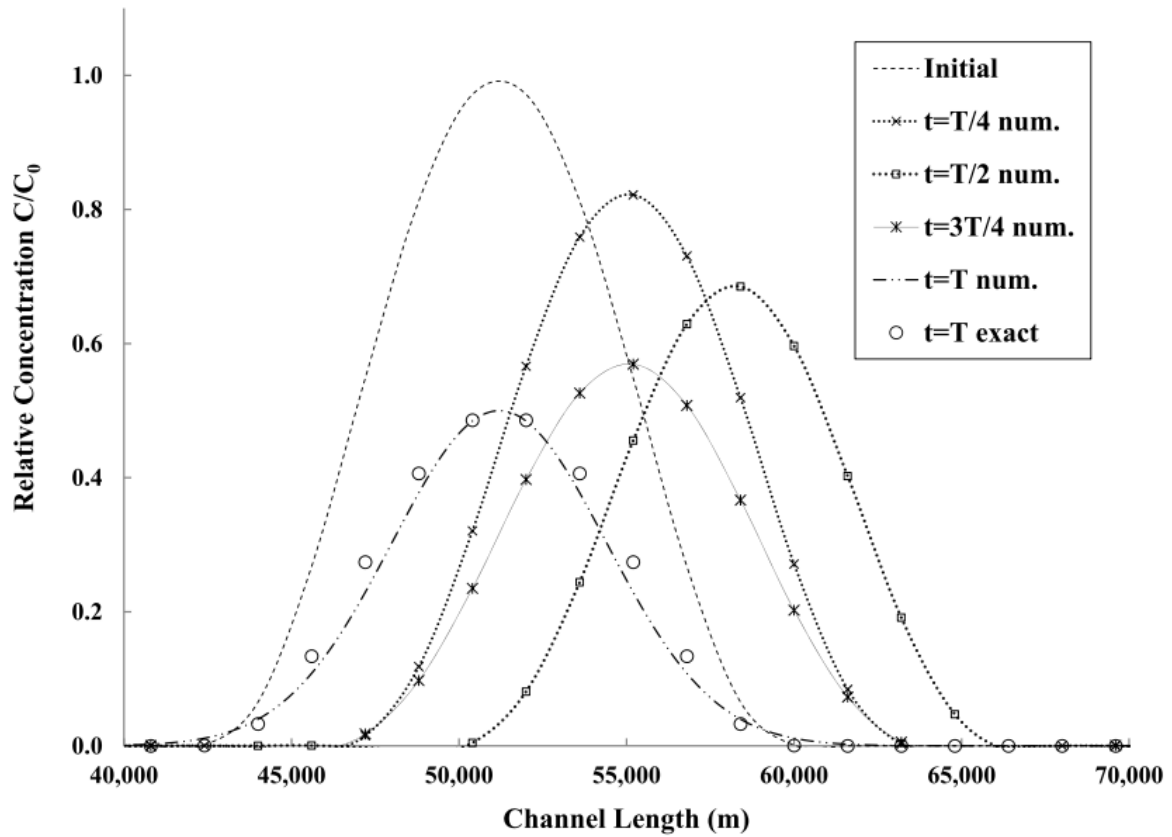


Figure 3-9. Evolution in time of a pollutant mass subjected to tidal flow field and linear decay,

$$\Delta t = 174.5 \text{ s and } \Delta x = 400 \text{ m.}$$

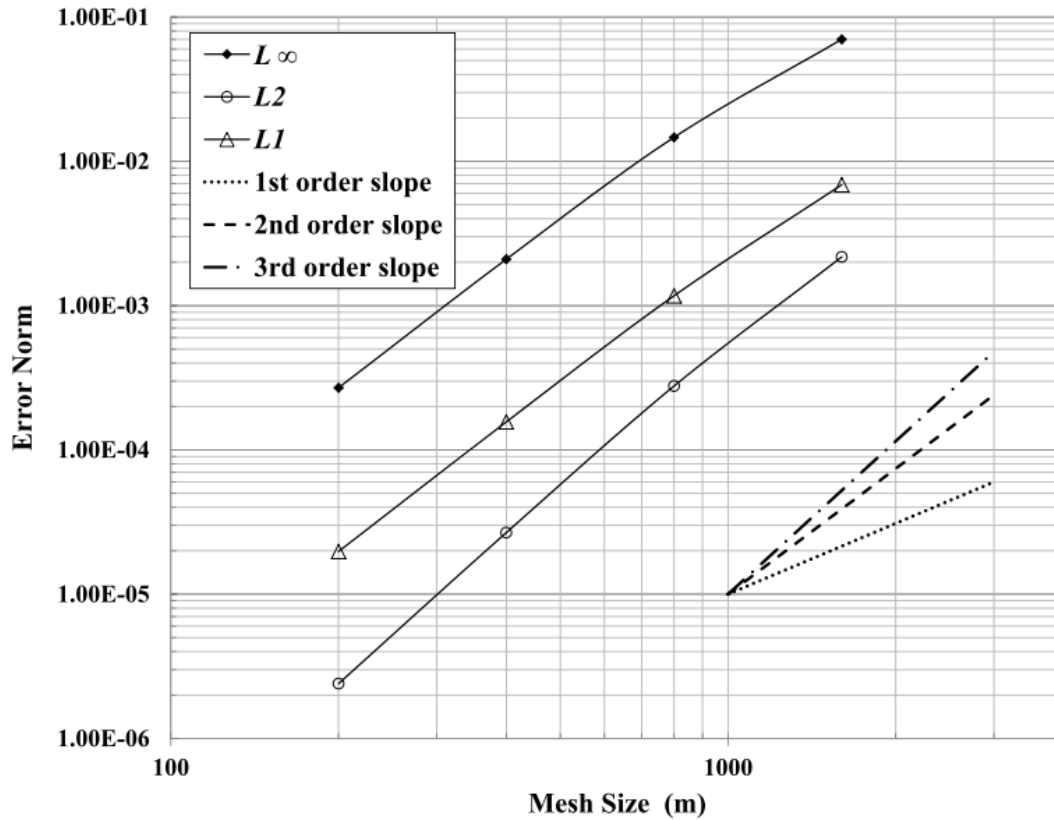


Figure 3-10. Observed versus formal order of accuracy. Mesh convergence study for the tidal advection-reaction test. Norm L_∞ measures the worst error in the domain; L_2 is the energy norm of the errors; and norm L_1 denotes the average of absolute errors in the domain. Three error norms show second order convergence rate.

Tables

Table 3-1. Summary of analytical solutions of primarily single-species transport equations. The described literature possesses particular emphasis on the purpose of code verification.

Author	Dimensionality and coordinate system	Transport equation			Solution Method	Note
		Velocity	Diffusivity	Source		
Fourier (1822)	1-D, Cartesian	Stagnant	Constant	No source, linear source	Eigenfunction expansion	Heat equation
Kirchhoff (1894)	1-D, Cartesian	Stagnant	Function of state variable	No source, linear source	Kirchhoff transformation	Linearizes the nonlinear heat equation
Boltzmann (1894)	1-D, Cartesian	Stagnant	Constant	No source, linear source	Reduction to ODE via similarity solution	First similarity solution for solving transport equation
Carslaw and Jaeger (1959)	1-D, 2-D and 3-D, Cartesian, cylindrical, conic and spherical	Stagnant	Time- and space-dependent, and concentration dependent	Nonlinear and linear	Laplace transform, integral transform, Green's function	Fundamental solutions, Stefan problem, almost covered all the knowledge to that point
Ogata and Banks (1961)	1-D, Cartesian	Uniform	Constant	No source	Laplace transform	One of the first known analytical solution of the ADR equation
Cho (1971)	1-D, Cartesian, 3 species	Uniform	Constant	First order reaction	Laplace transform	Pioneer on the analytical solutions of reactive transport
Bear (1972)	1-D, 2-D and Cartesian and radial	Uniform	Constant	Linear decay	Transform to known solutions, Laplace transform, eigenfunction expansion	All the analytical solutions of the ADR equation for groundwater to date are presented in chapter 10.6
Crank (1979)	1-D, 2-D and 3-D Cartesian, cylindrical and spherical	Stagnant	Time- and concentration-dependent	Nonlinear and linear	Green's function, separation of variables, Laplace transform	Fundamental solutions, moving boundary, Stefan problem, perhaps one of the most prolific contributions to the mathematics of diffusion equation
van Genuchten and Alves (1982)	1-D, Cartesian	Uniform	Constant	No source, zero order, first order, reactive first order	Laplace transform, eigenfunction expansion	The report almost gathered all the analytical and approximate solutions of 1-D ADR excluding cases of nonlinear source, and non-constant velocity and dispersivity
Mohsen and Pinder (1984)	1-D, Cartesian	Uniform and steady condition	Constant	No source	Fourier eigenfunction expansion	Used in numerical verification
Lassey (1988)	1-D, Cartesian	Uniform	Constant	Sorption and first order decay	Eigenfunction expansion (Bessel function)	The semi-analytical solution is implicit and needs numerical evaluation
Tirabassi (1989)	2-D, Cartesian, steady state	Uniform	Constant and $D(z)$	No source	Eigenfunction expansion (Bessel)	Air pollution, deposition of emission is linear function of

					function)	vertical velocity
Barry and Sposito (1989)	1-D, Cartesian	Time dependent	Time dependent	No source	Fundamental solution via Green's function, Laplace transform	Review on the general solution techniques and problems with closed-form solution
Yates (1990, 1992)	1-D, Cartesian	Uniform	Velocity and distance dependent	Linear sorption first order decay	Laplace transform, similarity solution, Bessel function	Solutions are in terms of hypergeometric function and needs numerical evaluation
Basha and El-Habel (1993)	1-D, Cartesian	Uniform	Constant, linear and exponential time dependent	Linear adsorption, first order reaction	fundamental solution	No closed-form solution for all cases, solutions need numerical evaluation
Ellsworth and Butters (1993)	3-D, Cartesian	Uniform	Constant	Impulse	Green's function, Laplace and Fourier transforms, eigenfunction expansion	Solutions need numerical evaluation
Philip (1994)	2-D and 3-D, radial	Uniform	Constant	No source	Transformation to known solutions	The solution is steady state and is not in closed-form
Aral and Liao (1996)	2-D, Cartesian	Uniform	Function of time	Linear decay	Fundamental solution	Closed-form solutions are given for constant, linear/exponential time dependent dispersivity
Logan (1996)	1-D, Cartesian	Uniform	Constant and distance dependent	Rate-limited adsorption, linear equilibrium isotherm, and decay	Complex separation of variables	Solution based on hypergeometric function, requires numerical evaluation
Zoppou and Knight (1997, 1999)	1-D and 3-D, Cartesian	Distance dependent	Distance dependent	No source	Transform to Ogata and Banks (1961) solution	Velocity field does not holds continuity of mass
Sun et al. (1999)	3-D, Cartesian	Constant	Constant	Multi-species linear reaction and sorption	Substitution of variables	Three example solved for 3/4 species in 1-D and 3-D
Leij and van Genuchten (2000)	3-D, Cartesian	Uniform unidirectional	Constant, Dx, Dy and Dz	equilibrium and nonequilibrium	Green's function	Different examples constructed and solved based on the fundamental solutions
Leij et al. (2000)	3-D, Cartesian,	Uniform unidirectional	Constant	Linear, equilibrium and nonequilibrium	Fundamental solution	Application of Green's function for infinite and semi-infinite 3-D solute transport
Logan (2001, 2008)	1-D, Cartesian, Radial	Uniform and steady condition	Constant	Linear decay, equilibrium and nonequilibrium	Separation of variables, Laplace, Fourier and integral transforms, Green's function, distribution solutions, eigenfunction expansion, and traveling wave, perturbation techniques	General review on the numerical and analytical solution techniques for ADR and heat equations

Khalifa (2003)	2-D, Cartesian and cylindrical	Uniform unidirectional	Constant	No source	Similarity solution, Lie group transformation	Solution based on hypergeometric functions
Neelz (2006)	1-D, Cartesian	Distance dependent	Distance dependent	No source	Solution by Zoppou and Knight (1997)	Discussed the limitation of the solution for code verification
Demetriou, et al. (2007)	2-D, Cartesian	Uniform unidirectional	Constant	No source	Similarity solution, Lie symmetry	Several cases have been solved, solution based on the Bessel functions
Cannon (2008)	1-D, Cartesian	Uniform unidirectional	time and space dependent, ad hoc cases of nonlinear	Arbitrary form of source discussed	Green's function, separation of variables, integral transform, variational principle, traveling wave	Fundamental solutions and transform techniques, Stefan problem. The book is a highly-acclaimed guide to heat diffusion equation
Chen et al. (2008)	2-D, Cartesian	Uniform unidirectional	Distance dependent	No source	Power series	Solution needs numerical evaluation not applicable for code verification purpose
Jaiswal et al. (2009)	1-D, Cartesian	Case: 1) Uniform and 2) non uniform	1) Time dependent 2) distance dependent	No source	Laplace transform	Flow field does not hold continuity of mass
Singh et al. (2009)	1-D, Cartesian	Time dependent	Time dependent	No source	Transform to homogeneous problem, Laplace transform, separation of variables	Full derivation of time dependent problem provided step by step
Guerrero et al. (2009)	1-D, Cartesian, transient and steady state	Constant	Constant	Linear decay	Integral transform, eigenfunction expansion	Results are series and not applicable for code verification (as we tested ~ 300 terms needed to go over the computer accuracy)
Guerrero and Skaggs (2010)	1-D, Cartesian	Distance dependent	Distance dependent	Linear distance dependent	Integral transform, separation of variables	Results do not have closed-form and are not applicable for code verification
Singh et al. (2010)	2-D Cartesian and cylindrical	Time dependent in x and y direction	Time dependent	No source	Reduction of advective term via substitution and Hankel transform	Solutions are series based
Kumar et al. (2010)	1-D, Cartesian	Cases 1) $u(x)$ 2) $u(t)$ 3) $u = \text{constant}$	Cases 1, 2) $D = \text{constant}$ b) $D = D(t)$	No source	Transformation to formerly known solutions	Space dependent solution does not hold conservation of water
Yadav et al. (2010)	1-D, Cartesian	Uniform flow	$D = D(t)$	Linear decay	Laplace transform	Dispersivity is linear and nonlinear function of time
Jaiswal et al. (2011)	2-D, Cartesian	a) $u(t)$ b) $u(x)$	Function of velocity	Impulse	Laplace transform, reduction to formerly known solutions	Flow field does not hold continuity of mass
Chen et al. (2011)	2-D, cylindrical	Uniform unidirectional	Constant	No source	Laplace and Hankel transform	It needs more than first 200 terms to reach required accuracy for code verification
Savovic and Djordjevich (2012)	1-D, Cartesian	a) Constant b) time and c) space dependent	a) Constant b) time and c) space dependent	No source	Solution by Kumar et al. (2010)	Solutions employed in code verification studies of a FDM code

Table 3-2. Accuracy metrics for assessment of numerical model results versus benchmark values.

Test	Scatter Index (<i>SI</i>) $\frac{\sqrt{\frac{1}{N} \sum_{i=1}^N (M_i - B_i)^2}}{\frac{1}{N} \sum_{i=1}^N B_i} = \frac{RMSE}{\bar{B}}$	Bias $\frac{1}{N} \sum_{i=1}^N (M_i - B_i)$	Coefficient of determination (<i>R</i> ²) $1 - \frac{\sum_{i=1}^N (M_i - B_i)^2}{\sum_{i=1}^N (M_i - \bar{B})^2}$
Linear ADR (Figure 3-2)	0.003423	0.000131	0.999806
Nonlinear diffusion reaction (Figure 3-3)	0.003076	0.000461	0.988702
ADR with nonlinear source term (Figure 3-4)	0.000685	0.000135	0.999992
ADR with nonlinear advective term (Figure 3-5)	0.000183	-0.000157	0.999999
Spatially dependent ADR (Figure 3-6)	0.000685	0.000135	0.999992
Temporally dependent ADR (Figure 3-7)	0.000183	-0.000157	0.999999
Tidal flow advection (Figure 3-8)	0.004300	0.002556	0.999903
Tidal flow advection decay (Figure 3-9)	0.000004	0.009627	0.994229

Table 3-3. Summary of the seven analytical solutions for numerical verification of transport solvers discussed in this paper.

Equation and limits $0 < t; 0 < D_0$	Analytical solution $C(x, t)$	Boundary condition	Note	Purpose
$C_t = (D_0 C_x)_x - (u_0 C)_x - \beta C$ $-\infty < x < \infty$ $0 < \beta$	$\frac{1}{\sqrt{4\pi D_0 t}} e^{-\beta t - \frac{(x-u_0 t)^2}{4D_0 t}}$	Based on the analytical solution ²	Conservative ADR equation with uniform flow, constant dispersivity and linear decay	Start verification with this analytical solution to check general discretization
$C_t = (D_0 e^C C_x)_x - \beta e^C$ $-\infty < x < \infty$ $0 < \beta$	$\ln \left(\frac{e^{x\sqrt{\frac{\beta}{D_0}} + K_1} e^{-x\sqrt{\frac{\beta}{D_0}} + \frac{\lambda}{\beta}}}{K_2 - \lambda t} \right)$	Based on the analytical solution	Diffusion Reaction with nonlinear dispersivity and nonlinear reaction	Verification of the solver for nonlinearity in dispersivity and reaction term
$C_t = u_0 C_x + D_0 C_{xx} - \beta C^2$ $-\infty < x < \infty$ $0 < \beta$	$\sqrt{\frac{2D_0}{\beta}} \frac{2(x + u_0 t)}{(x + u_0 t)^2 + 6D_0 t}$	Based on the analytical solution	ADR with uniform flow, constant dispersivity and nonlinear reaction	Verification of the solver for stiff nonlinear problems
$C_t = D_0 C_{xx} - C C_x$ $C(x \rightarrow \infty, t) = c_2$ $C(x \rightarrow -\infty, t) = c_1$ $-\infty < x < \infty$	$c_1 + \frac{c_2 - c_1}{1 + e^{(c_2 - c_1)(x - \frac{(c_2 + c_1)t}{2})/2D_0}}$	Based on the analytical solution	Choose c_1 and c_2 such that solutions remains positive, use D_0 to smear out sharpness of the shock	Verification of the solver for nonlinearity in advective term
$(Ax^{-1}C)_t = (A_0 D_0 x C_x)_x - A_0 u_0 C_x$ $0 < x < \infty$ $0 < A_0$	$\frac{C_0}{2} \left\{ \operatorname{erfc} \left(\frac{\ln \left(\frac{x}{x_0} \right) - (u_0 - D_0)t}{2\sqrt{D_0 t}} \right) + \exp \left(\frac{(u_0 - D_0) \ln \left(\frac{x}{x_0} \right)}{D_0} \right) \operatorname{erfc} \left(\frac{\ln \left(\frac{x}{x_0} \right) + (u_0 - D_0)t}{2\sqrt{D_0 t}} \right) \right\}$	Based on the analytical solution	ADR equation with mass conservative flow with spatially varying transport coefficients	Exposing bugs in spatial discretization of advection and diffusion
$(A_0 C)_t = (A_0 D_0 (2 + \cos \omega_t) C_x)_x - (A_0 u_0 (2 + \cos \omega_t) C)_x$ $0 < x < \infty$ $0 < A_0$	$\frac{C_0}{2} \left\{ \operatorname{erfc} \left(\frac{x - u_0 (2t + \frac{\sin(\omega_t t)}{\omega_t})}{2\sqrt{D_0 (2t + \frac{\sin(\omega_t t)}{\omega_t})}} \right) + \exp \left(\frac{u_0 x}{D_0} \right) \operatorname{erfc} \left(\frac{x + u_0 (2t + \frac{\sin(\omega_t t)}{\omega_t})}{2\sqrt{D_0 (2t + \frac{\sin(\omega_t t)}{\omega_t})}} \right) \right\}$	Based on the analytical solution	ADE with mass conservative flow time dependent varying transport coefficients	Exposing bugs in temporal discretization, efficiency of fractional-step method
$(AC)_t = -u(AC)_x - \beta C$ $u(x, t) = m \sin(n(l-x)) \sin(\omega_t t)$ $\zeta(x, t) = a \left[\frac{\cos(n(l-x))}{\cos(nl)} \right] \cos(\omega_t t)$ $A(x, t) = (d + \zeta(x, t))w$	$C(x, t_0) = C(x, t_0 + kT_{tide})$. Final pollution concentration will be the same as initial distribution after passing k tidal cycles, where k is a positive integer. Smooth Gaussian profile might be a good choice $[C(x, t_0) = K_1 e^{-\frac{(x-K_2)^2}{K_3^2}}]$ set K_i to maintain remote BC in the test	Based on the analytical solution, set K_i such that remote BC in the test is maintained	Advection-reaction in tidal flow advection linear $n = \frac{\omega_t}{\sqrt{gd}}$ $m = \frac{(a\sqrt{gd})}{d \cos(nl)}$	Verification of spatial and temporal defects in the discretization of advective term

² Dirichlet, Neumann and Robin boundary conditions might be constructed based on these analytical solutions

Chapter 4: Assessment of Sequential and Parallel Implementation of Current Methods for The Evaluation of Einstein's Integrals

4.1. Introduction

Numerous formulations have been proposed for the computation of the total sediment transport load during the last century (see Julien, 2002; Vanoni, 2006; García, 2008). Existing methods can be categorized in three main groups (adapted from Julien, 2002): a) formulae that are derived via regression on experimental data, b) formulae based on the balance of energy such that the work done to carry particles is related to the energy expenditure; and c) formulations based on other first principles. Among those methods, Einstein's method (Einstein, 1950) is based on first principles and it is built on the rigorous foundation of continuum mechanics (Julien, 2002; Guo and Julien, 2004; Vanoni, 2006; Shah-Fairbank et al., 2011).

Einstein's method is widely considered as one of the cornerstones of sediment mechanics (Julien, 2002; García, 2008). This method makes use of two integrals for the calculation of the suspended-sediment load. Without considering the multiplying factors, Einstein's integrals are defined as (Einstein, 1950):

$$J_1(E, z) = \int_E^1 \left(\frac{1-y}{y}\right)^z dy \quad (4-1)$$

$$J_2(E, z) = \int_E^1 \left(\frac{1-y}{y}\right)^z \ln y dy \quad (4-2)$$

in which, J_1 and J_2 are the first and second Einstein's integrals; E is the bedload-layer thickness, $E \in [0.0001, 0.1]$ (which is usually considered as $E = 2d$ in the absence of bed-forms and d is the particle diameter); y is the vertical coordinate, which is scaled with the water depth; and z is the Rouse (dimensionless) number, defined as the ratio of the particle fall velocity and the

product of the von Kármán constant κ , the inverse of the Schmidt number (β , Bombardelli and Jha, 2009; Jha and Bombardelli, 2009) and the shear velocity, u^* . The Rouse number varies between 0.1 and 6 in practical applications.

As analytical solutions of those integrals do not exist, Einstein (1950) provided nomograms for their calculation. Since using nomograms impedes the automation of Einstein's method, several researchers developed simplifications, as is the case of Colby and Hubbell (1961), Toffaleti (1968), and Simons et al. (1981). Einstein's method remained unused in computer codes until recently (Abad et al., 2008; Shah-Fairbank et al., 2011). In modern sediment-transport codes (such as HEC-RAS, U.S. Army Corps of Engineers, 2010), the difficulty of calculation of Einstein's integrals hinders the employment of Einstein's method. The problem is that using common numerical integration techniques is time consuming due to the sharp gradients in the integrand functions near the bed (Nakato, 1984; see also Figure 2 in Zamani and Bombardelli, 2016). To overcome this issue, several authors devised schemes to approximate Einstein's integrals, from computational approximations, to the use of convergent series solution, and regression based schemes (Nakato, 1984; Guo and Wood, 1995; Guo and Julien, 2004; Abad and García (Abad et al., 2006); Roland and Zanke (Abad et al., 2006); Srivastava (Abad et al., 2006); García, 2008; Shah-Fairbank et al., 2011). Given this menu of methods, there is the natural question on which one(s) is(are) the most convenient for each particular case.

In this technical note, we conduct a systematic study of existing methods of approximation of first and second Einstein's integrals including the method by Nakato (1984), series-based schemes by Guo and Julien (2004), regression formula by Abad and García (Abad et al., 2006), modification of Guo and Julien's method by Roland and Zanke (Abad et al., 2006),

and the method by Srivastava (Abad et al., 2006). We endeavor to uncover singularities or regions of inaccuracy in the above methods in order to provide “optimal” solutions in different ranges of all admissible Rouse numbers and bedload-layer thicknesses (960 sets of data). We assess the methods based on three criteria: a) accuracy, b) computational efficiency, and c) the efficiency of parallel versions of those schemes, which we present for the first time to the best of our knowledge.

Next section briefly introduces existing methods. (We provide their formulations in Appendix 1 for the sake of completeness.) Later on, we provide the assessment of accuracy and efficiency of the aforementioned methods. Then, we present the parallel versions of those methods and assess their efficiency. The paper finishes with an overall evaluation of all methodologies.

4.2. Methods for The Calculation of Einstein’s Integrals

Evidently, the first effort to compute Einstein’s integrals – instead of using his nomograms – was conducted by Nakato (1984). Nakato employed the additivity of integration intervals and divided the integrals into two zones of sharp and mild variations. Nakato computed the zone of mild changes numerically with the Simpson’s rule (Appendix 2). Then, he devised an analytical solution for the zone of sharp changes (see Appendix 1).

The second approximation to Einstein’s integrals was developed by Guo and Wood (1995). They recast a modification of the first Einstein integral into the beta function. They also used the first couple of terms in the expansion of an integral similar to the second Einstein’s integral to approximate this second integral. Guo and Wood's derivation was only applicable to

non-integer, and less-than-unity Rouse numbers; therefore, we do not consider their work in this manuscript.

The first major step towards the practical solution of Einstein's integrals was presented by Guo and Julien (2004). Guo and Julien resolved the issues of integer values of the Rouse number in the method by Guo and Wood (1995). In addition, they utilized integration by parts for both Einstein's integrals, to devise a recursive formula. They derived an infinite series-based solution for their recursive equation. These authors provided a comprehensive framework for solving the problem (Roland and Zanke (Abad et al., 2006); Srivastava (Abad et al., 2006)). A short overview of Guo and Julien's method is provided in the Appendix 1 as well.

The paper by Guo and Julien (2004) prompted three discussions in 2006, by Abad and García, by Roland and Zanke, and by Srivastava, all collected into one single note (Abad et al., 2006). Abad and García (Abad et al., 2006) devised a regression-based polynomial approximation of the solution of each integral. Abad and García claimed their regression formula is more practical and easy to implement in sediment-transport codes (Abad et al., 2008). Their equations can be found in Appendix 1.

Roland and Zanke in Abad et al. (2006) studied explicit approximations to improve Guo and Julien's series-based method. They built an explicit closure for the formula by Guo and Julien (2004); however, their method has large discrepancies in the values of the J_2 integral for high bedload-layer thicknesses ($E > 0.01$) with the "exact" value of the integrals (Abad et al., 2006). Roland and Zanke claimed that their J_2 algorithm implementation performs a couple of times faster than the method by Guo and Julien (2004). The suggested algorithm presents singularities in the integer Rouse numbers, as the authors themselves acknowledged (see Figures 1 to 3 in Roland and Zanke (Abad et al., 2006)). Their study was the first work which discussed

computational efficiency (to the best of our knowledge). Roland and Zanke's formulations are detailed in the Appendix 1, subsection 4.

Finally, Srivastava, in Abad et al. (2006), conducted a rigorous mathematical study of convergence regions of the partial sums by Guo and Julien (see sums in Eqs. (7) and (8)). He showed that in the Guo and Julien (2004) derivation, the series-based solution is either not, or slowly converging at some values of E and z . However, some of his concerns were not practically effective due to the physical range of the parameters. Srivastava derived another explicit formula based on Guo and Julien's recursive formula. In addition, he proposed successful remedies for the problem of singularities in series representation of the Einstein integrals. Additionally, he discussed about extra computational burden of switching between formulas in integer and non-integer Rouse number values. Details of his method are given in Appendix 1, subsection 5.

Guo and Julien (Abad et al., 2006) responded to the three above comments in a closure. They acknowledged that their formula for J_2 integral converges slowly. They also criticized the accuracy of Abad and García's regression, when the bedload-layer thickness is relatively low ($E < 0.01$). Furthermore, they stated that the Roland and Zanke's method is eventually equivalent to the combination of Guo and Wood's (1995) and Guo and Julien's (2004) algorithm. Finally, they conducted a study of all methods' speed and employed them in a real world example of sediment transport – in the Missouri River near Omaha, Nebraska. Guo and Julien (Abad et al., 2006) also provided their pseudo-code. Later on, their algorithm was successfully implemented in sediment-transport codes and verified in applications (Shah-Fairbank et al., 2011). In the next section of the paper we discuss computational efficiency and global and local accuracy of the abovementioned methods.

4.3. Assessment of the Efficiency and Accuracy of Existing Methods

We evaluated the error of and CPU time for each method over a comprehensive dataset of 960 pairs of values in the (E, z) space. The prediction errors of those five methods are given in Figures 1 and 2 for J_1 and J_2 integrals, correspondingly; the error metrics are computed versus numerical values obtained by the composite Simpson method (Press et al., 1992) with a dense mesh (details of the benchmark algorithm are given in Appendix 2). Figure 3 shows the CPU time of the methods – with different parameters – to calculate Einstein’s integrals for the same dataset of 960 values of (E, z) . The benchmarking machine had an Intel® Core™ i7-2670QM Processor with 4 physical cores and 8 GB RAM. Finally, statistical measures of accuracy of those five methods are given in Table 1. Definitions of those statistical metrics are given in Appendix 3. In the last two columns of Table 1, we also provide the results computed by the composite Simpson’s rule with different number of points for comparison.

From Figures 1 and 2, it is possible to notice that all methods provide an overall error less than 1% for all cases analyzed, which is a necessary feature. From those, Nakato’s method provides relatively-low errors, in particular for J_2 integral (circled solid line in Figures 1 and 2). The accuracy of Nakato’s method is comparable with that of the composite Simpson’s integration with 1000 points. However, Nakato’s method is the slowest compared to other methods (Figure 3).

The method by Guo and Julien is the most accurate method for approximation of the J_1 integral (Table 1 and Figure 1). The only issue with Guo and Julien algorithm is that its J_2 approximation algorithm is slowly converging for large values of the bedload-layer thickness. Also, the error of the J_2 integral is higher than for all other methods except for the regression formula by Abad and García (Table 1). Guo and Julien’s method is the fastest method for

computation of the J_1 integral (equal CPU time with Roland and Zanke's method). However, for the J_2 integral, this method requires almost an order of magnitude more time to provide results *with the equivalent accuracy of Srivastava method* (Table 1 and Figure 3). In our test problems (Table 1) we did not find significant improvement of the error metrics of computation of J_2 integrals, employing partial sums with more than 50 terms (right-hand term of Equation (8)).

We also set up a test to evaluate the accuracy of Eq. (10) as an explicit closure for the first right-hand side partial sum in the Eq. (8) – in calculation of the J_2 integral with Guo and Julien's method. Table 2 results show that Guo and Julien's closure is effective – to the precision of less than 0.3% – for all ranges of the Rouse number. Table 2 shows that the method of Guo and Julien (without closure; columns 3 to 7) is relatively-inaccurate in large Rouse numbers and therein, at least 200 first terms are needed to keep the error below one percent. Also the explicit closure by Srivastava – Eq. (17) – is more accurate than the closure by Guo and Julien (Eq. (10)).

Roland and Zanke's method has significant error as the bedload-layer reference height increases and the Rouse number is larger (Figures 1 and 2); also, it seems that their method is the least accurate – for all ranges of parameters – in the calculation of the J_2 integral (Figures 2 and Table 1). As both Figures 1 and 2 show, the error values of this method spike near the integer Rouse number. This method is the fastest method for computing both integrals.

Srivastava's method has a high error in the prediction of the J_1 integral; the error smoothly reduces with the increase of Rouse number. For computing the J_2 integral, the Srivastava's method is accurate (Table 1 and Figure 2) and is also among the fastest methods (alongside Abad and García's method). Srivastava also devised explicit closures for the Eq. (8). His closure overperforms the one by Guo and Julien in terms of accuracy (Table 2). A minor

issue with Srivastava's scheme is it has singularity near $z = 2.6$ (see Figure 2; see also Guo and Julien in Abad et al., 2006).

Abad and García's regression is the least accurate scheme in calculating the J_1 integral. However, it still produces results within the accuracy of 2%. Generally, Abad and García's method works better for higher bedload-layer thicknesses (Figures 1 and 2; and see also Guo and Julien in Abad et al., 2006). This method is among the fastest methods for both integrals and, as the authors mentioned in the original discussion, the method is easy to implement and it does not suffer from singularities.

It is worth pointing out at this time in the analysis that these evaluations refer to the mathematical accuracy of the computation of the Einstein's integrals. However, in practical terms, some of the issues expressed here could be considered moot, given the relative accuracy of the computation of the Rouse number (Vanoni, 2006), and bedload-layer thickness (Vanoni, 2006; García, 2008). In fact, the settling velocity and shear velocity are usually known with relative-high error and, thus, the computation of the J_1 and J_2 integrals is contaminated with the “input parameter uncertainty” (ASME V&V20, 2009). In addition, even if we assume that there is no inaccuracy in the values of E and z , there is a second type of inaccuracy in the Einstein's method. Since there are simplifying and distinct assumptions in the derivation of Rousean profile (see Vanoni, 2006; Bombardelli and Jha, 2009; Liu and Nayamatullah, 2014), the Einstein's method itself is subjected to “model structural uncertainty” (ASME V&V20, 2009). Considering those two type uncertainties, it can be argued that even excessive reducing of “numerical error” will not warrant improvement in overall error in sediment-transport modeling.

4.4. Parallelization Efficiency of Algorithms

Any advanced sediment-transport code requires multiple grain-size simulation capability to mimic non-uniform particle size distribution in natural streams (Papanicolaou et al., 2008). In sediment-transport software, hydrodynamics and transport solvers are commonly one-way coupled assuming a dilute concentration of particles (Papanicolaou et al., 2008); thus, all grain-classes are transported by a unique flow field in a master-slave connection. The above facts evoke utilizing parallel algorithms for sediment transport solvers to increase the computational efficiency (see for example, Khosronejad et al., 2011; Keshtpoor et al., 2015). We performed integration of Einstein integrals on multicore processors.

In general, shared-memory, message-passing, and implicit programming models can be used to write the parallel programs (MathWorks, 2015). Shared-memory models are very efficient and suitable to be used for multicore processors (and used in this study).

Parallel for-Loop (parfor) of MATLAB's *Parallel Computing Toolbox*TM was used to parallelize the calculations of the integrals on multicore (MathWorks, 2015). The performance of the parallelized version of the methods was evaluated on an Intel i7-2670QM multicore processor utilizing different number of cores for a dataset of 9000 pairs of inputs. Resulting speedups (see Appendix 4-C) for the J_1 and J_2 integrals are shown in Figures 4a and 4b, correspondingly.

The best performance is achieved by the composite Simpson's method, where the speedup is close to the ideal line for parallel computing of the J_1 (1.88, 2.81, and 3.53 with 2, 3, and 4 cores, respectively) and J_2 (1.91, 2.79, and 3.60 with 2, 3, and 4 cores) integrals. Nakato's method is slightly less efficient than composite Simpson's method in the J_1 integral, but its speedup ratio is nearly linear and again close to the ideal line. In parallel computing of the J_2

integral, Nakato's method performs well for 2 and 3 cores, however, the linear upward speedup trend reaches a plateau for 4 cores. The third best speedup for the J_1 integrals is the Guo and Julien's method with 1.77, 2.28, and 2.56 with 2, 3, and 4 cores. This method for the J_2 integrals – with one hundred points in the partial sum – has a better speedup factor than Nakato's method and it reaches 1.74, 2.23, and 2.99 with 2, 3, and 4 cores.

At this point, it is worth mentioning that distributing and mapping of data and tasks between the processing units impose extra overhead to the calculations; however, the overhead might be compensated by parallel-computing gained benefits. Apparently, any parallel algorithm is only efficient when the overall performance does not decrease by parallelization. In this study, the three explicit methods (Ronald-Zanke, Abad-García and Srivastava algorithms) do not become more efficient on multi-CPU as the overhead of distributing the computation dominates the efficiency gain by means of multi-processors. In some cases, the efficiency (even slightly) drops for both integrals using multi-cores. Srivastava's method is the least efficient method to parallelize by the algorithm which we used in this study. For example, the efficiency of Srivastava's method using 4 cores is 0.67 which is even below the single core computation. Figures 4a and 4b show that if we choose to perform the computation of Einstein's integrals on multi-processors, Guo and Julien's algorithm over-performs the other four existing methods. Additionally, sequential computing of Abad and García, Srivastava and Roland and Zanke's methods are more efficient than their parallel counterpart (at least for datasets up to 10000 pairs).

4.5. Summary and Conclusions

In this study, five existing methods for the calculation of Einstein's integrals were compared over a complete range of inputs. CPU time of the methods for a similar set of

parameters was determined. Error was assessed in various bedload-layer thicknesses and different Rouse numbers. Finally, the performance of parallel implementation of those methods was evaluated on the MATLAB embedded parallel platform.

Considering all aspects, in particular the tradeoff between accuracy (below a certain threshold) and computational time, we recommend the series-based solution method by Guo and Julien (2004) for computing the J_1 integral with only ten first terms of the partial sum (right-hand side term in Eq. (7)), which is relatively fast and at the same time accurate. Guo and Julien's method shows superiority for parallel computing of the J_1 integral. Besides Guo and Julien's method, Roland and Zanke's explicit modification of Guo and Julien's scheme is a reasonably accurate method, while it is nearly an order of magnitude faster than the original Guo and Julien's method. However, Roland and Zanke's method is only recommended for sequential processing.

For sequential computing of the J_2 integral, we recommend the Srivastava modification to the Guo and Julien's method, to account for left hand side partial sum of Eq. (8). It is more accurate and meanwhile faster than all methods (except Abad and García and Roland and Zanke). Also, it is worth mentioning that the regression formula of Abad and García provides relatively accurate results for the J_2 integral in particular for high bedload-layer thicknesses.

Appendices of Chapter 4

4-A. Existing methods of approximation of Einstein's integrals

4-A-1. Nakato's method

Nakato (1984) separated both Einstein's integrals into two regions: near the bedload-reference level ($E < y < \epsilon$), and the upper region ($\epsilon < y < 1$), as follows:

$$J_1 = \int_E^1 \left(\frac{1-y}{y}\right)^z dy = \int_E^\epsilon \left(\frac{1-y}{y}\right)^z dy + \int_\epsilon^1 \left(\frac{1-y}{y}\right)^z dy \quad (4-3)$$

$$J_2 = \int_E^1 \left(\frac{1-y}{y}\right)^z \ln y dy = \int_E^\epsilon \left(\frac{1-y}{y}\right)^z \ln y dy + \int_\epsilon^1 \left(\frac{1-y}{y}\right)^z \ln y dy \quad (4-4)$$

Nakato integrated the upper region (second term on the right-hand side) numerically with Simpson's rule, and derived the following formulas for the part close to the bedload-layer thickness (first term on the right-hand side):

$$\int_E^\epsilon \left(\frac{1-y}{y}\right)^z dy = F_1 + F_2 + F_3 \quad (4-5a)$$

in which F_i s are defined as:

$$F_1 = \frac{1}{1-z} (\epsilon^{1-z} - E^{1-z}); F_2 = \frac{1}{z-2} (\epsilon^{2-z} - E^{2-z}); F_3 = \frac{z(z-1)}{2(3-z)} (\epsilon^{3-z} - E^{3-z}); \quad (4-5b)$$

When the respective formulas become singular at $z = 1$, $z = 2$, and $z = 3$, the following expressions can be used instead:

$$F_1 = \ln \frac{\epsilon}{E}; F_2 = -2 \ln \frac{\epsilon}{E}; F_3 = 3 \ln \frac{\epsilon}{E} \quad (4-5c)$$

$$\text{In turn, } \int_E^\epsilon \left(\frac{1-y}{y}\right)^z \ln y dy = G_1 + G_2 + G_3 \quad (4-6a)$$

in which G_i s are defined as:

$$G_1 = \frac{\epsilon^{1-z}}{1-z} \left(\ln \epsilon - \frac{1}{1-z} \right) - \frac{E^{1-z}}{1-z} \left(\ln E - \frac{1}{1-z} \right); G_2 = \frac{z\epsilon^{2-z}}{z-2} \left(\ln \epsilon - \frac{1}{z-2} \right) - \frac{zE^{1-z}}{z-2} \left(\ln E - \frac{1}{2-z} \right);$$

$$G_3 = \frac{z(z-1)\epsilon^{3-z}}{2(3-z)} \left(\ln \epsilon - \frac{1}{3-z} \right) - \frac{z(z-1)E^{3-z}}{2(3-z)} \left(\ln E - \frac{1}{3-z} \right); \quad (4-6b)$$

When the respective formulas become singular at $z = 1$, $z = 2$, and $z = 3$, the following expressions can be used instead:

$$G_1 = \frac{1}{2}[(\ln \epsilon)^2 - (\ln A)^2]; G_2 = -(\ln \epsilon)^2 + (\ln A)^2; G_3 = \frac{3}{2}[(\ln \epsilon)^2 - (\ln A)^2] \quad (4-6c)$$

4-A-2. Guo and Julien's method

Guo and Julien (2004) derived closed-form, analytical solutions of the problem for integer values of Rouse number and for non-integer values they derived following formulas:

$$J_1(E, z) = \frac{z\pi}{\sin(z\pi)} - \left[\frac{(1-E)^z}{E^{z-1}} - z \sum_{n=1}^{\infty} \frac{(-1)^n}{(n-z)} \left(\frac{E}{1-E} \right)^{n-z} \right] \quad (4-7)$$

$$J_2(E, z) =$$

$$\frac{z\pi}{\sin(z\pi)} \left[\pi \cot(z\pi) - 1 - \frac{1}{z} + \sum_{n=1}^{\infty} \left(\frac{1}{n} - \frac{1}{z+n} \right) \right] - \left[\Phi(z) \left(\ln E + \frac{1}{z-1} \right) + z \sum_{n=1}^{\infty} \frac{(-1)^n}{(n-z)} \frac{\Phi(z-n)}{(1+n-z)} \right] \quad (4-8)$$

where $\Phi(z)$ is defined as:

$$\Phi(z) = \frac{(1-E)^z}{E^{z-1}} - z \sum_{n=1}^{\infty} \frac{(-1)^n}{n-z} \left(\frac{E}{1-E} \right)^{n-z} \quad (4-9)$$

Guo and Julien also suggested the following closure for the first infinite series in Equation (4-8) of the J_2 integral:

$$\sum_{n=1}^{\infty} \left(\frac{1}{n} - \frac{1}{z+n} \right) \approx \frac{\pi^2}{6} \frac{z}{(1+z)^{0.7162}} \quad (4-10)$$

4-A-3. Abad and García's regression

Abad and García (Abad et al., 2006) suggested the following formulas for Einstein's integrals based on regression analysis:

$$J_1 = (C_0 + C_1z + C_2z^2 + C_3z^3 + C_4z^4 + C_5z^5 + C_6z^6)^{-1} \quad (4-11)$$

$$J_2 = (D_0 + D_1z + D_2z^2 + D_3z^3 + D_4z^4 + D_5z^5 + D_6z^6)^{-1} \quad (4-12)$$

The coefficients of Equations (4-11) and (4-12) are given in Table 4-A1, based on Rouse number and reference bedload-layer thickness.

Table 4-A1: Regression coefficients for Equations (4-11) and (4-12)

E	C_0/D_0	C_1/D_1	C_2/D_2	C_3/D_3	C_4/D_4	C_5/D_5	C_6/D_6
0.001	8.0321	-26.273	-114.69	501.43	-229.51	41.94	-2.7722
	2.5779	-12.418	47.353	17.639	-13.554	2.8392	-0.2003
0.005	2.1142	-3.4502	12.491	60.345	-29.421	5.4215	-0.3577
	1.2623	1.0330	13.543	0.7655	-1.6646	0.3803	-0.0275
0.01	1.4852	0.2025	14.087	20.918	-10.91	2.034	-0.1345
	1.1510	2.1787	7.5672	-0.2777	0.570	0.1424	-0.0105
0.05	1.1038	2.6626	5.6497	0.3822	-0.6174	0.1315	-0.0091
	1.2574	2.3159	1.9239	-0.3558	0.0075	0.0064	-0.0006
0.1	1.1266	2.6239	3.0838	-0.3636	-0.0734	0.0246	-0.0019
	1.4952	2.2041	1.0552	-0.2372	0.0265	-0.0008	-0.00005

4-A-4. Roland and Zanke's method

Roland and Zanke (Abad et al., 2006) proposed the following formulas for Einstein's integrals:

$$J_1(E, z) = \left(\frac{1}{z-1}\right) \left[\frac{(1-E)^z}{E^{z-1}}\right] - \left(\frac{z}{z-1}\right) \left\{ \left(\frac{1}{z-2}\right) \left[\frac{(1-E)^{z-1}}{E^{z-2}}\right] - \left(\frac{z-1}{z-2}\right) \left\{ \left(\frac{1}{z-3}\right) \left[\frac{(1-E)^{z-2}}{E^{z-3}}\right] - \left(\frac{z-2}{z-3}\right) \left[\frac{(z-3)\pi}{\sin[(z-3)\pi]} - \frac{E^{4-z}}{4-z}\right] \right\} \right\} \quad (4-13)$$

$$J_2(E, z) = \left(\frac{1}{z-1}\right) \left\{ \ln E \frac{(1-E)^z}{E^{z-1}} - z \left[\left(\frac{1}{z-2}\right) \left(\ln E \frac{(1-E)^{z-1}}{E^{z-2}} - (z-1)J_2(E, z-3)J_1(E, z-2) \right) \right] + J_1(E, z) \right\} \quad (4-14)$$

They also suggested the following formulas for approximations for $J_2(E, z-3)$ and $J_1(E, z-2)$:

$$J_2(E, z - 3) = -\frac{(z-2)\pi\psi(z)}{\sin[(z-2)\pi]} - \frac{E^{3-z}}{3-z} \ln E + \frac{E^{3-z}}{(3-z)^2} \quad (4-15a)$$

$$\psi(z) = (1 - \gamma) - \ln|4 - z| + \frac{1}{3-z} + \frac{1}{2(4-z)} + \frac{1}{24(4-z)^2} \quad (4-15b)$$

$$J_1(E, z - 2) = \left(\frac{1}{z-2}\right) \left[\frac{(1-E)^{z-1}}{E^{z-2}}\right] - \left(\frac{z-1}{z-2}\right) \left[\frac{(z-2)\pi}{\sin[(z-2)\pi]} - \frac{E^{3-z}}{3-z}\right] \quad (4-16)$$

4-A-5. Srivastava's method

Srivastava (Abad et al., 2006) suggested a more accurate explicit closure which replaces Equation (4-10) by Guo and Julien (2004) to reduce the error:

$$\sum_{n=1}^{\infty} \left(\frac{1}{n} - \frac{1}{z+n}\right) \approx \ln(1 + 1781z) - \frac{0.1361z}{(1+1.284z)^{2.15}} \quad (4-17)$$

Then he resolved the problem of singularity in two of the terms in the infinite series expansion.

Srivastava introduced a change of variable as $E_* = \frac{E}{1-E}$ and derived the following closed-form

formulas for Einstein's integrals:

$$J_1(E_*, z) = -\frac{E_*^{1-z}-1}{1-z} + 2.061 \frac{E_*^{2-z}-1}{2-z} - 1.385 \frac{E_*^{2.6-z}-1}{2.6-z} + \frac{0.3327}{0.6703+z} \quad (4-18)$$

$$J_2(E_*, z) = \frac{E_*^{1-z}[1-(1-z)\ln E_*]-1}{(1-z)^2} - 1.903 \frac{E_*^{2-z}[1-(2-z)\ln E_*]-1}{(2-z)^2} + 2.022 \frac{E_*^{2.6-z}[1-(2.6-z)\ln E_*]-1}{(2.6-z)^2} - \frac{0.2914}{1.652+z} \quad (4-19)$$

4-B. Composite Simpson's rule

The composite Simpson rule for numerical integration is given below. This method has a truncation error of $O(h^4)$, therefore the methods is sometime called the cubic Simpson rule (Press at al., 1992):

$$\int_a^b f(x)dx = \frac{h}{3} \sum_{j=1}^{\frac{n}{2}} [f(x_{2j-2}) + 4f(x_{2j-1}) + f(x_{2j})] + \frac{h^4(b-a)}{180} \max |f^{(4)}(\mu)| \quad (4-20)$$

where $\mu \in [a, b]$; $h = \frac{b-a}{n}$; $x_0 = a$; $x_n = b$; and $x_j = a + jh$.

This method - with very dense mesh - was used as benchmark in our comparisons.

4-C. Statistics of model skill assessment

The following statistics are used in the paper to evaluate method results denoted by “ M ” versus a benchmark “ B ” (Chung et al., 2009; Zamani and Bombardelli, 2014):

$$\text{a) } Bias = \frac{1}{N} \sum_{i=1}^N (M_i - B_i) \quad (4-21)$$

Bias is a measure of over or under prediction of models. Essentially a value closer to zero for bias is ideal.

$$\text{b) } RMSE = \sqrt{\frac{1}{N} \sum_{i=1}^N (M_i - B_i)^2} \quad (4-22)$$

Root mean square error (RMSE) is a common metric for numerical prediction error, which amplifies large errors over the computation domain. RMSE values closer to zero is ideal.

$$\text{c) } SI = \frac{RMSE}{\frac{1}{N} \sum_{i=1}^N M_i} \quad (4-23)$$

Scatter index (SI) is another measure of error, which is scaled by the average value of the benchmark, and thus non-dimensionalized. It is worth mentioning that SI is more informative than RMSE index, since high (or low) values of RMSE can be misleading in cases of extremely high (or low) values of model results. For example in Table 1 composite Simpson’s method with 2000 points has a RMSE of an order 10^2 in the approximation of J_2 integral, while this method is a reasonably accurate method.

$$\text{d) } R^2 = 1 - \frac{\sum_{i=1}^N (M_i - B_i)^2}{\sum_{i=1}^N (M_i - \bar{M})^2} \quad (4-24)$$

Coefficient of determination (R^2) is a popular statistic which quantifies goodness-of-fit between method’s results and benchmark data. It varies between -1 and 1, with 1 indicating excellent agreement.

e) Parallelization speedup: is a metric in evaluation of parallel computing efficiency that shows relative performance improvement as a task is executed on multiprocessors compared to single processor.

Chapter Four References

1. Abad, J.D., Buscaglia, G., García, M.H. (2008). “2D Stream Hydrodynamic, sediment transport and bed morphology model for engineering applications.” *Hydrological Processes*, 22: 1443-1459.
2. Abad, J.D., García, M.H., Roland, A., Zanke, U., Srivastava, R., Guo, J., Julien, P.Y. (2006). “Discussion and closure to Efficient Algorithm for Computing Einstein Integrals by Junke Guo and Pierre Y. Julien.”, *J. Hydraul. Eng.* 132:337-339.
3. ASME-V&V 20 Committee (2009). “Standard for verification and validation in computational fluid dynamics and heat transfer.” American Society of Mechanical Engineers, New York.
4. Bombardelli, F.A., Jha, S.K. (2009). “Hierarchical modeling of the dilute transport of suspended sediment in open channels.” *Environmental Fluid Mechanics*, 9(2), 207-235.
5. Chung, E.G., Bombardelli, F.A., Schladow, S.G. (2009). “Modeling linkages between sediment resuspension and water quality in a shallow, eutrophic, wind-exposed lake.” *Ecological Modelling*, 220(9), 1251-1265.
6. Colby, B.R., Hubbell, D.W. (1961). “Simplified methods for computing total sediment discharge with the modified Einstein procedure” (No. 1593). USGPO.
7. Einstein, H.A. (1950). “The bed-load function for sediment transportation in open channel flow.” Bull. No.1026. Washington, DC, USA: USDA Tech.
8. García, M.H. (Ed.) (2008). “Sedimentation Engineering (No. 110): Chapter 2, Sediment Transport and Morphodynamics.” ASCE Publications.
9. Guo, J., Julien, P.Y. (2004). “Efficient algorithm for computing Einstein integrals.” *J. Hydraul. Eng.*, 130 (12), 1198–2001.

10. Guo, J., Wood, W.L. (1995). "Fine suspended sediment transport rates." *J. Hydraul. Eng.*, 121(12), 919–922.
11. Jha, S.K., Bombardelli, F.A. (2009). "Two-phase modeling of turbulence in dilute sediment-laden, open-channel flows." *Environmental Fluid Mechanics*, 9(2), 237-266.
12. Julien, P.Y. (2002). "Erosion and Sedimentation." Cambridge University Press.
13. Keshtpoor, M., Puleo, J.A., Shi, F., Ma, G. (2015). "3D numerical simulation of turbulence and sediment transport within a tidal inlet." *Coastal Engineering*, 96: 13-26.
14. Khosronejad, A., Kang, S., Borazjani, I., Sotiropoulos, F. (2011). "Curvilinear immersed boundary method for simulating coupled flow and bed morphodynamic interactions due to sediment transport phenomena." *Advances in Water Resources*, 34(7), 829-843.
15. Liu, X., Nayamatullah, M. (2014). "Semianalytical Solutions for One-Dimensional Unsteady Nonequilibrium Suspended Sediment Transport in Channels with Arbitrary Eddy Viscosity Distributions and Realistic Boundary Conditions." *J. Hydraul. Eng.*, 140(5), 04014011.
16. MathWorks (2015). "Parallel Computing Toolbox™ User's Guide." Revision Version 6.7.
17. Nakato, T. (1984). "Numerical Integration of Einstein's Integrals, I1 and I2." *J. Hydraul. Eng.*, 110(12), 1863–1868.
18. Papanicolaou, A., Elhakeem, M., Krallis, G., Prakash, S., Edinger, J. (2008). "Sediment Transport Modeling Review-Current and Future Developments." *J. Hydraul. Eng.*, 134(1), 1-14.
19. Press, W.H., Teukolsky, S.A., Vetterling, W.T., Flannery, B.P. (1992). "Numerical Recipes: The art of scientific computing." Cambridge.
20. Shah-Fairbank, S., Julien, P., Baird, D. (2011). "Total Sediment Load from SEMEP Using Depth-Integrated Concentration Measurements." *J. Hydraul. Eng.*, 137(12), 1606-14.

21. Simons, D.B., Li, R.M., Fullerton, W. (1981). "Theoretically derived sediment transport equations for Pima County, Arizona." Prepared for Pima County DOT and Flood Control District, Tucson, AZ, Fort Collins, CO: Simons, Li and Associates.
22. Toffaleti, F.B. (1968). "A Procedure for computation of total river sand discharge and detailed distribution, bed to surface." Technical Report No. 5, Committee on Channel Stabilization, U.S. Army Corps of Engineers.
23. U.S. Army Corps of Engineers (2010). "HEC-RAS River Analysis System Hydraulic Reference Manual." Version 4.1, Public Release.
24. Vanoni, V.A. (Ed.). (2006). "Sedimentation engineering (No. 54)." Reissue, ASCE Publications.
25. Zamani, K., Bombardelli, F.A. (2014). "Analytical solutions of nonlinear and variable-parameter transport equations for verification of numerical solvers." *Environ Fluid Mech.* 14(4), 711-742.
26. Zamani, K., Bombardelli, F.A. (2016). "Novel methods to calculate sediment volumetric flow rate with Einstein's integrals: semi-analytical and numerical approaches." To be submitted to *Journal of Hydraulic Engineering*.

Figures

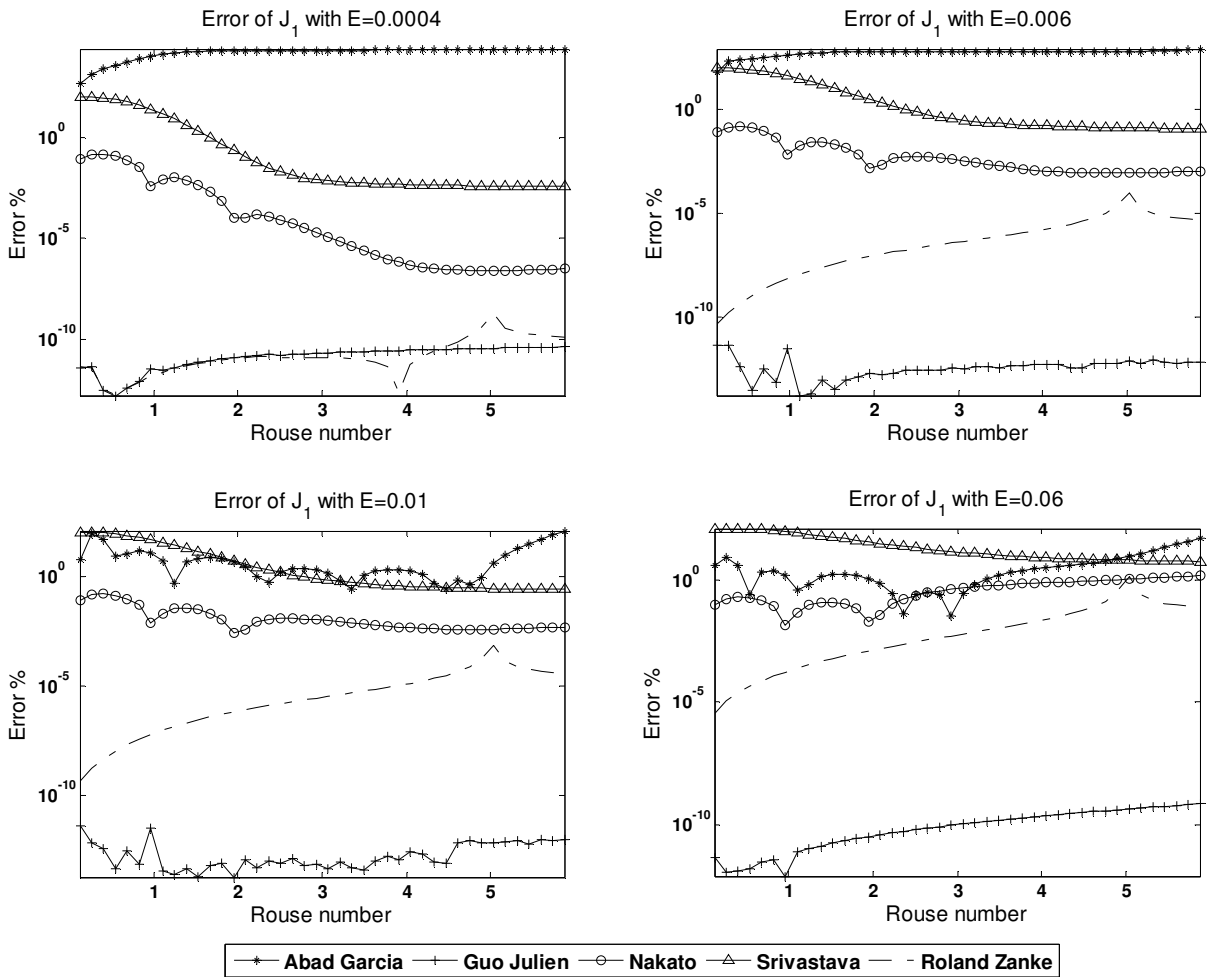


Figure 4-1. Local relative error of five methods for the calculation of the J_1 Einstein integral for different values of bedload-layer thickness, over various Rouse numbers (Guo and Julien's method with 10 terms in the partial sum of Eq. (4-7)).

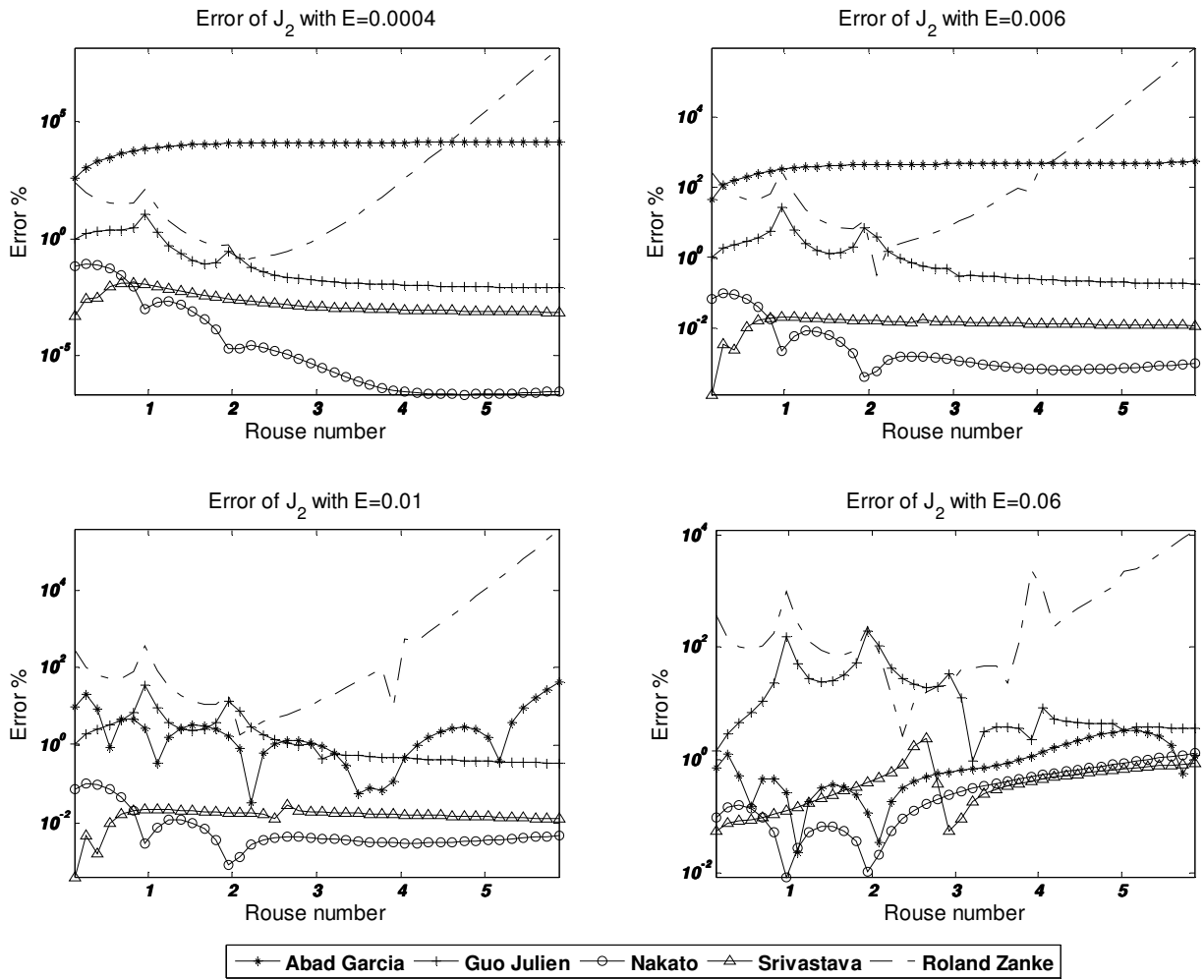


Figure 4-2. Local relative error of five methods for the calculation of the J_2 Einstein integral for different values of bedload-layer thickness, over various Rouse numbers (Guo-Julien's method with Eq. (4-10) closure for the first infinite sum and 50 terms in the second partial sum).

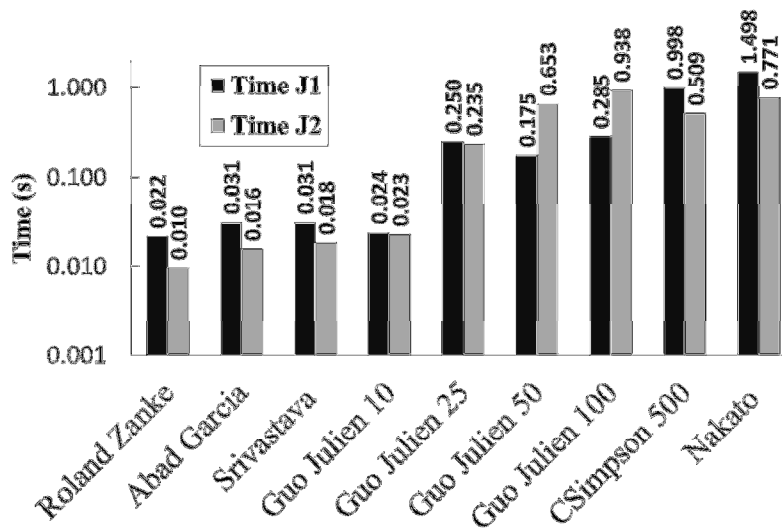


Figure 4-3. CPU time of various methods for computing Einstein’s integrals for a set of 960 pair values of Rouse number and bedload-layer thickness. The number after “Guo Julien” refers to the number of terms in the partial sum of the infinite series (left term in Equation (4-8)).

Composite Simpson method results were obtained with 500 points.

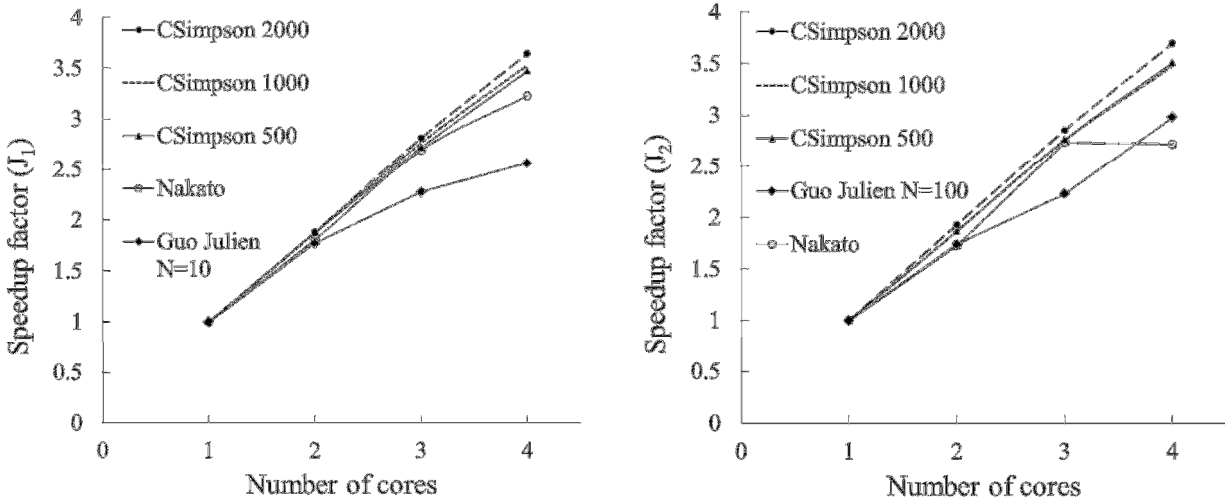


Figure 4-4. Speedup for the parallelization of existing methods for the calculation of Einstein's integrals (left: J_1 and right: J_2 integral). In this case, Guo and Julien's method was executed with Eq. (4-10) closure and the first 100 terms in the partial sum of Eq. (4-8) for computing the J_2 integral. It is worth mentioning that the above curves are computed for a dataset of 9000 Rouse numbers and bedload-layer thicknesses.

Tables

Table 4-1. Global accuracy of existing methods of calculation or approximation of Einstein's integrals (tested over a data set of 960 bedload-layer thicknesses and Rouse numbers).

Measure	Abad and García	Guo and Julien (N=100)	Guo and Julien (N=50)	Guo and Julien (N=25)	Guo and Julien (N=10)	Nakato	Roland and Zanke	Srivastava	Composite Simpson (N=2000)	Composite Simpson (N=500)	
J_1	Bias	2.2101E+5	7.81117E-9	7.81117E-9	7.81117E-9	7.81117E-9	4.50330E+2	-1.24235E+1	1.23151E+4	3.40689E+00	8.09726E+2
	RMSE	5.9352E+6	4.49951E-7	4.49951E-7	4.49951E-7	4.49951E-7	2.93424E+3	4.24792E+1	1.28230E+5	6.37503E+1	1.50814E+4
	Scatter Index	1.7032E+0	1.37863E-13	1.37863E-13	1.37863E-13	1.37863E-13	8.98917E-4	1.30155E-5	3.94381E-2	1.95329E-5	4.61974E-3
	R²	0.9956	1.00	1.00	1.00	1.00	0.9999	1.00	0.9999	1.00	0.9998
J_2	Bias	-1.3602E+5	-6.0262E+4	-6.0262E+4	-6.0261E+4	-6.02612E+4	-1.5019E+3	-3.38259E+10	1.1046E+3	-1.70948E+1	-4.04983E+3
	RMSE	1.1242E+7	7.1140E+5	7.1140E+5	7.1140E+5	7.11400E+5	1.1345E+4	7.16365E+11	2.4658E+4	3.21416E+2	7.57938E+4
	Scatter Index	-8.0043E-1	-5.0921E-2	-5.0922E-2	-5.0922E-2	-5.09226E-2	-8.1554E-4	-2.11693E+1	-1.7728E-3	-2.31069E-5	-5.44731E-3
	R²	0.9978	0.9999	0.9999	0.9999	0.9999	0.9999	0.9246	0.9999	0.9999	0.9999

Table 4-2. Accuracy of the partial sum in the J_2 convergent series approximations with various number of terms (in %).

Approximation		Guo & Julien explicit closure (Eq. (4-10))	Srivastava explicit closure (Eq. (4-17))	Partial sum with 10 terms*	Partial sum with 20 terms*	Partial sum with 50 terms*	Partial sum with 100 terms*	Partial sum with 200 terms*
Error %	$z = 0.5$	0.240178	0.047984	7.574728	3.925805	1.605325	0.808652	0.405838
	$z = 1.5$	0.232877	0.005490	10.422207	5.514373	2.286010	1.157081	0.582129
	$z = 2.5$	0.225064	0.013587	12.702128	6.846634	2.875378	1.462238	0.737437
	$z = 3.5$	0.279809	0.021046	14.623828	8.016032	3.408224	1.741168	0.880210
	$z = 4.5$	0.228926	0.023806	16.290325	9.067205	3.900604	2.001648	1.014284

* Note: number of terms in the partial sum of the left term in Eq. (4-8).

Chapter 5: Novel Methods to Calculate Sediment Volumetric Flow Rate with Einstein's Integrals: Semi-Analytical and Numerical Approaches

5.1. Introduction

The main objective in the assessment of erosion and sedimentation processes in coastal areas, and in river restoration projects, is the computation of the total sediment volumetric flow rate. Those rates can be later used for the computation of changes in bed levels, in order to determine the size of scour holes or the amount of the deposited sediment (see García, 2008; Bombardelli and Moreno, 2012). There are numerous methods to account for total sediment transport in a streamflow; however, they all fall in three main categories. The simplest approach consists in using empirical equations based on the measurement and statistical regression such as Brownlie (1981), and Karim and Kennedy (1983). The second common approach is one in which energy principle is utilized between the rate of work done on the sediment particles in turbulent flow and the rate of energy expenditure. Bagnold (1966), Engelund and Hansen (1972), Yang (1973), and Ackers and White (1973) methods are in this second category. Finally there are formulations based on the conservation of mass, such as methods by Einstein (1950), Colby (1964), and Simons, Li and Fullerton (1981). Among those three categories, some of them consider different particle sizes, e.g., Einstein, (1950) and Toffaleti, (1968); whereas others only account for total sediment discharge, e.g., methods by Engelund and Hansen (1972) or Meyer-Peter and Muller (1948).

Einstein's method is one of the cornerstones of theoretical sediment mechanics (Einstein, 1950) because it allows for the computation of those sediment volumetric flow rates via balance

laws. The method is obtained after integration of *Rouse concentration distribution* and the product of that distribution and the *law of the wall*, over depth (Julien, 2002; García, 2008). The first and second Einstein's integrals (without considering multiplier coefficients) are consequently defined as:

$$J_1(E, z) = \int_E^1 \left(\frac{1-y}{y} \right)^z dy \quad (5-1)$$

$$J_2(E, z) = \int_E^1 \left(\frac{1-y}{y} \right)^z \log(y) dy, \quad (5-2)$$

where E is the relative bedload-layer thickness, y is the dimensionless distance from the bed, and z is the *Rouse number*. Relative bedload-layer thickness is defined as $E = \frac{b}{H}$ where b denotes a location above the bed (usually – in absence of bedforms – $b = 2d_s$ [L] in which d_s is particle diameter); H [L] is the water depth; $E \in (10^{-5}, 10^{-1})$ $\left[\frac{L}{L} \right]$ Guo and Julien (Abad, et al. 2006; García, 2008); $y \in (E, 1)$ $\left[\frac{L}{L} \right]$. In turn, the Rouse dimensionless number is defined as $z = \frac{w_s}{\beta \kappa U_*}$, where w_s $\left[\frac{L}{T} \right]$ is the particle settling velocity, β [–] is a measure of the turbulent Schmidt number (ratio of sediment diffusion coefficient to kinematic eddy viscosity), κ [–] is von Kármán constant and U_* $\left[\frac{L}{T} \right]$ is the shear velocity. In the above integrals $z \in (0.1, 6)$, as Rouse numbers larger than six correspond to little or no motion of particles (Julien, 2002; Vanoni, 2006; García, 2008; Bombardelli and Jha, 2009) and Rouse numbers below 0.1 is considered as washload (Julien, 2002; Vanoni, 2006; García, 2008). The above-mentioned integrals need to be solved either in each time step or sub-stepping cycle of 1-D and 2-D depth-averaged sediment-transport numerical packages for each particle size class (Zamani et al., 2016).

The above-mentioned integrals do not have closed-form analytical solution in terms of elementary functions, except for integer values of z (Table 5-A1 in Appendix). Although from

the continuum mechanics viewpoint the derivation of Einstein's integrals is more robust as compared to two other treatments of the same problem – empirical formulas and equations based on conservation of energy (Guo and Julien 2004; Vanoni, 2006; Shah-Fairbank et al., 2011). Einstein method is not widely used in sediment-transport software as computing of the J_1 and J_2 integrals is challenging (Shah-Fairbank et al., 2011). For example the HEC package does not include Einstein's method for computing sediment discharge (U.S. Army Corps of Engineers, 2010), while it uses a simplified version of this method suggested by Toffaleti (1968).

To include Einstein method in sediment transport packages, several methods have been used to calculate J_1 and J_2 integrals, from retrieving values from a pre-calculated monograms (Einstein 1950; Vanoni, 2006), to regression-based formula (Abad and García in Abad et al. 2006; García, 2008); to closed-form solution based on *beta function* (Guo and Wood, 1995); to series-based solution (Guo and Julien, 2004; Roland and Zanke, (Abad et al., 2006); Srivastava, (Abad et al., 2006)); and to numerical integration (Nakato, 1984). The work of Zamani et al. (2016) on the former methods of computing Einstein integrals revealed that there were issues of zones of slow convergence, local singularity, and dissimilarity of convergence and asymptotic behavior of infinite series that have been overlooked in some of the above-mentioned studies.

Figure 5-1 shows a section-view schematic of riverine sediment and velocity distribution in depth. Sediment particles above bedload-layer thickness ($a < h \leq H$) are treated as suspended load and particles rolling, sliding or saltating below that level ($0 < h \leq a$) are known as bedload. The distribution of suspended sediment in depth is governed through the Rouse concentration profile. Based on Rousean distribution, Einstein, in his classic 1950 monograph, assumed von Karman-Prandtl logarithmic law for velocity and derived the total sediments discharge solely based on balance laws:

$$q_t = \sum_{size\ i} q_{t_i} \quad (5-3)$$

$$q_{t_i} = q_{b_i} + q_{s_i} = q_{b_i} + \int_{a_i}^H u(h)c_i(h)dh \quad (5-4a)$$

$$q_{t_i} = q_{b_i} + \int_{a_i}^H c_{\delta_i} \frac{U_*}{\kappa} \left[\frac{H-h}{h} \frac{a_i}{H-a_i} \right]^{z_i} \log \frac{30h}{d_{s_i}} dh = q_{b_i} \left[1 + J_{1i} \log \left(\frac{30H}{d_{s_i}} \right) + J_{2i} \right] \frac{0.216a_i^{z_i-1}}{(1-a_i)^z} \quad (5-4b)$$

in which $q_{t_i} \left[\frac{M}{TL^2} \right]$ is the sediment discharge of size class i , $c_{\delta} \left[\frac{M}{L^3} \right]$ is sediment concentration at the bedload-layer reference level a (Figure 5-1), $u(h) \left[\frac{L}{T} \right]$ is channel-wise velocity as a function of depth h [L], $c(h) \left[\frac{M}{L^3} \right]$ is concentration of sediment in depth h , subscript i refers to sediment size class, and the rest of parameters are defined beforehand.

Once the total sediment-transport load computed – via Einstein’s method – those values can be used for the solution of Exner equation in 1-D, 2-D, and quasi-2D sediment-transport codes (García, 2008). Although Einstein method is the most advanced in terms of theoretical rigor (Guo and Julien, 2004; García, 2008; Zamani et al. 2016), it is not implemented in common engineering sediment transport packages until recently (for example: Abad et al. 2008; Shah-Fairbank et al., 2011), whereas energy-based methods such as the ones suggested by Ackers and White (1973) and Yang (1973) have been commonly used in sediment-transport packages for decades (García, 2008).

This paper devises and tests four new methods for calculation of the Einstein’s integrals. First, in the next section, we employ a Gauss-Kronrod adaptive integration technique for Einstein’s integrals. Second, we provide a numerical trick to increase the efficiency of Einstein’s integrals via recycling computed values from numerical integrational of one integral and using it in another. Third, in section three, we use asymptotic series to approximate Einstein’s integrals. In section four we assess semi-analytical solutions based on special-functions for tackling Einstein’s integrals. In section five we discuss the efficiency of those methods in parallel

computing, and we finish the paper with discussion of the results and conclusions in sections six and seven.

5.2. New Numerical Schemes for Integration of J_1 and J_2

Among the existing methods for the Einstein's integrals, there are not many *numerical solutions* of the Einstein's integrals except Nakato (1984), who used the Simpson's integration rule. Zamani et al. (2016) stated that even with 1000 points, the error of composite Simpson's rule is still significant as their detailed analysis reveals that with composite Simpson rule, the leading order of error scales with the product of the fourth power of discretization size and gradient of integrand function (Press et al., 1992; Zamani et al., 2016). We delved in to the methods of improvement the numerical integration procedure for the problems. In that line, plotting the J_1 and J_2 integrands versus depth on semi-logarithmic scale as in Figure 5-2, reveals that sharp changes happen near the bed. Nakato (1984) recognized and devised his solution method according to this fact. The issue of sharp gradients is however more serious for coarser sediment particles, as changes can be as high as eight orders of magnitude in Rouse numbers close to 5. That explains why the accuracy of classical numerical integration methods (such as composite Simpson) for equally-spaced abscissae was slowly increased with adding to the number of discretization points. To overcome the shortcoming of those integration methods we resort to "adaptive quadrature" method for integration, to locally refine the mesh size as needed.

5.2.1 Gauss-Kronrod quadrature

In general, adaptive numerical integration refers to procedures of numerical approximation of an integral to a pre-specified precision by "adaptively" refining the integration

intervals. There are several methods for adaptive integration (see Gonnet, 2012); the pseudo-code of most commonly used one – which we employed in this study – is given below:

Algorithm 5-1: Recursive adaptive integration of function $f(x)$ with tolerance ε_0 on $[a, b]$

```

integrate ( $f, a, b, \varepsilon_0$ )
1:  $Q_n[a, b] \approx \int_a^b f(x)dx$ 
2:  $\varepsilon \approx \left| Q_n[a, b] - \int_a^b f(x)dx \right|$ 
3: if  $\varepsilon \leq \varepsilon_0$ 
    return  $Q_n[a, b]$ 
   else
     $m \leftarrow \frac{a+b}{2}$ 
    return integrate ( $f, a, m, \varepsilon_0$ ) + integrate ( $f, m, b, \varepsilon_0$ )
   end if

```

In algorithm 5-1, $Q_n[a, b]$ refers to an approximation of the integral of function $f(x)$ with a numerical method over n points from the lower limit a to upper limit b . ε is the *global* measure of error in the method that might be calculated with linear or nonlinear combination of function values in the integral. In turn, ε_0 is the pre-defined tolerance for global error in numerical integration.

Gauss quadrature is an extension of Newton-Cotes type of numerical integration to non-equally-spaced points in order to obtain higher accuracy with evaluation of the integrand function on identical number of points (Press et al., 1992). The quadrature rule for approximation of integration of function $f(x)$ on $x \in [a, b]$ is stated as:

$$Q_n[a, b] = \int_a^b f(x)dx \approx \frac{b-a}{2} \sum_{i=1}^n w_i f\left(\frac{1}{2}((b-a)t_i + a + b)\right) \quad (5-5)$$

where w_i is the weight function corresponding to the abscissa t_i on the interval $t \in [-1, 1]$ which is the transformation of the original integration interval $x \in [a, b]$ chosen based on *Legendre polynomials*.

Motivated by an analogous idea as the Runge-Kutta-Fehlberg method for numerical integration of ODEs (e.g. Press et al., 1992), Piessens et al. (1983) suggested embedded linear error estimation based on the difference between two numerical approximations with quadrature of degrees n_1 (Gauss points) and $n_2 = 2n_1 + 1$ (Kronrod points) as follows:

$$\varepsilon \sim |Q_{n_1}[a, b] - Q_{n_2}[a, b]| \quad (5-6)$$

Herein, abscissae are chosen such that the Gauss points are incorporated in the Kronrod points; consequently, $Q_{n_1}[a, b]$ and $Q_{n_2}[a, b]$ are calculated with only n_2 evaluations of the integrand function $f(x)$. Specifically a local error estimation based on the work by Piessens et al. (1983) was used:

$$\varepsilon = \min \left\{ 1, (200 |Q_{n_1}[a, b] - Q_{n_2}[a, b]|)^{\frac{3}{2}} \right\} \quad (5-7)$$

It is worth mentioning that our method was adapted from the algorithm of QUADPACK mathematical library (Piessens et al., 1983). Quadrature's abscissae and weight factors for Q_{n_1} and Q_{n_2} which were employed in this work are provided in Table 5-A2 (Appendix). Figure 5-3 shows the Einstein's integrals which were calculated by Gauss-Kronrod method with $n_1 = 7$, $n_2 = 15$, and $\varepsilon_0 = 10^{-6}$, other runs with lower global error tolerance level were conducted and the results are exactly similar. The computational time of this method is very small, and it is comparable with series-based methods (Guo and Julien, 2004; Zamani et al., 2016); however, in the GK quadrature method's accuracy can be pre-defined as opposed to the existing methods of calculation of the Einstein's integral.

5.2.2. Expedite calculation via recycling the evaluated integrand

As may be readily noticed, integrands in Eqs (5-1) and (5-2) are rather similar, with J_2 having an extra factor, $\log y$, compared to J_1 . In this section, we explore the possibility of taking

advantage of the similarity between the two integrands in order to arrive at a method that accelerates the computational procedure. Since significant computational burden of any numerical integration method – regardless of being varying or fixed abscissae – is always the evolution of the integrand (Press et al., 1992), we recycle the values of the integrand function evaluations in the computation of one integral, and reuse it for the calculation of the second integral, to save computational time. This numerical trick was implemented for both composite Simpson’s rule and GK quadrature.

A comprehensive dataset of 32 Rouse numbers and 30 bedload-layer thicknesses was used to evaluate the speedup efficiency with the retrieving integrand function numerical method. Table 5-1 shows the relative savings in CPU time after implementation of the above-mentioned integrand-retrieving trick compared to the computation via the original composite Simpson and Gauss-Kronrod numerical integrations. The integrand retrieving procedure, in fixed-abscissae methods (e.g. composite Simpson), only boils down to a single extra vector operation, which is computationally very affordable. However, in varying-abscissae methods (e.g. Gauss-Kronrod quadrature), the method has to compensate for additional overhead operations to keep the record of the varying bases of integration.

As Table 5-1 demonstrates, in the case of retrieving the integrand function of J_2 to calculate J_1 with composite Simpson rule, we would save 13-26% of the calculation time. In the case of retrieving the integrand function of J_1 to calculate J_2 with composite Simpson rule we have a welcomed improved efficiency (29-35%).

It is worth mentioning that the similar technique was implemented for the Gauss-Kronrod adaptive quadrature; however, the results were not satisfactory. The reason is as follows: In the first case – recycling J_2 results for calculation the J_1 integral – although there was a slight

improvement in the computational time (approximately 6%), the calculated results did not meet the predefined accuracy ε_0 . And in the other case, employing J_1 values for calculation J_2 integral with GK 7-15 quadrature method, the computational overhead of book-keeping of varying Gauss-points' not only counter balance the saved time due to vectorized multiplication of “ $\log y$ ” values, but also surpasses the initial time of calculation of the integrand from scratch. Therefore, we simply conclude for the Einstein's integrals, in the case of Gauss Kronrod 7-15 method, the integrand function retrieving technique is not useful for efficiency improvement.

5.3. Approximation via Asymptotic Expansion

Perturbation techniques and asymptotic series are approximate mathematical-physics methods to find a *local* estimation of solution in the absence of exact solution in terms of familiar functions (Bender and Orszag, 1999). There have been several attempts to use perturbation theory techniques to approximate Einstein's integrals in the past. Nakato (1984) utilized integration by parts to derive an expansion of the sharp-varying part of Einstein's integrals; however, he did not conduct his mathematical analysis for the entire integration region. Later on, an elementary expansion of the J_2 integrand was tried by Guo and Wood (1995), however, the range of Rouse numbers they used did not cover the entire physical spectrum. Also such authors neglected the bedload-layer thickness in their integral's degeneration via elementary expansion. Given those restrictions, in this section we present an appropriate series approximation for Einstein's integrals using the virtue of perturbation theory. We wanted to find an asymptotic series which is convergent for a wide range of bedload-layer thicknesses and Rouse numbers. For the sake of the physical point of view, we assume perturbation quantities (z, E) are real and positive.

We explored the Maclaurin series expansion of the J_1 and J_2 integrals considering different truncation points, i.e. one term, two terms, ..., five terms (Bender and Orszag, 1999). Near-bed expansion of Einstein's integrals – up to six terms – is given in the Appendix A4. Figures 5-4 and 5-5 show the percentage of the series approximations' error compared to a machine precision accurate result, which is obtained with GK quadrature with $\varepsilon_0 = 10^{-14}$, computed by series expansion of the J_1 and J_2 integrals, for four different bedload-layer thicknesses over the feasible range of Rouse numbers ($0.1 < z < 6$). It can be seen that none of the expansions provide acceptable results for $z < 2.5$. Still, in the case of $2.5 < z$ with only two-term-truncated series, accurate results are obtainable with error below one percent. Also both Figures 5-4 and 5-5 show the error generally rises as bedload-layer thickness is increased. Furthermore, a closer look at those figures indicates that there is not a substantial increase in accuracy for expansions with more than two terms. Therefore, based on the error analysis for different number of terms in the expansion, we suggest the following formula for approximation of Einstein's integrals:

$$J_1(z, E) \approx \left\{ \left(-1 + \frac{1}{y} \right)^z \left[-\frac{y}{-1+z} + \frac{zy^2}{(-2+z)(-1+z)} \right] \right\}_{y=E}^{y=1} + O(y^3) \quad (5-8)$$

$$J_2(z, E) \approx \left\{ \left(-1 + \frac{1}{y} \right)^z \left[\frac{(-1+\log y - z \log y)y}{(-1+z)^2} + \frac{(-3z+2z^2+2z \log y - 3z^2 \log y + z^3 \log y)y^2}{(-2+z)^2(-1+z)^2} \right] \right\}_{y=E}^{y=1} + O(y^3) \quad (5-9)$$

Notice that both Einstein's integrals have closed-form analytical solution in integer Rouse numbers so the problem of singularity in integer z values in Eqs. (5-8) and (5-9) can be avoided (Table 5-A1 in Appendix).

Figure 5-6 shows the values of J_1 and J_2 integrals which are computed by two-term series expansion of the corresponding integral, Eqs. (5-8) and (5-9). As mentioned above, in both cases the values are acceptable in the Rouse numbers corresponding to coarse particles.

5.4. Semi-Analytical Solution by Hypergeometric Functions

Apart from various mathematical applications, hypergeometric special functions have been widely utilized in applied physics (Slater, 1966). Generalized hypergeometric function “ ${}_pF_q$ ” is defined as (Abramowitz and Stegun, 1965; Zwillinger, 2014):

$${}_pF_q(a_1, \dots, a_p; b_1, \dots, b_q; x) = \sum_{n=0}^{\infty} \frac{(a_1)_n \dots (a_p)_n x^n}{(b_1)_n \dots (b_q)_n n!} \quad (5-10a)$$

in which $a_i, b_i, x \in \mathbb{C}$ (complex variables), and the radius of convergence is $|x| < 1$. In Eq. (5-10a) $(a_p)_n$ refers to the notation of *Pochhammer symbol*, which is defined as (Slater, 1966; Zhang and Jin, 1996):

$$(a_p)_n = a_p(a_p + 1) \dots (a_p + n - 1) \quad (5-10b)$$

Among hypergeometric functions, ${}_2F_1$ is known as Gauss hypergeometric function and it appears widely in mathematical physics (Zwillinger, 2014). Gauss hypergeometric function is defined as:

$${}_2F_1(a, b; c; x) = 1 + \frac{ab}{c \times 1} x + \frac{a(a+1)b(b+1)}{c(c+1) \times 1 \times 2} x^2 + \frac{a(a+1)(a+2)b(b+1)(b+2)}{c(c+1) \times 1 \times 2 \times 3} x^3 + \dots \quad (5-11)$$

As it has been stated by A.R. Kacimov (Abad et al., 2006), an alternative approach to tackle Einstein’s integrals is through hypergeometric functions. The analytical solutions of the J_1 and J_2 integrals in terms of hypergeometric functions are as follows (solution can be obtained by Maple and MATHEMATICA):

$$J_1 = \int \left(\frac{1-y}{y}\right)^z dy = \frac{y^{1-z}}{1-z} {}_2F_1(1-z, -z; 2-z; y) \quad (5-12)$$

$$J_2 = \int \left(\frac{1-y}{y}\right)^z \log y dy = -\frac{y^{1-z}}{(1-z)^2} [z {}_3F_2(1-z, 1-z, 1-z; 2-z, 2-z; y) + (z-1)(\log y - 1) {}_2F_1(1-z, -z; 2-z; y)] \quad (5-13)$$

Although those analytical solutions seem like a great step forward, the above special functions need numerical evaluation. Thus we prefer to name Eqs. (5-12) and (5-13) “semi-analytical” solutions of Einstein’s integrals. There are still some difficulties: methods for numerically evaluating hypergeometric functions are not highly advanced to date (Zhang and Jin, 1996), with exception of Confluent $({}_1F_1)$ and Gauss $({}_2F_1)$ hypergeometric functions, since those functions have commonly appeared in computational physics (Slater, 1966; Zhang and Jin, 1996). In addition, those numerical methods are not always stable, even if they are employed in convergence range of parameters of the function (Zhang and Jin, 1996; Michel and Stoitsov, 2008; Pearson et al., 2014). The final drawback of using hypergeometric functions is that those numerical methods are generally too slow, unless they were specifically designed/manipulated with prior information about the parameters and argument (Zhang and Jin, 1996; Pearson et al., 2014).

5.4.1. Manipulation of the hypergeometric function solution

First consider the fact that value of any hypergeometric function – regardless of its parameters – are equal to one when its argument is zero:

$${}_pF_q(a_1, \dots, a_p; b_1, \dots, b_q; 0) = 1 \quad (5-14)$$

Therefore, we take advantage of this property and reform the Einstein’s integrals with elementary algebra to transform one of the limits to zero, to reduce the computational cost by a factor of two. We introduce the change of variable $t = 1 - y$ in Eqs. (5-1) and (5-2) and rework those equations:

$$J_1 = \int_0^{1-E} \left(\frac{t}{1-t} \right)^z dt \quad (5-15)$$

$$J_2 = \int_0^{1-E} \left(\frac{t}{1-t}\right)^z \log(1-t) dt \quad (5-16)$$

Eq. (15) has a closed-form analytical solution based on the Gauss hypergeometric function:

$$J_1(E, z) = \frac{(1-E)^{z+1}}{z+1} {}_2F_1(z, z+1; z+2; 1-E) \quad (5-17)$$

In turn, as two times numerical evaluation of ${}_3F_2$ in Eq. (5-13) is computationally expensive, we resort to perturbation theory to rework Eq. (5-16) into a more convenient form.

Since $0 < t < 1 - E$, we can expand $\log(1 - t)$ around zero:

$$\log(1 - t) = -t - \frac{t^2}{2} - \frac{t^3}{3} - \frac{t^4}{4} - \dots \quad (5-18)$$

Then Eq. (5-16) becomes:

$$J_2 = \int_0^{1-E} \left(\frac{t}{1-t}\right)^z \left(-t - \frac{t^2}{2} - \frac{t^3}{3} - \frac{t^4}{4} - \dots\right) dt \quad (5-19)$$

which leads us to a series-based analytical solution as:

$$J_2(E, z) = -\sum_{n=1}^{\infty} \left(\frac{(1-E)^{1+n+z}}{n(1+n+z)} {}_2F_1(z, z+n+1; z+n+2; 1-E)\right) \quad (5-20)$$

For two reasons the right hand side infinite series of Eq. (5-20) demonstrates an asymptotic behavior. Firstly, as both z and n are positive numbers and $z < z + n + 2$ and $z + n + 1 < z + n + 2$, we can conclude that as n becomes large, the Gauss hypergeometric function in the Eq. (5-20) can be approximated by considering only the first m terms of the series

with truncation error of $O\left(\left(\frac{1}{z+n+2}\right)^{-(m+1)}\right)$, (see Abramowitz and Stegun, 1965; page 565,

equation 15.7.1). Secondly, given that $\delta = 1 - E < 1$, as n increases, the coefficient $\frac{(1-E)^{1+n+z}}{n(1+n+z)}$

could be scaled with $\frac{\delta^n}{n^2}$, which rapidly approaches toward zero. Therefore, it is safe to assume

Eq. (5-20) shows an asymptotic behavior and to consider its partial sum instead of the infinite series. Still, we expect slow convergence for coarse particles.

5.4.2. Approximation based on hypergeometric function

At this point, we have to find a numerical scheme to evaluate Gauss hypergeometric function with real values of parameters and argument to use Eqs. (5-17) and (5-20) for our problem. The Appendix A.5 will provide two numerical methods to that end. The third numerical method we used in this paper for computing Einstein's integrals through Eq. (5-17) and (5-20) was a subroutine which was developed by Jin (2015) from a numerical computation library of special functions.

Figure (5-7) shows Einstein's integrals which are calculated via formula of Eqs. (5-17) and (5-20) and Taylor series expansion of Eq. (5-A7). Figure (5-8) shows Einstein's integrals which are calculated via formula of Eqs. (5-17) and (5-20) and the hypergeometric function special solver by Jin (2015). As seen, both methods have excellent agreement with the results of composite Simpson method with dense mesh (10000 nodes) in the case of high bedload-layer thickness; however, the accuracy of the results is reduced when it comes to smaller values of E . The J_2 integral results error is relatively larger compared to J_1 integral.

Quantitative comparisons of those semi-analytical methods and all other methods which we developed in this paper are given in Table 5-2. That is to mention the statistics of Table 5-2 are computed for a dataset of 960 pairs (32 Rouse numbers and 30 bedload-layer thicknesses) to uncover any local/global flaws in the methods. In Table 5-2, columns six to eight display the metrics that account for both composite Simpson's methods of recycling J_2 integration values from J_1 and vice-versa.

5.5. Efficiency of Parallelization of New Algorithms

Given that in real rivers and estuaries there are various particle sizes, an “ideal” sediment-transport packages has to carry out the functionality of simulating multi-fraction of particles to reproduce non-uniformity in the particle sizes in nature (Khosronejad et al., 2011; Keshtpoor et al., 2015; Zamani et al., 2016). Thus, we consider employing parallel computation of Einstein’s integrals. In this study we used shared-memory simulation for distributing computation based on particle size on different computational cores.

We employ the PCT toolbox of MATLAB to execute computations on a multicores desktop (MathWorks, 2015). Among various opinions, we used *parfor* loops for parallelism to distribute grain sizes computations on multi-processors. A machine with *Intel i7-2670QM*, four-core processor and 8 GB memory was used to benchmark the parallel efficiency of the new methods. In this study, we run a dataset of 10,000 pairs of (E, z) on one, two, three and four CPUs and assessed computational time improvement on multi-core, compared with the sequential run of same dataset on a single CPU. Table 5-3 shows the rate of efficiency improvement via parallel computing of GK-quadrature, recycling method with composite Simpson’s rule and Maclaurin series expansion. It is worth to mention here that, we did not consider the methods based on Gauss hypergeometric functions for parallel computing, due to their enormous computational burden and relative low accuracy.

Table 5-3 shows the efficiency of adaptive Gauss-Kronrod, composite Simpson and series expansion on parallel platforms. It can be noticed that although series expansion is very efficient in sequential computing, it not only does not become more efficient in parallel computing, but also it performs less efficiently due to the overhead of distributing over multicores. The efficiency of series based method remains almost the same for two cores and

thereafter it reduces as number of cores increases to three and four. The other two methods – GK quadrature and composite Simpson – both perform well in parallelization as both have linear speedup as the number of cores increases. Still, composite Simpson integration to some extent over-performs in parallelization compared to adaptive GK quadrature.

5.6. Discussion of New Methods

The four new approaches were tested against a full dataset of all feasible Rouse numbers and bedload-layer reference depths. Figure 5-9 shows the comparison of computation time of different methods which are benchmarked on a machine with Intel® Core™ i7-2670QM Processor and 8 GB of RAM. Considering the statistical measures of goodness-of-fit, which are given in Table 5-2 and computational time of methods – Figure 5-9 – we can extract the following lessons.

Maclaurin series expansion of Einstein’s integrals – Eqs. (5-8) and (5-9) – is the fastest method. The speed of this method is well comparable to explicit methods by Abad-García, Roland-Zanke, and Srivastava (Zamani et al., 2016). Series expansion method has relatively accurate results for Rouse numbers higher than 2.5, in particular this method provides close to exact values for the J_2 integral in high Rouse numbers. In the J_1 integral series expansion including more than the first two terms would not reduce the error. Similarly, in the J_2 integral’s series expansion best accuracy is reached with two terms. In addition, Figures 5-4 and 5-5 shows that those series expansions tend to provide more accurate results in lower bedload-layer thicknesses (which is intuitive since the expansion was performed about the bed). It is relevant to mention that the statistical measures of error in series expansion of J_2 integrals is better than composite Simpson method with 2000 nodes or GK 7-15 with $\varepsilon_0 = 10^{-6}$ (Table 5-2). Also

Table 5-2 shows that computation of J_1 integral with two-term series expansion is comparable with composite Simpson's method in measures of error, while this series expansion is executed orders of magnitude faster than the composite Simpson's method.

Besides series expansions, we used a numerical trick to increase the efficiency of numerical integration via saving the evaluated integrand function of one of the Einstein's integrals and recycle it for the second one. This technique did not improve computation time in the GK quadrature due to the extra overhead prompted by book-keeping of changing integration nodes. Conversely, this technique was very fruitful for fixed abscissae integration methods (composite Simpson rule). In retrieving the J_1 integral from J_2 integral values via vectorized dividing, we gained $\sim 25\%$ speedup without any compromising in accuracy (Table 5-1). The second case, retrieving J_2 integral from J_1 values via vectore multiplication, yielded even better results, it saves $\sim 30 - 35\%$ of computing time. It is worth mentioning that composite Simpson rule is not the best method for Einstein's integrals due to sharply varying nature of the integrand functions. The results of composite Simpson integration with 2000 node was still less accurate than GK quadrature with $\varepsilon = 10^{-6}$, while it took 50% more CPU time (Table 5-2 and Figure 5-9). Our further investigation revealed with 6000 nodes, composite Simpson rule would be able to produce the accuracy of adaptive GK quadrature with error tolerance of $\varepsilon_0 = 10^{-6}$, which proves superiority of adaptive integration method in comparison with fixed-abscissa methods.

The third new method we used herein was adaptive Gauss-Kronrod quadrature. This method has an inner accuracy-based switch which locally refines the discretization size to meet pre-defined tolerable error. Due to the nature of Einstein's integrals this method provided very accurate results, way more accurate than other methods (Table 5-2). In computing J_1 integrals, GK quadrature results' RMSE were nine orders of magnitude less than composite Simpson's

method, with same execution time (GK with $\varepsilon_0 = 10^{-6}$ and composite Simpson with $N = 1000$). The similar comparison for J_2 integral shows that composite Simpson with $N = 1000$ had five orders of magnitude larger RMSE than GK quadrature.

Finally, based on the former statements of Kacimov and Guo-Julien (Abad et al., 2006), we tried to numerically evaluate the analytical solutions of Einstein's integrals which are in the form of hypergeometric special functions. We reorganized the integral limits via change of the variable to reduce the computational costs. Then we used three different methods; Eqs. (5-A6) and (5-A7), and a library of special functions by Jin (2015). Those methods had stability problems in particular in cases of low bedload-layer thicknesses. The solution with Gauss hypergeometric function took too many terms to converge and in some cases the truncated series has a large error compared to the machine precision result. We also tried the use embedded hypergeometric solvers of MATLAB and MATHEMATICA packages; however, those solvers were extremely slow for our purpose. Therefore, we tend to believe semi-analytical solutions with hypergeometric functions should not be used for computation of Einstein's integrals, unless a robust and fast algorithm for real-value parameters is devised.

As a final point, we studied the performance of GK quadrature, composite Simpson's rule and series-based expansion in parallel processing. The best efficiency was reached by composite Simpson rule which approximately obtained 1.94, 2.86, and 3.70 for 2, 3, and 4 cores. The speedup factor of adaptive Gauss-Kronrod method was slightly lower than the composite Simpson's method with $\sim 1.93, 2.74, 3.44$ for 2, 3, and 4 cores respectively. On the other hand, while asymptotic series expansion runs very fast in sequential processing, its overhead of distribution over multiprocessors is high. Thus the parallelization of asymptotic series expansion

of the Einstein's integrals reduces the computational speed. Next section recaps all of our investigations about new efficient algorithms for calculation of Einstein's integrals.

5.7. Summary and Conclusions

This paper devised four new methods for approximation of the J_1 and J_2 integrals. The first method we used was mesh-adaptive numerical integration with Gauss-Kronrod quadrature rule. Then we employed a numerical technique to retrieve one of the Einstein's integrals from the recycling of already computed values in the second one, to abridge the computational time. This method was effective with the composite Simpson integration technique; however, application of similar strategy for GK quadrature was not satisfactory. Later on, we employed a Maclaurin series expansion to find a fast, asymptotic series-based solution for Einstein's integrals. Results were astonishingly fast and accurate for heavy particles, but the error for smaller particles was significant. At the end, we investigated various hypergeometric solvers to approximate Einstein's integrals via semi-analytical solutions based on hypergeometric functions. The results were very slow (and in some cases inaccurate) especially for finer particles and low values of E . All newly developed methods have been rigorously validated with statistical metrics of validation over a full dataset of admissible Rouse numbers and bedload-layer thicknesses.

All in all, we first suggest Gauss Kronrod adaptive integration as it is fast and efficient in parallelization. In addition, as global error in this method is set by the user and never exceeds the pre-defined values, the accuracy of this method is completely controlled. This method is a perfect tool for the higher accuracy with affordable computational time which is well comparable to Guo and Julien's (Guo and Julien, 2004) method with 50 terms. In addition, GK method has a linear speedup which is slightly below to ideal, for multiprocessor computing. The second

possibility is using GK quadrature for finer particles ($z < 2.5$) and change gear to Maclaurin series expansion with two first terms for the J_1 and J_2 integrals for coarser particles ($2.5 < z$). Then we can take advantage of high speed of series expansion without compromising the accuracy. As the methods we developed in this paper were comprehensively verified via various model skill assessment metrics, implementation of them in a sediment-transport package and validation against real-world measured data would be the future path of this research.

Appendices of Chapter 5

5-A. Analytical solutions of Einstein's integrals in integer Rouse numbers

Table 5-A1. Analytical solutions of Einstein's integrals in integer Rouse numbers.

Rouse number	$J_1(E)$	$J_2(E)$
$z = 1$	$-1 + E - \log E$	$1 - E + E \log E - \frac{\log^2 E}{2}$
$z = 2$	$\frac{1}{E} - E + 2 \log E$	$-2 + \frac{1}{E} + E + \frac{\log E}{E} - E \log E + \log^2 E$
$z = 3$	$\frac{3}{2} + \frac{1}{2E^2} - \frac{3}{E} + E - 3 \log E$	$\frac{15}{4} + \frac{1 - 12E - 4E^3 + 2(1 - 6E + 2E^3) \log E - 6E^2 \log^2 E}{4E^2}$
$z = 4$	$-\frac{10}{3} + \frac{1}{3E^3} - \frac{2}{E^2} + \frac{6}{E} - E$ $+ 4 \log E$	$-\frac{55}{9} + \frac{1}{9E^3} - \frac{1}{E^2} + \frac{6}{E} + E + 2 \log^2 E$ $-\frac{(-1 + 6E - 18E^2 + 3E^4)}{3E^3} \log E$
$z = 5$	$\frac{65}{12} + \frac{1}{4E^4} - \frac{5}{3E^2} + \frac{5}{E^2}$ $-\frac{10}{E} + E - 5 \log E$	$\frac{1295}{144} + \frac{9 - 80E + 360E^2 - 1440E^3 - 144E^5 - 360E^4 \log^2 E}{144E^4}$ $+\frac{12(3 - 20E + 60E^2 - 120E^3 + 12E^5)}{144E^4} \log E$
$z = 6$	$-\frac{77}{10} + \frac{1}{5E^5} - \frac{3}{2E^4} + \frac{5}{E^3}$ $-\frac{10}{E^2} + \frac{15}{E} - E + 6 \log E$	$-\frac{7399}{600} + \frac{1}{25E^5} - \frac{3}{8E^4} + \frac{5}{3E^3} - \frac{5}{E^2} + \frac{15}{E} + E$ $-\frac{(-2 + 15E - 50E + 100E^3 - 150E^4 + 10E^6)}{10E^5} \log E + 3 \log^2 E$

5-B. Quantitative measures of method adequacy

Four common indices of model skill assessment are used in this study to provide quantitative bases for comparison of various methods of computation/approximation of Einstein's integrals. Bias (equation 5-A1) is a measure to define over/under prediction of a method. Root Mean Square of Error (RMSE) is a measure of misfit (equation 5-A2). In turn,

Scatter Index (SI) is a dimensionless measure of misfit of model and benchmark values (equation 5-A3). Finally, Coefficient of Determination “R²” (equation 5-A4) is a widely used statistics to depict how close the model fitted the benchmark values (Zamani and Bombardelli, 2014).

$$\text{Bias} := \frac{1}{N} \sum_{i=1}^N (M_i - B_i) \quad (5-A1)$$

$$\text{RMSE} := \sqrt{\frac{1}{N} \sum_{i=1}^N (M_i - B_i)^2} \quad (5-A2)$$

$$\text{SI} := \frac{\sqrt{\frac{1}{N} \sum_{i=1}^N (M_i - B_i)^2}}{\frac{1}{N} \sum_{i=1}^N M_i} \quad (5-A3)$$

$$R^2 := 1 - \frac{\sum_{i=1}^N (M_i - B_i)^2}{\sum_{i=1}^N (M_i - \bar{M})^2} \quad (5-A4)$$

In which, M denotes model results, B referrers to benchmark values, and N is the number of observations.

5-C. Coefficients of Gauss-Kronrod method

Table 5-A2. Weights of Gauss-Kronrod (7-15) abscissae.

Gauss Node ($\pm x_i$)	Gauss Weight (w_i)	Kronrod Node ($\pm x_i$)	Kronrod Weight (w_i)
0	0.4179591836734693877551020	0	0.2094821410847278280129992
		0.2077849550078984676007	0.2044329400752988924141620
0.4058451513773971669066064	0.3818300505051189449503698	0.4058451513773971669066064	0.1903505780647854099132564
		0.5860872354676911302941448	0.1690047266392679028265834
0.7415311855993944398638648	0.2797053914892766679014678	0.7415311855993944398638648	0.1406532597155259187451896
		0.8648644233597690727897128	0.1047900103222501838398763
0.9491079123427585245261897	0.1294849661688696932706114	0.9491079123427585245261897	0.0630920926299785532907007
		0.9914553711208126392068547	0.0229353220105292249637320

Note: Above values computed based on the scheme suggested by Laurie (1997).

5-D. Expansion of Einstein's integrals using Maclaurin series

$$1. \quad J_1: \int \left(\frac{1-y}{y}\right)^z dy = \left(-1 + \frac{1}{y}\right)^z \left[-\frac{y}{-1+z} + \frac{zy^2}{(-2+z)(-1+z)} - \frac{2zy^3}{(-3+z)(-2+z)(-1+z)} + \frac{6zy^4}{(-4+z)(-3+z)(-2+z)(-1+z)} - \frac{24zy^5}{(-5+z)(-4+z)(-3+z)(-2+z)(-1+z)} + \frac{120zy^6}{(-6+z)(-5+z)(-4+z)(-3+z)(-2+z)(-1+z)} + O[y]^7 \right]$$

$$2. \quad J_2: \int \left(\frac{1-y}{y}\right)^z \log y dy = \left(-1 + \frac{1}{y}\right)^z \left[\frac{(-1+\log y - z \log y)y}{(-1+z)^2} + \frac{(-3z+2z^2+2z \log y - 3z^2 \log y + z^3 \log y)y^2}{(-2+z)^2(-1+z)^2} + \frac{(-16z+13z^2-z^4+12z \log y - 22z^2 \log y + 12z^3 \log y - 2z^4 \log y)y^3}{(-3+z)^2(-2+z)^2(-1+z)^2} + \frac{(-180z+170z^2-5z^3-26z^4+5z^5+144z \log y - 300z^2 \log y + 210z^3 \log y - 60z^4 \log y + 6z^5 \log y)y^4}{(-4+z)^2(-3+z)^2(-2+z)^2(-1+z)^2} - \frac{2(1728z-1838z^2+135z^3+385z^4-135z^5+13z^6-1440z \log y + 3288z^2 \log y)y^5}{(-5+z)^2(-4+z)^2(-3+z)^2(-2+z)^2(-1+z)^2} - \frac{2(-2700z^3 \log y + 1020z^4 \log y - 180z^5 \log y + 12z^6 \log y)y^5}{(-5+z)^2(-4+z)^2(-3+z)^2(-2+z)^2(-1+z)^2} + \frac{(2(-50400z+59052z^2-7252z^3-14595z^4+7175z^5-1257z^6+77z^7+43200z \log y)y^6)}{((-6+z)^2(-5+z)^2(-4+z)^2(-3+z)^2(-2+z)^2(-1+z)^2} + \frac{(2(-105840z^2 \log y + 97440z^3 \log y - 44100z^4 \log y + 10500z^5 \log y - 1260z^6 \log y + 60z^7 \log y)y^6)}{((-6+z)^2(-5+z)^2(-4+z)^2(-3+z)^2(-2+z)^2(-1+z)^2} + O[y]^7 \right]$$

5-E. Numerical solvers for Gauss hypergeometric function

In this appendix we provide numerical methods to calculate Gauss hypergeometric functions which have been used in Eqs. (5-17) and (5-20). In particular, we would be interested in a fast method to evaluate hypergeometric functions with positive, real parameters and argument, compatible to the physical nature of Einstein's integrals. As the Gauss hypergeometric function, ${}_2F_1(a, b; c; x)$ satisfies the hypergeometric differential equation:

$$x(x-1)\frac{d^2w}{dx^2} + [c - (a+b+1)x]\frac{dw}{dx} - abw = 0 \quad (5-A5)$$

almost any numerical method to handle the above ODE can be utilized to compute Gauss hypergeometric functions: from a Taylor series expansion, to an expansion based on Buchholz polynomials (Zhang and Jin, 1996; Pearson et al., 2014), to an asymptotic series expansion via Watson's Lemma (Bender and Orszag, 1999), and to quadrature methods and Runge-Kutta type methods (Tamura, 2007).

In this part we give a brief review of two numerical schemes to compute Gauss hypergeometric function. A more complete discussion of methods for general evaluation of Gauss hypergeometric function is not within the scope of this research (comprehensive discussions can be found in Zhang and Jin, 1996; Tamura, 2007; Michel and Stoitsov, 2008; Pearson et al., 2014). Two methods via Taylor series expansions, which are utilized for numerical evaluation of Gauss hypergeometric function, are given in the next paragraphs.

In the first method we use a basic Taylor series expansion to compute power series of ${}_2F_1(a, b; c; x)$ as follows:

$$C_0 = 1; S_0 = C_0 \quad (5-A6a)$$

$$C_{k+1} = C_k \times \frac{(a+k)(b+k)}{c+k} \times \frac{x}{k+1}; S_{k+1} = S_k + C_{k+1}; \quad k = 0, 1, 2, \dots, N_{max} \quad (5-A7b)$$

in which, C_k refers to the k -th term of the Taylor series expansion of Eq. (5-10), and S_k is the partial sum of the infinite series of the Gauss hypergeometric function. The stopping criteria we used here is defined as either three consecutive terms of $\frac{|C_{k+1}|}{|S_k|}$, $\frac{|C_k|}{|S_{k-1}|}$; and $\frac{|C_{k-1}|}{|S_{k-2}|}$ are being less than a user required tolerance ε_0 or reaching to maximum number of terms N_{max} . As we see in the following, this method shows remarkable accuracy and efficient results in low bedload-layer thicknesses for computing Einstein's integrals. The maximum number of terms which is needed for computing the result depends on the size of the argument x , and $(1 - E)$, and it is between 200 to 1000 terms, as given in Figure 4.3 of Pearson et al. (2014). Rigorous numerical analysis of stability and stopping criteria are given in such a reference.

The second method to compute ${}_2F_1(a, b; c; x)$ we used herein is an approximation based on the recurrence relation of a term via values of previous two terms, as follows:

$$S_{-1} = S_0 = 1, S_1 = \frac{ab}{c}x \quad (5-A7a)$$

$$r_k = \frac{(a+k-1)(b+k-1)}{k(c+k-1)}; k = 2, 3, 4, \dots, N_{max} \quad (5-A7b)$$

$$S_k = S_{k-1} + (S_{k-1} + S_{k-2})r_k x; k = 2, 3, 4, \dots, N_{max} \quad (5-A7c)$$

in which, terms are defined as in Eq. (5-A6) and the stopping criteria is either reaching the predefined maximum number of terms N_{max} or the three consecutive scaled multiplication factors: $\frac{|S_{k+1}-S_k|}{|S_k|}$, $\frac{|S_k-S_{k-1}|}{|S_{k-1}|}$, and $\frac{|S_{k-1}-S_{k-2}|}{|S_{k-2}|}$ are reduced to a value below the predefined tolerance ε_0 . For more information on the convergence and stability criteria see Zhang and Jin (1996), and Pearson et al. (2014).

Chapter Five References

1. Abad, J.D., Buscaglia, G., García, M.H. (2008). "2D Stream Hydrodynamic, sediment transport and bed morphology model for engineering applications". *Hydrological Processes*, 22: 1443-1459.
2. Abad, J.D., García, M.H., Roland, A., Zanke, U., Srivastava, R., Guo, J., Julien, P.Y. (2006). "Discussion and closure to Efficient Algorithm for Computing Einstein Integrals by Junke Guo and Pierre Y. Julien", *J. Hydraul. Eng.*, 132:337-339.
3. Abramowitz, M., Stegun, I.A. (1965). "Handbook of Mathematical Functions." Dover, New York.
4. Ackers, P., White, W.R. (1973). "Sediment transport new approach and analysis". *Journal of Hydraul. Eng.*, ASCE, 99(11): 2041-2060.
5. Bagnold, R.A. (1966). "An approach to the sediment transport problem from general physics". Prof. Paper 422-1, U. S. Geol. Surv.
6. Bender, C.M., Orszag, S.A. (1999). "Advanced Mathematical Methods for Scientists and Engineers I". Springer Science & Business Media.
7. Bombardelli, F.A., Jha, S.K. (2009). "Hierarchical modeling of the dilute transport of suspended sediment in open channels". *Environmental fluid mechanics*, 9(2): 207-235.
8. Bombardelli, F.A., Moreno, P.A. (2012). "Exchanges at the bed sediments-water column interface". *Fluid Mechanics of Environmental Interfaces*, 221.
9. Brownlie, W.R. (1981). "Prediction of Flow Depth and Sediment Discharge in Open Channels," Report No. KH-R-43A, California Institute of Technology, W.M. Keck Laboratory of Hydraulics and Water Resources, Report No. KH-R-43A, Pasadena, CA.

10. Colby, B.R. (1964). "Practical Computations of Bed-Material Discharge." *Journal of the Hydraulics Division, ASCE*, 90(HY2): 217-246.
11. Einstein, H.A. (1950). "The bed-load function for sediment transportation in open channel flow." Bull. No.1026. Washington, DC, USA: USDA Tech.
12. Engelund, F., Hansen, E. (1972). "A Monograph on Sediment Transport in Alluvial Streams." Teknisk Forlag, Copenhagen.
13. García, M.H. (Ed.) (2008). "Sedimentation Engineering (No. 110)", ASCE Publications.
14. Gonnet, P. (2012). "A review of error estimation in adaptive quadrature." *ACM Computing Surveys (CSUR)*, 44(4): 22.
15. Guo, J., Julien, P.Y. (2004). "Efficient algorithm for computing Einstein integrals." *J. Hydraul. Eng.*, 130 (12): 1198–2001.
16. Guo, J., Wood, W.L. (1995). "Fine suspended sediment transport rates." *J. Hydraul. Eng.*, 121(12): 919–922.
17. Jin, J. (2015). Online at: <http://jin.ece.illinois.edu/routines/routines.html> (Accessed on 7/12/15).
18. Julien, P.Y. (2002). "Erosion and Sedimentation." Cambridge University Press.
19. Karim, F., Kennedy, J.F. (1983). "Missouri River Computer-Based Predictors for Sediment Discharges and Friction Factors of Alluvial Streams." MRD Sediment Series, U.S. Army Corps of Engineers, No. 29, Missouri River. MO.
20. Keshtpoor, M., Puleo, J.A., Shi, F., and Ma, G. (2015). "3D numerical simulation of turbulence and sediment transport within a tidal inlet." *Coastal Engineering*, (96): 13-26.

21. Khosronejad, A., Kang, S., Borazjani, I., and Sotiropoulos, F. (2011). "Curvilinear immersed boundary method for simulating coupled flow and bed morphodynamic interactions due to sediment transport phenomena." *Advances in Water Resources*, 34(7): 829-843.
22. Kronrod, A.S. (1965). "Nodes and weights of quadrature formulas." *Sixteen-place tables*, New York: Consultants Bureau (Translation from the Russian).
23. Laurie, D. (1997). "Calculation of Gauss-Kronrod quadrature rules." *Mathematics of Computation of the American Mathematical Society*, 66(219), 1133-1145.
24. MathWorks (2015). "Parallel Computing Toolbox™ User's Guide." Version 6.7.
25. Meyer-Peter, E., Müller, R. (1948). "Formulas for bed-load transport". *Proceedings of the 2nd Meeting of the International Association for Hydraulic Structures Research*. 39–64.
26. Michel, N., Stoitsov, M.V. (2008). "Fast computation of the Gauss hypergeometric function with all its parameters complex with application to the Pöschl–Teller–Ginocchio potential wave functions." *Computer Physics Communications*, 178(7), 535-551.
27. Nakato, T. (1984). "Numerical Integration of Einstein's Integrals, I1 and I2." *J. Hydraul. Eng.*, 110(12): 1863-1868.
28. Pearson, J.W., Olver S., Porter, M.A. (2014). "Numerical Methods for the Computation of the Confluent and Gauss Hypergeometric Functions". arXiv:1407.7786 [math.NA]
29. Piessens, R., de Doncker-Kapenga, E., Uberhuber, C.W., Kahaner, D.K. (1983). "QUADPACK A Subroutine Package for Automatic Integration." Springer-Verlag.
30. Press, W.H., Teukolsky, S.A., Vetterling, W.T., Flannery, B.P. (1992). "Numerical Recipes: The art of scientific computing." Cambridge.
31. Shah-Fairbank, S., Julien, P., Baird, D. (2011). "Total Sediment Load from SEMEP Using Depth-Integrated Concentration Measurements." *J. Hydraul. Eng.*, 137(12), 1606-14.

32. Simons, D.B., Li, R.M., Fullerton, W. (1981). "Theoretically derived sediment transport equations for Pima County, Arizona." Prepared for Pima County DOT and Flood Control District, Tucson, AZ, Fort Collins, CO: Simons, Li and Associates.
33. Slater, L.J. (1966). "Generalized Hypergeometric Functions." Cambridge, UK: Cambridge University Press.
34. Tamura, Y. (2007). "Numerical Evaluation of Generalized Hypergeometric Functions for Degenerated Values of Parameters." arXiv:math/0703082 [math.CA].
35. Toffaleti, F.B. (1968). "A Procedure for computation of total river sand discharge and detailed distribution, bed to surface." Technical Report No. 5, Committee on Channel Stabilization, U.S. Army Corps of Engineers.
36. U.S. Army Corps of Engineers (2010). "HEC-RAS River Analysis System Hydraulic Reference Manual." Version 4.1, Public Release.
37. Vanoni, V.A. (Ed.). (2006). "Sedimentation engineering (No. 54)". ASCE Publications
38. Yang, C.T. (1973). "Incipient motion and sediment transport." Journal of the Hydraulics Division, ASCE, 99 (HY10), 1670–1704.
39. Zamani, K., Bombardelli, F.A. (2014). "Analytical solutions of nonlinear and variable-parameter transport equations for verification of numerical solvers", Environ Fluid Mech. 14(4), 711-742.
40. Zamani, K., Bombardelli, F.A., Kamrani-Moghaddam, B., García, M.H. (2016). "Assessment of sequential and parallel implementation of current methods for the evaluation of Einstein integrals." Submitted to Journal of Hydraulic Engineering ASCE.
41. Zhang, S., Jin, J.M. (1996). Computation of special functions. Wiley-Interscience.
42. Zwillinger, D. (Ed.). (2014). Table of integrals, series, and products. Elsevier.

Figures

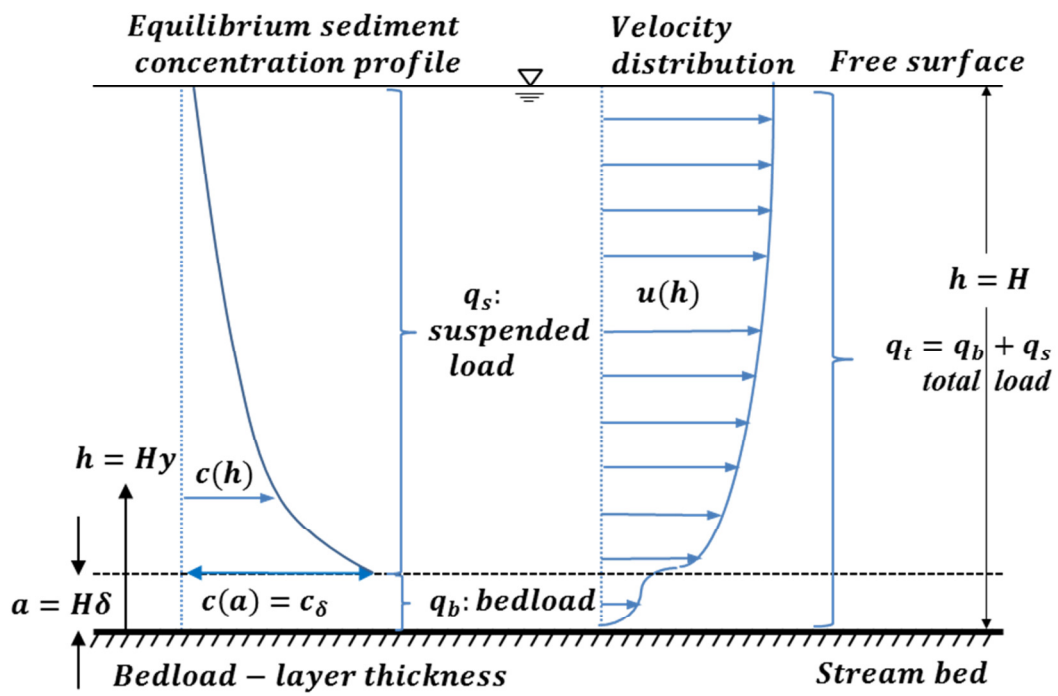


Figure 5-1. Schematic of sediment particles and velocity distribution in free surface flow.

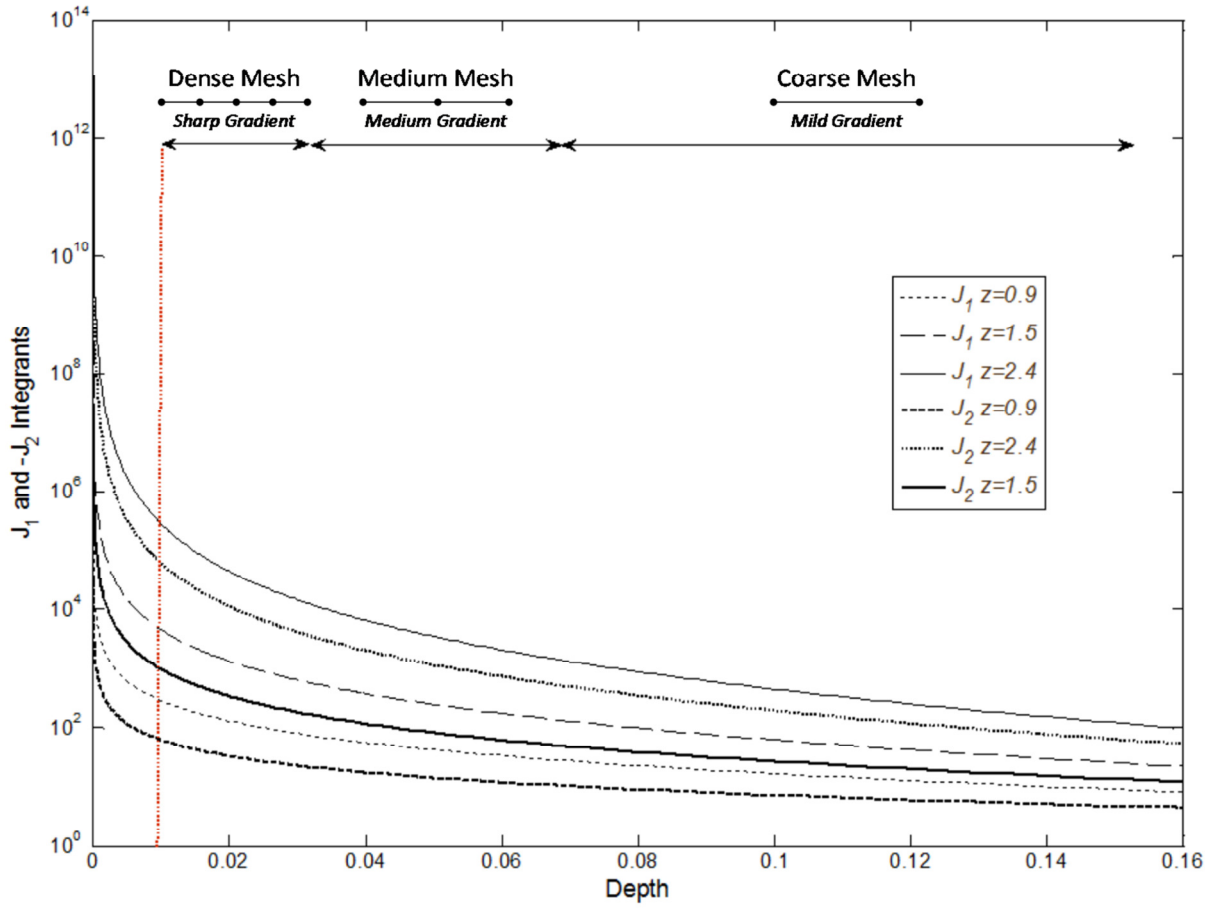


Figure 5-2. Schematics of adaptive integration mesh size based on rate of change of integrand function with various Rouse numbers for the first and second Einstein's integrals.

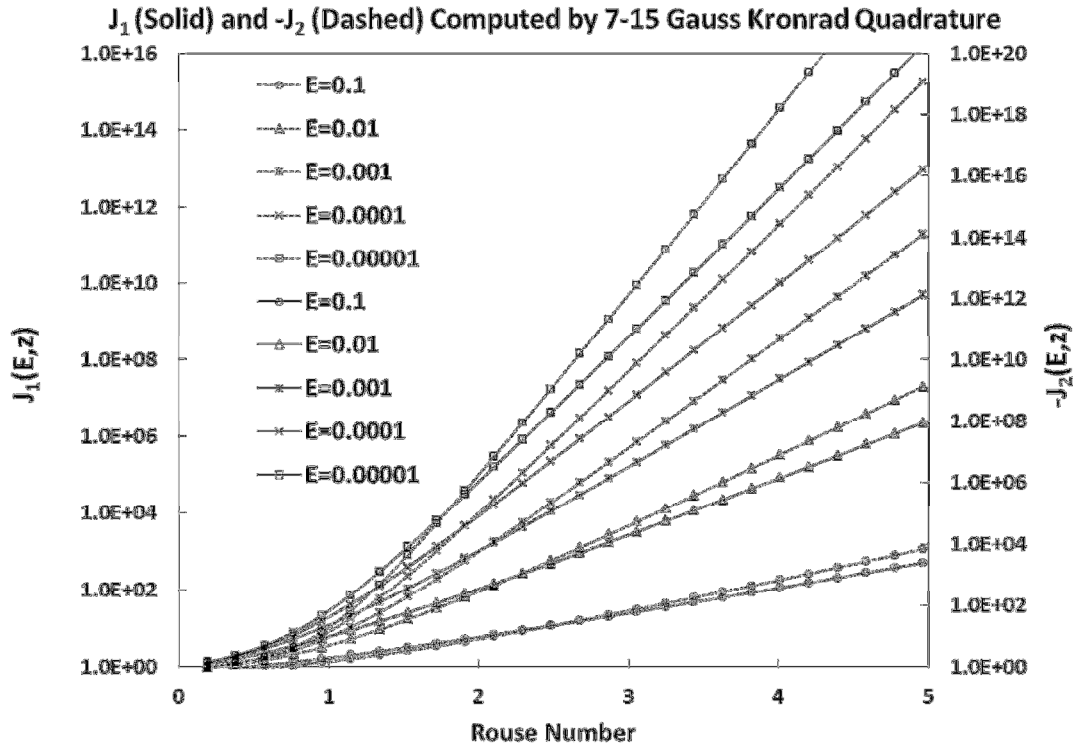


Figure 5-3. Plot of the Einstein integrals J_1 and J_2 computed by Gauss-Kronrod 7-15 quadrature.

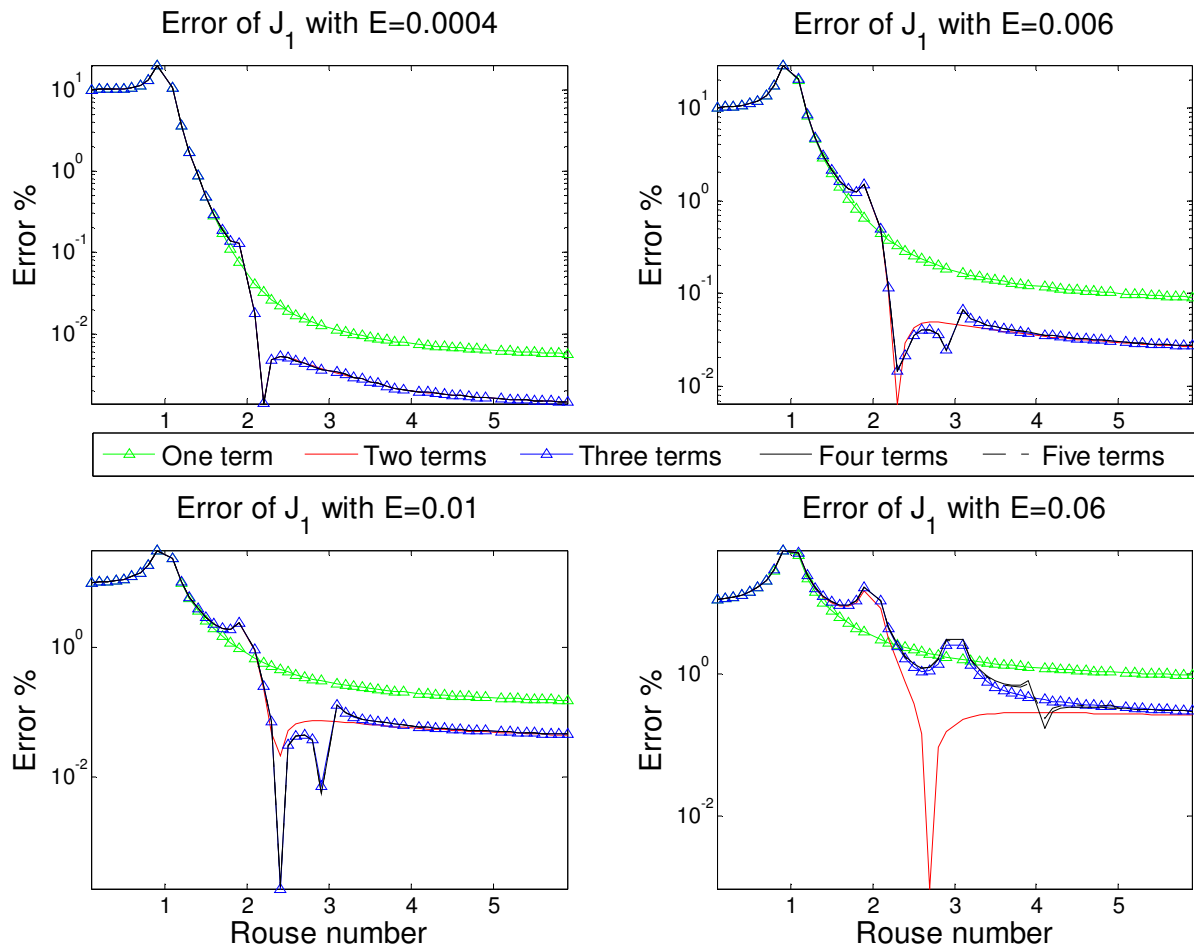


Figure 5-4. Error of Maclaurin expansion of the J_1 integral with different number of terms.

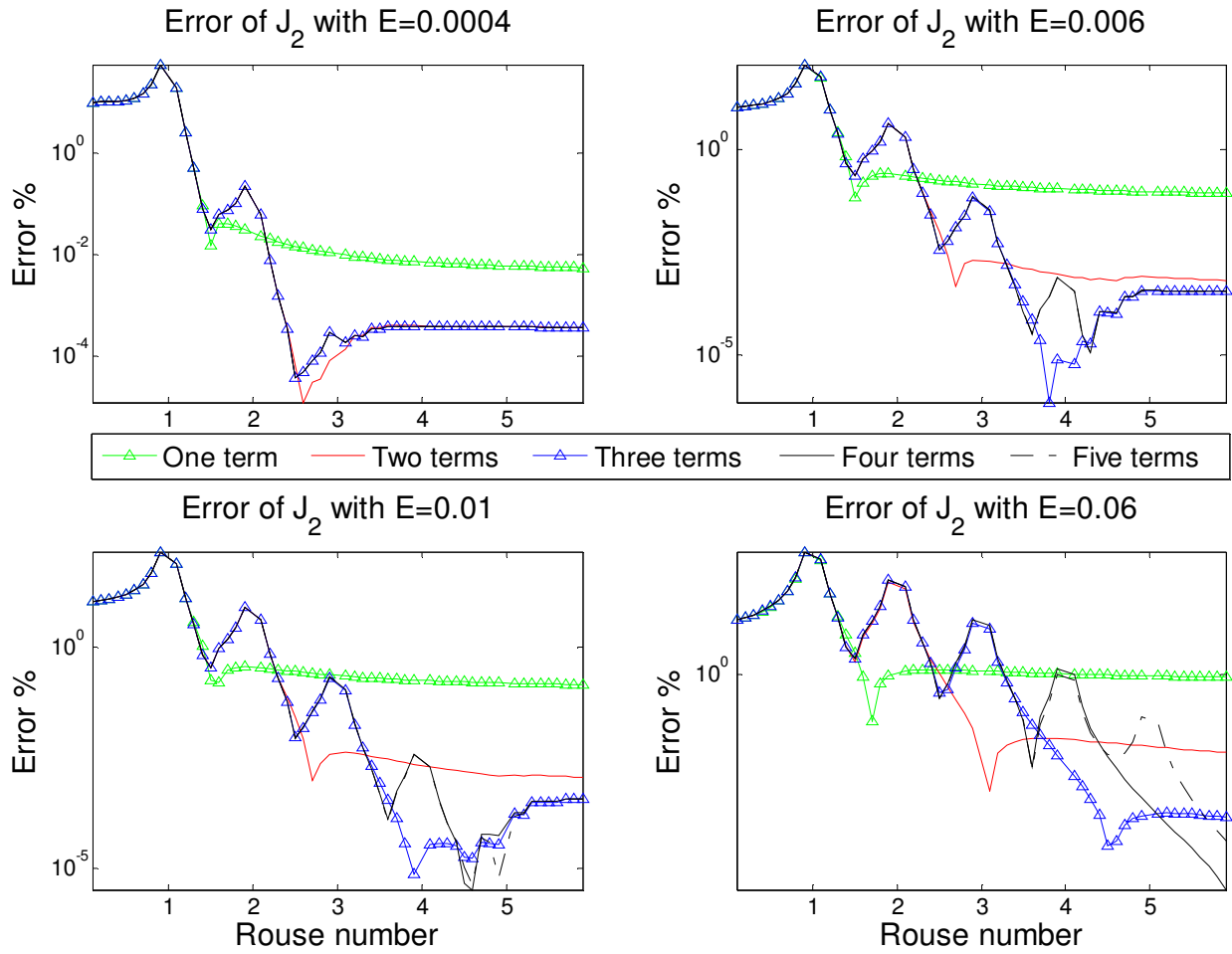


Figure 5-5. Error of Maclaurin expansion of the J_2 integral with different number of terms.

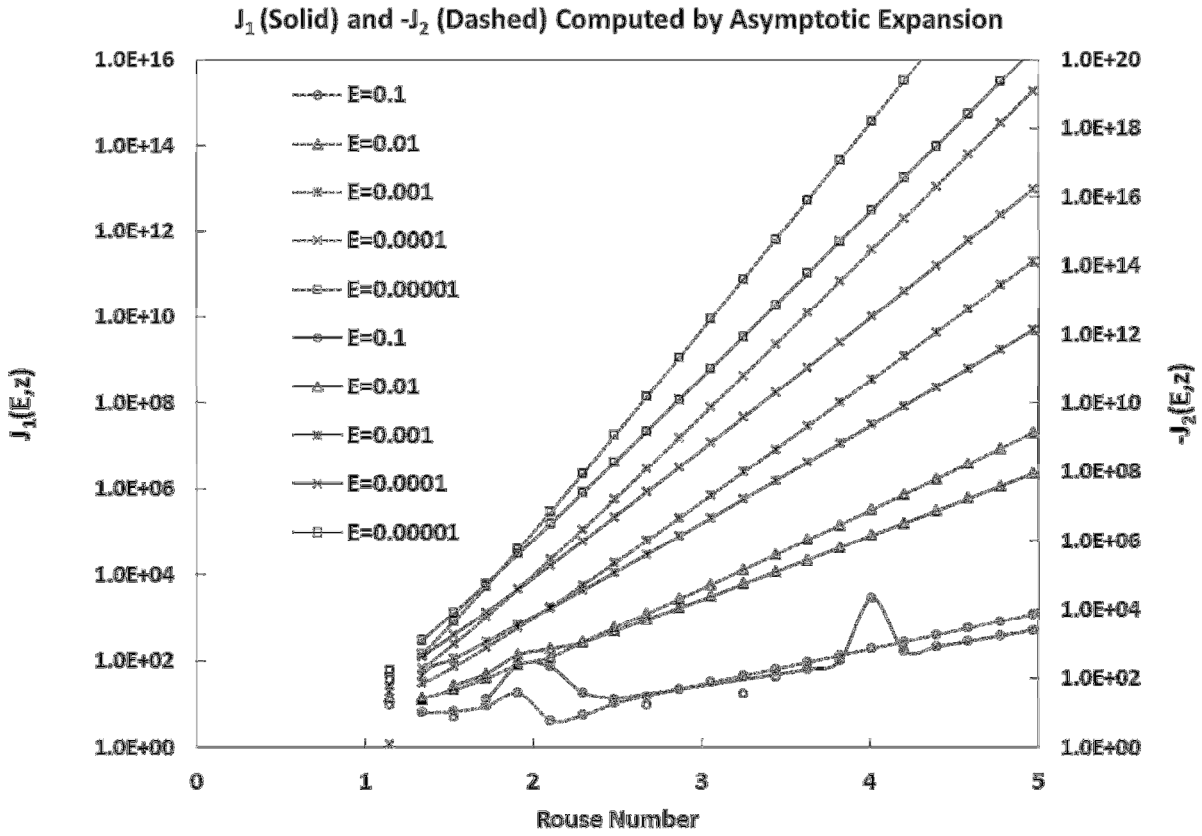


Figure 5-6. Plot of the Einstein integrals J_1 and J_2 computed by two term Maclaurin series expansion of Einstein integrals.

J_1 (Solid) and $-J_2$ (Dashed) Computed by Gauss Hypergeometric Function (a)

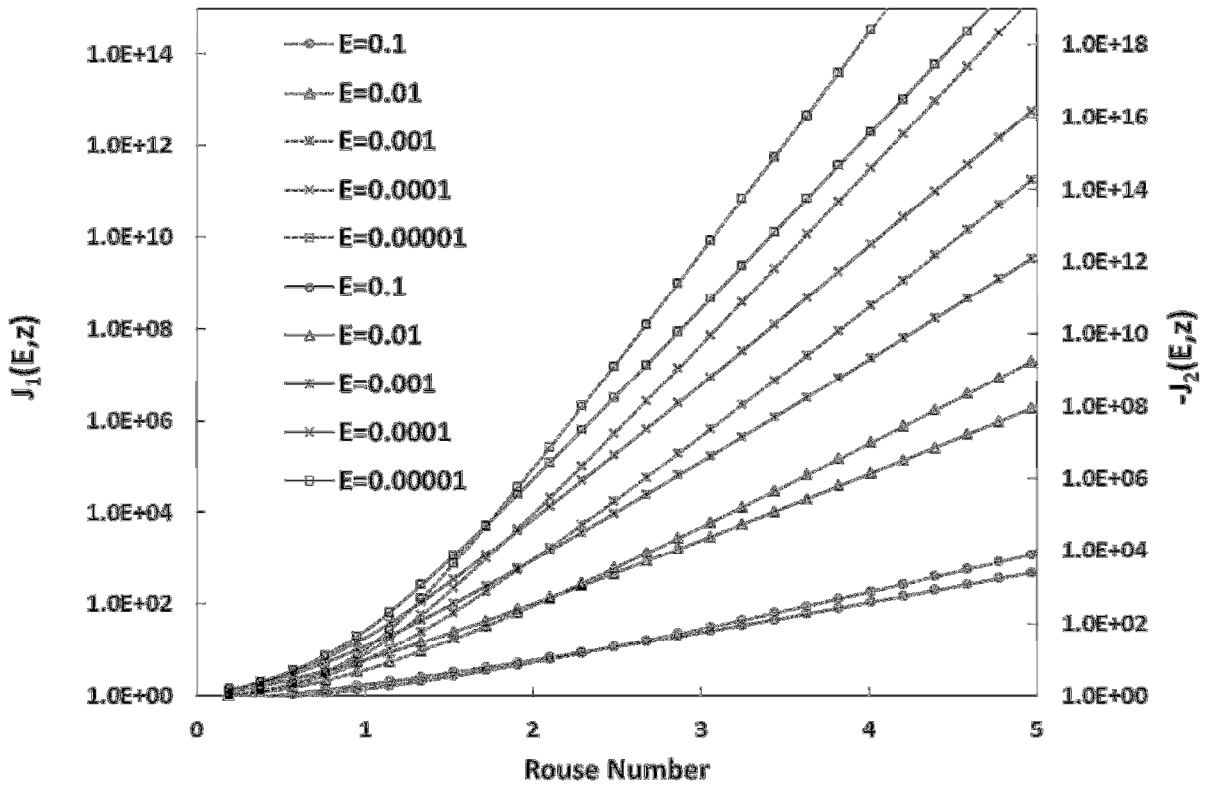


Figure 5-7. Plot of the Einstein integrals J_1 and J_2 computed by Gauss hypergeometric function via method of Eq. (5-A6).

J_1 (Solid) and $-J_2$ (Dashed) Computed by Hypergeometric Function (b)

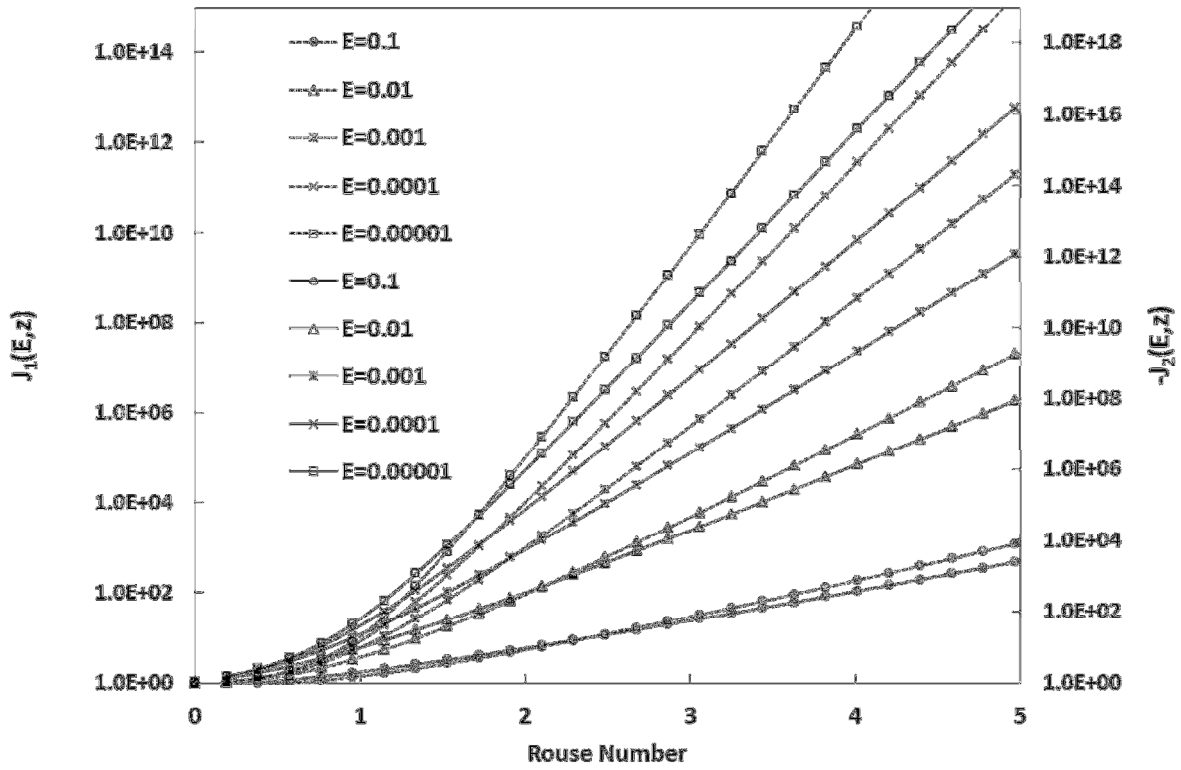


Figure 5-8. Plot of the Einstein integrals J_1 and J_2 computed by Gauss hypergeometric function via numerical library by Jin (2015).

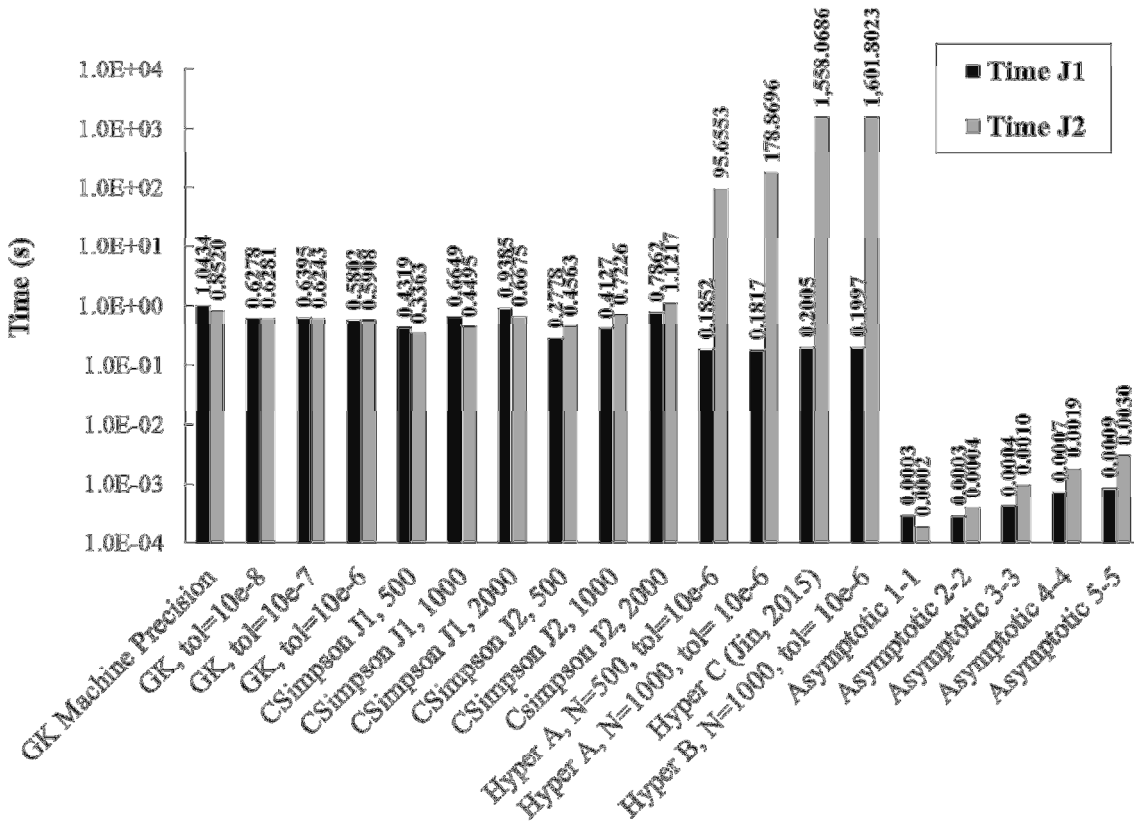


Figure 5-9. CPU time of new developed methods for computing a set of 960 Rouse numbers for various bed layer thicknesses (same platform and same dataset as Figure 5-5).

Table 5-1. Relative speed up of J_1/J_2 integration methods via retrieving the integrand functional values from the J_2/J_1 numerical integration. Values averaged based on a dataset of 960 values of bedload-layer thickness and Rouse number.

Integration method	CSimpson J_1 from J_2 $N = 100$	CSimpson J_1 from J_2 $N = 200$	CSimpson J_1 from J_2 $N = 500$	CSimpson J_1 from J_2 $N = 1000$	CSimpson J_2 from J_1 $N = 100$	CSimpson J_2 from J_1 $N = 200$	CSimpson J_2 from J_1 $N = 500$	CSimpson J_2 from J_1 $N = 1000$	GK 7-15 J_2 from J_1	GK 7-15 J_1 from J_2
Relative decrease of CPU time	20.8%	16.7%	26.4%	12.6%	33.3%	30.6%	35.5%	29.6%	-7.2%	6.6% *

*Note: In the case of recycling the J_1 integral from J_2 integral, the results are less accurate than the case that they are calculated with the original GK 7-15 method.

Table 5-2. Global accuracy of new methods of calculation or approximation of Einstein integrals (tested over a dataset of 960 bedload-layer thicknesses and Rouse numbers)

Method:	Adaptive Gauss-Kronrod Quadrature			Composite Simpson J_1 (similar values for J_2)			Hypergeometric functions				Asymptotic Series Expansion					
	Measure	Tolerance $\epsilon = 10^{-8}$	Tolerance $\epsilon = 10^{-7}$	Tolerance $\epsilon = 10^{-6}$	N=500	N=1000	N=2000	Eq. (5-A/): N=1000; $\epsilon = 10^{-6}$	Eq. (5-A/): N=1000; $\epsilon = 10^{-6}$	Eq. (5-A/): N=1000; $\epsilon = 10^{-6}$	Jin (2015)	1 term	2 terms	3 terms	4 terms	5 terms
J_1	Bias	2.1541E-03	3.8211E-02	2.8255E+00	3.7148E+10	4.4320E+09	3.6774E+08	4.7753E+11	4.7753E+11	4.7753E+11	4.7753E+11	7.6539E+08	2.2919E+08	2.2980E+08	2.2980E+08	2.2980E+08
	RMSE	3.1626E-02	4.9980E-01	3.9299E+01	5.0333E+11	6.0376E+10	5.0237E+09	6.0758E+12	6.0758E+12	6.0758E+12	6.0758E+12	9.2306E+09	2.7647E+09	2.7711E+09	2.7711E+09	2.7711E+09
	Scatter Index	6.6174E-14	1.0458E-12	8.2229E-11	9.7721E-01	1.2517E-01	1.0504E-02	1.5657E+04	1.5657E+04	1.5657E+04	1.5657E+04	1.9283E-02	5.7820E-03	5.7955E-03	5.7955E-03	5.7955E-03
J_2	R^2	1.00	1.00	1.00	1.00	9.99E-1	1.00	1.00	5.71E-1	5.71E-1	5.71E-1	5.71E-1	1.00	1.00	1.00	1.00
	Bias	-1.9242E-2	-2.8730E-1	3.0829E+4	2.6731E+11	3.2256E+10	-2.6938E+9	3.1854E+12	3.1854E+12	4.2287E+2	1.3335E+0	-4.8724E+9	3.3038E+6	-5.8290E+3	1.8550E+1	1.4129E+1
	RMSE	2.6604E-1	3.7129E+0	5.3433E+5	3.6214E+12	4.3931E+11	3.6791E+10	4.0726E+13	4.0726E+13	4.0309E+3	3.4067E+1	5.9472E+10	3.6016E+7	4.9723E+4	2.3515E+2	4.1064E+2
J_1	Scatter Index	-8.3465E-14	-1.1648E-12	-1.6763E-07	-1.0483E+00	-1.3645E-01	-1.1533E-02	-1.9734E+04	-1.9497E+04	-1.2646E-09	-1.0688E-11	-1.8630E-02	-1.1299E-05	-1.5600E-08	-7.3773E-11	-1.2883E-10
	R^2	1.00	1.00	1.00	9.99E-1	1.00	1.00	6.00E-1	6.00E-1	1.00	1.00	1.00	1.00	1.00	1.00	1.00

Table 5-3. Speedup factor for parallel computing of new methods with various parameters, run on a dataset of 10000 pairs of (E, z) values.

Method:	Asymptotic 2-2	GK adaptive quadrature $\varepsilon_0 = 10^{-5}$	GK adaptive quadrature $\varepsilon_0 = 10^{-7}$	GK adaptive quadrature $\varepsilon_0 = 10^{-9}$	CSimpson J_1 recycling $N = 2000$	CSimpson J_1 recycling $N = 5000$	CSimpson J_2 recycling $N = 2000$	CSimpson J_2 recycling $N = 5000$
Time of execution one core	2.63E-1 [s]	1.19E+1 [s]	1.20E+1 [s]	1.25E+1 [s]	1.96E+1 [s]	4.75E+1 [s]	2.30E+1 [s]	5.57E+1 [s]
Speedup for two cores	1.028 [S/S]	1.931 [S/S]	1.933 [S/S]	1.927 [S/S]	1.981 [S/S]	1.976 [S/S]	1.942 [S/S]	1.930 [S/S]
Speedup for three cores	0.966 [S/S]	2.787 [S/S]	2.749 [S/S]	2.681 [S/S]	2.868 [S/S]	2.895 [S/S]	2.858 [S/S]	2.866 [S/S]
Speedup for four cores	0.845 [S/S]	3.462 [S/S]	3.475 [S/S]	3.371 [S/S]	3.698 [S/S]	3.747 [S/S]	3.683 [S/S]	3.672 [S/S]

Chapter 6: Air Distribution in Hydraulic Jumps via Two-Phase Flow Theory

6.1. Introduction

In an open channel where the gravity-driven flow is predominantly one directional, hydraulic jump is a shock that connects supercritical and subcritical flow (Chow, 1959). Although it is a ubiquitous phenomenon in natural and manmade flows, even after a century of numerous studies, the details of this complex flow are not completely understood for all ranges of Froude numbers (Gonzalez and Bombardelli, 2005).

The flow in hydraulic jumps is characterized by strong turbulence, intense fluctuation of the water surface, significant energy dissipation, and complex air entrainment/detrainment (Waniewski et al., 2001; Chanson, 2009). Due to these features, a hydraulic jump can be utilized to dissipate energy, to mix chemicals, or to aerate a flow, of which the latter is the motivation of this study. The major forms of air entrainment in hydraulic jumps are: splash impact, air entrainment due to turbulence, and leading-edge entrainment (Waniewski et al., 2001; Chanson, 2009; Kiger and Duncan, 2012).

Over the last five decades, the knowledge of two-phase in hydraulic jumps has increased vastly owing to experimental and theoretical studies. To the best of our knowledge, Kalinske and Robertson (1943) were the first who experimentally investigated hydraulic jumps taking into account air entrainment. Later on, Rajaratnam (1962) conducted seminal studies on flow and turbulence patterns of hydraulic jumps followed by two-phase flow measurements. Resch et al. (1974) measured air fraction and bubble frequency with a hot film anemometer. Most recent experimental studies of hydraulic jumps concerned with void fraction are: Mossa and Tolve

(1998), Chanson and Brattberg (2000), Waniewski et al. (2001), Murzyn et al. (2005 a and b), Chanson and Gualtieri (2007), Chanson (2010), Chachereau and Chanson (2011), Leandro et al. (2012), Zhang et al. (2013), Wang and Chanson (2015).

The majority of numerical studies of hydraulic jumps have modeled only the liquid phase flow. Abbott et al. (1969) solved the 1-D shallow water equation as the first numerical model of hydraulic jumps. Thereafter, owing to the notable progress in shock capturing methods in 1980s, Rahman et al. (1991), Lemos (1992), and Chippada et al. (1994) simulated hydraulic jump in 2-D. Historically, most numerical simulations of hydraulic jumps ignored the two-phase nature of the flow, and took the conventional one-phase approach with a few exceptions (Gonzalez and Bombardelli (2005) and Ma et al. (2011), Mortazavi et al. (2014)).

Finally, there are numerous theoretical studies on hydraulic jumps. Rayleigh (1914) was the first who discussed hydraulic jumps as a problem of mathematical discontinuity. There is a considerable body of literature on hydraulic jump after 1950s. The classic book by Chow (1959) is perhaps the most comprehensive contribution to the knowledge of hydraulic jumps it covered all the knowledge of hydraulic jumps to that point. Chanson (2009), and Bon et al. (2009) and the references therein provide the recent knowledge on the hydraulic jumps. In addition to those, Kiger and Duncan (2012) discussed the latest knowledge on air entrainment mechanism in the breaking waves and jets. Table 6-1 lists the most relevant experimental investigations in the literature that discuss two-phase flow features of hydraulic jumps.

On the other hand, the Burgers' equation is a nonlinear scalar evolution equation which was originally derived for investigation of the problem of fluid turbulence. It has been noticed afterwards that Burgers' equation can be a powerful model for a broad range of problems which involve concurrent effects of nonlinearity and dissipation (for example, sound waves propagation

in viscous medium (Debnath, 2012); density wave in traffic flow (Bellomo and Dogbe, 2011); hydromagnetic waves in finite electrical conductivity medium (Olesen, 2003); and viscoelastic wave in solids (Camacho et al., 2008)). In addition to the aforementioned fields, this equation is of particular interest in water resources studies, from internal waves (Sandstrom and Oakey, 1995), to flow in vadose zone (Warrick and Parkin, 1995; Nasser et al., 2012). Recently, it was employed as a descriptive model to study fluvial structures in geomorphology (Passalacqua et al., 2006; Pelletier, 2007), and was used to test nonlinear transport models (Zamani and Bombardelli, 2014).

Analytical solutions can provide insight into the physical processes of air bubble distribution in hydraulic jump. In addition, analytical solutions have a profound impact on the development and verification of the numerical techniques for nonlinear PDEs (Zamani and Bombardelli, 2014). Chanson (1995, 2010) used continuum mixture theory and assumed an infinitesimal volume above the channel bed, Cartesian domain, and a point source air entrainment to elucidate transport of air bubbles within a hydraulic jump. He used the *method of images* to solve the scalar transport equation within the aforementioned domain (Chanson, 2012). Chanson took four simplifying assumptions to derive his analytical solution: homogenous turbulence, steady-state flow, uniform flow, and particularly constant rise velocity of bubbles.

In this paper we extend the former analytical solution describing air distribution in hydraulic jumps; however we consider the nonlinear bubble rise velocity. Nonlinear bubble rise velocity is a significant factor in air bubble dynamics. Waniewski et al. (2001) noticed that the nonlinear buoyancy effect is the second most important driving cause within hydraulic jump after turbulence.

The remainder of the paper is organized as follows. In section two we formulate the governing equations. We show in section three the mathematical details of transformation of the governing PDE to the well-known form of Burgers' equation, and indicate that it can be explicitly solved through the *traveling wave solution* method. Then in sections four we compare the analytically derived solution with lab measurements. Quantitative accuracy measures reveal the newly derived analytical solution is capable of make a good replica of the observed air concentration in the hydraulic jump. We provide empirical-analytical representation of air entrainment in hydraulic jumps in section five. Finally, we provide the noticeable remarks of the study in the section six.

6.2. Formulation of Interpretative Model

Figure 1 shows a sketch for the aeration problem in hydraulic jumps. Here, variables were assumed to be almost constant in transverse direction, and flow was considered two dimensional and steady. Air primarily enters water through two mechanisms: a) jet-type impingement from the jump toe (Rajaratnam, 1962; Waniewski et al., 2001; Chanson, 2009); b) surface turbulence entrainment in the recirculation region (Mossa and Tolve, 1998; Chanson, 2009) and c) splash effect entrainment (Waniewski et al., 2001; Chanson, 2009). Laboratory observations reveal that the former effect in the hydraulic jump is dominant aeration mechanism compared to the air entrainment by the surface roller and turbulence (Waniewski, 2001; Chanson and Gualtieri, 2007; Chanson, 2009).

To derive the governing equation based on the continuum theory of multiphase mixtures (Allen et al., 1988; Drew and Passman, 1999; Crowe et al., 2012), we assume each of the gaseous and liquid phases present at every “point” in the continuum domain. The second

essential assumption is that air bubbles' size is smaller than the scales in which flow properties vary significantly; therefore, we can define derivatives of the properties within the flow. In addition we ensemble average for gas and water phases (Drew and Passman, 1999; Crowe et al., 2012). Considering no evaporation, condensation and exchange between phases we can write the conservation of mass for phase k (air or water):

$$\frac{\partial(\bar{\rho}_k \alpha_k)}{\partial t} + \frac{\partial}{\partial x_i} (\bar{\rho}_k \alpha_k \tilde{u}_{ki}) = \Gamma = 0; \quad i = 1, 3 \quad (6-1)$$

Herein, tildes indicate ensemble-averaged variables, k refers to the phase, and u_{ki} denotes the velocity of phase k in the i -th direction. In turn, x_i and t denote the spatial and time coordinates, respectively.

Usually velocity of the disperse phase (sediment or air bubbles) is different from the carrier phase velocity (water in this case), as represented by the concept of bubble-rise velocity (Clift et al., 2005) or the notion of lag velocity (Parker, 2004; Garcia, 2008; Muste et al., 2009). However, it has been customarily assumed in previous studies that bubbles move at the same velocity of water in the horizontal direction; further in the vertical direction, experimental evidence suggest that the vertical water velocity is virtually zero, so that, the so-called "slip velocity" can be used to characterize the vertical bubble velocity. Thus we assume $\tilde{u}_a = \tilde{u}_w$ and $\tilde{v}_a = u_r$, where the subscripts "a" and "w" indicate air and water, respectively, and u_r is bubble rise velocity. For the air phase in steady state then we have:

$$\frac{\partial}{\partial x_i} [(\bar{\rho}_a + \rho'_a)(\bar{C} + C')(\bar{u}_i + u'_i)] = 0$$

$$\frac{\partial}{\partial x_i} [\bar{\rho}_a \bar{C} \bar{u}_i + \bar{\rho}_a C' \bar{u}_i + \bar{\rho}_a \bar{C} u'_i + \bar{\rho}_a C' u'_i + \rho'_a \bar{C} \bar{u}_i + \rho'_a C' \bar{u}_i + \rho'_a \bar{C} u'_i + \rho'_a C' u'_i] = 0$$

$$\frac{\partial}{\partial x_i} [\bar{\rho}_a \bar{C} \bar{u}_i + \bar{\rho}_a \overline{C' u'_i} + \overline{C' \rho'_a u'_i} + \overline{C' \rho'_a u'_i} + \bar{u}_i \overline{\rho'_a C'} + \overline{\rho'_a C' u'_i}] = 0$$

If we assume $\rho'_a \cong 0$; an assumption supported by empirical evidence (Crowe et al., 2012):

$$\frac{\partial}{\partial x_i} [\bar{\rho}_a \bar{C} \bar{u}_i + \bar{\rho}_a \overline{C' u'_i}] = 0$$

$$\frac{\partial}{\partial x_i} [\bar{\rho}_a (\bar{C} \bar{u}_i + \overline{C' u'_i})] = 0$$

If $\bar{\rho}_a$ is not a function of space:

$$\frac{\partial}{\partial x_i} (\bar{C} \bar{u}_i + \overline{C' u'_i}) = 0$$

$$\frac{\partial}{\partial x_i} (\bar{C} \bar{u}_i) = -\frac{\partial}{\partial x_i} (\overline{C' u'_i})$$

$$\frac{\partial \bar{u}_i}{\partial x_i} + \bar{u}_i \frac{\partial \bar{C}}{\partial x_i} = -\frac{\partial}{\partial x_i} (\overline{C' u'_i})$$

$$\frac{\partial(\bar{\rho}_a \bar{C})}{\partial t} + \frac{\partial}{\partial x_i} (\rho_a \tilde{C} \tilde{u}_i) = 0 \quad (6-2)$$

If we consider the flow to be steady and two dimensional ($i = 1, 2$):

$$\frac{\partial}{\partial x_i} (\rho_a \tilde{C} \tilde{u}_i) = 0 \quad (6-3)$$

The above equation governs the instantaneous quantities. By decomposing the instantaneous quantities to a mean component and fluctuation component ($\tilde{C} = C + C'$ and $\tilde{u}_i = u_i + u'_i$) and averaging over turbulence:

$$\frac{\partial}{\partial x_i} (C u_i) = -\langle \frac{\partial C' u'_i}{\partial x_i} \rangle \quad (6-4)$$

Replacing $\langle C' u'_i \rangle = -D_t \frac{\partial C}{\partial x_i}$, and with scaling based on the characteristic lengths and time scales we might be able to show the channel-wise gradient of air concentration is negligible in comparison with the gradient of air-concentration in depth. The equation (6-4) will be simplified to the form of (Chanson, 2009):

$$U \frac{\partial C(x,y)}{\partial x} + V \frac{\partial C(x,y)}{\partial y} = \frac{\partial}{\partial y} \left(D_t \frac{\partial C(x,y)}{\partial y} \right) \quad (6-5)$$

where U [L/T] is streamwise flow velocity, $C(x, y)$ [L^3/L^3] is the void fraction ratio in the air-water mixture, x and y [L] are horizontal and vertical coordinates respectively, V [L/T] is the velocity in y direction, and D_t [L^2/T] is air bubbles' turbulent diffusivity in the vertical direction. In other words, we simply consider the transport of a scalar quantity (air concentration) in the steady, incompressible, turbulent flow and neglect the conservation momentum of air bubbles.

Entrained air bubbles to the jump are convected within the flow and meanwhile they are diffused in the direction wall-normal direction via turbulent diffusion. Assume that the velocity distribution in the depth is uniform, u_0 . If we assume homogenous turbulence without wall influence, then we have $D_t = D_0$. Chanson (1995) suggested an approximation of $D_0 = 0.045h_1u_1$ for the turbulent diffusivity inside hydraulic jumps.

The slip velocity of a single air bubble in still water is a function of several parameters i.e. the size and the shape of bubble, the density difference between air and water, and the water viscosity and surface tension, as well as temperature and gravity. Besides those, the hydrodynamic conditions have effect on the slip velocity (Kulkarni and Joshi, 2005; Chanson, 2012). If assume air weight is negligible compared to water weight, the rise velocity can be approximated as:

$$v_r = v_h \sqrt{\frac{1}{\rho_w(y)g} \left| \frac{\partial P}{\partial y} \right|} \quad (6-6)$$

where g [L^2/T] is gravity, P [M/LT^2] is the dynamic pressure, v_h [L/T] is the bubble slip velocity under hydrostatic conditions (see Appendix 6-A), ρ_w [M/L^3] is the water density and other parameters are as defined previously. The air-water mixture density can be approximated as:

$$\rho_m = \rho_w(1 - C) + \rho_a C \quad (6-7a)$$

In case of a dilute mixture:

$$\rho_m \approx \rho_w(1 - C) \quad (6-7b)$$

Merging equation (6-7b) with the equation (6-6), the relation between hydrostatic and non-hydrostatic bubble slip velocity is:

$$v_r = v_h \sqrt{1 - C} \quad (6-8)$$

Inserting the above factors in equation (6-1), the differential transport equation of air distribution in the hydraulic jump can be mathematically expressed by:

$$u_0 \frac{\partial C(x,y)}{\partial x} + v_h \sqrt{1 - C(x,y)} \frac{\partial C(x,y)}{\partial y} = D_0 \frac{\partial^2 C(x,y)}{\partial y^2} \quad (6-9)$$

Chanson (1995) measured and reported D_0 values. In the present work, the diffusivity of bubbles and hydrostatic rise velocity are taken as constants, and velocity is assumed uniform (Chanson, 1995, 2009).

6.3. Analytical Solutions for Lower and Upper Regions

6.3.1. Approximation for the lower and shear region

Although equation (6-9) describes a two-dimensional, steady-state, advective-dispersive transport, it could be treated similarly to a one dimensional, non-steady, advection-diffusion equation (ADE) given that their mathematical structures are identical. There is substantial literature on the solution techniques of one dimensional linear ADE and nonlinear Burgers' equation (for example see Sachdev, 2008; Zamani and Bombardelli, 2014). Existing techniques are not directly applicable to solve equation (6-9) because of the nonlinear form of the bubble's

rise velocity. Taking into account the value of air fraction ($C < 50\%$) in the shear region, we expand the square root factor using Taylor series:

$$\sqrt{1-C} = \sum_{n=0}^{\infty} \frac{(-1)^n (2n)!}{(1-2n)(n!)^2 4^n} (-C)^n \quad (6-10)$$

If we truncate the expansion after the first two terms, for the void fraction ratio within the range of (0 – 50%), the “error” of the approximation lies below 1%. Figure 6-2 shows the comparison of the “exact” value of the rise velocity versus its linearized approximation.

$$\sqrt{1-C} \cong 1 - \frac{4}{7}C \quad (6-11)$$

Substituting equation (6-11) in the equation (6-9), gives:

$$u_0 \frac{\partial C}{\partial x} + v_h \left(1 - \frac{4}{7}C\right) \frac{\partial C}{\partial y} = D_0 \frac{\partial^2 C}{\partial y^2} \quad (6-12)$$

6.3.2. Analytical solution procedure

Introducing a new vertical space variable $y = z + \frac{v_h}{u_0}x$ we can remove the advective term containing $\frac{\partial C}{\partial y}$, from the equation (6-12) (new variable is moving along the characteristics), the change of variable yields:

$$u_0 \frac{\partial C}{\partial x} - \frac{4}{7}v_h C \frac{\partial C}{\partial z} = D_0 \frac{\partial^2 C}{\partial z^2} \quad (6-13)$$

Now, it is convenient to express equation (6-13) in dimensionless form. To that end, the following coordinate transformations are introduced:

$$Y = \frac{4}{7} \frac{v_h}{D_0} z \quad (6-14a)$$

$$X = \frac{16}{49} \frac{v_h^2}{D_0 u_0} x \quad (6-14b)$$

Using the new coordinates – Eq. (6-14) – and rework Equation (6-13), it can re-written in nondimensional form as:

$$\frac{\partial C}{\partial X} - C \frac{\partial C}{\partial Y} = \frac{\partial^2 C}{\partial Y^2} \quad (6-15)$$

which is the classic form of the Burgers' equation.

The *Hopf-Cole transformation* (Sachdev, 2008) and *travelling wave* solution are two common ways of explicitly solving Burgers' equation (Zamani and Bombardelli, 2014). Hereby, we use the travelling wave $\xi = Y - aX$ where ξ represents a fixed profile, moving with the constant wave speed a .

$$C(X, Y) = K(\xi) = K(Y - aX)$$

By replacing $C(X, Y)$ via the chain rule, we can degenerate the equation (6-15) to the form of a second order, nonlinear, reducible ODE:

$$K''(\xi) + K(\xi)K'(\xi) + aK'(\xi) = 0 \quad (6-16)$$

Equation (6-15) can be solved by direct integration with respect to ξ ; the answer is:

$$K(\xi) = K(Y - aX) = \frac{\sqrt{2} \tanh\left(\frac{\xi + A_2}{\sqrt{2}A_1}\right) - aA_1}{A_1} \quad (6-17)$$

Rebuilding the solution in the original variables we obtain:

$$C(x, y) = \frac{1}{A_1} \left(\sqrt{2} \tanh \left(\frac{\frac{4v_h(y - \frac{v_h x}{u_0}) - a \frac{16}{49D_0} \frac{v_h^2}{u_0} x + A_2}{\sqrt{2}A_1}} \right) - aA_1 \right) \quad (6-18)$$

where A_1 , A_2 and a are values which have to be defined based on the boundary conditions.

6.3.3. Boundary conditions

The specification of physical boundary conditions in hydraulic jumps is complicated, due to the moving nature of the free surface. Based on the available experimental measurements (Chanson, 1995; Chanson and Brattberg, 2000; Murzyn et al., 2005; Chanson and Gualtieri, 2007) we define the boundary condition as follows:

$$C(x = 0, y) = C_0(y) \quad (6-19)$$

$$C(x_{toe} < x < L_a, y_{max}) = C_{max}(x) \quad (6-20)$$

$$C(x_{toe} < x < L_a, y \rightarrow -\infty) = 0 \quad (6-21)$$

where L_a is the aeration length of the hydraulic jump. $C_0(y)$ depends on the inflow condition, in partially developed inflow condition $C_0(y) = 0$ and in case of fully developed inflow there is pre-jump surface aeration and $C_0(y)$ starts at one and in drop and asymptotes to zero as depth increases with an *erfc function-type* behavior.

6.3.4. Analytical solution for air bubbles distribution in the upper region

For the sake of completeness, we also provide an analytical solution of the air concentration in the upper part of the hydraulic jump. Air entrainment/detrainment in the free surface of hydraulic jump is essentially dominated by the interfacial aeration. For that reason, Chanson (1995) suggested the analytical solution for the two dimensional axisymmetric free jet can be adopted to represent the air-bubbles distribution in the upper region (Murzyn et al., 2005):

$$C(x, y) = \frac{1}{2} \left[1 + erf \left(\frac{y - y_{c50\%}}{2 \sqrt{\frac{Dx}{V}}} \right) \right] \quad (6-22)$$

where erf is the error function and air concentration value asymptotes to one as $y \rightarrow \infty$. In the next two sections we provide the comparison of the newly derived analytical solution for lower region (6-18) and the upper region analytical solution (6-22).

6.4. Experimental Validation of the Analytical Solution

In the derivation of the analytical solution for the air, we made some simplifying assumptions regarding the nature of the processes that take place in the transport of bubbles. In this section, we validate the obtained solution and assess its competence in the representation of the phenomenon. To that end, we use three laboratory measured datasets: tests P10 and C2 by Chanson and Qiao (1994) and run T8-5 by Chanson and Brattberg (2000).

The tests by Chanson and Qiao (1994) were performed in a rectangular, $3.2 - m$ long glass-made (floor and walls), horizontal channel with $0.25 m$ width. Inflow condition was not fully developed in both runs. The instrumentation they were employed: single-tip conductivity probe, with inner platinum electrode ($\phi = 0.35 mm$); pointer gauge; and Pitot tube. Experiments P10 and C2 were conducted with $Fr = 6.05$ and 5.66 , and jump toe locations were $X_{toe} = 0.89$ and $0.669 m$, respectively. Air concentration distribution inside the jump was measured with analog samplings during 60 to 300 s. Discharge was measured with a sharp-crested weir which was located at the end on the channel. More details on the test and instrumentation are found in Chanson (1995).

Test T8-5 by Chanson and Brattberg (2000) was conducted in a geometrically identical channel. Discharge was measured trough a V-notch weir. Mean flow velocity and turbulence fluctuations were measured through a Pitot tube with 1% accuracy. The void fraction was measured using a dual-tip conductivity probe with a platinum electrode with smaller size

($\phi = 0.25 \text{ mm}$). In this test, air-bubble data were digitally recorded for 10 s. The positioning of instruments in this test was partially automated and it was tuned for the accuracy of 0.01 mm. This experiment was done with $Fr = 8.485$ and jump toe was located at $X_{toe} = 0.5 \text{ m}$ from the gate. Like the tests P10 and C2, the inflow condition was also partially developed (Chanson and Brattberg, 2000).

For the statistical comparison of observed and analytical model values of air concentration in hydraulic jumps, bias, scatter index and coefficient of determination are used. Bias is the sum of the error and it is a measure to unveil over/under prediction. Scatter index (SI) is related to the root mean square error ($RMSE$), which is normalized by the average values of the observed quantity. Coefficient of determination (R^2) is a common statistical measure used to assess how well a model captures observed data.

$$SI(\%) = \frac{\sqrt{\frac{1}{N} \sum_{i=1}^N (A_i - O_i)^2}}{\frac{1}{N} \sum_{i=1}^N O_i} \times 100 = \frac{RMSE}{\bar{O}} \times 100 \quad (6-25)$$

$$Bias = \frac{1}{N} \sum_{i=1}^N (A_i - O_i) \quad (6-26)$$

$$R^2 = 1 - \frac{\sum_{i=1}^N (A_i - O_i)^2}{\sum_{i=1}^N (A_i - \bar{O})^2} \quad (6-27)$$

In the above equations, A is the air concentration calculated by the analytical model; O is the observed air concentration; the mean value is denoted by overbar and N is number of observations. Table 6-3 shows the error statistics of air concentration calculated by the new analytical solution which defines lower region and shear region of hydraulic jumps.

6.5. Air Entrainment and Detrainment

Air entrainment/detrainment characteristics of hydraulic jumps were empirically studied by several researchers (Rajaratnum, 1961; Hager, 1992; Chanson, 1995; Murzyn et al., 2005; Chanson and Gualtieri, 2007). Basically, depth-average air concentration is significant near the jump toe, and reduces towards the end of the jump. In this section, first we assess the empirical formulas to account for the location of maximum and streamwise air concentration and compared them with formulas by Rajaratnum (1961) and Hager (1992). Second, we propose a new model for relative air entrainment versus the jump length. All of the above relations are validated against the experimental results of Chanson (1995), Murzyn et al. (2005), and Chanson and Gualtieri (2007).

6.5.1. Distribution and location of maximum air concentration

In the multiphase flow literature of hydraulic jumps, it is mentioned that the maximum air concentration would happen in a close proximity of the jump toe. Hager (1992, 1995) suggested that the maximum air concentration happens at the $x_{a_{max}} = 1.9y_2$. The other relation which is suggested by Rajaratnam (1962) is based on the upstream Froude number:

$$C_{air} = (C_{air_{max}}) \sqrt{\frac{9x_a}{L_a} e^{(1-\frac{9x_a}{L_a})}} \quad (6-29)$$

in which, $\frac{x_a}{L_a}$ is the dimensionless streamwise length coordinate and $C_{air_{max}}$ is the maximum air concentration in the jump length which is either found by measurement or approximated as a function of upstream Froude number as:

$$x_{a_{max}} = 1.8y_2 \left(\frac{Fr_1}{4.8} e^{1-\frac{Fr_1}{4.8}} \right)^{10} \quad (6-30)$$

The above formula is recommended for Froude numbers less than ten. Figure 6-9 shows the experimental location of maximum air concentration against the empirical formula and, as it can be seen, the experimental values deviate from the empirical formula as the upstream Froude number exceeds 10. And Figure 6-10 shows the air concentration as a function of streamwise coordinate which is non-dimensionalized by aeration length. In this figure we used data collected by Chanson (1995), Murzyn et al. (2005), and Chanson and Gualtieri (2007) to assess the formula by Rajaratnam (1962).

6.5.2. Distribution of mass of air in hydraulic jump

In this section, we suggest a novel empirical-analytical relation for entrained air mass in the hydraulic jump. First we discuss how to find air mass in each cross-section of the hydraulic jumps based on then measurements along the hydraulic jump. Then we devise a mathematical relation for the mass of air along hydraulic jumps.

We need a function to define mass such that:

$$\frac{\partial M_a(x=x_{toe})}{\partial x} \rightarrow \infty \quad (6-30a)$$

$$\frac{\partial M_a(x=L_a)}{\partial x} = \mathbf{0} \quad (6-30b)$$

$$M(x = L_a) = \beta \rho_{air} \quad (6-30c)$$

Equation (6-30a) accounts for the instantaneous air entrainment in the jump toe. Equation (6-30b) shows that after passing the aeration length there will be a balance between entrained and detrained air. In turn, equation (6-30c) defines that at the end of the aeration length the entrained mass is equal to the product of the *jump air entrainment ratio* " β " and air density (Hager, 1992).

There are various experimental formulae to approximate β ; we use the one by Hager (1992) herein:

$$\beta = 0.018(Fr_1 - 1)^{1.245} \quad (6-31)$$

Based on the physics of air entrainment/detrainment phenomenon and the above mentioned boundary conditions (Eq. 6-30) we assume a superposition of Gamma distribution and trimmed ramp function for the air mass in the jump:

$$M(x) = \beta \rho_{air} \left(\frac{L_a + |x| - |x - L_a|}{2L_a} + \frac{k_3}{\Gamma(k_1)k_2^{k_1}} x^{k_1-1} e^{-\frac{x}{k_2}} \right) \quad (6-32)$$

Herein, k_i , $i = 1, 2, 3$ are regression factors, $\Gamma(\cdot)$ is the gamma function, and L_a is the aeration length. Figure 11 shows the measured air mass in the hydraulic jump by Chanson (1995), Murzyn et al. (2005) and Chanson and Gualtieri (2007), against equation (6-32).

6.6. Summary and Conclusions

A new analytical solution to elucidate the air fraction distribution in the developing turbulent shear region of hydraulic jump has been obtained. This analytical solution still assumes simplifying assumptions, as follows: homogeneous turbulence in vertical column; uniform steady unidirectional flow; and it neglects the air concentration gradient in the flow direction. However, the previous exact solutions of the same phenomenon have been derived with the assumption of constant bubble rise velocity whereas in this study the nonlinear bubble slip velocity was considered. In this study, we first derived a process-based model for void fraction distribution in hydraulic jumps, and then this governing equation was degenerated to a Burgers'

type equation through transformations and mathematical calculations. In the last part, the simplified governing equation was solved analytically using traveling wave solutions.

To validate the newly derived analytical solution, we checked the results versus lab measurements. We compared the analytical solution with the three datasets: tests P10 and C2 from Chanson and Qiao (1994), and test T8-5 Chanson and Brattberg (2000). Taking everything into account, the derived analytical solution not only captures the trend of the measured air distribution considerably, but also in the lower region it shows excellent agreement with the benchmark.

We also used the data collected by Chanson (1995), Chanson and Brattberg (2000), Murzyn et al. (2005), and Chanson and Gualtieri (2007) to assess the air distribution in the roller region of hydraulic jumps (Chanson, 1995). The validation results the analytical solution greatly resembles the distribution of air bubbles in the hydraulic jumps. We also looked into the extension of both solutions into the turbulence shear region. Both of the solutions (recirculation region and lower region) are not able to mimic the air bubble distribution in the shear region of the hydraulic jump.

Appendix of Chapter 5

6-A. Bubbles rise velocity under hydrostatic conditions

Air bubbles' terminal rise velocity in quiescent flows depends on several parameters: viscosity and surface tension of water, bubble size and shape, density of water and air (Michaelides, 2006). Chanson and Brattberg (2000) showed that in the turbulent shear region of hydraulic jumps, bubbles are around one millimeter in size while the recirculating region includes both large and small bubbles as well as air-water packets near the surface. Murzyn et al. (2005) indicated that the vast majority of bubbles are larger than 1 *mm* in Sauter mean diameter. Waniewski et al. (2001) reported the size of the air-bubbles within the range of 0.001 to 0.5 *mm*, where the majority of them were approximately of 0.04 *mm*.

For an individual, isolated small bubble ($d < 0.1$ *mm*), which is approximately a sphere due to the surface tension being the dominant effect on its shape, Stokes' law gives accurate description of hydrostatic, bubble-rise velocity (Stokes, 1880):

$$v_h = \frac{2}{9} \frac{g(\rho_w - \rho_a)}{\mu_w} d^2 \quad (6-A1)$$

where d is equivalent air-bubble diameter and μ_w is water viscosity. For spherical bubbles with diameters less than a millimeter, the rise velocity is approximated by (Bhaga and Weber, 1981; Kulkarni and Joshi, 2005):

$$v_h = \frac{1}{18} \frac{g(\rho_w - \rho_a)}{\mu_w} d^2 \quad (6-A2)$$

For bubble sizes larger than 1 *mm*, various relations have been suggested (e.g. Kulkarni and Joshi, 2005):

$$v_h = \sqrt{\frac{2.14\sigma}{\rho_w d} + 0.52gd} \quad (6-A3)$$

where σ is surface tension between water and air. In the above relation, “ d ”, the equivalent air bubble diameter is correlated to the *bubble chord length* (Clark and Turton, 1988). Bubble chord length distribution follows a gamma shape distribution with a peak size around 1 mm (Chanson, 1996, page 157; Waniewski, 2001; Chanson 2004, page 367). The concept of d loses its meaning in regions where $C > 0.25$. Murzyn et al. (2005) found that in hydraulic jumps the distribution of bubble diameters does not influenced by the Froude number or vertical position and bubbles have an almost uniform size of around 4 mm everywhere.

Chapter Six References

1. Abbott, M. B., Marshall, G., and Rodenhuis, G. S. (1969). “Amplitude-dissipative and phase-dissipative scheme for hydraulic jump simulation.” 13th Congress IAHR, (Int. Assoc. of Hydr. Res.). Tokyo, Japan, 1: 313-329.
2. Air Entrainment”, in Proc. XXXI IAHR Congress, Seoul, Korea,
3. Allen, M. B., Herrera, I., and Pinder G. F. (1988). “Numerical modeling in science and engineering.” John Wiley & Sons, Inc.
4. Babb, A. F., and Aus, H. C. (1981). “Measurements of air in flowing water.” J Hydraul Div ASCE 107(2): 1615–1630.
5. Bélanger, J. B. (1828). “Essai sur la Solution Numérique de quelques Problèmes Relatifs au Mouvement Permanent des Eaux Courantes.”, Carilian-Goeury, Paris, France, (in French).
6. Bellomo, N., and Dogbe C. (2011), “On the modeling of traffic and crowds: A survey of models, speculations, and perspectives.” SIAM Rev., 53(3), 409-463.
7. Bhaga, D., and Weber M. E. (1981). “Bubbles in viscous liquids: shapes, wakes and velocities.” J. Fluid Mech., 105:61-85, doi: 10.1017/S002211208100311X.
8. Buscaglia, G.C., Bombardelli, F.A. and García, M.H. (2002). “Numerical modeling of large-scale bubble plumes accounting for mass transfer effects.” Int. J. Multiphase Flow, 28, pp. 1763-1785.
9. Camacho, V., R.D. Guy, and J. Jacobsen (2008), Traveling waves and shocks in a viscoelastic generalization of Burgers' equation, SIAM J. Appl. Math., 68, 1316-1332. Fclift
10. Carollo, F., Ferro, V., and Pampalone, V. (2012). “New Expression of the Hydraulic Jump Roller Length.” J. Hydraul. Eng., 138(11), 995–999. doi: 10.1061/(ASCE)HY.1943-7900.0000634.

11. Chachereau, Y., and Chanson, H. (2011). “Bubbly flow measurements in hydraulic jumps with small inflow Froude numbers.” *Int. J. Multiphase Flow*, 37:555–564.
12. Chanson, H. (1995). “Air bubble entrainment in free surface turbulent flow.” Report CH46/95, Department of Civil Engineering, University of Queensland.
13. Chanson, H. (1997). “Air bubble entrainment in free-surface turbulent shear flows.” Academic Press, London, UK, p. 401.
14. Chanson, H. (2009). “Current Knowledge in hydraulic jumps and related phenomena. A survey of experimental results.” *European Journal of Mechanics B/Fluids* 28: 191-210.
15. Chanson, H. (2010). “Convective transport of air bubbles in strong hydraulic jumps.” *Int. J. Multiphase Flow*, 36: 798–814.
16. Chanson, H., and Brattberg, T. (2000). “Experimental study of the air-water shear flow in a hydraulic jump.” *Int. J. Multiphase Flow*, 26:583–607.
17. Chanson, H., and Gualtieri, C. (2007). “Experimental analysis of Froude number effect on air entrainment in the hydraulic jump.” *Environ. Fluid Mech.*, 7: 217-238.
18. Chanson, H., and Qiao, G. L. (1994). “Air bubble entrainment and gas transfer at hydraulic jumps.” Research Report No. CE149. Department of Civil Engineering University of Queensland, Australia. P. 68.
19. Chippada, S., Ramaswamy, B., and Wheeler, M.F. (1994). “Numerical simulation of hydraulic jump.” *Int. J. for Numer. Methods Eng.*, 37: 1381 -1397.
20. Chow, V.T. (1959). “Open Channel Hydraulics.” McGraw–Hill.
21. Clark, N.N., and Turton, R. (1988). “Chord length distributions related to bubble size distributions in multiphase flows.” *Int. J. Multiphase Flow*, 14(4): 413-424.

22. Clift, R., Grace, J.R., & Weber, M.E. (2005). "Bubbles, drops, and particles." Courier Corporation.
23. Crowe, C.T., Schwarzkopf, J.D., Sommerfeld, M., and Tsuji, Y. (2012). "Multiphase flows with droplets and particles." 2nd edition, CRC Press.
24. Debnath, L. (2012), Nonlinear Partial Differential Equations for Scientists and Engineers, 2nd Ed., Birkhauser.
25. Drew, D. A., and Passman, S. L. (1999). Theory of multicomponent fluids.
26. Gonzalez, A. and Bombardelli, F. (2005) "Two-Phase Flow Theory and Numerical Models for Hydraulic Jumps, Including Air Entrainment", In Proc. XXXI IAHR Congress, Seoul, Korea.
27. Hager, W. H. (1992). "Energy dissipators and hydraulic jumps." Kluwer Academic, MA.
28. Hager, W.H., Bremen, R., and Kawagoshi, N. (1990). "Classical hydraulic jump: length of roller." Journal of Hydraulic Research, 28(5): 591-608.
29. Hager, W.H., Vischer, D.L. (Eds.) (1995). "Energy dissipaters". IAHR Hydraulic Structures Design Manual 9. Rotterdam; Brookfield; A.A. Balkema.
30. Jha, S.K., and Bombardelli, F. A. (2010). Toward two-phase flow modeling of nondilute sediment transport in open channels. Journal of Geophysical Research: Earth Surface, 115(F3).
31. Kalinske, A.A., and Robertson, J. M. (1943). "Closed conduit flow." Transactions, ASCE, 108, 1435-1447.
32. Kiger, K.T., and Duncan, J. H. (2012). "Air-entrainment mechanisms in plunging jets and breaking waves." Annu. Rev. Fluid Mech., 44:563–96.

33. Kulkarni, A.A., and Joshi, J. B. (2005). "Bubble formation and bubble rise velocity in gas-liquid systems: a review." *Ind. Eng. Chem. Res.*, 44: 5873-5931.
34. Leandro, J., Carvalho, R., Chachereau, Y., and Chanson, H. (2012). "Estimating void fraction in a hydraulic jump by measurements of pixel intensity." *Exp. Fluids*, 52:1307–1318, doi 10.1007/s00348-011-1257-1.
35. Lemos, C.M. (1992). "A simple numerical technique for turbulent flows with free surfaces." *Int. J. Numer. Methods Fluids*, 15:127-146.
36. Liu, M., Rajaratnam, N. and Zhu, D. (2004). "Turbulence structure of hydraulic jumps of low Froude number." *J. Hydraul. Eng.*, 130: 511-520.
37. Ma, J., Oberai, A.A., Lahey, R.T., and Drew, D.A. (2011). "Modeling air entrainment and transport in a hydraulic jump using two-fluid RANS and DES turbulence models." *Heat Mass Transfer*, 47:911–919, doi: 10.1007/s00231-011-0867-8.
38. Michaelides, E.E. (2006) *Particles, Bubbles and Drops – Their Motion, Heat and Mass Transfer*, World Scientific Publishers, New Jersey.
39. Mortazavi, M., Le Chenadec, V., (2014) "Numerical simulation of a turbulent hydraulic jump: Characterization of the free interface and large bubble structure." Annual Research Report. Center for Turbulence Research
40. Mossa, M., and Tolve, U. (1998). "Flow visualization in bubbly two-phase hydraulic jump." *J. Fluids Eng.*, 120:160–165.
41. Murzyn, F., Mouaze, D., and Chaplin, J. R. (2005). "Air–water interface dynamic and free surface features in hydraulic jumps." *Journal of Hydraulic Research*, 45:5, 679-685.
42. Murzyn, F., Mouaze, D., and Chaplin, J. R. (2005). "Optical fibre probe measurements of bubbly flow in hydraulic jumps." *Int. J. Multiphase Flow*, 31:141–154.

43. Muste, M., Yu, K., Fujita, I., & Ettema, R. (2009). Two-phase flow insights into open-channel flows with suspended particles of different densities. *Environmental fluid mechanics*, 9(2), 161-186.
44. Nasser, M., Daneshbod, Y., Pirouz, M., Gh. R. Rakhshandehroo, and Shirzad, A. (2012). "New Analytical Solution to Water Content Simulation in Porous Media." *J. Irrig. Drain Eng.*, 138(4), 328–335. doi: 10.1061/(ASCE)IR.1943-4774.0000421.
45. Olesen, P. (2003), An integrable version of burgers equation in "Magnetohydrodynamics", *Physical Review E*, 68, 016307.
46. Passalacqua, P., F. Porte-Agel, E. Foufoula-Georgiou, and C. Paola (2006). "Application of dynamic subgrid-scale concepts from large-eddy simulation to modeling landscape evolution." *Water Resource Research*, 42, W06D11, doi:10.1029/2006WR004879.
47. Rahman, M. M., Faghri, A., and Hankey, W. L. (1991). "Computation of turbulent flow in a thin liquid layer of fluid involving a hydraulic jump." *J. Fluids Eng.*, 113(3): 411-419.
48. Rajaratnam, N. (1962). "An experimental study of air entrainment characteristics of the hydraulic jump." *J. Inst. Eng. India*, 42:247–273.
49. Rayleigh, L. (1914). "On the theory of long waves and bores." *Proc. R. Soc. Lond. A* 90, 324–328.
50. Resch, F., Leutheusser, H., and Alemum, S. (1974). "Bubbly two-phase flow in hydraulic jump." *J. Hydraul. Div. ASCE*, 100:137–149.
51. Sachdev, P. L. (2008). "Nonlinear diffusive waves." Cambridge University Press.
52. Sandstrom, H., and N. S. Oakey (1995). "Dissipation in internal tides and solitary waves." *J. Physical Oceanography*, 25, 604–614.
53. Stokes, G. G. (1880). "Mathematical and physical papers." 1, Cambridge University Press.

54. Thandaveswara B. S. (1974). "Self aerated flow characteristics in developing zones and in hydraulic jumps." PhD Thesis, Department of Civil Engineering, Indian Institute of Science, Bangalore, India, p. 399.
55. Valle', B. L., and Pasternack G. B. (2002). "TDR measurements of hydraulic jump aeration in the South Fork of the American River, California." *Geomorphology*, 42(1–2), 153– 165.
56. Valle', B. L., and Pasternack, G. B. (2006). "Air concentrations of submerged and unsubmerged hydraulic jumps in a bedrockstep-pool channel." *J. Geophys. Res.*, 111, F03016, doi: 10.1029/2004JF000140.
57. Wang, H. and Chanson, H. (2015). "Experimental Study of Turbulent Fluctuations in Hydraulic Jumps." *J. Hydraul. Eng.*, 141(7), 04015010.
58. Waniewski, T. A., Hunter, C., and Brennen C. E. (2001). "Bubble measurements downstream of hydraulic jumps." *Int. J. Multiphase Flow*, 27, 1271–1284.
59. Warrick, A. W., and G. W. Parkin (1995). "An analytical solution for one-dimensional drainage: Burgers' and simplified forms." *Water Resour Res*, 31, 2891– 2894.
60. Zamani, K., and Bombardelli, F. A. (2014). "Analytical solutions of nonlinear and variable-parameter transport equations for verification of numerical solvers." *Environ. Fluid Mech.*
61. Zhang, G., Wang, H., & Chanson, H. (2013). Turbulence and aeration in hydraulic jumps: free-surface fluctuation and integral turbulent scale measurements. *Environmental fluid mechanics*, 13(2), 189-204.

Figures:

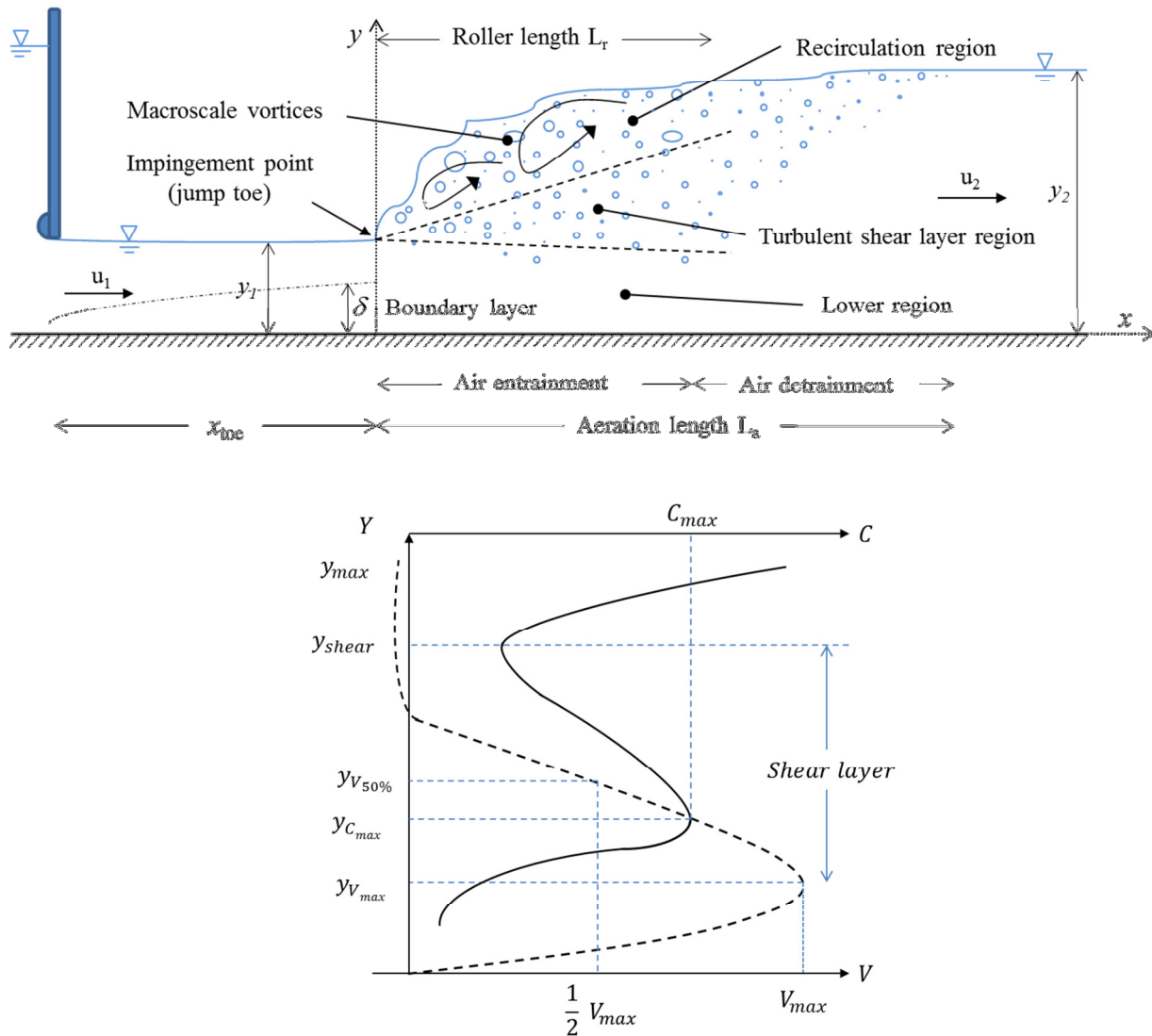


Figure 6-1. Schematic of air concentrations in hydraulic jumps; Top) we use x to denote the stream-wise direction, and y to the vertical direction. Hager et al. (1990) and Hager (1992) suggested $L_r = y_1 \left(160 \tanh \left(\frac{Fr_1}{20} \right) - 12 \right)$ and $L_a = y_2 (3.5 \sqrt{Fr_1 - 1.5})$ for roller length and aeration length of hydraulic jump based on upstream Froude number. Carollo et al. (2012) recommended a relation based on the ratio of upstream and downstream depths for roller length as: $L_r = \frac{2.244}{\left(\frac{y_1}{y_2} \right)^{1.272}}$. Murzyn et al. (2007) found linear relations for L_r based on Froude and Weber numbers as: $L_r = 7.5 y_1 (Fr_1 - 1.3)$ and $L_r = 0.17 y_1 We_1$. Hager (1992) stated that maximum air concentration occurs near to jump toe at $x_{c_{max}} = \frac{1}{9} L_a$. Bottom) A schematic of velocity and air-concentration distribution in depth after (Chachereau and Chanson, 2011).

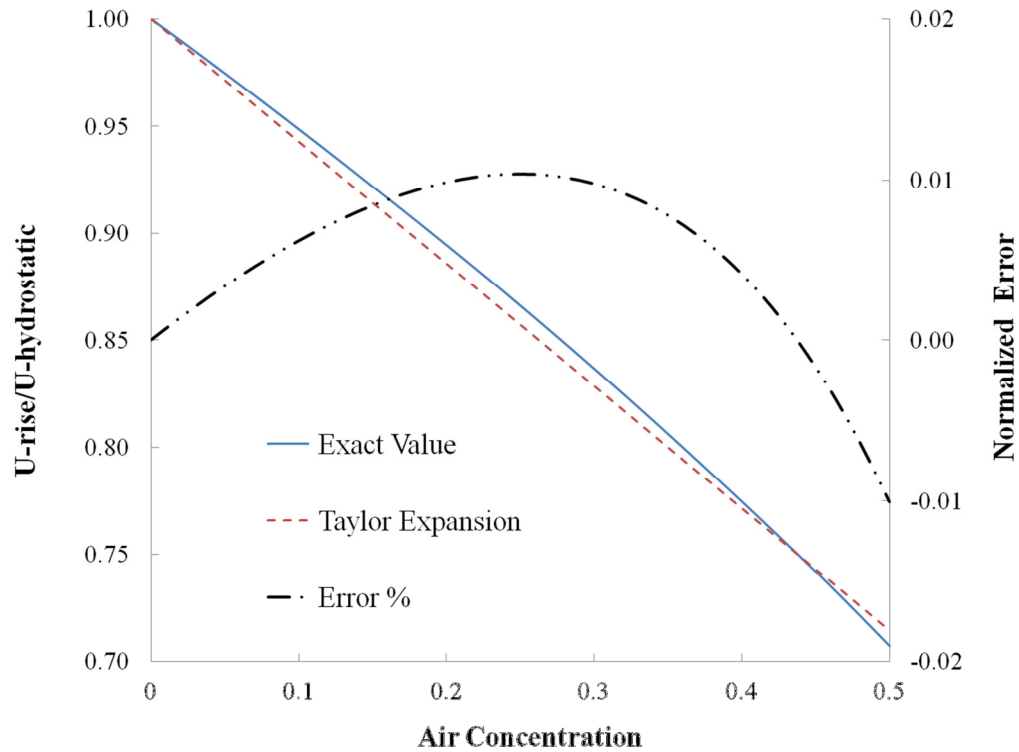


Figure 6-2. Approximation $\sqrt{1 - c}$ with the first two terms of Taylor series expansion, exact value (solid blue) versus approximated (maroon color dashed line), normalized truncation error versus concentration (right axes).

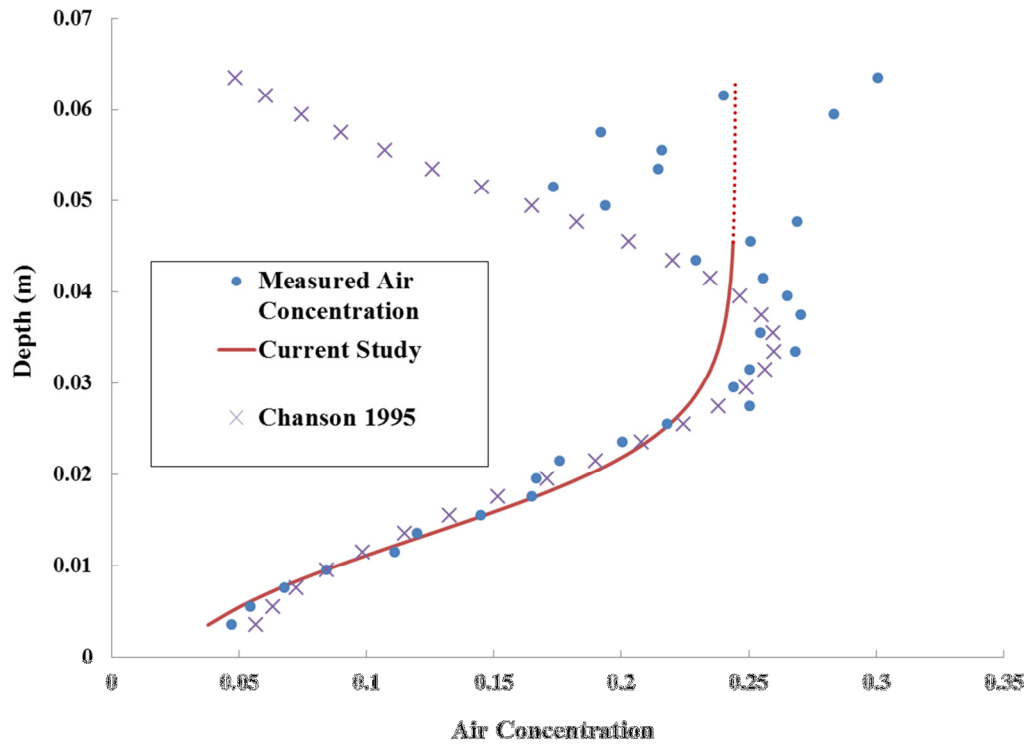


Figure 6-3. Comparison of air distribution in depth at location $x - x_{toe} = 0.2 \text{ m}$ from the jump toe, analytical solution (solid line) versus measurements (dots), and former formula by Chanson (1995), (cross). Run T8-5 by Chanson and Brattberg (2000); $Fr = 8.48$.

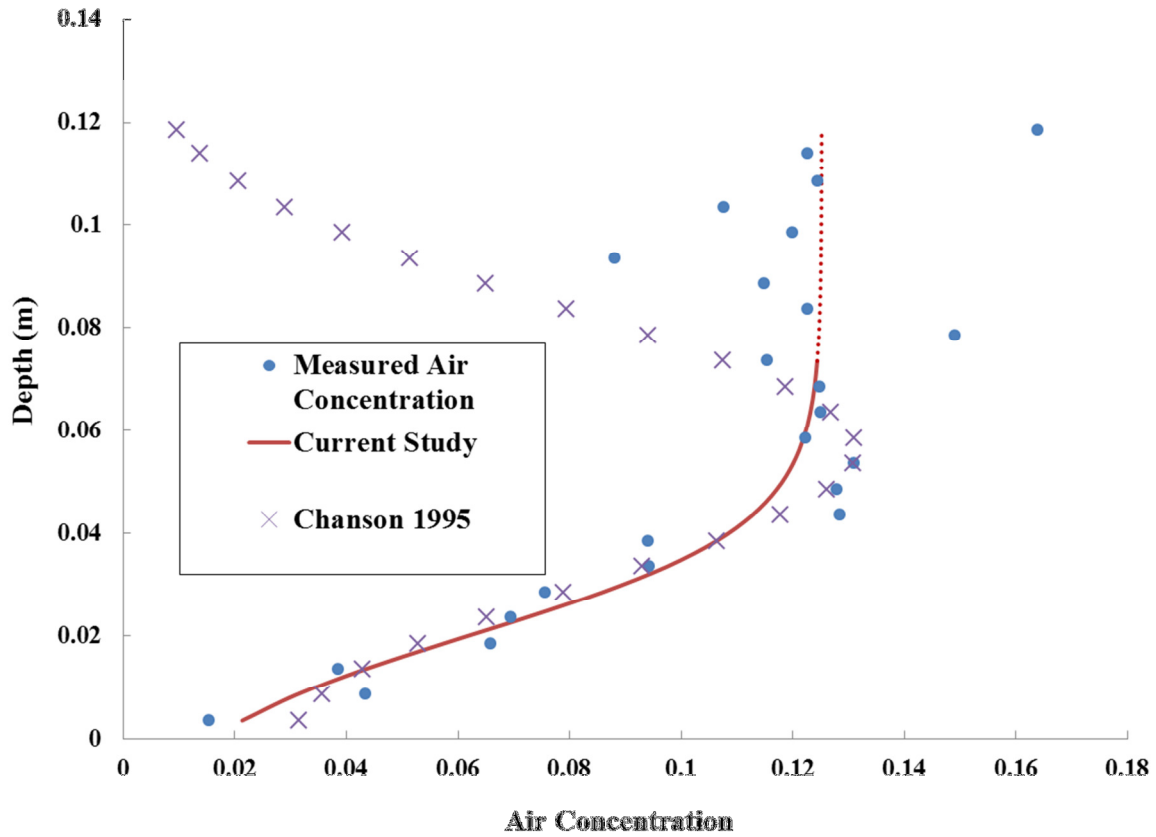


Figure 6-4. Comparison of air distribution in depth at location $x - x_{toe} = 0.4 \text{ m}$ from the jump toe, analytical solution (solid line) versus measurements (dots) and former formula by Chanson (1995), (cross). Run T8-5 by Chanson and Brattberg (2000), $Fr = 8.48$.

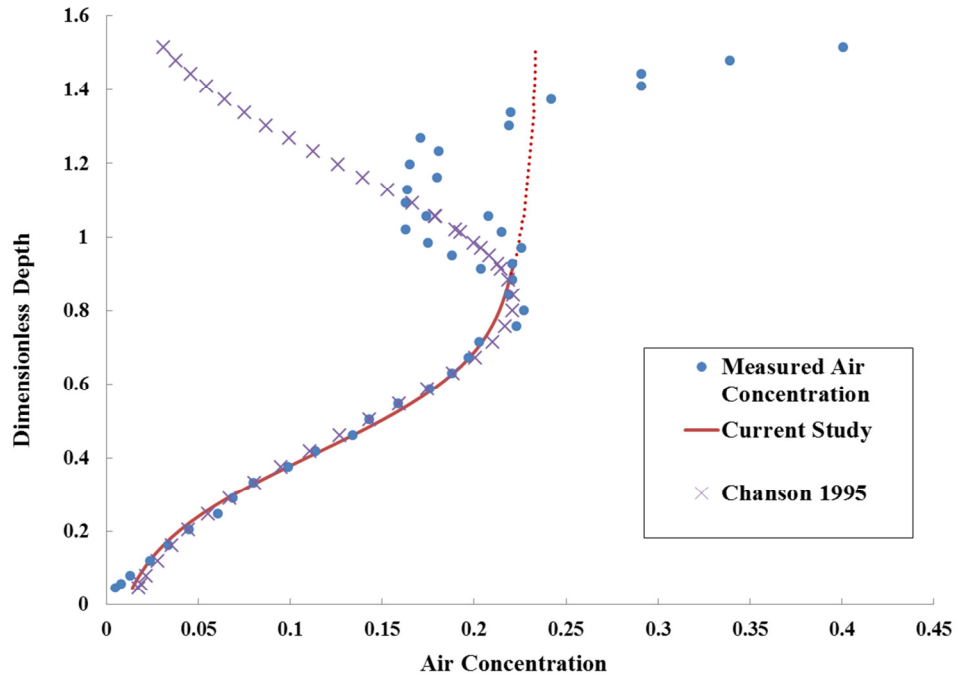


Figure 6-5. Comparison of air distribution in depth at location $x - x_{toe} = 0.07 \text{ m}$ from the jump toe, analytical solution (solid line) versus measurements (dots) and former formula by Chanson (1995), (cross). Run P10-C5, $Fr = 6.05$, (Chanson 1995).

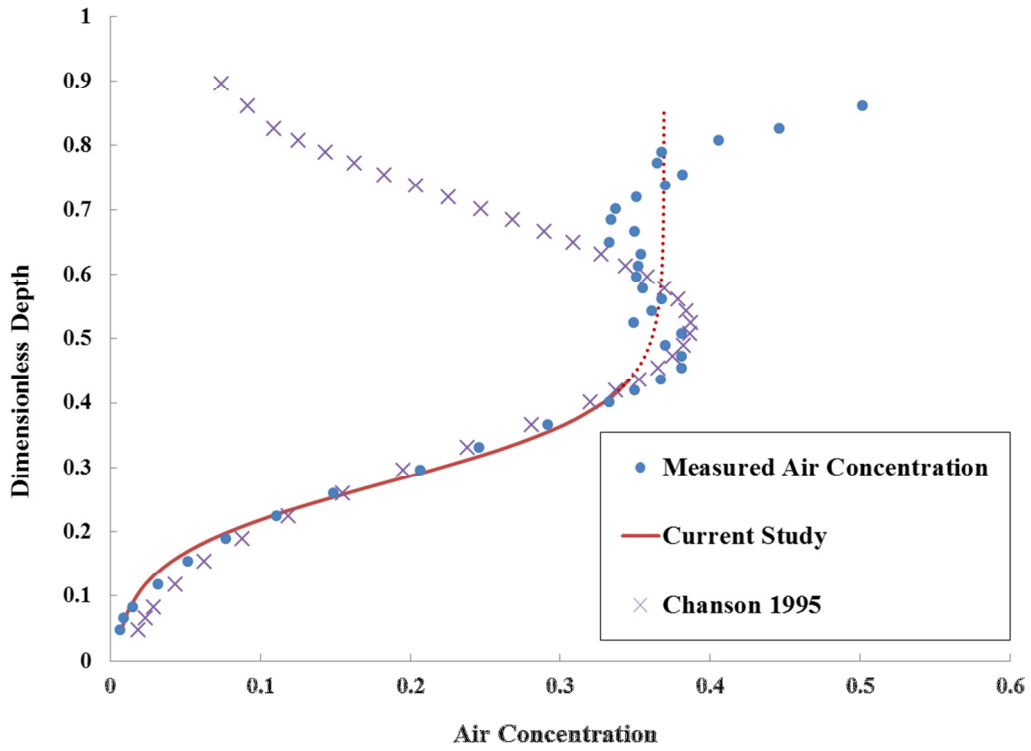


Figure 6-6. Comparison of air distribution in depth at location $x - x_{toe} = 0.1 \text{ m}$ from the jump toe, analytical solution (solid line) versus measurements (dots), and former formula by Chanson (1995), (cross). Run P10-C6, $Fr = 6.05$, Chanson (1995).

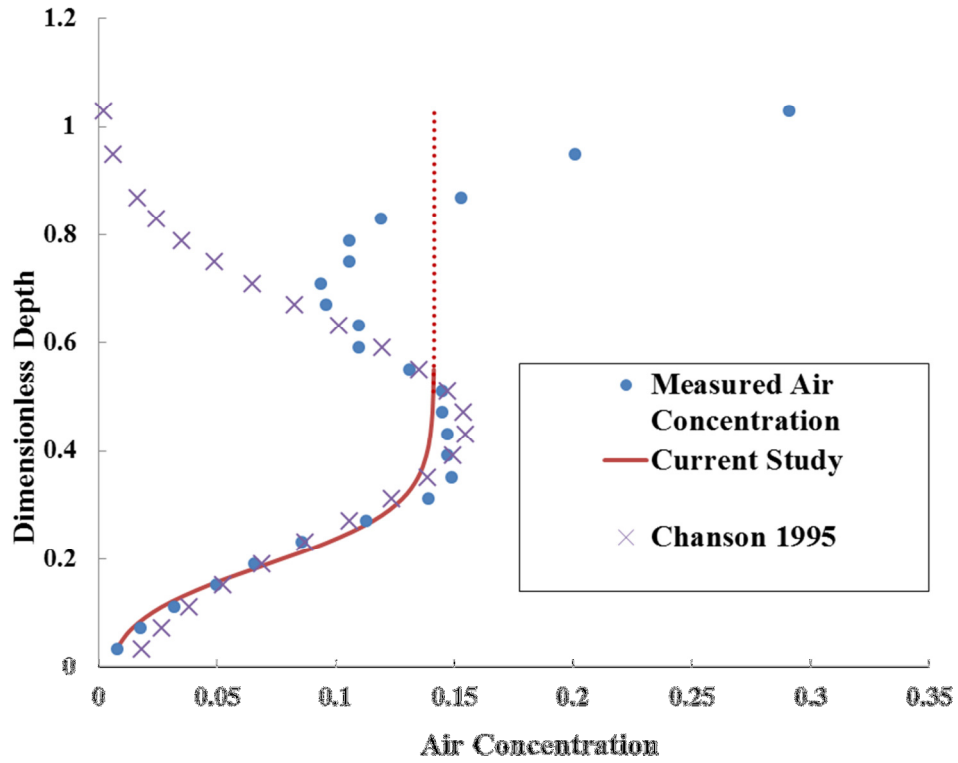


Figure 6-7. Comparison of air distribution in depth at location $x - x_{toe} = 0.2 \text{ m}$ from the jump toe, analytical solution (solid line) versus, run P10-C7 Chanson 1995 (dots), and former formula by Chanson (1995), (cross), $Fr=5.66$.

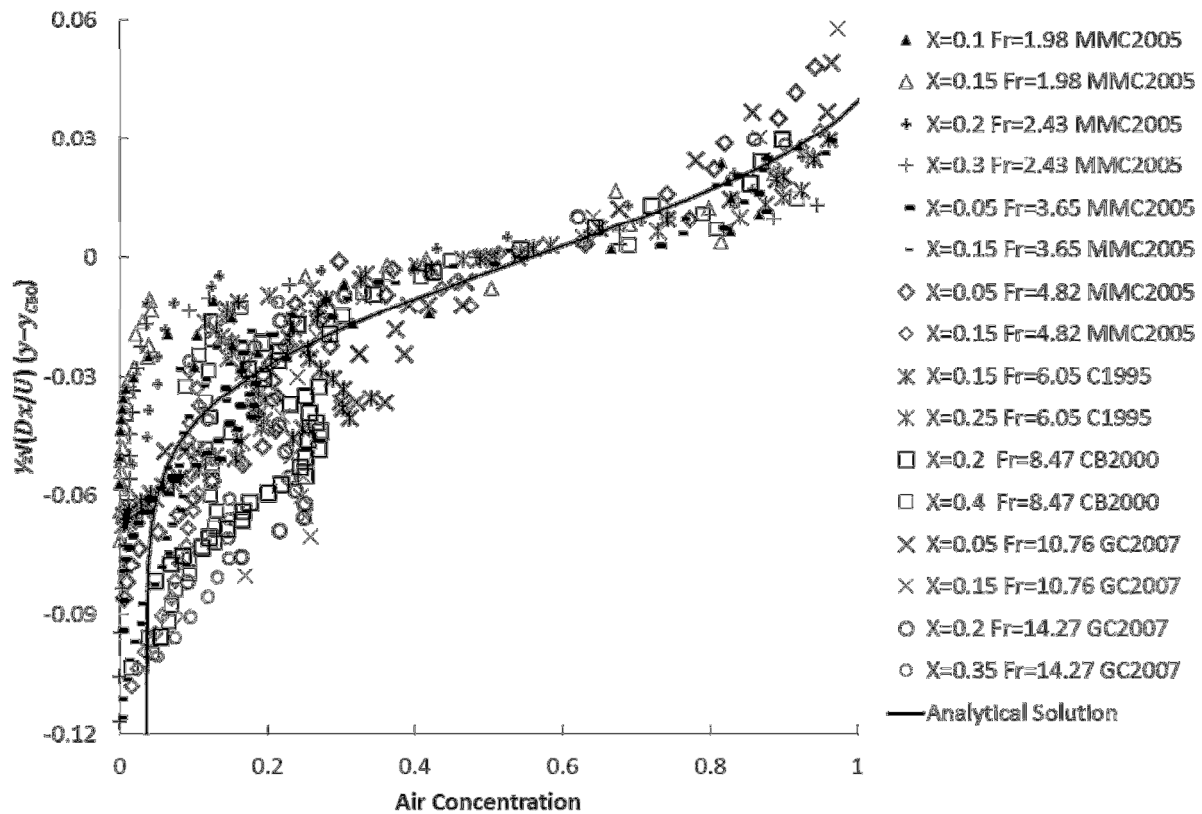


Figure 6-8. Comparison of normalized depth versus air concentration data with and analytical solution given by equation (6-22) (solid line). Froude numbers vary from 2 to 14, statistics of the comparison in the recirculation and shear layer regions are provided in Table 6-3. Datasets of $Fr=1.98$, 2.43 , 3.65 and 4.82 are tests a, b, c, and d of Murzyn et al. (2005), respectively. All data of $Fr=6.05$ were measured by Chanson (1995). $Fr=8.47$ measured by Chanson and Brattberg (2000) and $Fr=10.76$ and $Fr=14.27$ are reported by Gualtieri and Chanson (2007).

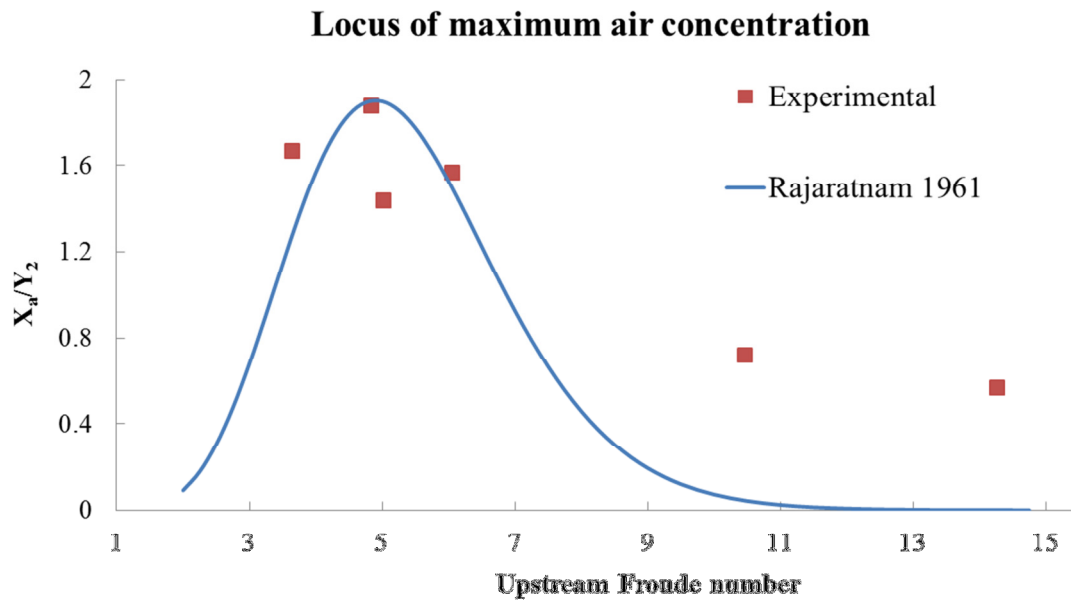


Figure 6-9. Location of maximum air concentration, experiment versus empirical formulae by Rajaratnam (1962).

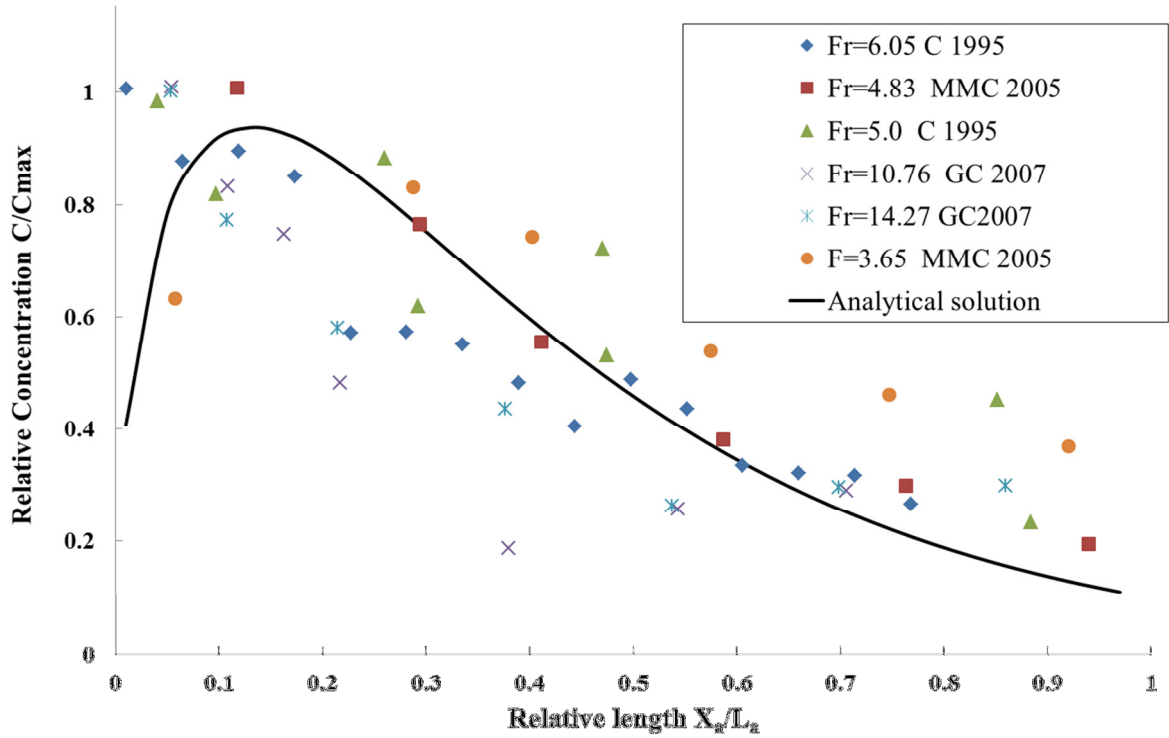


Figure 6-10. Air concentration distribution along the hydraulic jump.

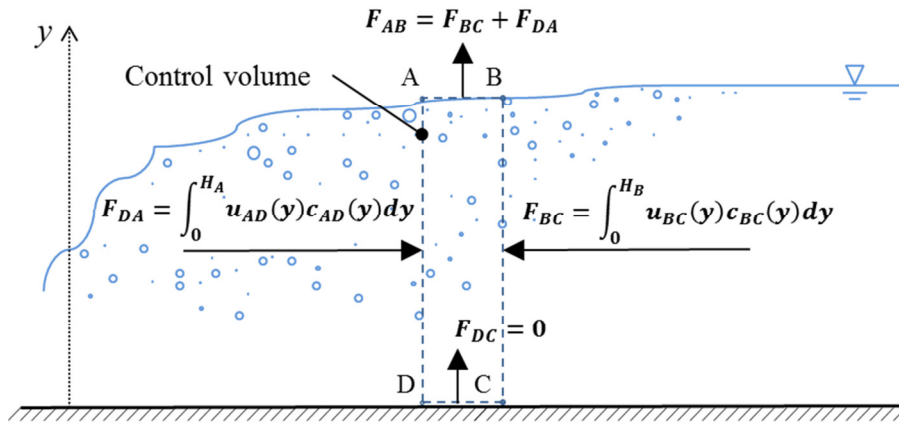


Figure 6-11. Schematic of interfacial air mass exchange calculation methodology based on mass balance.

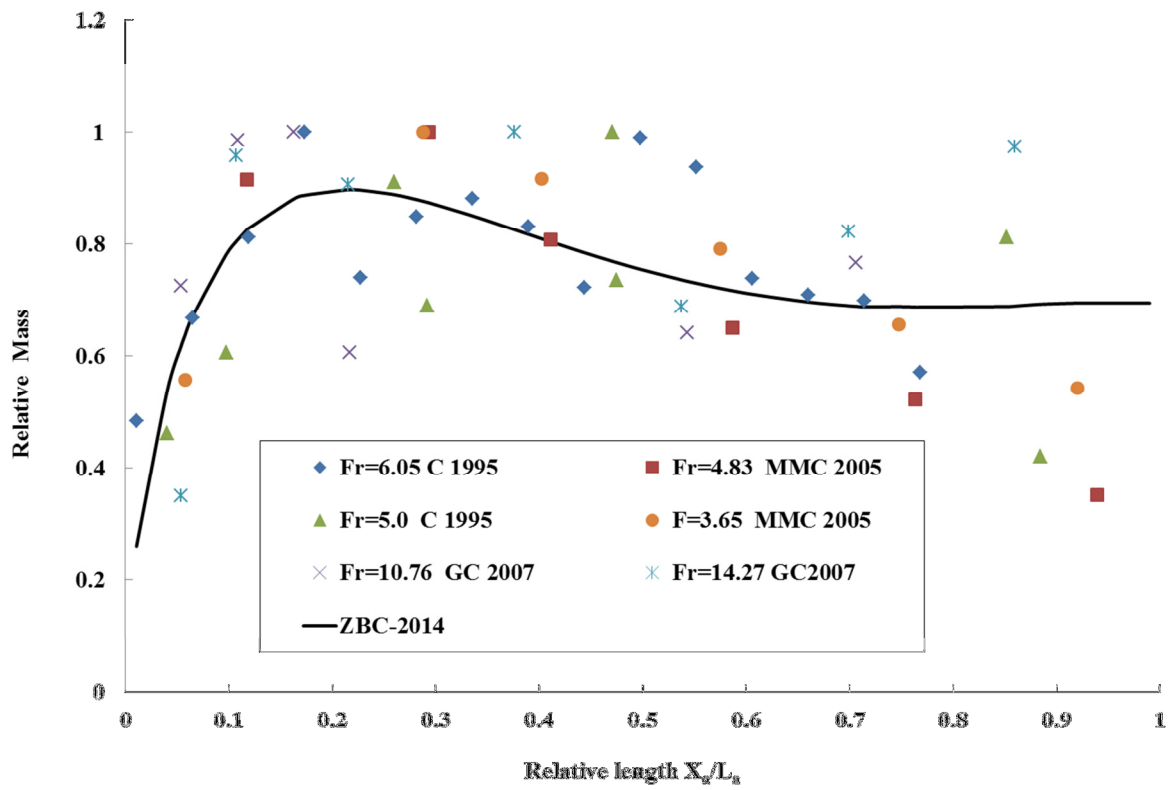


Figure 6-12. Entrapped air mass distribution along the hydraulic jump.

Table 6-1. Summary of experimental investigations of hydraulic jump with particular emphasis on air entrainment.

Study	Flow Conditions	Measurement technique
Rajaratnam (1962)	$Fr_1 = 2.42 - 8.72$, $d_1 = 0.025\text{ m}$, $W = 0.305\text{ m}$	Electric resistive probe calibrated against Saint Antony Falls Lab benchmark for up to 20% air concentration only
Resch et al. (1974)	$Fr_1 = 3.0 - 8.0$, $d_1 = 0.012 - 0.039\text{ m}$, $W = 0.39\text{ m}$	Hot-film anemometry DISA 55A87 (0.6 mm sensor)
Thandaveswara (1974)	$Fr_1 = 7.16 - 13.31$, $d_1 = 0.010 - 0.152\text{ m}$ partially developed inflow conditions	Dual tip conductivity probe
Babb and Aus (1981)	$Fr_1 = 6.0$, $d_1 = 0.035\text{ m}$, $W = 0.46\text{ m}$	Conical hot-film anemometry DISA 55R42 (0.4 mm sensor)
Hoyt and Sellin (1989)	$Fr_1 = 2.5 - 3.5$, $W = 0.105\text{ m}$, $d_1 = 0.035\text{ m}$	Drag-reducing additive polyacrylamide, photograph and visual observation
Chanson and Qiao (1994)	$Fr_1 = 5.0 - 8.1$, $d_1 = 0.016 - 0.17\text{ m}$, $W = 0.25\text{ m}$ partially developed inflow conditions	Single tip conductivity probe (0.35 mm inner electrode)
Mossa and Tolve (1998)	$Fr_1 = 6.42 - 7.33$, $d_1 = 0.185 - 0.020\text{ m}$, $W = 0.40\text{ m}$ partially developed inflow conditions	Image processing
Chanson and Brattberg (2000)	$Fr_1 = 6.33 - 8.48$, $d_1 = 0.014\text{ m}$, $W = 0.25\text{ m}$, partially developed inflow conditions	Dual tip conductivity probe (25 μm inner electrode)
Waniewski et al. (2001)	$Fr_1 = 11.5 - 19.3$, $d_1 = 0.32 - 0.6\text{ cm}$, $W = 0.152\text{ m}$, partially developed inflow	Phase Doppler anemometry
Murzyn et al. (2005)	$Fr_1 = 2.0 - 4.8$, $d_1 = 0.021 - 0.059\text{ m}$, $W = 0.30\text{ m}$ partially developed inflow conditions	Dual tip optical fiber sensors
Valle and Pasternack ^a (2002)	Three cases of submerged jump, strong free surface jump and large free surface jump with $Q = 40 - 85\text{ m}^3\text{s}^{-1}$	Field measurement with TDR probe
Valle and Pasternack ^b (2006)	$W \sim 2\text{ m}$, $Fr = 1.2 - 2$, bedrock step pool channel, submerged and sloping jumps	Dual-rod CS615 probe

Gualtieri and Chanson (2007)	$Fr_1 = 2.0 - 4.8$, partially developed inflow conditions	$d_1 = 0.012\ m$,	$W = 0.25\ m$,	Single tip phase-detection probe (0.35 mm)
Chanson (2010)	$Fr_1 = 5.1 - 11.2$, 0.5 m partially developed inflow conditions	$d_1 = 0.017 - 0.019\ m$,	$W =$	Dual tip phase-detection probe (0.25 mm)
Leandro et al. (2012)	$Fr_1 = 4.4 - 5.1$, partially developed inflow conditions	$d_1 = 0.039\ m$,	$W = 0.50\ m$	Dual tip conductivity probe (0.25 mm inner electrode) and bubble image velocimetry (BIV)
Lin et al. (2012)	$Fr_1 = 2.43 - 5.35$, 0.5 m	$d_1 = 1.92 - 2.00\ cm$	$W =$	PIV for flow and BIV for air

^{a)} The study was conducted in a natural stream with mixed alluvial-bedrock section in South Fork American River; Upper Chili Bar, Little Maya, and First Threat, three station downstream of Chili Bar Dam, California. ^{b)} The study region was a bedrock natural stream in upper South Fork American River basin, Sierra Nevada, California.

Table 6-2. Flow and measurement condition of experimental data which is used for validation of equations (6-18) and (6-22).

Reference and Run	W (m)	Q (L/S)	x_{toe} (m)	y_1 (m)	u_1 (m/S)	Fr_1	We	Re	Instrumentation
Chanson (1995) test P10	0.25	10.5	0.89	0.017	2.47	6.05	36.5	4.2×10^4	Single-tip phase-detection probe ($\emptyset = 0.35$ mm)
Chanson and Brattberg (2000) test T8-5	0.25	10.99	0.50	0.014	3.14	8.47	42.1	4.4×10^4	Dual-tip phase-detection probe ($\emptyset = 0.025$ mm)
Murzyn et al. (2005) test a	0.30	26.55	0.43	0.059	1.50	1.98	41.3	8.8×10^4	Dual-tip phase detection probe ($\emptyset = 0.01$ mm)
Murzyn et al. (2005) test b	0.30	22.63	0.44	0.046	1.64	2.44	39.9	7.5×10^4	Dual-tip phase detection probe ($\emptyset = 0.01$ mm)
Murzyn et al. (2005) test c	0.30	19.68	0.34	0.032	2.05	3.66	41.6	6.5×10^4	Dual-tip phase detection probe ($\emptyset = 0.01$ mm)
Murzyn et al. (2005) test d	0.30	13.80	0.36	0.021	2.19	4.83	36.0	4.6×10^4	Dual-tip phase detection probe ($\emptyset = 0.01$ mm)
Gualtieri and Chanson (2007) run 7/2/2006	0.25	12.20	0.50	0.013	3.813	10.76	48.91	4.9×10^4	Single-tip phase-detection probe ($\emptyset = 0.35$ mm)
Gualtieri and Chanson (2007) run 8/2/2006	0.25	14.50	0.50	0.012	4.874	14.26	60.28	5.8×10^4	Single-tip phase-detection probe ($\emptyset = 0.35$ mm)

Table 6-3. Validation statistics of new analytical solution (6-18) for lower region compared to observation and numerical simulation.

Validation Benchmark	Lower region			Shear layer		
	SI (%)	Bias	R ²	SI (%)	Bias	R ²
CFD model, $x = 0.4$ m, Waltz (2009)	3.41	0.042	0.907	20.01	0.019	0.619
Test T8-5, $x = 0.2$ m, Chanson and Brattberg (2000)	8.10	-0.006	0.967	23.50	-0.0003	0.652
Test T8-5, $x = 0.4$ m, Chanson and Brattberg (2000)	9.48	-0.0009	0.945	14.0	-0.0005	0.532
Test P10, $x = 0.07$ m, Chanson (1995)	4.84	-0.0005	0.994	14.74	0.0027	0.683
Test P10, $x = 0.1$ m, Chanson, (1995)	6.22	-0.002	0.994	7.39	-0.0005	0.663
Test P10, $x = 0.2$ m, Chanson, (1995)	11.0	-0.0002	0.948	33.7	-0.0003	0.558

Table 6-4. Validation statistics of upper part analytical solution (6-22) compared to observation and numerical simulation.

Validation Benchmark	Recirculation region			Shear layer		
	SI (%)	Bias	R ²	SI (%)	Bias	R ²
All 541 Data points	8.9	0.013	0.909	55.6	0.166	0.735
Chanson (1995) test P10	4.1	-0.067	0.937	43.2	-0.102	0.566
Chanson and Brattberg (2000) test T8-5	11.47	0.02	0.990	49.2	0.147	0.638
Murzyn et al. (2005) test a	4.57	-0.02	0.944	76.2	0.259	0.76
Murzyn et al. (2005) test b	8.84	0.006	0.955	77.1	0.277	0.72
Murzyn et al. (2005) test c	7.11	-0.025	0.874	67.47	0.206	0.707
Murzyn et al. (2005) test d	4.97	0.004	0.961	56.2	0.176	0.813
Gualtieri and Chanson (2007) run 7/2/2006	9.58	0.023	0.860	28.3	0.055	0.567
Gualtieri and Chanson (2007) run 8/2/2006	9.04	0.044	0.852	48.2	0.143	0.378

Chapter 7: Numerical Model Verification

7.1. Introduction

Growth in computational power in recent decades, in addition to cost and scale effects of physical models, increased the popularity of computational simulation in design, analysis, and optimization of engineering projects (Roache, 2009). Unfortunately, coding and simulation errors are not uncommon among computational models. These computational errors may seriously affect the professional career of a code user (see for example: Miller, 2006; Keenan, 2012) or they could end up in extreme engineering tragedies. For example, faulty numerical modeling of snowmelt led to a severe flood in Colorado River in 1983 (Hatton, 1997). Another catastrophic case happened on August 23, 1991, in the North Sea where a 700 million dollar oil rig sank due to inaccurate design of a condeep¹. Post-audit of the numerical model showed that the failure was due to a problematic finite element code computation by NASTRAN (Collins et al., 1997). The examples above strongly suggest that, without reliable “verification,” modelers should not put too much trust in numerical modeling.

In the literature of numerical modeling of Partial Differential Equations (PDEs), verification is defined as “solving the equations right” versus validation which is defined as “solving the right equations” (Roache, 1997). Verification is the set of activities which has to be done to build confidence in the results of a numerical model. Verification has two fundamental aspects: a) solver (code) verification and b) solution (calculation) verification. Solver verification is a procedure of checking the code for bugs, inconsistencies and imperfections (Roache, 2009; Oberkampf and Roy, 2010). Solver verification is a one-time activity which must be conducted by code developer(s) or whoever modifies a code for his/her particular use. There is no need to

¹ Abbr. concrete deep water structure

repeat solver verification activities unless the source code is changed. On the other hand, solution verification is the process of quantitatively assessing the error in numerical solutions which has to be performed in each and every application of the code which is considerably changed compared to each other. Solution verification is among the duties of the model user. In the following section, the techniques of verification in computational fluid mechanics are briefly discussed.

7.2. Verification Criteria for Numerical Solvers

Formal proof of correctness of a solver is not forthcoming; however, there are activities which are able to provide a framework for a reliable testing of a computer code. The criteria for code verification are suggested as follows (in order of increasing rigor, Knupp and Salari, 2003):

- Expert judgment after extensive use in wide range of problems.
- Error quantification.
- Consistency-convergence test.
- Order of convergence test.

The expert's judgment is used when results are given to an expert and he/she will assess it to make sense. This criterion is very loose and with all the respect for Dr. Patrick Knupp as one of the pioneers of "V&V" we do not recognize it as "formal" verification method. Error quantification consists in assessing misfit between numerical results and a reliable benchmark (reliable benchmark will be discussed in the rest of this section). This criterion is more advanced and objective compared to the expert's opinion; however, there are many cases in which there is a hidden bug in the code, inconsistency between parts or a mis-implementation of a solver where the issue does not amplify error such that modeler can notice that there is problem evident (for

example, see Ateljevich et al., 2011). The third level is checking if the solver results "converge" as the discretization size in time and space shrink. Finally, the most rigorous measure is similar to the third level (consistency and convergence test) while the quantitative measure of convergence is being studied. Comparing observed order of convergence with formal order of convergence of the scheme is the most restrictive verification test and many researchers agree on the extreme efficiency of this method in uncovering imperfections in coding and implementation of numerical software (Roache, 1997, 2009; Knupp and Salari, 2003; Wang et al., 2008; Graziani, 2008; Oberkampf and Roy, 2010; Ateljevich et al., 2011; Zamani and Bombardelli, 2014). The next section provides insight into the techniques of performing mesh convergence test.

7.2.1. Mesh-convergence study as a verification method

The crux of mesh convergence test is rooted in the Lax Equivalence Theorem. This theorem states that convergence implies both consistency and stability in the analysis of Finite Difference Method of numerical discretization of PDEs (Lax and Richtmyer, 1956). Later on many researchers employed the same concept of Lax Equivalence Theorem for Finite Element Method (FEM), Finite Volume Method (FVM), and Boundary Element Method (BEM) for the purpose of code verification (Roache, 2009). Mesh-convergence tests are well-accepted methods for verifying numerical solvers in computational fluid mechanics. They consist of reducing the mesh size (both spatial and time steps) and in checking the evolution of the ratio of error metrics. Grid-convergence tests check if the formal grid accuracy of the numerical scheme is reproduced by the code. Coding bugs and implementation errors could be detected via this vehicle. The question here is how to determine error when conducting mesh convergence tests since, for most of the PDEs of interest in engineering, there is no analytical solution. The general roadmap for

any verification study (solver or solution) is shown in the Figure 7-1. The first preference for conducting mesh convergence studies is the Method of Exact Solution (MES). In this method, the evolution of errors is observed based on an exact solution as a benchmark (Zamani and Bombardelli, 2014).

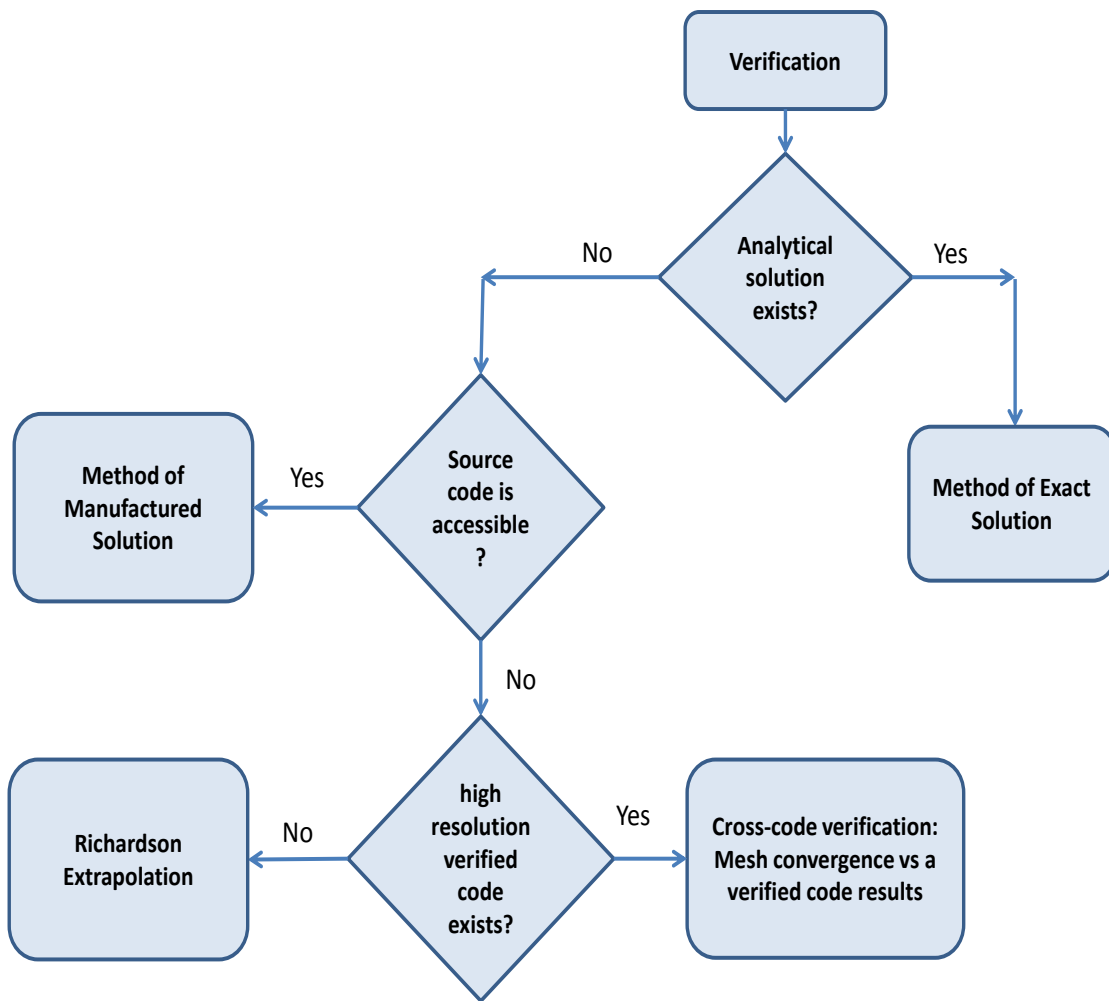


Figure 7-1. Suggested procedural flow of code verification actions in different situations.

MES is the most convenient code verification method. Unfortunately, we are not fortunate enough to have an analytical benchmark for all system of PDEs. Therefore, other alternatives of code verification should be considered. In the absence of analytical solutions, if

the source code is open to modifications, the Method of Manufactured Solution² (MMS) could be utilized (Roache, 2009; Zamani and Bombardelli, 2014). MMS has its own drawbacks and it must be performed with special care. MMS is considered a very strong error probe. If the source code is not accessible, which is the case in most of the commercial CFD packages, we have to do "Black Box Testing" (Ateljevich et al., 2011). Black Box Testing constitutes a set of practices for computational code testing in the situation where only input and output of results are available. The first common method of Black Box Testing is checking the error evolution versus the results of the exact same problem (similar initial and boundary condition) solved with higher resolution, already verified code on the dense mesh. And, finally, in the case where the corresponding analytical solution does not exist, access to the source code is restricted, and another reliable high resolution solver of the same governing equation is not available, the verification study must be performed via Richardson Extrapolation (Roache and Knupp, 1993). Careless application of the above mentioned techniques may result in vague outcomes or erroneous interpretation. The next part discusses the assumptions and prerequisites of mesh convergence studies.

7.2.2. Ambiguity in the mesh convergence test

Due to the fact that the derivation of the Lax Equivalence Theorem makes several assumptions, any violation of these assumptions may affect the results of the mesh convergence study. A modeler may find an order of convergence lower than the expected order of convergence in a simulation because of the issues not related to bugs or imperfection of the code. In the following paragraphs, we briefly discuss common pitfalls a modeler may encounter in the verification process:

² In the CFD verification literature variations of this method is called "Man Made Solution" or "Prescribed Forcing Method" which are identical to the MMS in principles.

- Smoothness of the solution: shock presence or shock formation in a numerical solution may strongly impact the convergence of the solution in various ways. For example, a shock may trigger an auxiliary numerical scheme to deal with the effect of shock (van Leer, 1979) or it may directly affect the order of global convergence measures (Zamani and Bombardelli, 2014).
- Iteration error: the final outcome of all discretizations of a PDE such as FEM, FDM, FVM, etc. is a sparse system of algebraic equations. In real scale problems, this sparse matrix is solved by iterative methods (Saad, 1996). In a mesh convergence study, it is usually assumed that the iteration error in the solution is at least two orders of magnitude lower than discretization error. However, this issue could cause crucial confusion in several cases (Roache, 2009).
- Difficulties induced by the scale of the problem: if the test problem for the mesh convergence study is chosen in such a way that one phenomenon is dominant and its effect is larger than the others in orders of magnitude, the imperfection in the low effect phenomenon may be concealed by the dominant effect. For example, code verification of a transport solver should not be performed in very low and very high Peclet numbers (Zamani and Bombardelli, 2014).
- Appropriate convergence zone: a mesh convergence study has to be done for mesh sizes which are fine enough to capture the problem completely. In coarser mesh sizes, oscillatory convergence-behavior occurs which may cause serious misinterpretations of the mesh convergence results. Figure 7-2 shows the convergence-behavior versus the mesh size.

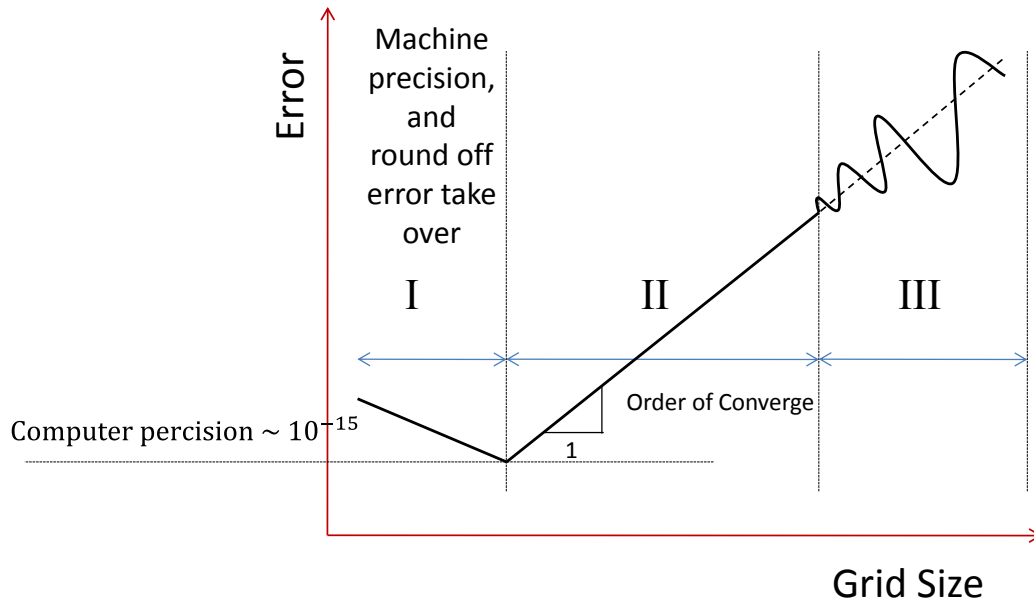


Figure 7-2. Schematic of asymptotic zone of convergence (after Graziani, 2008). In the zone one, round off error and iteration error take over; zone two is appropriate zone for numerical modeling and mesh convergence test; and zone three is mesh sizes where the problem is under resolved.

- Problem of PDE identicalness: a mesh convergence test has to be done on exactly identical differential equations which mean the exact same geometry, initial condition and boundary conditions. In that regard, implementation of boundary-fitted cells may cause problems of solving slightly different domains in a mesh convergence study (Wang et al., 2008). Other common problems in environmental fluid mechanics are cases where, with mesh refinement, a different physical problem is solved, like Large Eddy Simulation (LES) turbulence models (Roache, 1997).
- Problem of order of accuracy of other pre/post-processing algorithm(s): any extra pre-processed or post-processed value which is used in verification must be computed via a high order method. For example, in the case of Richardson Extrapolation of lid driven cavity flow

problem (example one below), since the formal convergence order of the Navier-Stokes solver we used is 2nd order, the interpolation of the fine results to the location of coarser grid points must be developed with a interpolation method of an order three or higher. Although this issue seems trivial, overlooking it may cause confusion in code verification activities.

- Nature of integrated values: the ultimate goal of any verification study is uncovering bugs or weaknesses in the model. Along that line, any fragmented information on the convergence behavior would be more fruitful than the integrated information. For example, local values of velocity convergence will reveal more information than global values of the same phenomenon. Therefore, we suggest separate analysis of the boundary and inner domain values of interest for rigorous mesh convergence studies. Global metrics for mesh convergence studies are given below.

7.2.3. Error measures and their qualification

When dealing with numbers we can identify them as being large or small. Arrays and vectors are functions of many elements but we need to measure their size - an index for them to be small or large. Norms are used as a measure in this context. Realizing that the size of a vector or matrix should depend on the magnitude of all elements in the arrays, we arrive at the definition of matrix norms. By definition, a norm is a single number that depends on the magnitude of all elements in the matrix. A norm of matrix v should satisfy the following three conditions:

$$\|v\| \geq 0 \text{ and } \|v\| \text{ if and only if } v = 0 \quad (7-1)$$

$$\|cv\| = |c|\|v\| \text{ for any scalar } c \quad (7-2)$$

$$\|v + w\| \leq \|v\| + \|w\| \text{ for matrices } v \text{ and } w \quad (7-3)$$

The following three vector/matrix norms are commonly used and called the maximum norm (infinity norm), energy norm (second norm), and first norm (taxicab norm):

$$L_{\infty} = \|v\| = \max |v_i| \quad (7-4)$$

$$L_2 = \frac{1}{n} \left(\sum_{i=1}^n |v_i|^2 \right)^{\frac{1}{2}} \quad (7-5)$$

$$L_1 = \frac{1}{n} \sum_{i=1}^n |v_i| \quad (7-6)$$

We can define v as any state variable of interest in fluid mechanics (velocity, pressure, depth, temperature, etc.) or the error between v_{num} and v_{exact} , or error between coarse and fine solution of state variables $|v_{\text{coarse}} - v_{\text{fine}}|$. L_{∞} , Equation (7-4), is the most restrictive norm for mesh convergence studies, as it produces the "worst" situation in the domain so the lower "convergence rate" will be obtained by employing this norm. In contrast, L_2 and L_1 act as a "smoother" norms, so the convergence rates obtained via these norms are less restrictive than the convergence rate calculated via the infinity norm or even the original values of the state variable of interest.

7.2.4. Observed order of accuracy

"Observed order of accuracy" is the actual order of accuracy delivered by a numerical solver (versus the "formal order of accuracy" which is the order of the employed numerical scheme). For the sake of simplicity, we assume cases in which a benchmark for error calculation exists. Calculation of the order of convergence in cases in which the exact solution is not available is conceptually similar and details can be found in Knupp and Salari (2003) or Roache

(2009). Let's assume a Taylor series expansion for the numerical solution to the discrete equation u_h based on the grid spacing h , as h goes to zero:

$$u_h = u_h|_{h=0} + h \frac{\partial u}{\partial h}|_{h=0} + \frac{h^2}{2} \frac{\partial^2 u}{\partial h^2}|_{h=0} + \dots + \frac{h^{p-1}}{(p-1)!} \frac{\partial^{p-1} u}{\partial h^{p-1}}|_{h=0} + O(h^p) \quad (4-7)$$

The above equation is the basis for calculating p (observed order of accuracy). As the mesh size tends toward zero, the higher order terms of error become negligible, therefore we may write:

$$\epsilon_h = Ch^p + O(h^{p+1}) \approx Ch^p \quad (7-8)$$

where ϵ_h is the error on the mesh size h , and C is a constant which depends on the numerical method of discretization and other factors. If we repeat the calculation for mesh size of $2h$ we would have:

$$\epsilon_{2h} \approx C(2h)^p \quad (7-9)$$

eliminating C between the above two relation we can calculate " p " (observed order of convergence) between the two mesh sizes as follows:

$$p = \frac{\ln\left(\frac{\epsilon_{2h}}{\epsilon_h}\right)}{\ln(2)} \quad (7-10)$$

This concept can be generalized to non-integer mesh refinement ratio $r = \frac{h_{\text{coarse}}}{h_{\text{fine}}}$ as well. For more details and derivation, please see Oberkampf and Roy (2010), Chapters 5 and 8.

7.3. VAVUQ: Toolkit for Verification and Validation, and Uncertainty Quantification in Environmental-Fluid-Mechanics Simulations

To conduct code and calculation verification of models of interest in Environmental Fluid Mechanics, a Matlab code was developed at the Department of Civil and Environmental Engineering of the University of California, Davis. VAVUQ has a GUI (graphical user interface) with the capability of loading, visualizing and post-processing files in text, binary and excel format. The toolkit can be utilized for the following purposes:

- Code and calculation verification studies, including: Richardson extrapolation, verification against a benchmark: MES, MMS, and Dense Mesh Solution or Cross-solver-verification. VAVUQ is able to post-process results of structured (uniform and non-uniform) and unstructured meshes. In addition, this toolkit processes the verification in integrated (globally on all cells) and disintegrated domains (point-wise, inner, and boundary cells) and provides individual log of the verification for each part (please see examples one and two).
- Model validation: VAVUQ calculates common metrics of quantitative model skill validation based on the numerical results and measured benchmark values: RMSE, Scatter Index, Bias Index and Coefficient of Determination (please see example three).
- Visualization of the error distribution over the domain via high-order spline extrapolation (please see example four below).
- Uncertainty Quantification: VAVUQ calculates the upper and lower limit of the numerical simulation error for 99% and 95% confidence in the results based on the Roache's Grid Convergence Index "GCI" (please see example five).

VAVUQ is coded in the most general form and it can be employed for verification studies of any PDE of interest in water resource engineering including: Navier-Stokes Equation, Saint-Venant's Equation, Richards Equation, Burgers' Equation, etc. In the following sections, some examples of the application of VAVUQ are presented.

7.3.1. Example one: Richardson extrapolation

A two-dimensional lid-driven cavity flow is a classical problem for code testing associated with Navier-Stokes solvers (Ghia et al., 1982). The problem domain and boundary conditions are straightforward. The standard case is a viscous fluid inside a square domain with Dirichlet boundary conditions on all sides, with three stationary sides and a moving lid (with velocity tangent to the side). The schematic of this physical set up is shown in the Figure 7-3. In this example, we solved a 2-D lid driven cavity flow with a commercial CFD code (Flow-3D).

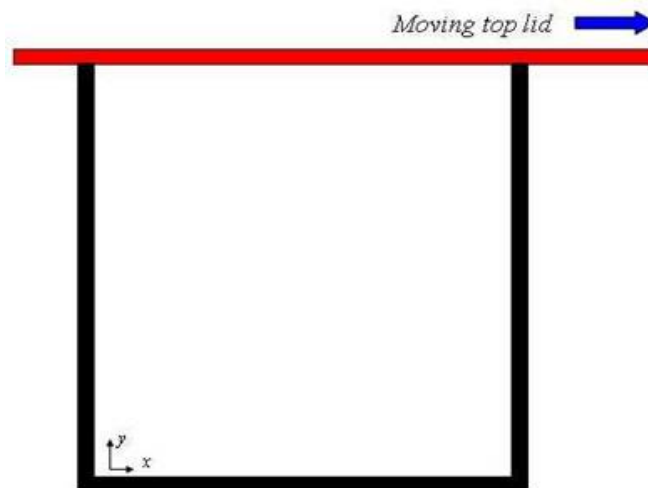


Figure 7-3. Schematic of lid-driven cavity flow (after Ghia et al., 1982)

We solved the flow with four different mesh sizes and conducted Richardson extrapolation on three state variables (pressure, x-wise velocity and y-wise velocity components) (Yuen, 2014). Given that local discontinuity may affect mesh convergence results, the study was

conducted for three categories: a) Inside the domain b) on the boundaries and, c) globally. Table 7-1 shows the formal order of convergence of the pressure and the two velocity components inside the domain, on the boundary and globally produced by VAVUQ. The results of the mesh convergence study show that in the inner-domain cells the solver almost reaches 2nd order convergence in pressure and approximately $p \approx 1.7$ in velocity simulation. However, in the boundary cells, the order of convergence dramatically drops to near zero. Direct implementation of velocity boundary condition on the boundary cells next to the lid explains why the lowest convergence ratio happens in lid-wise velocity component. Lastly, the global order of convergence is something in between the inner domain and outer skin of the domain.

Table 7-1. Convergence rates of two dimensional lid driven cavity flow on the grid resolutions of $h_4 = 92 \times 92$; $h_3 = 128 \times 128$; $h_2 = 182 \times 182$ and $h_1 = 256 \times 256$ and $r_{12} = \frac{h_1}{h_2}$; $r_{23} = \frac{h_2}{h_3}$; $r_{34} = \frac{h_3}{h_4}$.										
Refinement comparison	Variable	Inner Cells			Boundary Cells			Global		
		$P(L_1)$	$P(L_2)$	$P(L_\infty)$	$P(L_1)$	$P(L_2)$	$P(L_\infty)$	$P(L_1)$	$P(L_2)$	$P(L_\infty)$
$h_3 - h_2 - h_1$	Pressure	2.020	2.077	2.124	0.850	0.541	0.745	0.850	0.550	0.745
	u	1.750	1.645	1.679	0.249	0.017	0.825	1.205	1.300	1.406
	w	1.764	1.650	1.792	0.982	0.232	0.574	0.982	0.399	0.574
$h_4 - h_3 - h_2$	Pressure	1.943	2.026	2.116	0.910	0.560	0.774	0.910	0.568	0.773
	u	1.792	1.646	1.691	0.295	0.048	0.954	1.425	1.506	1.489
	w	1.778	1.665	1.818	1.050	0.245	0.579	1.050	0.429	0.579

7.3.2. Example two: mesh convergence test with known benchmark (MES)

In this example, VAVUQ is used to find the order of convergence of an ADR solver versus an analytical solution of advection reaction in tidal flow in a dead-end harbor. Details of the solution and implementation can be found in Zamani and Bombardelli (2014).

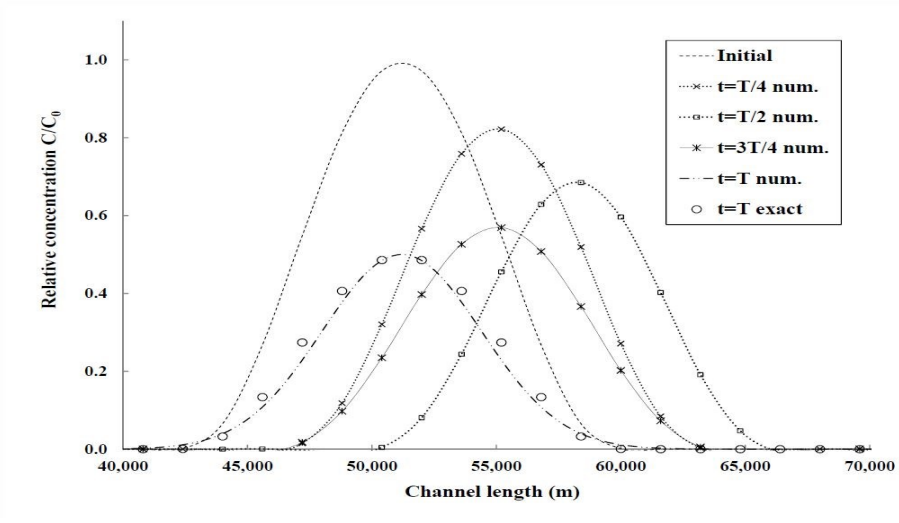


Figure 7-4. Numerical and analytical solution of concentration plume in a dead-end harbor subjected to tidal forcing (Zamani and Bombardelli, 2014).

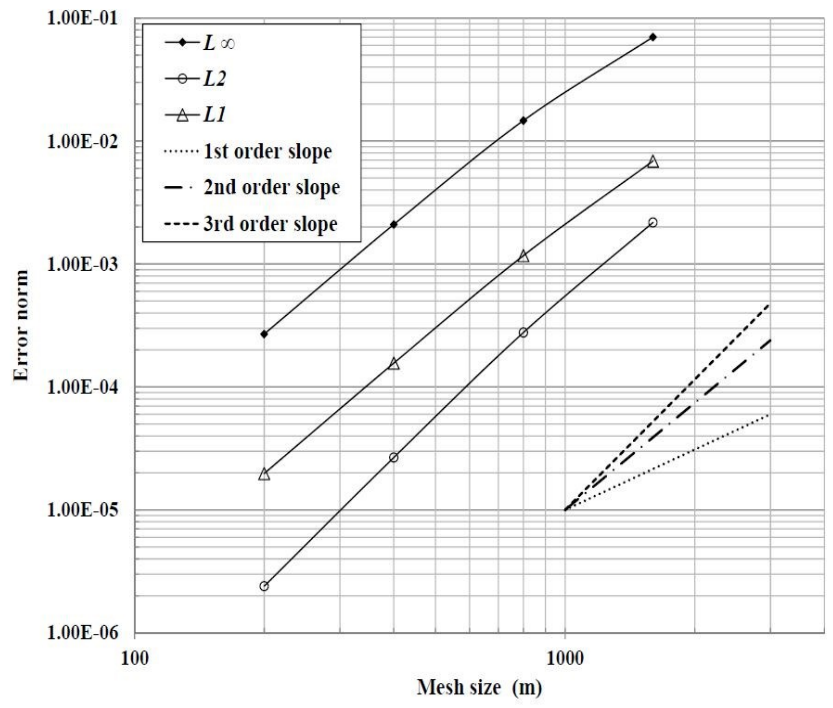


Figure 7-5. Mesh convergence study for four mesh sizes, tidal advection reaction of a pollution in dead-end harbor basin.

7.3.3. Example three: quantitative model skill assessment (validation)

In this case, VAVUQ is used for validation of a numerical simulation through comparison against laboratory measurements. The physical phenomenon is a two-phase flow of air-water mixture in hydraulic jump (Zamani and Bombardelli, unpublished). Figure 7-6 shows the profile of the free surface simulated with three different resolutions versus the measurements by Murzyn et al. (2007) at University of Southampton. VAVUQ calculated the numerical values in the positions as data points via a high-order extrapolation. Then, four common metrics of model validation were calculated to provide an objective comparison benchmark for comparison (Willmott et al., 2012; Zamani and Bombardelli, 2014). The metrics employed are as follows:

$$\text{Bias} = \frac{1}{N} \sum_{i=1}^N (M_i - B_i) \quad (7-11)$$

$$R^2 = 1 - \frac{\sum_{i=1}^N (M_i - B_i)^2}{\sum_{i=1}^N (M_i - \bar{B})^2} \quad (7-12)$$

$$\text{RMSE} = \sqrt{\frac{1}{N} \sum_{i=1}^N (M_i - B_i)^2} \quad (7-13)$$

$$\text{SI}(\%) = \frac{\sqrt{\frac{1}{N} \sum_{i=1}^N (M_i - B_i)^2}}{\frac{1}{N} \sum_{i=1}^N B_i} \times 100 \quad (7-14)$$

where M refers to the results of numerical model value and B is the value corresponding to the experimental data (benchmark). This is a good example of how a finer mesh solution, which is converging, does not necessarily lead to better representation of physical phenomenon. Or in other words “verification” and “validation” are individual activities.

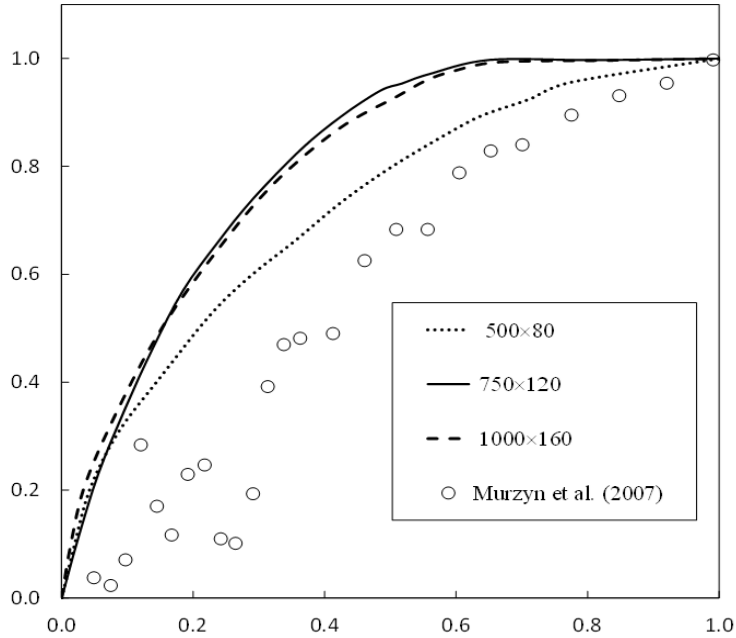


Figure 7-6. Numerical model of hydraulic jump: Modeled free surface profile versus laboratory measurements by Murzyn et al. (2007).

Table 7-2. Metrics of models skill validation for three different simulation free surface profile of air-water mixture in hydraulic jump.

Mesh Size	Bias	Scatter Index	RMSE	R ²
500 × 80	0.183	0.353	0.222	87.4%
750 × 120	0.271	0.438	0.314	76.7%
1000 × 160	0.267	0.431	0.308	78.9%

7.3.4. Example four: visualization of the results' difference in various meshes

VAVUQ is able to manipulate numerical results coming from different mesh sizes and visualize the error. This visualization is valuable to the code/calculation verification process as it helps the modeler efficiently narrow down the problematic part of the modeling. Figure 7-7

shows the visualization of misfit (difference) between mesh sizes of 128×128 and 182×182 for the simulation of pressure in lid driven cavity flow (Yuen, 2014).

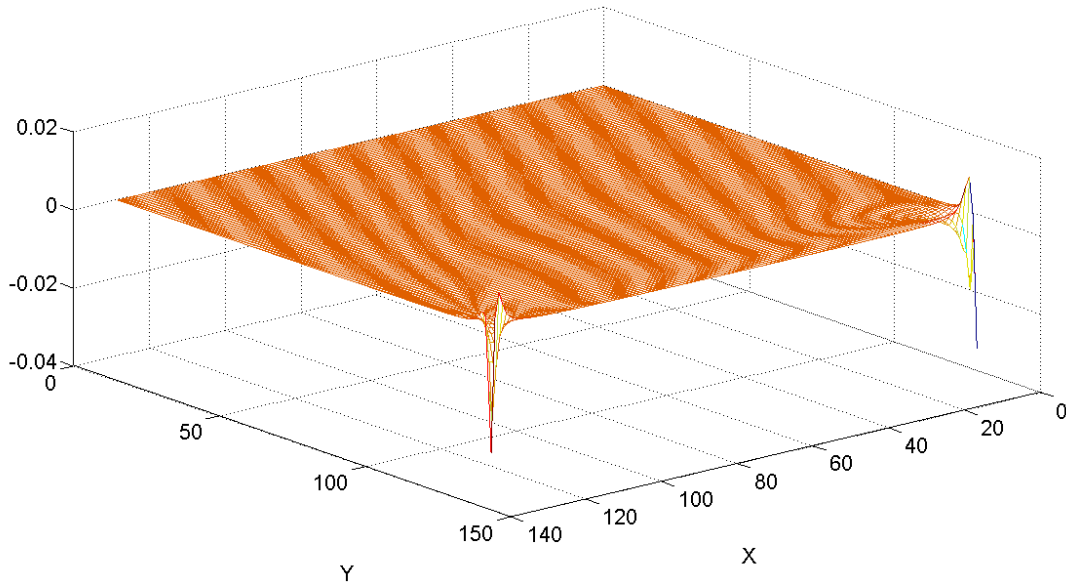


Figure 7-7. Difference in pressure numerical calculation between two different meshes sizes, for a lid-driven cavity flow. Most of the difference happens in the top right and top left corners next to the moving lid.

7.3.5. Example five: numerical uncertainty quantification

By definition, uncertainty in numerical modeling has three components: uncertainty in initial and boundary conditions, " U_{input} "; uncertainty in the mathematical model, " U_{model} "; and uncertainty in numerical solution able to calculate the uncertainty in the numerical simulation. Then based on the most reliable results (finest mesh) it is able to calculate the lower and upper range of the numerical error. The value of these bounds of the error depends on several factor including: a) number of mesh refinements, b) required confidence interval (99% or 95%), c) mesh type (structured or unstructured), and d) the observed order of the convergence of the solver (Roache, 2009). In general, the safety factor " FS " for numerical uncertainty quantification

considered to be between one and five. And for uncertainty quantification, at least results of four different mesh sizes are needed. Figure 7-8 shows the relative misfit between the finest mesh and the second finest mesh in a vertical cross section of a 3D modeling of Gust Chamber (Yuen, 2014, unpublished data). Figure 7-9 shows the upper and lower range of the numerical difference based on the Roache's Grid Convergence Index (GCI), both calculated via VAVUQ toolkit. of the PDE " U_{num} ." The overall uncertainty can be computed as follows:

$$U_{value} = \sqrt{U_{num}^2 + U_{input}^2 + U_{model}^2} \quad (7-15)$$

From the above components of the uncertainty, quantifying U_{input} is out of the scope of this work. In turn, " U_{model} " is within the scope of "model validation" not "model verification". However, VAVUQ is

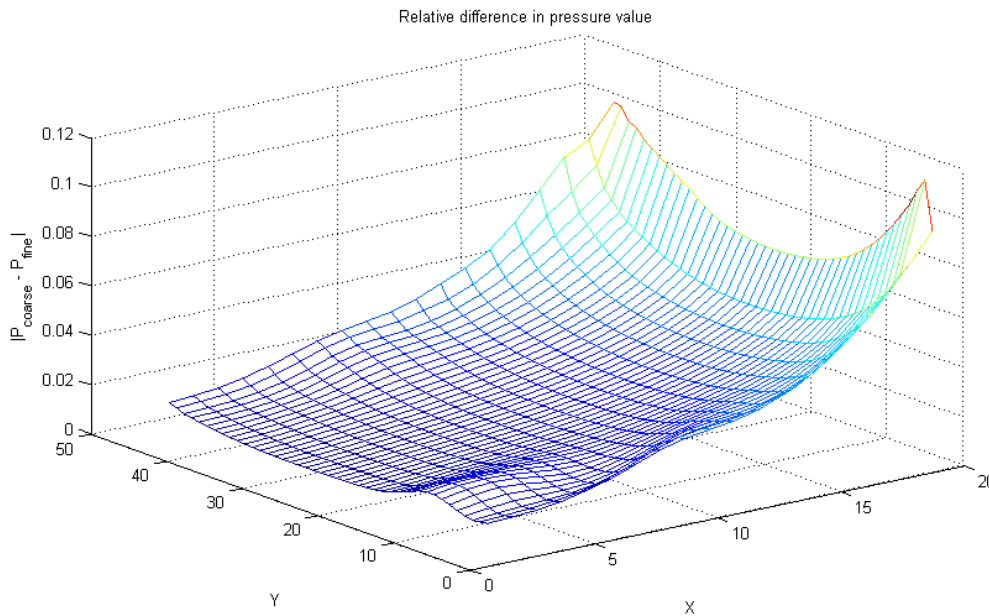


Figure 7-8. Pressure numerical solution difference between the finest mesh and the second finest mesh.

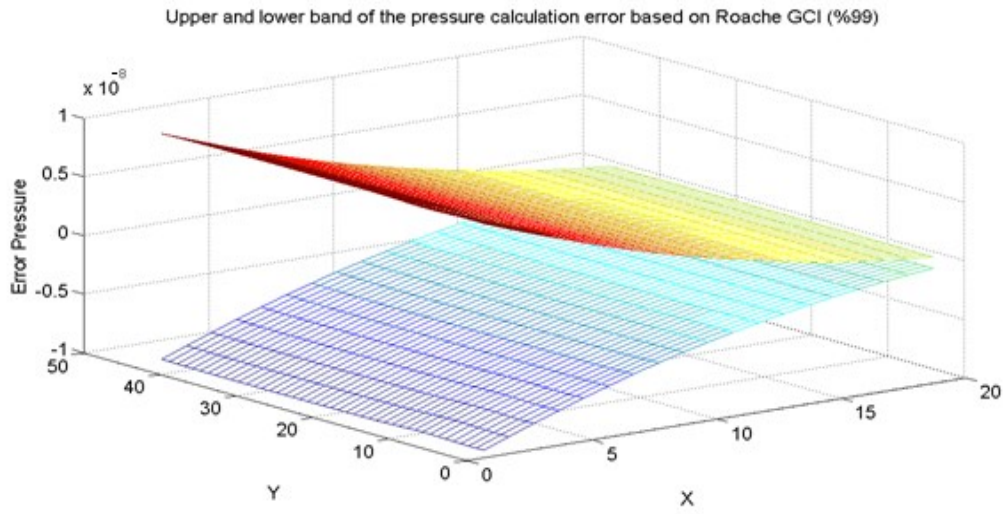


Figure 7-9. Upper and lower range of numerical calculation difference based of GCI for confidence interval of 99% and four mesh refinements (structured mesh).

Appendix of Chapter 7

7-A. Snapshots from VAVUQ GUI

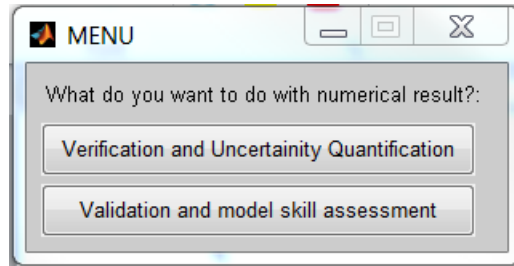


Figure 7-10. Choose between Verification and Validation subroutines.

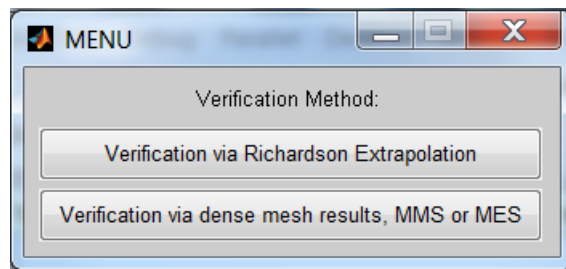


Figure 7-11. Verification with and without known benchmark solution.

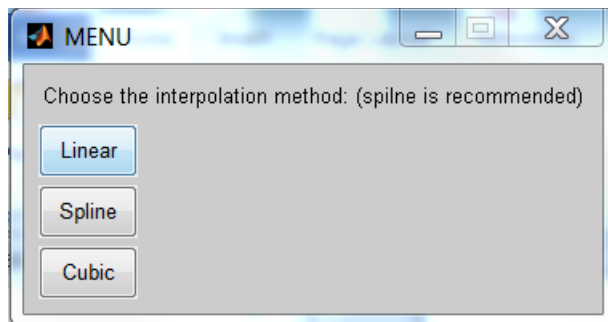


Figure 7-12. Interpolation method for conversion of results to same grid points

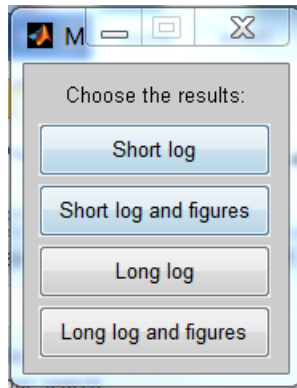


Figure 7-13. Selection of output level of details.

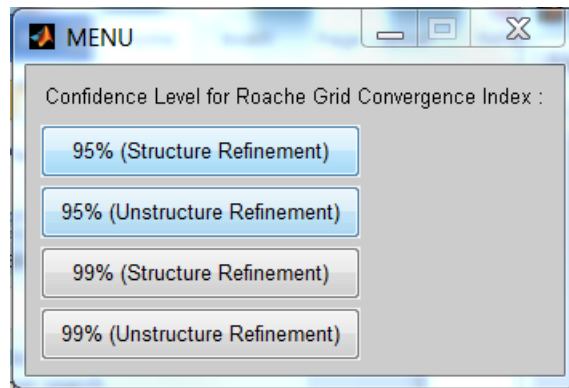


Figure 7-14. Confidence level for uncertainty quantification.

Chapter Seven References

1. ASME V&V 20-2009. Standards for Verification and Validation in Computational Fluid Dynamics and Heat Transfer, An American National Standard. ASME.
2. Ateljevich E, Zamani K, Bombardelli FA, Anderson J (2011). Using software quality and algorithm testing to verify a one-dimensional transport model. ASCE/EWRI World Environmental and Water Resources Congress, Palm Springs, CA.
3. Ghia U, Ghia KN, Shin CT (1982). High-Re solutions for incompressible flow using the Navier-Stokes equations and a multigrid method, *Journal of Computational Physics*. 48: 387-411.
4. Knupp PM, Salari K (2003). *Verification of computer codes in computational science and engineering*. Chapman and Hall/CRC.
5. Oberkampf WL, Roy CJ (2010). *Verification and validation in scientific computing*. Cambridge University Press, Cambridge.
6. Roache PJ (1997). Quantification of uncertainty in computational fluid dynamics. *Annual Review of Fluid Mechanics*, 29, 123–160.
7. Roache PJ (2009). *Fundamentals of verification and validation*. Hermosa Publishers.
8. Roache PJ, Knupp PM (1993) Completed Richardson Extrapolation. *Communications in Numerical Methods in Engineering*, 9(5): 365–374.
9. Saad Y (1996). *Iterative methods for sparse linear systems*. (2nd edition) PWS.
10. Van Leer B (1979). Towards the Ultimate Conservative Difference Scheme. V. A Second Order Sequel to Godunov's Method. *Journal of Computational Physics*, 32(1): 101–136.
11. Wang SY, Roache PJ, Schmalz RA, Jia Y, Smith PE (2008). Verification and validation of 3D free-surface flow models. ASCE, EWRI.

12. Willmott CJ, Robeson SM, Matsuura K (2012). A refined index of model performance. *Int J Climatol* 32:2088–2094.
13. Yuen, A.C.K. (2014). A Study on the Generation of Bottom Shear Stress in Gust Microcosms Using Numerical Modeling Techniques, M.Sc. Thesis Civil and Environmental Engineering, University of California, Davis.
14. Zamani K, Bombardelli FA (2014). Analytical solutions of nonlinear and variable-parameter transport equations for verification of numerical solvers. *Journal of Environmental Fluid Mechanics*.

Chapter 8: Conclusions and Future Path of Research

8.1. Final Words

The research presented in this dissertation was about "reliable" modeling of environmental flows. A comprehensive framework for verification, validation and uncertainty quantification (VVUQ) of models of environmental fluid mechanics was developed. Recent techniques of VVUQ have been adopted from computer science and nuclear engineering fields into environmental fluid mechanics models to yield high-quality, reliable modeling of transport phenomenon. The rest of the research in this thesis discusses application of those methods towards improvement of reliability and efficiency of two-phase flow models of solid-water mixtures and air-water mixtures. I provide a brief chronological review of the research path of my PhD, followed by major conclusions of each chapter and trajectory for future works in the next paragraphs.

A prelude on major scientific and industrial motivations of my research, and main goals of the dissertation was given in Chapter 1. Chapter 2 provided a literature review of the field and had two main parts. First was a review of methods and packages for analytical and numerical modeling of pollutant transport in the unsaturated zone, and second a critical review of current state of practice and knowledge gaps in wetland and tidal marsh environments. The former was published as the Chapter 68 in "Chow's handbook of applied hydrology, Second edition" by Vijay P. Singh and the latter was a part of a review paper which was accepted for publication in the ASCE Journal of Hydrologic Engineering (written by ASCE-EWRI Wetland Hydrology Technical Committee). The section on the vadose zone transport reviews the fundamental equations of flow in unsaturated porous media. Then, a review of deterministic approaches for solving passive transport in vadose zone is given including analytical solutions and numerical

methods. Next, formulation of reactive transport and multi-domain transport in vadose zone is provided, followed by a comprehensive review of software packages for analytical and numerical modeling of solute transport in porous media. In the rest of Chapter 2 I reviewed sediment transport models for wetlands and shallow-water vegetated areas. I went through the hierarchy of sediment transport models based on number of dimensions, steadiness of equation, complexity of governing equations (fully dynamic wave, kinematic wave, and diffusive wave), turbulence closures, and the ability/quality of including vegetation in the flow solver.

For future researches in the field of pollutant transport modeling in the vadose zone, I believe effects of micro-heterogeneity and upscaling techniques are at the frontier of the knowledge gap and need to be addressed towards better modeling of transport in the vadose zone. In turn, the future of wetland sediment-transport modeling can be improved by filling two knowledge gaps. First, we need a clear mechanistic understanding of the biochemical reactions of vegetation and bio-sources of sediment in wetlands. And second, upscaling techniques have to be applied to account for the effect of vegetation heterogeneity on the flow.

Chapter 3 presented analytical solutions for verification of transport codes. All numerical codes developed to solve the advection-diffusion-reaction (ADR) equation need to be verified before they are moved to the operational phase. In this chapter, I initially provided four new one-dimensional analytical solutions designed to help in code verification; these solutions are able to handle the challenges of the scalar transport equation, including nonlinearity and spatiotemporal variability of the velocity and dispersion coefficient, and of the source term. Then, I provided a solution of Burgers' equation in a novel setup. Proposed solutions satisfy the continuity of mass for the ambient flow, which is a crucial factor for coupled hydrodynamics-transport solvers. At the end of this chapter, I solved hypothetical test problems for each of the solutions numerically,

and I used the derived analytical solutions for code verification. I provided assessments of result accuracy based on well-known model skill metrics.

To improve the numerical solutions of the ADR equation for the objective of code verification in Chapter 3, I suggest two methods besides Method of Exact Solutions (MES). First, I strongly advocate using Method of Manufactured Solution (MMS). MMS is the most reliable method to verify all possible flaws and check all nonlinear terms in a discretization of a PDE (Roache, 2002 and 2009; Oberkampf and Roy, 2010). The second method to improve the benchmark solutions for code verification is the “Method of Nearby Problems” (MNP) (Roy et al., 2007; Oberkampf and Roy, 2010). Although this method is not as strong as MMS in generating benchmark solutions for verification of nonlinear terms, it has the practical advantage of preserving the natural scales of the problem for code and calculation verification purposes.

Chapter 4 of my dissertation was on the comprehensive assessment of current methods of approximation of Einstein’s integral for total sediment discharge, in sequential and parallel computing. Einstein’s integrals constitute one of the most salient developments in theoretical sediment-transport mechanics. I reported a comprehensive analysis of the accuracy and computational efficiency of proposed methods for the calculation of the Einstein’s integrals. To the best of my knowledge, this comprehensive assessment had not been undertaken before for all ranges of Rouse numbers and bedload-layer thicknesses. I first determined the accuracy of the proposed methods through comparison against the results of a dense-mesh, high-order numerical integration technique. For an infinite series solution, a comprehensive study of accuracy versus number of terms in the partial sum was performed. Then, the CPU times of those methods over a full set of Rouse numbers and bedload-layer thicknesses are compared. Finally, parallel versions of the methods were presented and their parallel efficiency was assessed. Based on the analyzed

criteria (accuracy, convergence, CPU time, and parallelization capability) I evaluated the overall efficiency of the methods.

To improve the former methods of I discussed in Chapter 4, I suggest techniques to improve the speed of convergence of an infinite series. To that end, I think generalized Shanks transformation can be employed (Shanks, 1955; van Dyke, 1975). The second technique which I think will provide promising results – for explicit closure for an infinite series – is Richardson Extrapolation (see Chapter 8 of Bender and Orszag, 1999; Weniger, 2003). The other drawback of former methods which might be improved is finding analytically remedies for singularities such as the work by Srivastava (Abad et al., 2006).

Following the research of Chapter 4, I developed four new methods for the calculation of Einstein's integrals in Chapter 5 of this dissertation. The first two involve numerical strategies; the third is based on a series expansion, and the fourth involves a semi-analytical approach. The first method is an adaptive numerical-integration approach using Gauss-Kronrod quadrature and multi-step refinement. The second method is a novel numerical trick that recycles computational values and that provides a 30% increase in efficiency. Third method is based on asymptotic-series expansions of Einstein's integrals, which performed well for finer particles in suspension (small Rouse numbers); however, results were less precise for coarser particles (high Rouse numbers). Fourth, I derived a new semi-analytical solution utilizing hypergeometric functions with corresponding numerical methods to evaluate the semi-analytical solution. All of these new methods were benchmarked on their accuracy, CPU time, and parallelization performance with model skill assessment techniques. The best overall outcome was by nested Gauss-Kronrod quadrature.

Although the adaptive integration (nested Gauss-Kronrod) showed remarkable efficiency in both sequential and parallel computing, I think there is still way to improve the efficiency of numerical integration of Einstein's integrals. Designing a special quadrature according to behavior of integrands of Einstein's integrals would be the ultimate step forward for fast and accurate integration (Davis and Rabinowitz, 2007). Mathematical details of devising a quadrature for a function can be seen in Kythe and Schäferkötter (2004), and Davis and Rabinowitz (2007).

Chapter 6 of my dissertation is on two-phase flow of air and water in hydraulic jumps. Hydraulic jump with bubbly two-phase flow and fluctuating free surface is a complex phenomenon that has important applications in industry and environmental fluid mechanics. Previous studies assumed advective-dispersive character to elucidate distribution of void fraction in the hydraulic jump. With that means, an analytical solution derived to describe distribution of air bubbles in hydraulic jump. In spite of the simplifying assumptions, agreement between this analytical solution and lab measurements is confirmed in couple of experimental studies. In this chapter I enhanced the analytical solution of the void fraction in the hydraulic jump. I consider the buoyancy effect on the air bubbles and analytically solve the scalar transport equation for the nonlinear bubble rise velocity. The new analytical solution was validated versus four datasets measured by Chanson and Qiao (1994), and Chanson and Brattberg (2000), Murzyn et al. (2005 a and b) and Chanson and Gualtieri (2007). The comparisons reveal an excellent agreement between derived analytical solution and measurements in the lower region. Then, I used the new empirical data sets to evaluate former analytical solution which was suggested for the air distribution in the upper region of hydraulic jumps. At the end of the chapter I developed a new

empirical-analytical relation for defining the air mass entrainment and detrainment in the hydraulic jumps and validate it through the experimental data.

The future of this research depends on more accurate understanding of the phenomena. Free surface two-phase flow of air bubbles and water is a very complex interaction of turbulence, surface tension and nonlinear waves. Those factors made measurements harder and less accurate compared to that of single phase flows (Chanson, 2009). Given reliable lab measurements of flow and air concentration, analytical descriptions of air concentration inside hydraulic jump can be improved with new methods of including variable velocity in the analytical solutions. Example of those methods – based on perturbation technique – can be seen in the work of Liu and Nayamatullah (2014).

Chapter 7 is on using Software Quality Assurance (SQA) and Verification, Validation and Uncertainty Quantification (VVUQ) towards development of a more reliable modeling product. I introduce an open-source, user friendly, numerical post-processing software to assess reliability of the modeling results of environmental fluid mechanics' codes. Verification and Validation, Uncertainty Quantification (Davis-VAVUQ), is an open-source toolkit which is developed for general V&V proposes. The package is composed of all necessary routines for code and solution verification, quantification of uncertainty in numerical discretization, and quantitative model skill assessment. In this work, The VAVUQ implementation of V&V techniques and user interfaces would be discussed. VAVUQ is able to read Excel, MATLAB, ASCII, and Binary files and it would produce log of the results in txt format. Next, each capability of the code is discussed through an example: First example is a solution verification of a 2D Navier-Stokes solver via Richardson extrapolation. Second example is a code verification of a sediment transport code via MES. Third example is a validation of two-phase free surface

flow in hydraulic jump via common metrics of model skill assessment. Fourth example is error visualization for lid-driven cavity flow of example one. Finally the fifth example is uncertainty quantification in the numerical discretization of pressure in lid-driven cavity flow. At the end, I discussed practical considerations and common pitfalls in interpretation of V&V results.

In overview, after a literature review of pollutant transport in the vadose zone and of the sediment transport in wetlands (Chapter 2), my PhD dissertation had two main themes: First, three chapters were on two-phase flow of air-water mixture and solid-water mixture. I improved the efficiency and accuracy of sequential/parallel methods of computing total sediment discharge with Einstein's method. I designed analytical solutions and empirical regression based solution to elucidate 2D distribution of air bubbles in hydraulic jumps. Second, I devised analytical solutions of nonlinear and viable coefficient passive transport equation for verification of solvers. In addition, I developed a package of auxiliary tools for VVUQ in computational mechanics. I employed my software for verification and validation of my mathematical models in this research.

Chapter Eight References

1. Abad, J.D., García, M.H., Roland, A., Zanke, U., Srivastava, R., Guo, J., Julien, P.Y. (2006). “Discussion and closure to Efficient Algorithm for Computing Einstein Integrals by Junke Guo and Pierre Y. Julien”, *J. Hydraul. Eng.*, 132:337-339.
2. Bender, C.M., Orszag, S.A. (1999), *Advanced mathematical methods for scientists and engineers*, Springer
3. Chanson, H. (2009). “Current Knowledge in hydraulic jumps and related phenomena. A survey of experimental results.” *European Journal of Mechanics B/Fluids* 28: 191-210.
4. Chanson, H., and Brattberg, T. (2000). “Experimental study of the air-water shear flow in a hydraulic jump.” *Int. J. Multiphase Flow*, 26:583–607.
5. Chanson, H., and Gualtieri, C. (2007). “Experimental analysis of Froude number effect on air entrainment in the hydraulic jump.” *Environ. Fluid Mech.*, 7: 217-238.
6. Chanson, H., and Qiao, G. L. (1994). “Air bubble entrainment and gas transfer at hydraulic jumps.” *Research Report No. CE149. Department of Civil Engineering University of Queensland, Australia.* P. 68.
7. Davis, P.J., Rabinowitz, P. (2007). *Methods of numerical integration.* Courier Corporation.
8. Kythe, P.K., Schäferkötter, M.R. (2004). *Handbook of computational methods for integration.* CRC Press.
9. Liu, X., Nayamatullah, M. (2014). Semianalytical solutions for one-dimensional unsteady nonequilibrium suspended sediment transport in channels with arbitrary eddy viscosity distributions and realistic boundary conditions, *Journal of Hydraulic Engineering*, 140(5), 04014011.

10. Murzyn, F., Mouaze, D., and Chaplin, J. R. (2005). "Air–water interface dynamic and free surface features in hydraulic jumps." *Journal of Hydraulic Research*, 45:5, 679-685.
11. Murzyn, F., Mouaze, D., and Chaplin, J. R. (2005). "Optical fibre probe measurements of bubbly flow in hydraulic jumps." *Int. J. Multiphase Flow*, 31:141–154.
12. Oberkampf W.L., Roy, C.J. (2010) "Verification and validation in scientific computing." Cambridge University Press, Cambridge
13. Roache, P.J., (2002), "Code Verification by the Method of Manufactured Solutions", *J. of Fluid Eng.*, 124: 4-10.
14. Roache, P.J., (2009), "Fundamentals of Verification and Validation", Hermosa Publishers.
15. Roy, C.J., Raju, A., Hopkins, M.M. (2007). "Estimation of Discretization Errors using the Method of Nearby Problems," *AIAA Journal*, Vol. 45, No. 6, pp. 1232-1243.
16. Shanks, D. (1955), "Non-linear transformation of divergent and slowly convergent sequences", *Journal of Mathematics and Physics* 34: 1–42.
17. van Dyke, M.D. (1975), *Perturbation methods in fluid mechanics*, Parabolic Press.
18. Weniger, E.J. (2003). "Nonlinear sequence transformations for the acceleration of convergence and the summation of divergent series". arXiv:math.NA/0306302v1.

Appendix A: Using Software Quality and Algorithm Testing to Verify a One-dimensional Transport Model¹

A.1. Introduction

In this paper, we describe our approach and experiences developing a software verification framework for a one dimensional (1-D) transport model of advection, dispersion and reactions or sources (ADR). We begin by describing the motivation and requirements for testing. Our acceptance criteria are driven by the requirements for the model, but are crafted according to principles from both the software and numerical testing fields. We then describe the components and implementation of the test suite, emphasizing the incremental nature of the tests, quantitative criteria for testing, and the similarities and tension between the silent, automatic perspective of software testing and the verbose, graphical outputs required for public reporting of numerical verification results.

The testing framework described in this paper was developed as part of a project to create a new transport module for the Delta Simulation Model 2 (DSM2) (DSM2, 2011) a 1-D hydrodynamic and transport model for flow and water quality in the Sacramento-San Joaquin Delta. Our target problems include river and estuary advection, and 1-D approximations of common mixing mechanisms and source terms associated with conservative and non-conservative water quality kinetics including sediment transport. The transport code is described briefly below followed by the development of the testing framework. The two are tightly coupled

¹ This appendix was published as: Ateljevich, E., Zamani, K., Bombardelli, F. A., Anderson, J. (2011). Using software quality and algorithm testing to verify a one-dimensional transport model. In ASCE EWRI World Environmental and Water Resources Congress, Palm Springs, CA.

-- since the transport module was created from scratch, it provided an opportunity to structure the code to be rigorously tested.

The model used to illustrate the testing framework is based on the 1-D transport equations in conservative form:

$$\underbrace{\frac{\partial(A(x,t)C(x,t))}{\partial t}}_{\text{Time evolution}} + \underbrace{\frac{\partial(A(x,t)C(x,t)u(x,t))}{\partial x}}_{\text{Advection}} = \underbrace{\frac{\partial}{\partial x}\left(A(x,t)K(x,t)\frac{\partial C(x,t)}{\partial x}\right)}_{\text{Dispersion}} + \underbrace{R(x,t,C(x,t))}_{\text{Source/Reaction}} \quad (1)$$

where x is the distance, t is time, A is the wetted area, C is the scalar concentration, u is the flow velocity, K is the longitudinal dispersion coefficient, and R is the source term (deposition, erosion, lateral inflow and other forms of sources and sinks). Equation (1) describes the mass conservation of a pollutant in dissolved phase, or suspended sediment away from the streambed.

The problem domain includes estuarine river channels and even some small open water areas roughly approximated as channels. The main transport process is advection, and the mixing mechanisms we anticipate are turbulent diffusion, gravitational circulation, and shear dispersion (Fischer et al., 1979; Abbott and Price, 1994). We anticipate the shear dispersion to dominate over the turbulent diffusion. We also expect the gravitational circulation to exert an important role in mixing. We additionally contemplate significant, non-linear source terms from sediment, chemical and biological processes, though none of the processes are so quickly varying as to constitute truly stiff reactions.

Our algorithms include an explicit scheme for advection based on a finite-volume method (FVM) discretization and the Lax two-step method (Colella and Puckett, 1998) with van Leer

flux limiter (Saltzman, 1994); it also includes an implicit, time-centered Crank-Nicolson scheme for dispersion (Fletcher, 1991). The advection and reaction solver are coupled as a predictor corrector pair, and dispersion is implemented separately using operator splitting.

A.2. Testing Requirements

The tests described in this paper are all designed around suitability of the solver for estuary transport problems. The required accuracy on target modeling applications and choice of algorithm influence the testing requirements and the components of our algorithm test suite.

The scales of estuary transport determine the range of relative strength over which we test advection, diffusion and reactions, which is mostly intermediate Peclet number flow. Our target accuracy is strict second order for individual operators and near second order for the algorithm as a whole. Second order allows a coarser discretization for a modest increase in work per volume of fluid, which is efficient. A second-order algorithm also gives us a buffer of accuracy as details like networks of channels and coarse boundary data are added. At the time of writing this paper, our splitting is first order Godunov splitting. Some authors (e.g. Leveque 1986) have observed that near second-order accuracy can be achieved with first order splitting, and the design of the tests probes this point.

Two features of the algorithm feature into the design of our test. First, the scheme requires a flow field (flow discharges and flow areas) that preserves mass continuity. In some cases, tests from the literature were written in non-conservative or primitive form and had to be reworked in conservative form. Second, we employ operator splitting and wanted to exercise the equations with and without known vulnerabilities (such as time-varying boundaries and nonlinear source terms) of this class of algorithm.

A.3. Testing Principles

Flow and transport codes inherently comprise both numerical algorithms and pieces of software. Well-developed testing literature exists for both. Oberkampff and Trucano (2002) describe some elements of software quality engineering (SQE) in the context of numerical verification, and note some cultural reasons why it is seldom implemented.

Figure 1 is adapted from this work and depicts the relationship between software testing components and algorithmic testing such as convergence tests. We regard numerical verification as our key responsibility and the numerical verification toolset as our greatest assets. Nonetheless, we also comment below on how these tools feature as tests and how, at times they seem in tension with the principles of good software testing.

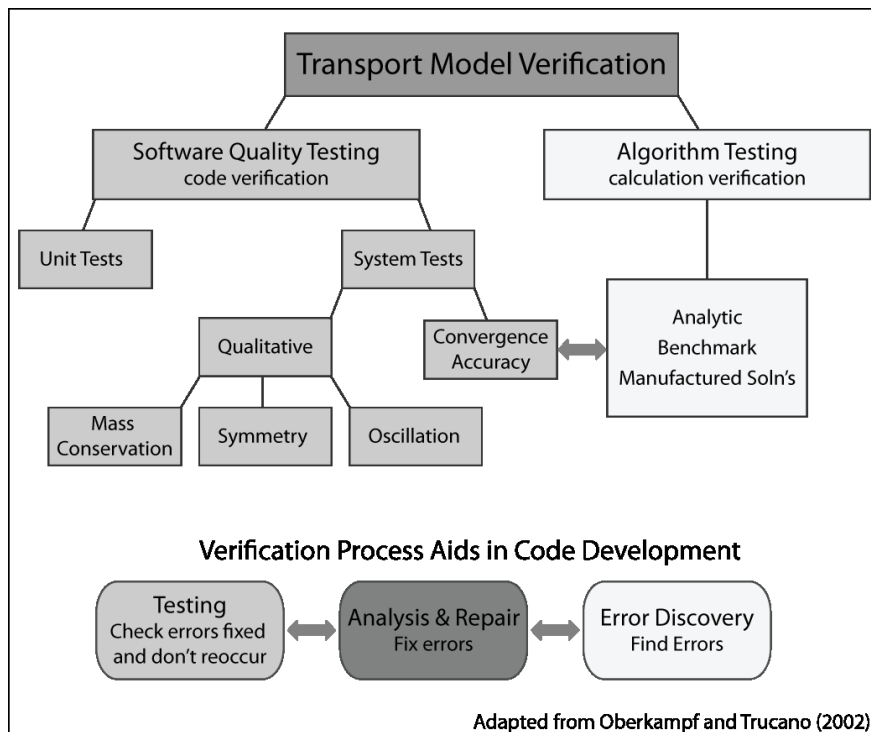


Figure A-1. Relationship between software testing components and algorithmic testing.

Software testing principles. The principles that we want to emphasize are:

1. Testing should be automatic and continuous.
2. The approach should foster exact specification of every unit of code.
3. Testing should provide assurance of whether a set of specifications is met.

One goal of tests is that they be a continuous assessment of the code. The entire testing system is a *regression* suite that establishes a gauntlet through which future code changes must be passed. A consequence of automation is that tests must be phrased in terms of binary *assertions*, true and false statements that can be tested without human intervention and that reveal whether the aspect of the code under consideration is correct. Convergence criteria are a rigorous basis for assertions, either by requiring strict convergence criteria (“the algorithm is - second order accurate in time and space”) or a regression criterion (“convergence will not get any worse than last time the code was tested”).

The software testing literature further distinguishes between *unit tests* of atomic routines and *system tests* of larger subtasks. For example, the evaluation of a gradient might be a unit of code and it would have a unit test. Convergence tests and other algorithm tests are examples of system tests.

The unit testing point of view is that code must be exercised over a range of inputs that covers every line. For instance, to test a gradient routine with a slope limiter, a developer would want to cover:

1. smooth cases in the middle of the mesh.
2. behavior near the edges of the mesh, where one-sided differences may be used instead of central differences.
3. cases that test the limiters with steep or zero gradients in both directions.

Any system test will certainly exercise the gradient code in the middle of the mesh, which in any event can seldom be wrong without being obvious. However, system-level tests might miss the more unusual cases. For example, a convergence test may miss a bug in the limiter for the case of steep decreasing slope for several reasons. First, convergence is often assessed with limiters turned off, as they are locally order reducing. Second, it is hard to fiddle with the problem in just the right way to make sure the left, right, and center cases of the gradient limiter are all triggered. This is particularly true when trying to exercise other units of code at the same time – parameter choices made to fully exercise gradient limiter the may lessen the coverage of another unit.

Although the software and algorithm tests are separate, information discovered during one test can aid in the further development of another test. We began our coding with near-100% coverage by unit tests. These tests were part of the debugging and development processes. Later, discoveries made in the context of system tests were analyzed and pushed back into unit tests whenever possible. The unit test was expanded to verify that the newly discovered error from the algorithm test was fixed and does not reoccur. This flow of information is indicated in Figure 1.

One example of this accumulation of tests is our unit test for fluid mass conservation. The observation that our algorithm requires accurate mass conservation of the fluid came from the tidal test case. The flow field we used for this case was adapted for 1-D from Wang et al. (2009). The original solution was based on a linearization and is not mass conservative in 1-D, causing significant problems with transport convergence. Once this requirement was discovered, a unit test was introduced into the suite to check this property for any flow field. At the same time, we found we had to tailor some of the analytical results we were using for other tests.

A second example involved periodic flow. Our uniform flow convergence tests originally had a reversal of flow midway through the test. The out-and-back setup is convenient for advection because the initial condition and final concentration field are the same. We also believed we were exercising the code in two directions. In fact, an error accumulated in the positive direction was cancelled by the return pass in the negative direction. We passed the periodic test but failed analogous unidirectional tests. Originally, the discovery was fortuitous, because the unidirectional test was “unofficial”; now we test directional dependence using a combination of periodic and unidirectional flow

Numerical verification and algorithmic testing.

An important category of a system test includes the algorithm tests normally associated with verification of numerical codes. Algorithm tests serve multiple purposes. They are intended in part to discover bugs and in part to convince ourselves and others of the merit of the algorithm to solve the equations to which it is directed.

One of the well-recognized and the standard verification methods of computational fluid dynamics codes is based on the notion of mesh convergence (Roache, 2009). Mesh convergence for models that solve partial differential equations is assessed by successively refining the spatial and temporal discretizations. As the mesh is refined, the error estimates (for us usually an L_1 norm, or sum absolute error) should decrease at a *convergence rate* that is algorithm dependent (Leveque, 2002). A second order accurate algorithm, denoted $O(2)$ or $O(\Delta t^2, \Delta x^2)$ should have its error go down proportional to the square of the step sizes. By checking convergence, we ensure that the model is consistent with an underlying formulation rather than numerical artifacts. Failure to converge usually represents either a bug in the implementation or a difficulty of the algorithm on a class of problem.

The verification toolkit is largely targeted at providing test problems and methods to estimate error in situations where an analytical solution is not available from the literature. When nonlinearity, spatially varying coefficients and other complexities are introduced, tricks must be introduced to obtain good test problems.

Depending on the context, error and convergence are usually estimated one of two ways:

- When successive refinements are assessed relative to an analytical solution, we have a direct estimate of error and the ratio allows us to estimate a *convergence rate*.
- When successive grids are compared to one another, we can invoke the concept of Richardson extrapolation and Grid Convergence Index (Roache, 2009) to indirectly estimate error and convergence even when no solution is available.

In practice, we found the Method of Manufactured Solutions (MMS, Roache, 2009) was able to supply analytical verification problems for all the cases not covered directly in the literature.

At least in theory, convergence rates can be stipulated as a project requirement and software testing assertion. Convergence rates, not absolute error, are what numerical methods tend to promise and they are very useful in the discovery of code defects. Still, the main goal in practice is a more accurate solver. Therefore, the superiority of methods should be assessed based on both convergence and accuracy (Roache, 2009).

The convergence ratio in a very coarse grid oscillates around its main value; as the grid size is refined, convergence becomes monotonic until the mesh size reaches a point where the machine precision overtakes the truncation error of the numerical scheme. At this point error norms do not change, and the convergence rate is zero. Convergence ratios should be checked for intermediate grid sizes, preferably at the scale of the real phenomenon and discretization used

in practice. In the conclusions, we describe the challenge of dealing with tests that returned failed results when the convergence was just slightly below the target level.

As acceptance tests, algorithm tests should be conducted over a range of problems that exercise the major physical features that are to be modeled. The community may help with this by providing benchmarks, but we were unable to ascertain that any widely accepted benchmarks for a 1-D transport code. As system tests we believe that the tests should be *glass box*, targeting known or discovered vulnerabilities of the algorithm. The ability to use remote and active boundaries in our convergence tests, for instance, is specifically motivated by known problems related to operator splitting.

Finally, distinction might be made between the reportable set of algorithm tests and other types of system tests aimed at defect discovery. Important examples of the latter are tests of symmetry, such as a whether a 1-D model gives the same result when the upstream and downstream boundaries are swapped. Others are positivity preservation of constituents, mass conservation and oscillation detection. In the case of positivity preservation and mass conservation, it is typical to abstract this code for use both in the test suite and in the driver as a user option.

Overall, we agree with the conclusions of Salari and Knupp (2000) that system tests – particularly convergence tests – expose bugs well, particularly when an attempt is made to test symmetrically and over special cases. We feel that the incremental approach we describe in the next section further helps to isolate problems. Nevertheless, a close reading of Salari and Knupp (2000) does reveal that the convergence tests sometimes initially failed to pick up bugs that are exactly the sorts unit tests might catch (e.g. gaffes in corner cells).

A.4. Algorithm Test Suite Description

The algorithm testing used an incremental building block approach that adds complexity on two major dimensions (Figure 2):

- Operators: The tests were developed for a one-dimensional transport code that will be applied to an estuary. Thus the key processes tested are the operators of advection, dispersion and reaction (e.g. growth or decay). These are tested individually, then in combinations of growing complexity
- Flow field and physical setup: Our fixtures included the following cases
 - Uniform flow: This test involved uniform steady flow on a channel, sometimes with a reverse in direction halfway through the simulation. The mass transported is Gaussian. The suite includes advection, diffusion and reaction alone and in the combinations indicated in Figure 2.
 - Tidal flow: This test used a tidal flow field from Wang et al. (2009), adapted to be 1-D and mass conserving, to test advection and reaction. The test itself has no analytical solution, but is periodic in a way that is not symmetric.
 - Spatial variation (Zoppou): This test is due to Zoppou and Knight (1997) and includes velocity proportional to distance and diffusion coefficients proportional to distance squared. This test had to be modified for a conservative fluid flow.
- Boundary complexity: For the uniform flow and Zoppou tests, we include cases where the boundary is far away from the transported mass and cases where the boundary is actively part of the problem. This allows us to determine the extent to which convergence rates are affected by boundaries.

- Nonlinearity: In our final case, which uses the Zoppou and Knight (1997) fixture adapted using MMS solution, we include a non-linear source term.

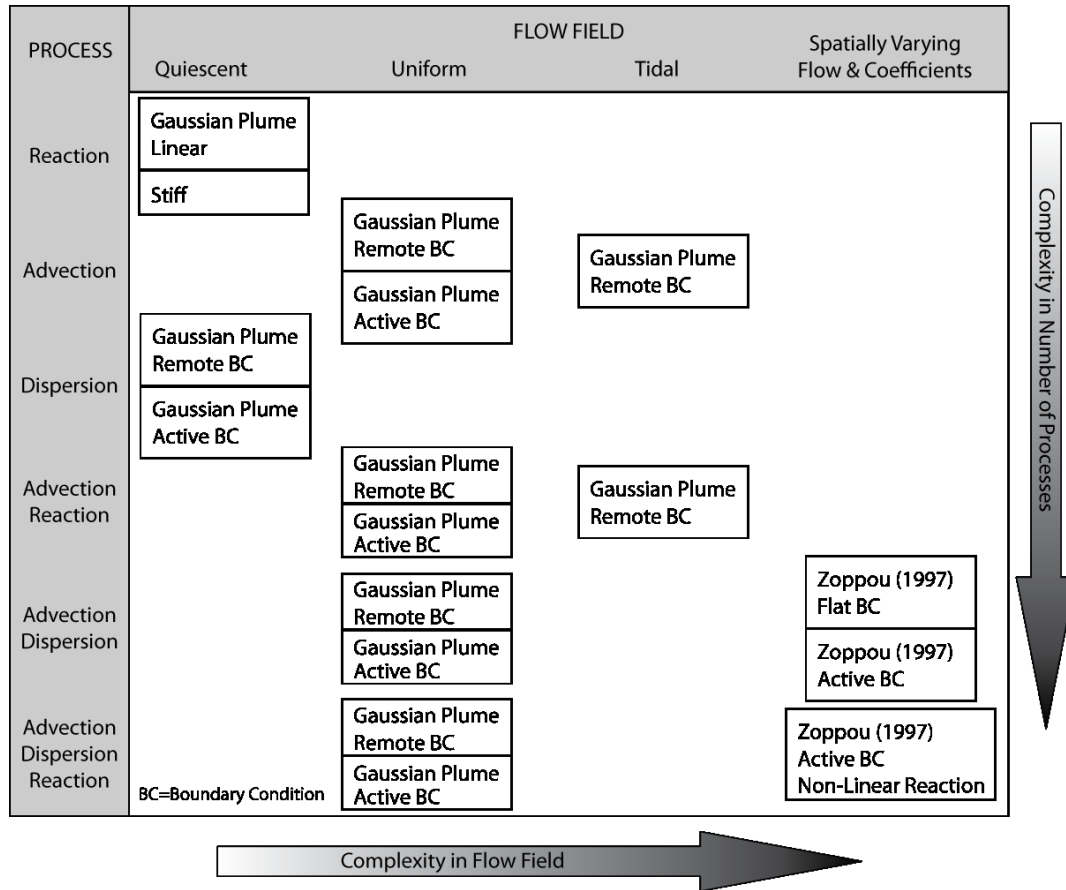


Figure A-2. Transport algorithm testing with incremental complexity.

These tests were conducted for a range of parameter values. Typically the Courant number (a measure of numerical stability of the algorithm), domain length, and dispersion and decay coefficients were fixed, and the grid spacing and time steps were adjusted to maintain the same Courant number. Detailed descriptions of the tests are beyond the scope of this paper and will appear in a planned journal article.

Our incremental suite can identify with good precision exactly which added layer of complexity causes a drop in order of accuracy. For instance, our example algorithm performs

well when boundaries are remote, but drops to a convergence rate of $O(1.4)$ or so in the presence of active boundaries.

The test architecture was implemented using the FORTRAN Unit Testing Framework (FRUIT) for logging assertions and counting pass rates. FRUIT is one of the few test frameworks available in this computer language. FRUIT does not appear to adhere to industry practices in the way it formats results (e.g., the JUnit format), but provides a variety of predefined assertions.

Both the system tests and the unit tests were developed with FRUIT, and the granularity for unit tests is one unit test module per solver module, one unit test routine per solver routine. Our code was designed for testing. In particular, computational routines were crafted according to the following three architectural considerations:

- We isolated any computations that could be described with easy-to-understand names, with the caveat that we did not want to degrade performance or prevent vectorization. Our routines tend to be simple, homogenous calculations over arrays (such as calculating the gradient over the entire domain) rather than long sequences of instructions on individual cells.
- Data are passed to computational routines by argument list. This leads to longer argument lists, but makes the description of input and output much surer – tests are much harder to program when data required by the routine is passed in “behind the scenes” using imported modules.
- The design allows us to dynamically swap in new sources, flow fields and boundary conditions without halting the tests or recompiling the code. This ability required function pointers and abstract interfaces, a relatively new FORTRAN feature.

A.5. Challenges and Issues with Tests

The key issues associated with unit tests were different than those associated with algorithm tests. The main challenge with unit tests seems to be culture: generating the will to write them and the skills to write them in a way that covers the unusual cases. Without the aid of special coverage tools, test coverage is up to the diligence and craftiness of the developers.

For algorithm tests, nominally we sought a second order convergence rate. A convergence criterion seemed in-keeping with the way numerical algorithm accuracy is expressed and is less arbitrary than a hard-wired, scale-dependent absolute standard. Early on, however, it was clear that the normal noise from observed convergence rates could spoil even a success when the rate is expressed as a hard assertion. It is challenging to deal with situations when a convergence test fails with a value close to the criterion, e.g. 1.97 instead of 2.0, which surely would pass a graphical acceptance test. This issue can be exacerbated by sensitivity to problem parameters.

When one of our tests did not cleanly converge at the specified level, we generally either fixed the code successfully or we searched for bugs until both of the following things happened:

- Convergence properties corresponded well to the expected strengths and limitations of our algorithm; and
- The solution was accurate: convergent above first order, excellent qualitative results when compared graphically to solutions and with relative errors of a hundredth of a percent.

We have done our best to support our claims when attributing any convergence deviations to specific algorithmic or problem quirks. Our incremental suite can identify with good precision

exactly which added layer of complexity causes a drop in order of accuracy. Where we intend to relax convergence criteria, we are in the process of changing our assertion criteria to an absolute accuracy requirement coupled with a regression standard for convergence. In our numerical code, cases with multiple operators and very active boundaries are the only ones in which we currently expect such a compromise.

Finally, there is sometimes a tradeoff between the requirements for verification and best practices for error discovery. Part of the community verification process for transport codes is the presentation of results in graphical format. Accommodating this type of display requires output beyond mere reports of assertion failures. We added the required verbosity option, but graphical interpretation plays no part in our regular testing practices other than as a debugging tool.

A.6. Conclusions

Our test suite succeeds both in finding bugs and in elucidating the strengths and weaknesses of a 1-D transport algorithm. We feel that our test suite is parsimonious and reasonably complete for tidal applications. Applying the framework to our own code, we have been able to work towards second order convergence for many tests and to isolate problems in special cases.

We believe the essential ideas in our approach are these:

- Codes must be written in a modular format with software testing in mind in order to apply the principals of software quality engineering. Each piece of code must have a clear purpose and criterion for success.

- Tests should be silent and automatic. Test criteria must be binary assertions. Assertions are written to provide more information than simply assessing graphs of expected vs computed results, however we include verbosity options to export data for graphs.
- There is a symbiotic relationship between software and algorithm tests; Code bugs detected with algorithm tests can lead to development of additional software regression tests to verify that a bug is fixed and to provide assurance that it does not reoccur.
- Convergence tests are the principal tool used in the algorithm verification literature. Our suite includes convergence tests on a combination of analytical problems from the literature and a manufactured solution using MMS.
- When convergence criteria are implemented as hard test assertions, account must be made of the small random noise typical of convergence results.
- Incremental addition of complexity helps to isolate the causes of problems and to establish that lower complexity solutions are correct.
- Symmetry and directionality tests help discover errors that may be hidden by the setup of the problem.

The software quality and algorithm testing framework described in this paper provides a useful starting point for researchers and practitioners wanting to verify transport codes. Having this rigorous test suite allows developers (1) to verify that each piece of code works properly both individually and as a combined system, (2) to ensure additions to the code do not adversely affect existing code, and (3) to find and fix code bugs that might otherwise be missed. Providing the end user with test results and the ability to rerun the tests themselves, assures the user that the code performs as expected and quantifies the code's strengths and weaknesses.

Appendix A References

1. Abbott, M. B., Price, W. A. (Eds.), (1994), "Coastal, Estuarial, and Harbour Engineers' Reference Book", Chapman & Hall.
2. Colella, P., Puckett, E. G., (1998), "Modern Numerical Methods for Fluid Flow", UC Davis Class Note.
3. DSM2 (2011). Delta Simulation Model 2 (DSM2) website, California Department of Water Resources, <http://baydeltaoffice.water.ca.gov/modeling/deltamodeling/models/dsm2/dsm2.cfm>.
4. Fischer, B. H., List, J. E., Koh, R. C., Imberger, J., Brooks, N. H., (1979), "Mixing in Inland and Coastal Waters", Academic Press, Inc.
5. Fletcher, C. A. J., (1991), "Computational Techniques for Fluid Dynamics", Springer.
6. Leveque, J.R., (1986), "Intermediate Boundary Conditions for Time-Split Methods Applied to Hyperbolic Partial Differential Equations", *Mathematics of Computation*, Vol. 47 (175), pp. 37-54.
7. Leveque, J. R., (2002), "Finite Volume Methods for Hyperbolic Problems", Cambridge University Press.
8. Oberkampf, W. L., Trucano T. G., (2002), "Verification and Validation in Computational Fluid Dynamics", SANDIA REPORT, No. SAND2002-0529.
9. Roache, P. J., (2009), "Fundamentals of Verification and Validation", Hermosa Publishers.
10. Salari, K., Knupp, P. (2000), "Code Verification by the Method of Manufactured Solutions", SANDIA REPORT, No. SAND2000-1444.
11. Saltzman, J., (1994), "An Unsplit 3D Upwind Method for Hyperbolic Conservation Laws", *J. of Computational Physics*, Vol. 115, pp. 153-168.

12. Wang, S. Y., Roache. P. J., Schmalz, R. A., Jia, Y., Smith, P. E., (2009), "Verification and Validation of 3D Free-Surface Flow Models", ASCE, EWRI.
13. Zoppou, C., Knight, J. H., (1997), "Analytical Solution for Advection and Advection-Diffusion Equation with Spatially Variable Coefficients", J. Hydraulic Eng., Vol. 123(2), pp. 144-148.

Appendix B: Hydrogeologic Characterization¹

B.1. Introduction

Understanding groundwater for engineering, agricultural or environmental activities require sufficient knowledge of subsurface geological and hydrological characteristics. Difficulties arise quantifying hydrogeological processes mainly due to incomplete characterization of subsurface properties at the required spatial scale. This scale ranges from the order of tens of meters for geothermal applications to kilometers for contamination problems to hundreds of kilometers for regional groundwater sustainability studies. Historically, many subsurface characterization techniques in hydrogeology were developed originally for petroleum and mining industries and subsequently adopted for groundwater engineering. Detailed references from these and related fields about hydrogeologic characterization exist, e.g., Charbeneau (2006), EPA (2015), Fetter (1999), Mitchell and Soga (2005), Rubin and Hubbard (2005), Todd and Mays (2005). The purpose of this chapter is to give a summary overview of some of the practicable techniques to characterize geological facies, structure, and permeability, as well as groundwater occurrence hydraulic head, and flow velocity. Due to scope restrictions many related techniques such as ground-penetrating radar, self-potential, remote sensing and GRACE data, inclinometry, environmental tracers, and seismic techniques are not covered here, and the treatment is restricted to saturated subsurface materials.

¹ This appendix was published as a book chapter: Zamani, K., Ginn, T.R., Nassar, M.K. (2016) “Hydrogeologic Characterization”, Chapter 47 in “Chow's Handbook of Applied Hydrology, Second Edition” by Ed. Vijay Singh, Published by McGraw-Hill Education.

B.2. Borehole Samples and Groundwater Monitoring Wells

Drilled wells are main source of subsurface hydrogeological information. In general, location selection, design, well drilling, and sampling phases of wells have to be conducted based on the purpose of the well, geologic structure of the site, expected groundwater occurrence and contamination, and location of the site. Drilling techniques used for well construction include hollow-stem augers, solid-stem augers, water/mud rotary, pneumatic rotary, sonic (vibrator), direct push and casing or cable. While hydraulic/pneumatic rotary and cable tool are the more common approaches for well construction, the investigation borehole drilling methods useful for obtaining core samples are hollow-stem auguring, rotary drilling, and direct push sampling. At contaminated sites, well casing and screens must be chemically compatible with the substances being monitored. For more information for on monitoring well design, drilling, installation and maintenance see ASTM D 5876 and 5978 standards (ASTM, 2011-2012).

B.2.1. Investigation borehole drilling

Site investigation with boreholes provides one-dimensional information on geologic structure and material properties via collection of core samples (e.g., ASTM, 2012a; Hunkeler, 2010). Rotary boring is a method of advancing a borehole in both rock and sedimentary formations up to depths of 350 meters, and generates core samples of diameters 10-25 cm. The drill shaft and bit are advanced within a metal core barrel that is advanced in sections to provide a temporary or permanent borehold casing. In direct rotary drilling, drilling mud or fluid is pumped down the drilling core to the bits and brings up the cuttings to the surface. In reverse-circulation rotary drilling, used for larger boreholes, the drilling fluid is pumped down the annulus between the borehole and the casing and returns through the drill barrel. This provides

the advantage of positive pressure to maintain the stability of the borehole during drilling. The method is called air-rotary drilling if instead of water, compressed air is being used. Subsurface materials returning to the surface with the drilling fluid provide qualitative if disturbed sample that can be used to characterize strata at depth. To acquire core samples, the drilling rod is raised and the drilling shaft and bit is replaced with a core sampler that is an inner bar. Some advanced bits are also able to obtaining a core sample when they are used for drilling. Disadvantages of this method compared to auger drilling and direct push techniques include potential contamination by drilling mud/fluid that may impact groundwater chemistry, and the relatively higher cost and infrastructure required.

Auger boring involves a spiral drill (augur) and is commonly used in relatively shallow and unconsolidated formations to depths up to 100 m (e.g., Hackett, 1987). A conventional auger would bring materials to the surface generally disturbed. The hollow-stem auger involves placement of the spiral drill inside a metal barrel, and core samples can be obtained as with rotary rigs by retrieving the drill and temporarily replacing it with a single or double sampling core. Advantages of this method include no involvement of drilling mud/fluid, lighter infrastructure and faster sampling at lower costs than rotary methods. Direct-push sampling is an even lighter-footprint approach that involves driving a metal barrel into the subsurface often using high-frequency hammering or vibration. Core sample retrieval may be done continuously using this method, by driving core barrel segments that are retrieved, or at intervals wherein a driven penetration tip is replaced at intervals with a segment of sample core barrel that is retrieved after it is driven till it is filled. Advantages of this method are the light equipment and rapid advancement while disadvantages include the small diameter core samples obtained and the requirement for penetrable subsurface materials.

Percussion boring (or cable-tool drilling) is a method in which soil and rock formations are broken by repeated blows of heavy chisel or bit hanging from a cable or drill rod. A steel casing is driven into the borehole behind the bit until the rock formation is reached. When the bottom of the hole is filled with broken rocks and sediments, water is added to the hole, if not already below the water table and the slurry of pulverised material is removed with bottom-loading bailer. An advantage of percussion drilling is unlike rotary drilling, no drilling fluid/mud circulated through the well, hence, induced contamination issue does not exist. The other advantage is percussion drilling is suitable for remote location due to low fuel consumption and small needs for water. This method is generally slower than other alternative drilling techniques, however, the drilling equipment are less expensive than rotary methods (ASTM, 2012a).

B.2.2. Cone penetrometry, permeametry, and electrical conductivity logging

The static penetration or cone penetration test (CPT) is a method to determine geotechnical properties of relatively shallow subsurface materials and to delineate stratigraphy of fine sand, clays and organic soils in particular (e.g., Rogers, 2006). The standard test apparatus consists of a steel cone with an apex angle of 55 to 60° and cross-section area of 10 cm² (other variations exist) that is driven at a speed of 1-2 cm/s while the tip resistance q_c and friction f_c are recorded as the instrument moves down at intervals which can be as small as 5 mm. Generally, two types of friction-cone penetrometers are used to measure q_c and f_c : mechanical and electrical, the latter provides more continuous profile compared to the former (cf. below, e.g., Harrington and Hendry, 2006). Several empirical curves that are useful in estimating the properties of subsurface have been suggested for the point resistance q_c and the friction ratio F_r , defined as the ratio of frictional resistance over cone resistance (e.g., Lunne et al., 1997, ASTM, 2012b). Some

electrical CPT has passive pressure transducer to record water pressure that is termed piezocone penetration test or “CPTU”. Advantages of this technology are low-cost and rapid characterization of strata and resistive-force of geomaterials; disadvantages include indirect relation of the measured quantity to hydrogeological properties and penetrometer blocking by strongly consolidated or hard-rock materials. For more information on conduction and interpretation of CPT for site investigation see ASTM (1995).

Butler and co-workers have extended the passive measurement of hydraulic pressure using direct-push equipment classically associated with cone penetrometry as done in the CPTU to active permeametry by inducing a hydraulic pressure at the porous cone tip and measuring the resulting pressure at different distances along the pushed shaft (Butler et al., 2002; 2007; Dietrich et al., 2008; Zshornack et al., 2013). This technique, termed DPP for direct push permeametry, measures the resulting pressure at can yield data on vertical variations in hydraulic conductivity with a resolution scale of 0.4m vertical separation for conductivity values associated with aquifer materials. The advantages of this technique are the low cost and minimal disturbance of the subsurface with high-resolution data. Disadvantages include penetrometer/permeametry refusal in tight materials, errors induced in the presence of very thin (less than 0.5m) layering structure and errors associated with bypass flow up along the penetrometer shaft; however these latter errors can be controlled by careful push strategies that take into account the structural properties expected to be encountered in the materials (e.g., Zshornack et al., 2013). Chapuis and Chenai (2010) provide a list of improvements derived from a geotechnical context for the hydrogeologic extensions of direct-push technology including using a cone tip that is the same or smaller diameter than the shaft in order to minimize bypass flow, using shape factors in order to more accurately determine the local conductivity values, and allowing sufficient time for hydraulic

equilibration to be attained prior to the collection of pressure data for identification of conductivity.

Direct push electrical conductivity logging is an alternative direct push technology that involves driving an electrical conductivity meter at sequential depths to obtain a vertical record of subsurface electrical conductivity. The device involves a metal rod with a pair of electrodes to incur an electrical current and two inner electrodes used to monitor the resulting voltage (e.g., Harrington and Hendry, 2006; Hunkeler, 2010). The advantages of this characterization approach are that electrical conductivity reflects water content and material type, with silts and clays and high water contents associated with a higher electrical conductivity than sands or gravels and lower water contents. When correlated with direct samples of the subsurface materials this technique can be used to distinguish identifiable stratigraphic units and thus to infer hydrogeologic properties. Combination of direct-push EC profiling with DPP or with small-scale slug tests provide combined data for the same bore that is useful for cross-validation of interpreted stratigraphy (e.g., Sellwood et al., 2005).

B.2.3. Electrical resistivity survey

Surface electrical resistivity (reciprocal of conductivity) test is a geophysical method for hydrogeological exploration that applies the same electrostatics of the direct push EC probe to larger scales, with current induced between two electrodes emplaced at the surface and monitoring electrodes measuring the difference in electrical potential (i.e., voltage), nearby and usually between the inducing electrodes. The current used is direct current, commutated direct current (i.e., a square-wave alternating current), or alternating current with low frequency (about 20 Hz). The resulting potential (volt) distribution can be related directly to electrical resistivity in

several idealized cases such as the case of perfectly layered strata or the case of homogeneous materials separated by a vertical dike (e.g., EPA, 2015). In the 1-D case, the electrical resistivity " ρ " of soil material is expressed as:

$$\rho = \frac{A \Delta V}{L I} \quad (\text{B-1})$$

where, A is the cross-section area of current path, L is the length of flow path, ΔV is voltage, i.e., change in electrical potential in volts, and I is the electrical current. Electrical resistivity is measured in the units of $\Omega \cdot \text{m}$ or $\Omega \cdot \text{cm}$. In case measurement is conducted over a real heterogeneous earth, the subsurface profile may consist of various layers with different resistivity and the symbol " ρ " is replaced with apparent resistivity " ρ_a ". The electrical resistivity of various soils and rocks depends largely on the pore water content; however, ion concentration is an important factor too. The general electrical resistivity ranges from less than 100 for clays to 200-3000 for sands, to 1500-2500 for fractured rock, to 3000-30000 for coarse gravels (e.g., Mitchell and Soga, 2005). There are several common procedures for measuring electrical resistivity of a soil profile with electrodes that are driven into the ground. Some of those include: Wenner array, Schlumberger, array, dipole-dipole, Lee, half-Schlumberger, polar dipole, bipole-dipole, and gradient arrays. Here, we briefly describe the first three methods which are widely utilized, relying heavily on EPA (2015). The Wenner array method consists of four in-line, equally spaced electrodes. The outer two electrodes are typically the current source and the inner two electrodes are the receiver electrodes (Loke et al., 1996; ASTM, 2010). In the Schlumberger array the potential electrodes are installed at the center of the electrode array with a small separation relative to the spacing between the current-inducing electrodes. The third common resistivity method involves the dipole-dipole array, that involves dipoles (two closely spaced

electrodes), to measure the changes of electrical properties with depth. In depth discussion of implementations, limitations and interpretation of electrical resistivity methods can be found in ASTM (2010) and in EPA (2015).

B.3. Hydraulic Methods for In-situ Conductivity Measurement

In situ hydraulic conductivity is classically viewed as the primary control on groundwater flow in response to gradients in hydraulic head, and essentially all groundwater textbooks include chapters on its characterization in place by perturbation of the hydraulic head in one borehole and its observation in the same or adjacent boreholes screened in the same aquifer material where the perturbation takes place, when identifiable (e.g., Todd and Mays, 2005; Fetter, 2000; Charbeneau, 2006). These techniques can be categorized into slug tests and pumping tests. A slug test involves the instantaneous change in the water level in a borehole followed by monitoring its return to pre-perturbation conditions. Most commonly a cylinder (“slug”) is emplaced (or removed) from the borehole, causing a sudden increase (or decrease) in the water level in the borehole. The return of water level in the borehole to initial conditions is monitored (water level in the borehole as a function of time, best obtained through a pressure transducer deep in the borehole) and analyzed to determine the local hydraulic conductivity. The local hydraulic conductivity is inferred by inversion of an approximation of Darcy’s law that results in the conductivity being proportional to the slope of the natural log of hydraulic head vs. time. The advantages of this approach are that only one borehole is needed, and no power source is required; the primary disadvantage is that the hydraulic property measured is particular to the local neighborhood of the borehole being used for the test.

Pumping tests involve extension of the slug test concept to one or more observation wells and continuous pumping at a fixed rate at a control well. Observation wells for this experiment are best as narrow-diameter wells that are screened only in the aquifer being pumped, termed “piezometers,” in order to eliminate artifacts due to storage in the monitoring well and adjacent flows. Because the hydraulic head change in this approach is typically measured in separate monitoring wells, the hydraulic conductivity values obtained are representative of the well-to-well separation scale, significantly larger than that of the slug test. The analyses of the hydraulic head drop (drawdown) data observed as a function of time in the monitoring well involves different equations depending on the nature of the pumping (constant or pulsed in steps), the confined vs. unconfined nature of the aquifer studies, and the impact of hydraulic boundaries (e.g., Charbeneau, 2000). For instance, in the confined case with constant pumping, assuming homogeneous and perfectly-layered aquifer materials, the Theis solution is used, and this can be simplified to the Jacob solution for later time parts of the observed drawdown. The more complex unconfined case is fortunately solved in Neuman (1974), and these and a suite of related solution approaches for pumping test data interpretation is available in numerous available codes (eg., www.aqtesolve.com).

B.3.1. Characterization of the hydraulic gradient and flow rates

As important as the stratigraphic understanding of the aquifer-aquitard structure of the subsurface and the corresponding hydraulic conductivities is the hydraulic gradient occurring within these formations, because the gradient and the hydraulic conductivity together dictate the natural groundwater flow direction and magnitude. The hydraulic gradient is the slope of the hydraulic head surface. In confined aquifers the hydraulic head is the level to which water will rise in a piezometer screened in the aquifer, and in unconfined aquifers the hydraulic head is

generally well-approximated by the water table. In the 2-D case with perfectly layered aquifer materials, the hydraulic head can be visualized as a surface just like topographic elevation, and the gradient is the slope of this surface. A convenient means of evaluating the slope in a given region is to emplace three piezometers in a right triangle layout, ABC, with B being the piezometer located at the right angle corner. Then the gradient is given by the two slopes, the head difference between piezometers at A and B, divided by the distance between the two, and the head difference between piezometers at B and C, divided by the distance between those two, respectively. It must be remembered that the 2-D assumption allows an approximation of what may be in reality be a 3-D gradient. A means of evaluating the vertical component of the gradient (that is, the 3rd dimension when the first two are horizontal), is via a “piezometer nest.” This is a series of piezometers installed in the same location but each screened at different depths. Vertical components of hydraulic gradients are particularly important in determining vertical fluxes across low-conductivity formations and in recharge areas.

Tracer testing provides an alternative approach to characterizing flow rates. The single-well point dilution tracer test involves emplacement of a tracer (typically dye or salt) in a known concentration in a well followed by monitoring of the change in concentration of the tracer in the well as a function of time. These data can be analyzed to estimate the ambient flow rate through its flow component through the well itself. This test typically takes a day and the analyses should take account of the well geometry and the artificially high hydraulic conductivity associated with the gravel pack associated with the well installation (e.g., Hunkeler, 2010). When more observation wells are available, this test can be generalized to a multi-well tracer test, in which the tracer is injected in one well and observed at other downstream wells. The disadvantages of this approach are the increased costs associated with installation of the additional monitoring

wells and the challenge in capturing the tracer when the flow is relatively fast compared to the rate of dispersion of the salt around the injection well. This latter aspect can lead to the tracer plume following a narrow path that may not be intercepted by the downstream well. Also this method requires knowledge of the downstream direction a priori.

Finally, vertical flows monitored within boreholes can provide useful information on hydraulic head and on conductivity profiles along the borehole (e.g., Molz et al., 1989; Paillet, 2000; USGS 2015). In the absence of pumping, passive flow may occur in a borehole screened in multiple aquifer formations (or in one very thick one) due to vertical hydraulic gradients. In this case the measurement of vertical flow rates, as a function of elevation within the borehole, reveals the difference in hydraulic head between the contributing and receiving formations or the hydraulic head difference between them, given the other. Such monitoring can be combined with pumping of a given well, in which case the flowmeter gives the relative flux rates entering (or leaving) the borehole as a function of distance. Given the knowledge of the hydraulic head within the formation, such data give the hydraulic conductivity variations along the borehole. Flowmetering in these cases can be done using a simple impeller, a heat tracer, or electromagnetic induction monitoring (e.g., USGS, 2015).

B.3.2. Recharge estimation

Characterization of the large scale behavior of subsurface flow systems is incomplete without quantification of the boundary fluxes of water entering or leaving the aquifer system. In fact if flow rates at all inflow boundaries are known for steady-state flow systems then only relative conductivity information is needed to allocate the flow to different portions of the aquifer, and if that aquifer is homogeneous with a constant conductivity then only the aquifer

geometry is needed to complete the understanding of the flow. Recharge estimation methods are many beyond the current scope and include the broad field of environmental tracer interpretation. USGS (2014) provides a summary tabulation of methods with references, advantages, and limitations. Here we briefly summarize two basic approaches to quantifying areal recharge resulting from a surface influx of water. The unsaturated zone water balance method (UZWB) uses unsaturated zone water saturation and tension (negative of pressure head) measurements before and after a recharge event (rainfall or irrigation) to quantify the increase in water content that occurs below the depth above which water is extracted by evapotranspiration. This depth is identified by changes in the water tension with depth, and the net increase in water content below this depth is areally averaged to determine net recharge. In the water table fluctuation (WTF) method, the data collected is the increase in water table elevation and the recharge is estimated as the areally averaged change in saturated thickness multiplied by the specific yield. Advantages of these methods are the high-resolution identification of event-based recharge that is a big improvement over annual water-balance estimates, and disadvantages are the requirement for multiple soil water data or water table data over the extent of the area in question. This latter requirement is the main limiter on the utility of the method for identification of event-based recharge on regional scales.

B.4. Summary

This chapter provides only the briefest survey of selected methods associated with the range of quantities requiring characterization for understanding subsurface hydrological cycles. Continued innovation in the numerous fields providing such data, including geophysical,

hydrological, electrical, is necessary to overcome our inability to characterize subsurface hydrogeological processes. The inaccessibility of the subsurface that makes hydrogeology the most challenging of the areas of environmental fluid mechanics.

Appendix B References

1. Aller, L. (Ed.). (1991). Handbook of suggested practices for the design and installation of ground-water monitoring wells (Vol. 1). Environmental Monitoring Systems Laboratory, Office of Research and Development, US Environmental Protection Agency.
2. ASTM, (1995), Designation: D 5778-95 Standard Test Method for Performing Electronic Friction Cone and Piezocone Penetration Testing of Soils.
3. ASTM, (2010), Designation D 6431: Standard Guide for Using the Direct Current Resistivity Method for Subsurface Investigation.
4. ASTM, (2011), Designation D 5978: Standard Guide for Maintenance and Rehabilitation of Groundwater Monitoring Wells.
5. ASTM, (2012a), Designation D 6286: Standard Guide for Selection of Drilling Methods for Environmental Site Characterization.
6. ASTM, (2012b), Designation D 5876: Standard Guide for Use of Direct Rotary Wireline Casing Advancement Drilling Methods for Geoenvironmental Exploration and Installation of Subsurface Water-Quality Monitoring Devices.
7. www.aqtesolve.com, accessed August 2015.
8. Butler JJ, Healey JM, McCall GW, Garnett EJ, Loheide SP (2002) Hydraulic tests with direct-push equipment. *Ground Water* 40: 25–36.
9. Butler, J.J., P. Dietrich, V. Wittig, and T. Christy. 2007. Characterizing hydraulic conductivity with the direct-push permeameter. *Ground Water* 45, no. 4: 409–419.
10. Campbell, G.S., C. Calissendorff, and J.H. Williams. 1991. Probe for measuring soil specific heat using a heat-pulse method. *Soil Sci. In Soc. Am. J.* 55:291–293.

11. Chapuis, R. P. and D. Chenai, (2010) Comment on “Characterizing hydraulic conductivity with the direct-push permeameter, by James J Butler Jr. Peter Dietrich, Volker Witting, and Tom Christy, July-August 2007, v. 45, no. 4, 409-419,” *Ground Water* 48(6): 792-795.
12. Charbeneau, R. J. (2006) *Groundwater Hydraulics and Pollutant Transport*, Waveland Press, Long Grove, Illinois, USA.
13. Dietrich P, Butler JJ, Faiss K (2008) A rapid method for hydraulic profiling in unconsolidated formations, *Ground Water* 46: 323–328.
14. Environmental Protection Agency, (2015), *Environmental Geophysics*, (8/8/2015) accessed online at: <http://www.epa.gov/esd/cmb/GeophysicsWebsite/pages/basicInformation.htm>.
15. Fetter, C. W. (1999). *Contaminant hydrogeology*. Upper Saddle River, NJ: Prentice Hall.
16. Fetter, C.W., (2000), *Applied hydrogeology (Fourth edition)*: Prentice-Hall, Inc., Englewood Cliffs, New Jersey, 691 p.
17. Hackett, G. (1987). *Drilling and Constructing Monitoring Wells with Hollow-Stem Augers Part 1: Drilling Considerations*. *Groundwater Monitoring & Remediation*, 7(4), 51-62.
18. Harrington G. A. and M. J. Hendry (2006) Using direct-push EC logging to delineate heterogeneity in a clay-rich aquitard. *Ground Water Monitoring Review* 26: 92–100.
19. Hunkeler, D., (2010). *Geological and Hydrogeological Characterization of the Subsurface*, in Timmis, K. N. (ed.) *Handbook of Hydrocarbon & Lipid Microbiology*, Springer, Berlin.
20. Jones, S. B.; Jon M. W.; and Dani O. 2002. Time domain reflectometry measurement principles and applications. *Hydrol. Process.* 16:141–153.
21. Lapham, W.W., Wilde, F.D., and Koterba, M.T., (1997), *Guide-lines and standard procedures for studies of groundwater quality Selection and installation of wells, and supporting documentation*: U.S.G.S. Water-Resources Investigations Report 96–4233, 110 p.

22. Mitchell, J.K., and K., Soga, (2005), Fundamentals of soil behavior. John Wiley and Sons.
23. Molz, F. J., R. H. Morin, A. E. Hess, J. G. Melville, and O. Guben (1989), The impeller meter for measuring aquifer permeability variations – evaluations and comparisons with other tests, *Water Resources Research* 25:1677-1683.
24. Neuman, S. P. (1974) Effect of partial penetration on flow in unconfined aquifers considering delayed gravity response, *Water Resources Research* 10(2): 303-312.
25. Paillet, F. L. (2000) A field technique for estimating aquifer parameters using flow log data, *Ground Water* 38(4): 510-521
26. Rogers, J. D. (2006). Subsurface exploration using the standard penetration test and the cone penetrometer test. *Environmental & Engineering Geoscience*, 12(2), 161-179.
27. Rubin, Y. and S. Hubbard (2005), *Hydrogeophysics*, , Springer, Delft, Netherlands, 405 pgs.
28. Sellwood, S.M., J.M. Healey, S. Birk, and J.J. Butler. 2005. Direct-push hydrostratigraphic profiling: Coupling electrical logging and slug tests. *Ground Water* 43, no. 1: 19–29.
29. Todd, D.K., and Mays, L.W., (2005), *Ground-water hydrology* (Third Edition): John Wiley and Sons, New York, 636 p.
30. USGS (2014) www.water.usgs.gov/ogw/gwrp/methods, accessed August 2015.
31. USGS (2015) www.water.usgs.gov/ogw/bgas/flowmeter, accessed August 2015.
32. Zshornack, L., G. C. Bohling, J. J. Butler Jr., and P. Dietrich (2013), Hydraulic profiling with the direct-push permeameter: Assessment of probe configuration and analysis methodology, *Journal of Hydrology* 496:195-204.